GALVANIZING OF A MEDIUM-MN

ADVANCED HIGH STRENGTH STEEL

MECHANICAL PROPERTY DEVELOPMENT AND GALVANIZING OF A

MEDIUM-MN THIRD-GENERATION ADVANCED HIGH STRENGTH STEEL

By: DANIELLA MARIE PALLISCO, B.Eng.

A Thesis

Submitted to the School of Graduate Studies

in Partial Fulfilment of the Requirements

for the Degree

Doctor of Philosophy

McMaster University

Doctor of Philosophy (2021)   McMaster University

(Materials Science and Engineering)   Hamilton, Ontario

TITLE: Mechanical Property Development and Galvanizing of

                     Medium-Mn Third Generation Advanced High Strength Steel

AUTHOR: Daniella Marie Pallisco, B.Eng. (McMaster University)

SUPERVISOR: Professor Joseph Robert McDermid

NUMBER OF PAGES: xxi, 196

Lay Abstract

The development of new automotive steels is challenging because the strategies used to make the steels both stronger and more formable (i.e., adding certain alloying elements and performing long heat treatments at high temperatures) can conflict with the application of Zn-based metallic coatings for corrosion protection. The aim of this research was to determine a heat treatment profile for a prototype steel that would allow it to meet the strength and ductility requirements for the next generation of automotive steels while maintaining its coatability. A two-step heat treatment was proposed. The first step conditioned the bulk material to develop very high strength and oxidized the surface. The steel was then immersed in an acidic solution to remove those surface oxides, then heated again to improve its ductility and facilitate the coating process. The target mechanical properties were achieved, and the coatings were high-quality and adherent.

Abstract

Medium-Mn third-generation advanced high strength steels (3G AHSS) are promising candidates for vehicle lightweighting due to their desirable balances of specific strength and ductility. However, the continuous galvanizing of these steels is challenging because their thermal processing routes are not always compatible with existing continuous galvanizing line (CGL) infrastructure and the selective oxidation of the main alloying elements during annealing can prevent reactive wetting of the substrate by the galvanizing bath. The conflicting objectives of achieving the desired mechanical properties and high-quality galvanized coatings were addressed in this work on a prototype 0.15C-5.6Mn-1.9Al-1.1Si (wt%) steel.

The alloy achieved the general mechanical property targets for 3G AHSS using a two-stage CGL-compatible thermal cycle. The martensitic pre-treatment resulted in a 80% martensitic-20% ferritic microstructure with no detectable retained austenite. Subsequent intercritical annealing for 120 s resulted in significant (0.2-0.3) volume fractions of lamellar retained austenite whose chemical composition was a strong function of intercritical annealing temperature. Hence, several combinations of yield strength, ultimate tensile strength (UTS), and total elongation (TE) were obtained due to differences in TRansformation-Induced Plasticity (TRIP) kinetics. An intercritical annealing temperature of 710°C resulted in the highest UTS × TE combination, which was attributed to these samples having a retained austenite chemical composition which enabled gradual exhaustion of the TRIP effect as well as extensive mechanical twinning. This processing route was selected for subsequent selective oxidation and reactive wetting trials.

The evolution of the selective oxide morphology, distribution, and chemistry during each annealing stage was determined as a function of process atmosphere pO_2. After the martensitic pre-treatment at dew points of –30°C, –10°C, and +5°C, a compact and complex external oxide layer (approximately 200 nm thick) was formed. An extensive internal oxide network ranging from

iv

6-10 μm deep was also formed, depleting the local matrix of solute and leaving a metallic Fe surface layer that was populated with extruded Fe nodules. Flash pickling with a hydrochloric acid-based solution dissolved the external MnO, $MnSiO_3$, and Mn_2SiO_4, leaving only dispersed $MnAl_2O_4$ nodules (approximately 50 nm thick) remaining on the surface. No significant evolution of the selective oxides occurred during intercritical annealing due to the large diffusion distances through the solute-depleted layer to the surface from the bulk matrix.

The experimental steel was successfully reactively wetted by a conventional 0.2 wt% Al (dissolved) galvanizing bath held at 460°C after an immersion time of 4 s. The primary wetting mechanism was direct wetting of the solute-depleted metallic Fe surface layer (which was aided by the additional surface area provided by the extruded Fe nodules). Evidence of several secondary reactive wetting mechanisms (such as oxide wetting, oxide lift-off, and bath metal infiltration) was also documented, showing that the antecedent $MnAl_2O_4$ nodules were not deleterious to reactive wetting in this case. The coatings were high-quality and adherent, as they resisted cracking or flaking after bending. Overall, this research shows that the two-stage processing route is promising for the production of Zn-coated third-generation advanced high strength steels.

Acknowledgements

joined this group, I never would have imagined we would be mandated to keep physically distant instead of clustering together to train, experiment, celebrate, or troubleshoot. I will always appreciate your words of encouragement and cherish the wonderful memories we made together. I hope there will soon come a day where you can struggle with the MARC coffee machine before a big group meeting again. (Make sure to plug it in to preheat it 15 minutes before you want to make coffee. Fill one of the disposable coffee cups to where the decorative lines are (~2/3 full) with ground coffee and add to the filter in the basket. When you're ready to make coffee, pour a carafe of water through the machine.)

Finally, I would like to express my immense gratitude to my friends and family. To my parents, Aldo and Donna, and sisters, Julia and Natalie, who provided me with every opportunity to live out my academic dreams and cheered me on every step of the way – I humbly say *thank you*. Lastly, I would like to thank my fiancé, Stephen, for his constant support and infinite patience.

Table of Contents

List of Figures

List of Tables

Abbreviations and Symbols

List of Abbreviations

AHSS	Advanced High Strength Steels
APT	Atom Probe Tomography
ART	Austenite Reversion Transformation
BCT	Body-Centered Tetragonal
BF	Bright Field
BIW	Body-in-White
CAFE	Corporate Average Fuel Economy
CGL	Continuous Galvanizing Line
CP	Complex Phase
CR	Cold-Rolled
DF	Dark Field
DP	Dual Phase
dp	Dew point
EDS	Energy-Dispersive X-Ray Spectroscopy
EELS	Electron Energy Loss Spectroscopy
FCC	Face-Centered Cubic
FIB	Focussed-Ion Beam
HAADF	High-Angle Annular Dark-Field
HCP	Hexagonal Close-Packed
HR-STEM	High-Resolution Scanning Transmission Electron Microscopy
IA	Intercritical Annealing
ICP-OES	Inductively Coupled Plasma – Optical Emission Spectroscopy
K-S	Kurdjumov-Sachs Crystallographic Orientation Relationship
L-IP	Lightweight Steels with Induced Plasticity
LOM	Light Optical Microscope/Microscopy
MART	Martensitic
MF	Martensitic-Ferritic
MGS	McMaster Galvanizing Simulator
NHTSA	National Highway Traffic Safety Administration
N-W	Nishiyama-Wassermann Crystallographic Orientation Relationship
PDF	Powder Diffraction File

PHS	Press-Hardened Steel
Q&P	Quenched and Partitioned Steel
RD	Rolling Direction
RSW	Resistance Spot Welding
SAD	Selected Area Diffraction
SEI	Secondary Electron Image/Imaging
SEM	Scanning Electron Microscope/Microscopy
SFE	Stacking Fault Energy
STEM	Scanning Transmission Electron Microscope/Microscopy
TD	Transverse Direction
TE	Total Elongation
TEM	Transmission Electron Microscopy
TRIP	Transformation-Induced Plasticity
TT	Through-Thickness Direction
TWIP	Twinning-Induced Plasticity
UHSS	Ultra-High Strength Steel
U.S. DOE	United States Department of Energy
UTS	Ultimate Tensile Strength
XPS	X-Ray Photoelectron Spectroscopy
XRD	X-Ray Diffraction
YS	Yield Strength
1D	One-Dimensional
2D	Two-Dimensional
3D	Three-Dimensional
1G	First-Generation
2G	Second-Generation
3G	Third-Generation

List of Symbols

a	Lattice parameter
a_i	Activity of species i
A	Sample cross-sectional area
A_O	Original sample cross-sectional area
at%	Atomic percent
$\vec{b}$	Burgers vector

C_1	Concentration of solute (in wt%) in bulk substrate
C_2	Concentration of solute (in wt%) in near-surface layer
d	Equilibrium separation distance of two partial dislocations
D_i	Diffusivity of species i
D_i'	Pre-exponential term to calculate diffusivity of species i
f_i	Volume fraction of phase i
g^*	Critical volume fraction of insoluble oxide resulting in blocked inward diffusion of oxygen
$\Delta G°$	Standard Gibbs free energy change
M_s	Martensite start temperature
M_s^σ	Deformation-induced martensite start temperature
$\left(N_M^O \right)_{crit}$	Critical mole fraction of alloying element M for the transition from internal to external oxidation
N_O^S	Mole fraction of adsorbed oxygen at the surface
pH_2	Partial pressure of hydrogen
pH_2O	Partial pressure of water
pO_2	Partial pressure of oxygen
Q_i	Activation energy for diffusion of species i
T_{atm}	Process atmosphere temperature
T_{dp}	Dew point temperature
vol%	Volume percent
V	Instantaneous volume fraction of retained austenite
V_O	As-annealed volume fraction of retained austenite
V_{MO_v}	Molar volume of oxide MO_v
wt%	Weight percent
α	Ferrite
α'	Martensite (body-centered tetragonal structure)
α_b	Bainite or bainitic ferrite
γ	Austenite
γ_{ret}	Retained austenite
Γ	Force acting between two partial dislocations

ε	Martensite (hexagonal close-packed structure)
ε	True strain
$\varepsilon_{fracture}$	True strain at fracture
μ	Shear modulus
v	Stoichiometric ratio between oxygen and metal atoms in oxide MO_v
σ	Engineering stress
σ_B	Back stress
σ_F	Forward stress prior to unloading
σ_R	Stress upon unloading
$\sigma_i(\varepsilon)$	Stress partitioned to phase i

Declaration of Academic Achievement

This thesis was prepared in partial fulfillment of the degree *Doctor of Philosophy* at McMaster University. The research was performed from May 2016 to August 2021 and examined the mechanical property development, selective oxidation, and reactive wetting of a prototype grade of third-generation advanced high strength steel during continuous hot-dip galvanizing heat treatments.

The author performed the experiments, analyzed the results, and prepared all manuscripts under the supervision of Professor Joseph McDermid. The major results of this research have been published in one peer-review journal publication, one submitted manuscript for a peer-review journal that is under review at the time this thesis was submitted, and one draft manuscript for submission to a peer-review journal. It should be noted that *Elsevier Ltd.*, the publisher of the journal *Materials Science and Engineering A,* permits authors to reuse their published articles in their theses/dissertations.

1. D.M. Pallisco, J.R. McDermid, Mechanical property development of a 0.15C–6Mn–2Al–1Si third-generation advanced high strength steel using continuous galvanizing heat treatments, Mater. Sci. Eng. A. 778 (2020) 139111. doi:10.1016/j.msea.2020.139111.

2. D.M. Pallisco, J.R. McDermid, Reactive wetting of a 0.15C-6Mn-2Al-1Si third-generation advanced high strength steel during continuous galvanizing heat treatments, Surf. Coat. Technol., Under Review (2021).

3. D.M. Pallisco, J.R. McDermid, On the selective oxidation of a 0.15C-6Mn-2Al-1Si third-generation advanced high strength steel during two-stage annealing treatments, Draft Manuscript.

1 Introduction

1.1 Overall Context

The increased demand in the automotive industry for the development and use of advanced high strength steels (AHSS) has arisen from the need to improve fuel efficiency while enhancing passenger safety. The Corporate Average Fuel Economy (CAFE) standards defined by the United States National Highway Traffic Safety Administration (NHTSA) require that fuel economy and carbon dioxide standards increase 1.5% per year for passenger cars and light trucks for model years 2021 through 2026 [1] with the objective of achieving an average fuel economy of 40.4 miles per gallon by 2026 [2]. To achieve these demands through mass reduction of the automotive body-in-white (BIW), materials with superlative combinations of strength, formability, and toughness are required. To this end, several first-generation (1G) AHSS grades, such as dual phase (DP), transformation-induced plasticity (TRIP), complex phase (CP), martensitic (MART) and press-hardened (PHS) steels are being employed in significant fractions for many structural components and safety-related applications. For example, Figure 1.1 shows that the 2021 Ford Mustang Mach-E BIW comprises significant fractions of AHSS, UHSS (ultra-high strength steels), and PHS.
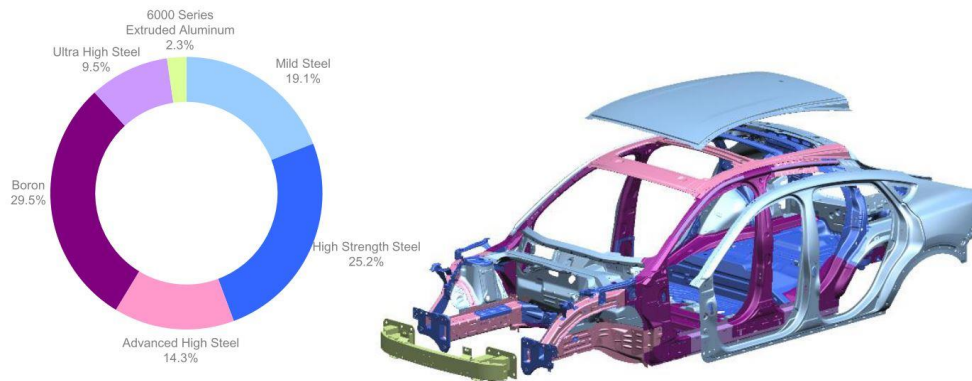
Figure 1.1: Material composition of the 2021 Ford Mustang Mach-E BIW comprising several grades of advanced steels, highlighting the significant use of AHSS, martensitic steels (labelled UHSS), and press-hardened martensitic steels (labelled boron steel) [3].

The microstructures of the 1G AHSS grades consist mainly of a ferritic matrix with various volume fractions of high-strength reinforcement phases such as martensite, bainitic ferrite, and/or transformable retained austenite. The strength-ductility balance of these steels, as indicated by the product of ultimate tensile strength (UTS) and total elongation (TE), is characterized by a UTS × TE ≤ 20,000 MPa% [4,5]. The second generation (2G) AHSS, such as high-Mn twinning-induced plasticity (TWIP) steels and lightweight steels with induced plasticity (L-IP) grades, were developed in order to improve upon the mechanical properties of the 1G AHSS. These microstructures consist of a transformable austenitic matrix that is stabilized by high levels of alloying additions, making them costly to produce and very difficult to galvanize using the continuous galvanizing process [6–8]. The general 2G AHSS property target envelope of 50,000 ≤ UTS × TE ≤ 80,000 MPa% is achieved by the activation of mechanical twinning and/or the deformation-induced ε-martensitic transformation [9]. Representative mechanical property target windows of the 1G and 2G AHSS grades are outlined in Figure 1.2.

It is evident in Figure 1.2 that a mechanical property envelope gap exists between the 1G and 2G AHSS. As such, the third generation (3G) AHSS are currently under development as a compromise between the 1G and 2G AHSS to fill this gap, as they offer superior mechanical properties to the 1G AHSS with leaner alloy compositions than the 2G AHSS. The production of materials that fulfill the 3G mechanical property targets for strength and ductility will permit the fabrication of thinner and lighter structural components than is possible with the 1G AHSS but more cost-effectively than producing them with 2G AHSS. The United States Department of Energy (U.S. DOE) has defined the 3G AHSS target mechanical property window of 36,000 ≤ UTS × TE ≤ 40,000 MPa% with specific targets of 1500 MPa UTS × 25% TE and 1200 MPa UTS × 30% TE, while the AutoSteel Partnership has specified a target of 1500 MPa UTS × 20% TE.

Matlock et al. [4,9] have advocated a more modest target envelope of UTS × TE ≥ 24,000 MPa%. The general property window for 3G steels, along with the specific U.S. DOE and AutoSteel Partnership targets, are shown in Figure 1.2.
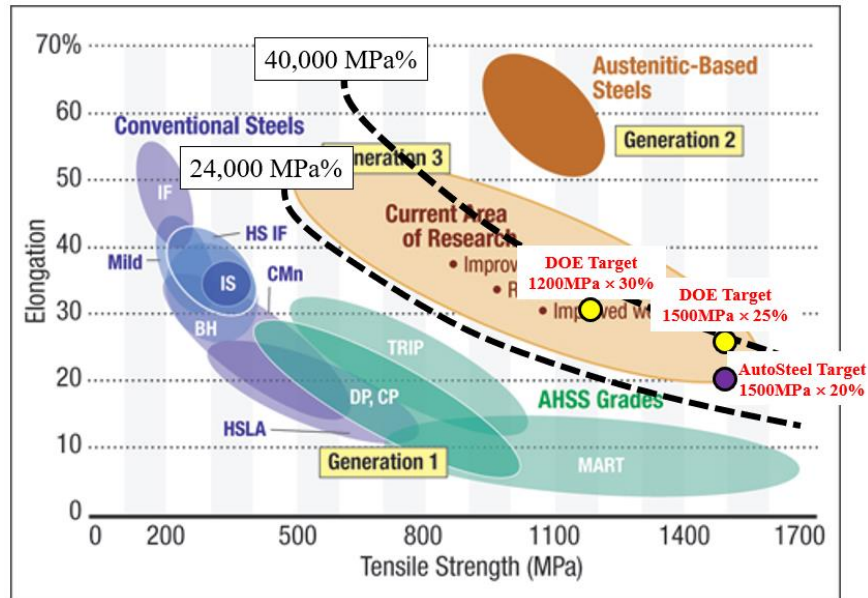
Figure 1.2: Classifications of AHSS generations with the 3G AHSS mechanical property target window and specific U.S. DOE and AutoSteel targets, after Shutte [10].

Several approaches to developing 3G AHSS grades have been proposed, and medium-Mn third-generation (3G) AHSS are amongst the promising candidate materials. These steels typically contain 5-10 wt% Mn with significant concentrations of elements such as C, Si, Al, Cr, and can contain microalloying additions of Ti, Nb, and/or V [11–21]. Thus, significant volume fractions of retained austenite can be chemically stabilized in the final as-annealed microstructure, such that the TRIP (and possibly TWIP) mechanism(s) is activated upon deformation, allowing the steel to maintain high work hardening rates and result in the desired balance of strength and ductility. It has been shown by several authors that the volume fraction and stability of retained austenite is a

strong function of the starting microstructure of the substrate as well as its thermal processing cycle [22–30].

It must be noted that automotive steels require some form of protection against aqueous corrosion in order to maintain the structural integrity and safety of the vehicle while in service. The continuous galvanizing process is amongst the most economical industrial-scale methods that can provide robust cathodic protection of steel substrates. Thus, it is highly desirable that 3G AHSS processing cycles be compatible with existing continuous galvanizing line (CGL) capabilities. A number of experimental substrates have been able to achieve the 3G AHSS mechanical property targets, but their processing routes employed long soaking times at the peak annealing temperature, such that the thermal cycles were incompatible with CGL capabilities [26,31–36]. In general, there is limited work in the literature that focuses on CGL-compatible thermal processing of 3G AHSS.

In addition to the physical limitations of CGL processing, further effort must be made to characterize the oxides of Mn, Si, Al, and Cr that form during annealing and determine whether they are deleterious to the successful reactive wetting of the substrate by the molten Zn(Al, Fe) bath. It is known that substantial coverage of the steel surface by an external oxide layer can prevent the formation of a well-developed $Fe_2Al_{5-x}Zn_x$ layer, resulting in a substrate with an inadequately adherent or defective coating [20,37–42]. Previous work on DP [43,44] and low-alloy TRIP-assisted [39–42,45,46] steels has shown that the process atmosphere oxygen partial pressure (pO_2) and alloy chemistry can be carefully selected in order to manipulate the selective oxide chemistry, morphology, and thickness such that successful reactive wetting is achieved. Moreover, recent work on a model 0.2C-6Mn-2Si steel has shown that typical Mn and Si contents in medium-Mn 3G AHSS substrates does not preclude reactive wetting by the Zn(Al, Fe) bath, provided an appropriate choice of process atmosphere pO_2 is employed [47,48]. Minor inclusions

of surface-active elements (such as Sn) to 1G and 3G steels are also being investigated as a means of reducing oxidation kinetics and improving reactive wetting [48–56].

1.2   Research Objectives

Although significant work has been dedicated to the development of steels that achieve the desired 3G AHSS mechanical properties, many processing strategies employ annealing temperatures and times that are incompatible with existing continuous galvanizing capabilities. Moreover, the successful industrial adoption of 3G AHSS requires strategies to control the selective oxidation of the substrate during thermal processing such that full reactive wetting can be achieved. Several challenges are anticipated due to the complex nature of the thermal processing cycles and the alloy compositions required to obtain 3G AHSS mechanical properties. To this end, the global objective of this thesis is to determine CGL-compatible thermal processing parameters for a prototype medium-Mn steel to achieve the defined mechanical property targets for 3G AHSS such that high quality galvanized coatings can be produced.

In Chapter 3, the microstructural and mechanical property development as a function of starting microstructure and intercritical annealing temperature will be elucidated. A candidate two-stage heat treatment that resulted in the desired 3G AHSS mechanical properties will be selected for a selective oxidation study, which will comprise Chapter 4. The effect of process atmosphere pO_2 during each of the two annealing stages on the selective oxide speciation, morphology, internal depth, and external thickness will be determined. In Chapter 5, a subset of the investigated process atmosphere pO_2 experimental matrix from the selective oxidation trials will be trialed for reactive wetting by a conventional CGL bath containing 0.2 wt% dissolved Al. The relationship between oxide chemistry, oxide morphology, and reactive wetting will be determined and a process window for successful galvanizing will be defined.

1.3 Thesis Layout

This thesis has been prepared in a sandwich format, with the layout as follows:

- Chapter 2 – Literature Review: This section provides an overview of the design strategy and physical metallurgy of medium-Mn 3G AHSS, including topics such as chemical composition, strengthening mechanisms, and microstructural development. In addition, an evaluation of the thermodynamics and kinetics of selective oxidation of AHSS during annealing treatments is included. This section concludes by examining the relationship between selective oxidation and reactive wetting of AHSS by conventional continuous hot-dip galvanizing baths.

- Chapter 3 – Microstructural and Mechanical Property Development: This chapter is a reproduction of the journal article entitled "Mechanical property development of a 0.15C-6Mn-2Al-1Si third-generation advanced high strength steel using continuous galvanizing heat treatments" published in *Materials Science and Engineering A* in 2020. This article demonstrated that the prototype 0.15C-6Mn-2Al-1Si (wt%) could achieve 3G AHSS mechanical property targets using CGL-compatible processing routes. The effects of starting microstructure and intercritical annealing temperature on retained austenite stability and, therefore, on retained austenite to martensite transformation kinetics and twinning-induced plasticity effects was also documented. The heat treatment that resulted in the best mechanical properties in this work was selected for additional selective oxidation and reactive wetting trials that are presented in the subsequent chapters of this thesis.

- Chapter 4 – Selective Oxidation: This chapter is a reproduction of the draft manuscript entitled "On the selective oxidation of a 0.15C-6Mn-2Al-1Si third-generation advanced high strength steel during two-stage annealing treatments". This work provides comprehensive documentation of the effect of process atmosphere pO_2 on the internal and external selective oxides that formed during each of the two annealing stages that were required to achieve the

3G AHSS mechanical property target envelope, as outlined in Chapter 4. It is intended to submit this article for publication in *Corrosion Science*.

- Chapter 5 – Reactive Wetting: This chapter is a reproduction of the manuscript entitled "Reactive wetting of a 0.15C-6Mn-2Al-1Si third-generation advanced high strength steel during continuous galvanizing heat treatments, under review in *Surface and Coatings Technology* at the time this thesis was submitted for examination. This article outlines the process window for the successful galvanizing of the experimental substrate by a conventional 0.2 wt% Al (dissolved) galvanizing bath. In addition, a novel reactive wetting mechanism was identified.

- Chapter 6 – Global Discussion: The effects of the thermal processing parameters on the mechanical properties, selective oxidation, and reactive wetting of the substrate are compiled and their relationships are discussed.

- Chapter 7 – Conclusions: This chapter summarizes the primary findings of this research.

- Chapter 8 – Future Work: This chapter includes some recommendations for future study in the areas of physical metallurgy, selective oxidation, and reactive wetting of medium-Mn 3G AHSS.

1.4   References

[1]   NHTSA, Corporate Average Fuel Economy, (2021). https://www.nhtsa.gov/laws-regulations/corporate-average-fuel-economy (accessed March 14, 2021).

[2]   NHTSA, Fact Sheet - SAFE Vehicles Rule, (2020). https://www.nhtsa.gov/files/14797a-saferuleinfographic033120v5tagpdf (accessed March 14, 2021).

[3]   M. Mikolaiczik, 2021 Mustang Mach-E, in: Gt. Des. Steel, 2021.

[4]   D.K. Matlock, J.G. Speer, Design Considerations for the Next Generation of Advanced High Strength Steel Sheets, in: H.C. Lee (Ed.), Proc. 3rd Int. Conf. Struct. Steels, Korean Institute of Metals and Materials, Seoul, Korea, 2006: pp. 774–781.

[5]   E. De Moor, P.J. Gibbs, J.G. Speer, D.K. Matlock, Strategies for Third-Generation Advanced High Strength Steel Development, AIST Trans. 7 (2010) 133–144.

[6]   M. Blumenau, M. Norden, F. Friedel, K. Peters, Use of pre-oxidation to improve reactive wetting of high manganese alloyed steel during hot-dip galvanizing, Surf. Coatings Technol. 206 (2011) 559–567. doi:10.1016/j.surfcoat.2011.07.088.

[7]   M. Blumenau, A. Barnoush, I. Thomas, H. Hofmann, H. Vehoff, Impact of selective oxidation during inline annealing prior to hot-dip galvanizing on Zn wetting and hydrogen-induced delayed cracking of austenitic FeMnC steel, Surf. Coatings Technol. 206 (2011) 542–552. doi:10.1016/j.surfcoat.2011.07.081.

[8]   M. Blumenau, M. Norden, F. Friedel, K. Peters, Reactive wetting during hot-dip galvanizing of high manganese alloyed steel, Surf. Coatings Technol. 205 (2011) 3319–3327. doi:10.1016/j.surfcoat.2010.11.053.

[9]   D.K. Matlock, J.G. Speer, Third Generation of AHSS: Microstructure Design Concepts, Springer, Jamshedpur, India, 2009. doi:10.1007/978-1-84882-454-6_11.

[10]   C. Shutte, SAE Technical Paper 2015-01-0405, 2015. doi:10.4271/2015-01-0405.

[11]   P. Payson, C.H. Savage, Martensite Reactions in Alloy Steels, Trans. ASM. 33 (1944) 261–280.

[12]   R.A. Grange, H.M. Stewart, The Temperature Range of Martensite Formation, Trans. AIME. 167 (1946) 467–490.

[13]   G. Thomas, J.G. Speer, D.K. Matlock, E. De Moor, Alloy Design for Fundamental Study of Quenched and Partitioned Steels, in: MS&T 2011 Conf. Proc., Columbus, Ohio, 2011: pp. 552–567.

[14]   A.E. Nehrenberg, The Temperature Range of Martensite Formation, Trans. AIME. 167 (1946) 494–498.

[15]   W. Steven, A.G. Haynes, The Temperature Formation of Martensite and Bainite in Alloy Steels - Some Effects of Chemical Composition, J. Iron Steel Inst. 183 (1956) 349–359.

[16]   K.W. Andrews, Empirical Formulae for the Calculation of Some Transformation Temperatures, J. Iron Steel Inst. 203 (1965) 721–727.

[17]   T. Kunitake, H. Ohtani, Calculating The Continuous Cooling Transformation Characteristics of Steel from its Chemical Composition, Sumitomo Search. 2 (1969) 18–21.

[18]   J.S. Kirkaldy, D. Venugopalan, Prediction of Microstructure and Hardenability in Low-Alloy Steels, in: A.R. Marder, J.I. Goldstein (Eds.), Proc. Phase Transformations in Ferrous Alloys, Metallurgical Society of AIME, Philadelphia, PA, 1983: pp. 125–148.

[19] R.L. Bodnar, T. Ohhashi, R.I. Jaffee, Effects of Mn, Si and Purity on the Design of 3.5NiCrMoV, 1CrMoV, and 2.25Cr-1Mo Baintic Alloy Steels, Metall. Mater. Trans. A. 20 (1989) 1445–1460.

[20] M.V. Li, D.V. Niebuhr, L.L. Meekisho, D.G. Atteridge, A Computational Model for the Prediction of Steel Hardenability, Metall. Mater. Trans. B. 29 (1998) 661–672.

[21] J. Mahieu, J. Maki, B.C. De Cooman, S. Claessens, Phase Transformation and Mechanical Properties of Si-Free CMnAl Transformation-Induced Plasticity-Aided Steel, Metall. Mater. Trans. A. 33 (2002) 2573–2580.

[22] W.Q. Cao, C. Wang, J. Shi, M.Q. Wang, W.J. Hui, H. Dong, Microstructure and mechanical properties of Fe–0.2C–5Mn steel processed by ART-annealing, Mater. Sci. Eng. A. 528 (2011) 6661–6666. doi:10.1016/j.msea.2011.05.039.

[23] H. Luo, Mechanical properties of Medium-Mn steel after a short intercritical annealing and its dependence on starting microstructures, in: 2nd HMnS Conf. Proc., 2014: pp. K2-85.

[24] N. Nakada, K. Mizutani, T. Tsuchiyama, S. Takaki, Difference in transformation behavior between ferrite and austenite formations in medium manganese steel, in: 2nd HMnS Conf. Proc., 2014: pp. K2-89. doi:10.1016/j.actamat.2013.10.067.

[25] N. Nakada, K. Mizutani, T. Tsuchiyama, S. Takaki, Difference in transformation behavior between ferrite and austenite formations in medium manganese steel, Acta Mater. 65 (2014) 251–258. doi:10.1016/j.actamat.2013.10.067.

[26] H. Luo, H. Dong, New ultrahigh-strength Mn-alloyed TRIP steels with improved formability manufactured by intercritical annealing, Mater. Sci. Eng. A. 626 (2015) 207–212.

[27] K.M.H. Bhadhon, J.R. McDermid, F.E. Goodwin, Effect of Galvanizing Heat Treatment on the Microstructure and Mechanical Properties of a 6Mn-1.5Si Third Generation Advanced High Strength Steel, in: Proc. 10th Conf. Zinc Zinc Alloy Coat. Steel Sheet, Galvatech 2015, Toronto, 2015: pp. 936–943.

[28] K.M.H. Bhadhon, J.R. McDermid, X. Wang, E.A. McNally, F.E. Goodwin, Fine-Scale Microstructure Characterization And Mechanical Properties Of CGL-Compatible Heat Treated Medium-Mn TRIP Steel, in: Proc. 11th Conf. Zinc Zinc Alloy Coat. Steel Sheet, Galvatech 2017, ISIJ International, Tokyo, 2017: pp. 493–500.

[29] D.M. Pallisco, K.M.H. Bhadhon, V. Patel, M. Pourmajidian, F.E. Goodwin, J.R. McDermid, 9-11: Galvanizing of Medium-Manganese Third Generation Advanced High Strength Steels, in: Proc. 4th Int'l Conf. Med. High-Manganese Steels, 2019: pp. 375–378.

[30] V. Patel, Microstructure and Mechanical Properties of Medium Mn Steel, McMaster University, 2019.

[31]   S. Lee, B.C. De Cooman, Annealing Temperature Dependence of the Tensile Behavior of 10 pct Mn Multi-phase TWIP-TRIP Steel, Metall. Mater. Trans. A. 45 (2014) 6039–6052. doi:10.1007/s11661-014-2540-6.

[32]   S. Lee, K. Lee, B.C. De Cooman, Observation of the TWIP + TRIP Plasticity-Enhancement Mechanism in Al-Added 6 Wt Pct Medium Mn Steel, Metall. Mater. Trans. A. 46A (2015) 2356–2363. doi:10.1007/s11661-015-2854-z.

[33]   K. Steineder, D. Krizan, R. Schneider, C. Béal, C. Sommitsch, On the microstructural characteristics influencing the yielding behavior of ultra-fine grained medium-Mn steels, Acta Mater. 139 (2017) 39–50.

[34]   B. Sun, N. Vanderesse, F. Fazeli, C. Scott, J. Chen, P. Bocher, M. Jahazi, S. Yue, Discontinuous strain-induced martensite transformation related to the Portevin-Le Chatelier effect in a medium manganese steel, Scr. Mater. 133 (2017) 9–13. doi:10.1016/j.scriptamat.2017.01.022.

[35]   B. Sun, D. Palanisamy, D. Ponge, B. Gault, F. Fazeli, C. Scott, S. Yue, D. Raabe, Revealing fracture mechanisms of medium manganese steels with and without delta-ferrite, Acta Mater. 164 (2019) 683–696.

[36]   R. Rana, E. De Moor, J.G. Speer, D.K. Matlock, Effects of Hot Band Annealing on the Mechanical Properties of Cold-Rolled and Intercritically Annealed Medium Manganese Steels, Metall. Mater. Trans. A. 50 (2019) 4016–4020. doi:10.1007/s11661-019-05363-1.

[37]   J. Mahieu, S. Claessens, B.C. De Cooman, Galvanizability of High-Strength Steels for Automotive Applications, Metall. Mater. Trans. A. 32 (2001) 2905–2908.

[38]   J. Maki, J. Mahieu, B.C. De Cooman, S. Claessens, Galvanisability of silicon free CMnAl TRIP steels, Mater. Sci. Technol. 19 (2003) 125–131. doi:10.1179/026708303225009300.

[39]   E.M. Bellhouse, J.R. McDermid, Selective Oxidation and Reactive Wetting during Galvanizing of a CMnAl TRIP-Assisted Steel, Metall. Mater. Trans. A. 42A (2011) 2753–2768. doi:10.1007/s11661-010-0192-8.

[40]   E.M. Bellhouse, J.R. McDermid, Selective Oxidation and Reactive Wetting During Hot-Dip Galvanizing of a 1.0 Pct Al-0.5 Pct Si TRIP-Assisted Steel, Metall. Mater. Trans. A. 43 (2012) 2426–2441. doi:10.1007/s11661-010-0192-8.

[41]   R. Sagl, A. Jarosik, D. Stifter, G. Angeli, The role of surface oxides on annealed high-strength steels in hot-dip galvanizing, Corros. Sci. 70 (2013) 268–275. doi:10.1016/j.corsci.2013.01.039.

[42]   R. Sagl, A. Jarosik, G. Angeli, T. Haunschmied, G. Hesser, D. Stifter, Tailoring of oxide morphology and crystallinity on advanced high-strength steel surfaces prior hot-dip galvanizing, Acta Mater. 72 (2014) 192–199. doi:10.1016/j.actamat.2014.03.037.

[43]   R. Khondker, A.I.M. Mertens, J.R. McDermid, Effect of annealing atmosphere on the galvanizing behavior of a dual-phase steel, Mater. Sci. Eng. A. 463 (2007) 157–165. doi:10.1016/j.msea.2006.09.116.

[44]   S. Alibeigi, R. Kavitha, R.J. Meguerian, J.R. McDermid, Reactive wetting of high Mn steels during continuous hot-dip galvanizing, Acta Mater. 59 (2011) 3537–3549. doi:10.1016/j.actamat.2011.02.027.

[45]   Y.F. Gong, H.S. Kim, B.C. De Cooman, Formation of Surface and Subsurface Oxides during Ferritic, Intercritical and Austenitic Annealing of CMnSi TRIP Steel, ISIJ Int. 48 (2008) 1745–1751. doi:10.2355/isijinternational.48.1745.

[46]   Y.F. Gong, Y.R. Lee, H.S. Kim, B.C. De Cooman, CMnAl TRIP Steel Surface Modification during CGL Processing, in: Asia-Pacific Galvaniz. Conf. 2009 Proc., Jeju Island, South Korea, 2009: p. A-41.

[47]   M. Pourmajidian, J.R. McDermid, Effect of Annealing Temperature on the Selective Oxidation and Reactive Wetting of a 0.1C-6Mn-2Si Advanced High Strength Steel During Continuous Galvanizing Heat Treatments, ISIJ Int. 58 (2018) 1635–1643. doi:10.2355/isijinternational.ISIJINT-2017-688.

[48]   M. Pourmajidian, J.R. McDermid, On the reactive wetting of a medium-Mn advanced high-strength steel during continuous galvanizing, Surf. Coatings Technol. 357 (2019) 418–426. doi:10.1016/j.surfcoat.2018.10.028.

[49]   A. Ruck, D. Monceau, H.J. Grabke, Effects of tramp elements Cu, P, Pb, Sb and Sn on the kinetics of carburization of case hardening steels, Steel Res. Int. 67 (1996) 240–246. doi:10.1002/srin.199605484.

[50]   Y. Zhang, Y. Zhang, F. Yang, Z. Zhang, Effect of Alloying Elements (Sb, B) on Recrystallization and Oxidation of Mn-Containing IF Steel, J. Iron Steel Res. Int. 20 (2013) 39–44. doi:10.1016/S1006-706X(13)60067-9.

[51]   L. Cho, M.S. Kim, Y.H. Kim, B.C. De Cooman, Influence of Minor Alloying Elements on Selective Oxidation and Reactive Wetting of CMnSi TRIP Steel during Hot Dip Galvanizing, Metall. Mater. Trans. A. 45 (2014) 4484–4498. doi:10.1007/s11661-014-2394-y.

[52]   L. Cho, E.J. Seo, G.S. Jung, D.W. Suh, B.C. De Cooman, Surface Selective Oxidation of Sn-Added CMnSi TRIP Steel, Metall. Mater. Trans. A. 47 (2016) 1705–1719. doi:10.1007/s11661-016-3331-z.

[53]   J. Oh, L. Cho, M.S. Kim, K. Kang, B.C. De Cooman, The Effect of Bi on the Selective Oxide Formation on CMnSi TRIP Steel, Metall. Mater. Trans. A. 47 (2016) 5474–5486. doi:10.1007/s11661-016-3735-9.

[54]   M. Pourmajidian, B. Langelier, J.R. McDermid, Effect of Process Atmosphere Dew Point and Tin Addition on Oxide Morphology and Growth for a Medium-Mn Third Generation Advanced Steel During Intercritical Annealing, Metall. Mater. Trans. A. 49 (2018) 5561–5573. doi:10.1007/s11661-018-4855-1.

[55]   G. Seyed Mousavi, B. Langelier, J.R. McDermid, Effect of Sn Addition, Process Atmosphere pO2, and Annealing Time on the Selective Oxidation of a C-2Mn-1.7Si (Wt Pct) Advanced High-Strength Steel During Continuous Galvanizing, Metall. Mater. Trans. A. 50 (2019) 2898–2911. doi:10.1007/s11661-019-05202-3.

[56]   K.M.H. Bhadhon, J.R. McDermid, F.E. Goodwin, Effect of process atmosphere dew point and minor Sn addition on the selective oxidation during intercritical annealing of a medium-Mn third-generation advanced high strength steel, in: Proc. 12th Conf. Zinc Zinc Alloy Coat. Steel Sheet, Galvatech 2021, ASMET, Vienna, Austria, 2021: pp. 404–412.

2   Literature Review

Although third-generation advanced high strength steels (3G AHSS) are a current topic of intense investigation, there is substantial scientific work on the first- and second-generation steels that provide some fundamental knowledge and insight into the processing-structure-property relationships that govern medium-Mn steels. Moreover, significant advances in the field of continuous hot-dip galvanizing have been achieved since the mid-1990s. This literature review is not intended to provide a comprehensive account of the current states of ferrous physical metallurgy and industrial galvanizing processes. It will, instead, document the design strategies for the development of 3G AHSS in general (and medium-Mn 3G AHSS in particular); summarize what is known about the microstructural evolution and strengthening mechanisms that govern the mechanical properties of medium-Mn 3G AHSS; and discuss the challenges of selective oxidation and reactive wetting of AHSS.

2.1   Design of Third-Generation Advanced High Strength Steels

A simple composite model based on the rule of mixtures was employed by Matlock et al. [1,2] to model the mechanical properties (i.e. total elongation, TE, and ultimate tensile strength, UTS) of dual phase ferrite + martensite and austenite + martensite microstructures with varying volume fractions of martensite. The calculated UTS and TE for different volume fractions of the microstructural constituents were plotted and superimposed on a graph illustrating the general mechanical properties of various AHSS grades. As can be seen in Figure 2.1, the 1G AHSS mechanical property band corresponded well to the ferrite + martensite models, while the 3G AHSS mechanical property targets were predicted by the mixed austenite + martensite models. It was assumed that the austenite would be fully stable and not undergo the deformation-induced transformation to martensite for the properties presented in Figure 2.1 [1–4].
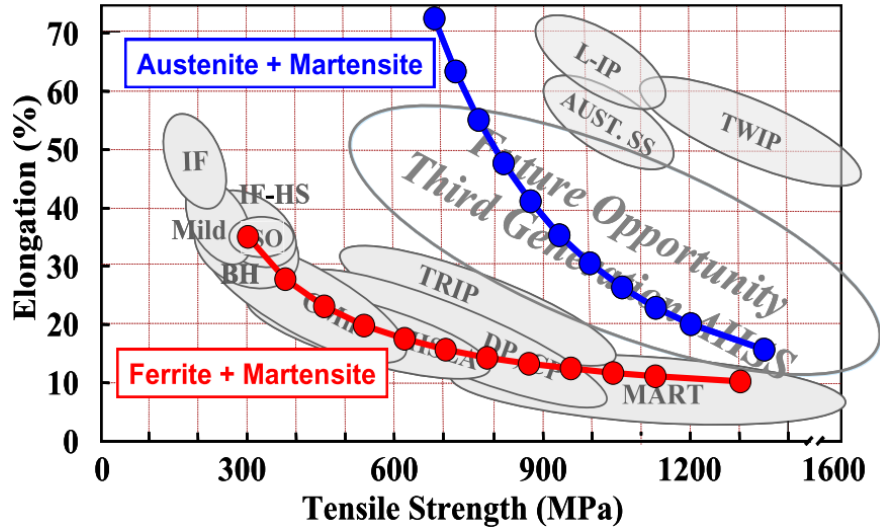
Figure 2.1: Predicted strength and ductility combinations of varying ferrite + martensite and austenite + martensite mixtures superimposed on the general properties of different advanced high strength steel families [4].

More sophisticated models can be fabricated if the austenite stability and martensitic transformation kinetics are considered in addition to the rule of mixtures. (The factors determining retained austenite stability will be elaborated upon in §2.2.3.3). While considering four hypothetical scenarios for austenite stability based on the Olson-Cohen model of retained austenite transformation [5,6], Matlock et al. [4] predicted the mechanical properties of ferrite + austenite microstructures with varying volume fractions of each constituent and different austenite stabilities. As seen in Figure 2.2, a grade consisting of ferrite with unstable austenite (curve D) that exhausted the deformation-induced martensitic transformation at low stresses/strains would display properties that align with the 1G AHSS (i.e. ferrite + martensite) property band. Contrastingly, the grades with more stable austenite (curves B and C) would exhibit more favourable transformation kinetics and undergo a more gradual austenite to martensite transformation, resulting in mechanical properties that would be more aligned with the 3G AHSS mechanical property target envelope. The stable austenite in A-type grades would have sluggish

transformation kinetics and not readily or completely transform to martensite upon deformation. As such, the development vector of the properties obtained for these grades could extend towards the property envelope exhibited by the fully austenitic 2G AHSS. Therefore, the model suggests that 3G AHSS mechanical property targets could be achieved by creating complex microstructures with significant (~0.40) volume fractions of relatively stable austenite that would exhibit significant strain hardening in a high-strength martensitic matrix. By extension, a grade with the same global composition could be processed differently in order to achieve different austenite stabilities with different transformation kinetics and target a different point in the 3G AHSS mechanical property target envelope.
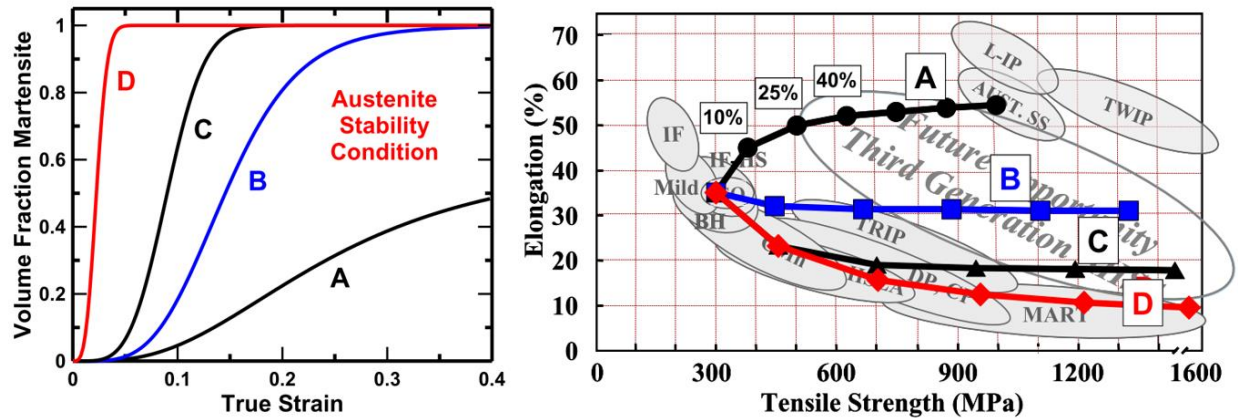
Figure 2.2: (a) Effect of austenite stability on the martensite fraction as a function of true strain illustrated by four steels with different hypothetical austenite stabilities. (b) Predicted mechanical property combinations corresponding to ferrite + austenite mixtures, where the austenite stabilities correspond to those in (a). The points on each data curve represent an initial austenite fraction ranging from 0 to 85%. Adapted from Matlock et al. [4].

Several approaches to developing these complex 3G AHSS microstructures have been proposed, including quenched and partitioned (Q&P) [2,7], enhanced dual phase [8,9], modified transformation-induced plasticity [10–15], ultrafine bainitic [16–22], and flash processed [23–25] steels. Although these compositions and processing routes have resulted in very interesting microstructures, in general these strategies are not compatible with continuous galvanizing line

(CGL) processing and/or have not resulted in mechanical properties that achieve 3G AHSS mechanical property targets. On the other hand, medium-Mn transformation- and twinning-induced plasticity steels are promising candidates for automotive applications since they can be processed in a CGL-compatible thermal cycle to achieve 3G AHSS targets [26–28]

2.2   Medium-Manganese TRansformation/TWinning-Induced Plasticity-Assisted Steels

Based on work by Grange and Miller [29,30], Merwin [31,32] proposed an alloying and processing concept to produce duplex ferrite + austenite microstructures in steels containing 5-7wt% Mn and 0.1wt% C by hot rolling, cold rolling, and intercritical annealing. The thermal cycles required to produce the desired duplex microstructures could be CGL-compatible if the intercritical annealing time were approximately 120 s and an overaging step (similar to the isothermal bainitic hold required for low-alloy TRIP-assisted steels) at approximately the same temperature as the galvanizing bath (i.e. around 460°C) were included. A schematic thermal profile of such a cycle is shown in Figure 2.3, adapted from Patel [28]. A wide variety of microstructures and mechanical property balances can be obtained by varying the starting microstructure, intercritical annealing parameters, and the alloy additions of Si, Al, Cr, and other elements. This section outlines typical chemical compositions; the microstructural development by means of austenite reversion during intercritical annealing; and strengthening mechanisms of medium-Mn TRIP/TWIP-assisted steels.
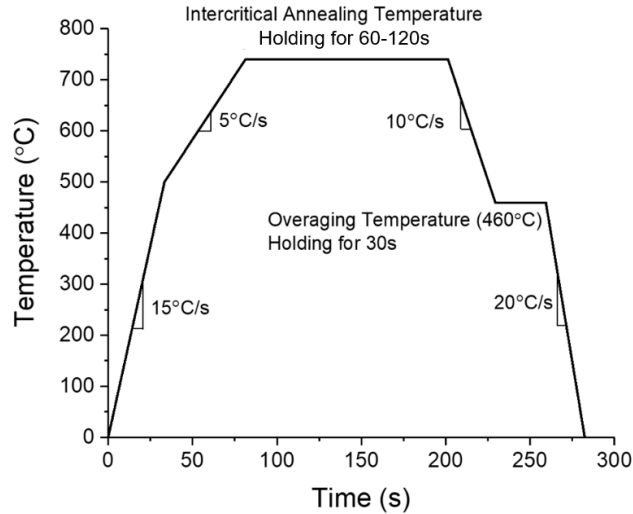
Figure 2.3: Schematic thermal profile for the CGL-compatible intercritical annealing of a medium-Mn 3G AHSS grade, after Patel [28].

2.2.1 Chemistry of Medium-Mn TRIP/TWIP-Assisted Steels

The mechanical properties of medium-Mn TRIP/TWIP-assisted steels are reliant upon the chemical and mechanical stabilization of significant volume fractions of retained austenite at room temperature [1,4,33–36]. To this end, C (0.05-0.4 wt%) and Mn (4-12 wt%) are chosen as austenite stabilizing elements [37] over Ni (which is costly) and Cu (which is known to cause problems with hot-shortness) [38]. The additions of C and Mn also provide additional solute strengthening to the alloy [39], as will be discussed in §2.2.3.1. The ferrite stabilizers Si (1-2 wt%) and Al (1.5-3 wt%) [37] are also considered for their abilities to act as nucleation inhibitors to carbide precipitation due to their low solubilities in cementite [40–47]. The prevention of carbide formation tends to increase C and Mn partitioning to intercritical austenite, which decreases its M_s and improves its chemical stability [47–49]. Si is also a potent solid solution strengthener (though not as potent as C) [39], but its selective oxidation in the CGL environment (as described in §2.3.1) has led to interest in its partial or complete replacement by Al, which will oxidize internally in the CGL environment [45,50]. However, Al is a weak solid solution strengthening element [39] (as shown

17

in §2.2.3.1 and Figure 2.10) so it is not perfectly substitutable for Si in high-strength alloys, such as in the 3G TRIP/TWIP steels. Despite their carbide-forming nature, Cr and/or Mo can be added to improve hardenability [48,51].

The low-alloy TRIP steel literature suggests that Ti, Nb, and V would be promising micro-alloying additions to medium-Mn 3G AHSS to promote grain refinement and precipitation strengthening through the formation of carbides and/or nitrides [52–55]. The effects of these microalloying additions on retained austenite stability are still disputed, despite significant research efforts. For example, previous work on Nb-containing low-alloy TRIP-assisted steels has proposed that Nb additions lower retained austenite stability due to the tying up of carbon by NbC precipitates [55] or by inhibiting carbon partitioning to retained austenite during the isothermal bainitic hold [56,57]. However, it has been reported that Nb additions increase the mechanical stability of retained austenite by refining the austenite grain size and thus lowering the martensite start (M_s) temperature [58,59], while others have suggested that Nb additions improve austenite chemical stability by delaying carbide precipitation during the bainitic transformation, thus increasing the volume fraction and the carbon content of retained austenite [58,60,61]

The effects of alloying additions on transformation temperatures must also be considered. Alloying with C, Mn, Si, Cr, Ni, and/or Nb will lower the M_s temperature, which results in improved retained austenite stability [48,59,62–64]. Additions of Si, Al, and P will increase the Ac_1 and Ac_3 temperatures, which may allow for improved austenite reversion kinetics due to the resulting increase in intercritical annealing temperature [65,66]. However, higher Al levels may result in the final microstructures containing significant fractions of α- and/or δ-ferrite [34,67–69].

Some recent work has been performed to determine the effects of so-called surface-active elements on the selective oxidation and reactive wetting of medium-Mn TRIP/TWIP grades. This

strategy was motivated by the work of several authors who documented the change in oxide morphology, reduction of oxide growth kinetics, and, thus, improvement in reactive wetting for low-alloy TRIP steels with minor Sn [70,71], Sb [70], and Bi [72] additions. Pourmajidian and McDermid showed that although they were able to successfully reactively wet a 0.1C-6Mn-2Si (wt%) steel by increasing the annealing atmosphere pO_2, their results were improved by adding 0.05wt% Sn to the baseline composition [73–75]. Additional discussion of this alloying concept and its effects on selective oxidation and reactive wetting is provided in §2.3.2.2.

2.2.2   Austenite Reversion Kinetics

The intercritical annealing of martensitic steels results in the so-called austenite reversion transformation (ART) [76,77]. This process is essential in forming sufficient volume fractions of intercritical austenite with adequate C and Mn to chemically stabilize it at room temperature, often resulting in ultra-fine grained complex-phase microstructures that result in the desired 3G AHSS mechanical properties. Significant research efforts have been dedicated to documenting the mechanisms that govern austenite reversion and how this transformation is affected by the starting microstructure of the steel.

Arlazarov et al. [78] examined a 0.1C-4.6Mn (wt%) alloy that was intercritically annealed from an as-received tempered martensitic microstructure. They determined that partial recrystallization occurred prior to carbide precipitation at high angle grain boundaries (such as prior austenite grain boundaries), and these regions became austenite nucleation sites. Hence, the resulting globular microstructure contained homogeneously distributed austenite. However, when intercritically annealing their substrate following an austenitization (750°C for 30 min) and quenching treatment to obtain a martensitic starting microstructure, carbides precipitated at low- and high-angle lath and grain boundaries, resulting in a mixed microstructure with lamellar and globular constituents. A schematic of the proposed ART mechanisms is shown in Figure 2.4. After

intercritical annealing at 670°C for holding times between 1-21 hours, the properties were relatively stable with yield strengths varying from 510-570 MPa, ultimate tensile strengths of approximately 1020-1100 MPa, and uniform elongations of approximately 12%. They performed a follow-up study on the same alloy [79] from the martensitic starting microstructure but with a lower intercritical annealing temperature of 650°C and intercritical annealing times of 3 minutes to 30 hours. Significantly more variability in the mechanical properties were observed as a function of intercritical annealing time, as shown in Figure 2.5(a), with yield strengths ranging from approximately 400-700 MPa, ultimate tensile strengths ranging from 760-900 MPa, and total elongations ranging from 15-32 %. The differences in mechanical properties were attributed to the different retained austenite volume fractions (see Figure 2.5(b)) and stabilities, where increasing intercritical annealing times resulted in lower austenite stability. SEM micrographs (Figure 2.5(c)) showed the dual blocky and lamellar nature of the microstructural constituents, and TEM micrographs (Figure 2.5(d)) provided evidence of plasticity enhancement via the transformation and twinning of retained austenite.

Additional insight into the nature of the retained austenite morphology after annealing was provided by Kim et al. [80] in their study of the microstructural evolution of a 0.2C-2.2Mn-1.5Si (wt%) alloy. They examined one cold-rolled starting microstructure comprising ferrite and pearlite (Figure 2.6 (a)), as well as two different martensitic starting microstructures, where one (labelled M1, Figure 2.6(b)) had a small volume fraction (approximately 0.03) of retained austenite in the otherwise martensitic microstructure, and the other (labelled M2, Figure 2.6(c)) had no detectable retained austenite. The samples that were intercritically annealed from the cold-rolled starting microstructure had the slowest austenite reversion kinetics, which was attributed to the relatively slow dissolution of the larger cementite particles found in this starting microstructure. As shown

in Figure 2.6(d), the final microstructure had a globular morphology. In contrast, the initial retained austenite in the M1 starting microstructure manifested in a lamellar morphology which coarsened during intercritical annealing, resulting in a lamellar final microstructure (Figure 2.6(e)). However, the M2 martensitic microstructure that did not have any significant initial retained austenite required carbide precipitation at high-angle grain boundaries to provide sites for austenite nucleation and growth, resulting in a globular morphology with some lamellar packets (Figure 2.6(f)). The microstructural evolution of the CR and M2 martensitic microstructure after intercritical annealing are consistent with the aforementioned findings of Arlazarov et al. [78].
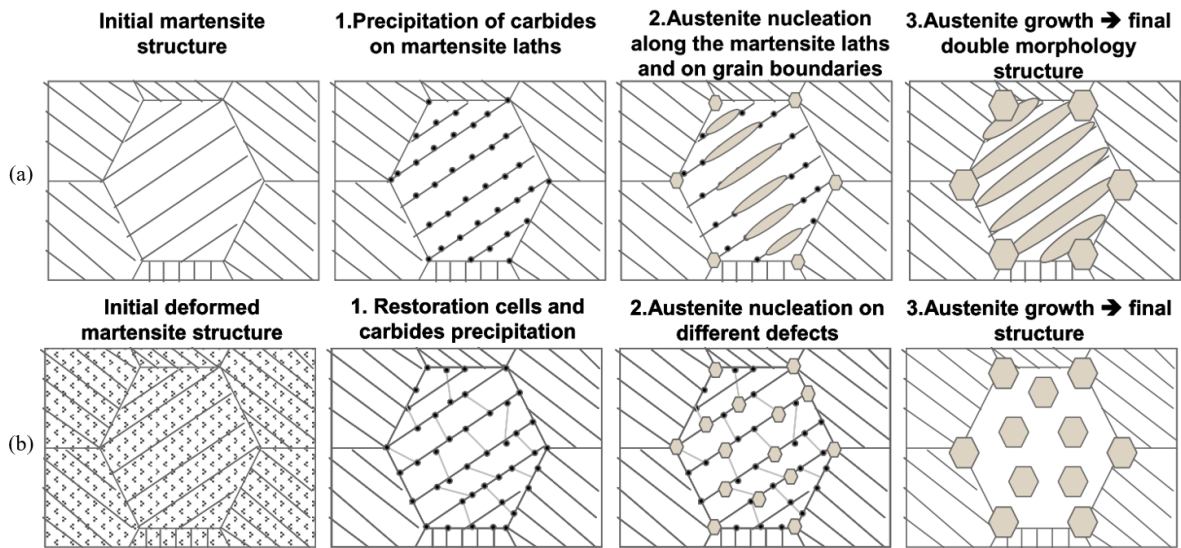
Figure 2.4: Schematic diagrams of the austenite reversion processes for initial microstructures comprising (a) fresh martensite and (b) cold-rolled martensite + bainite, as proposed by Arlazarov et al. [78]
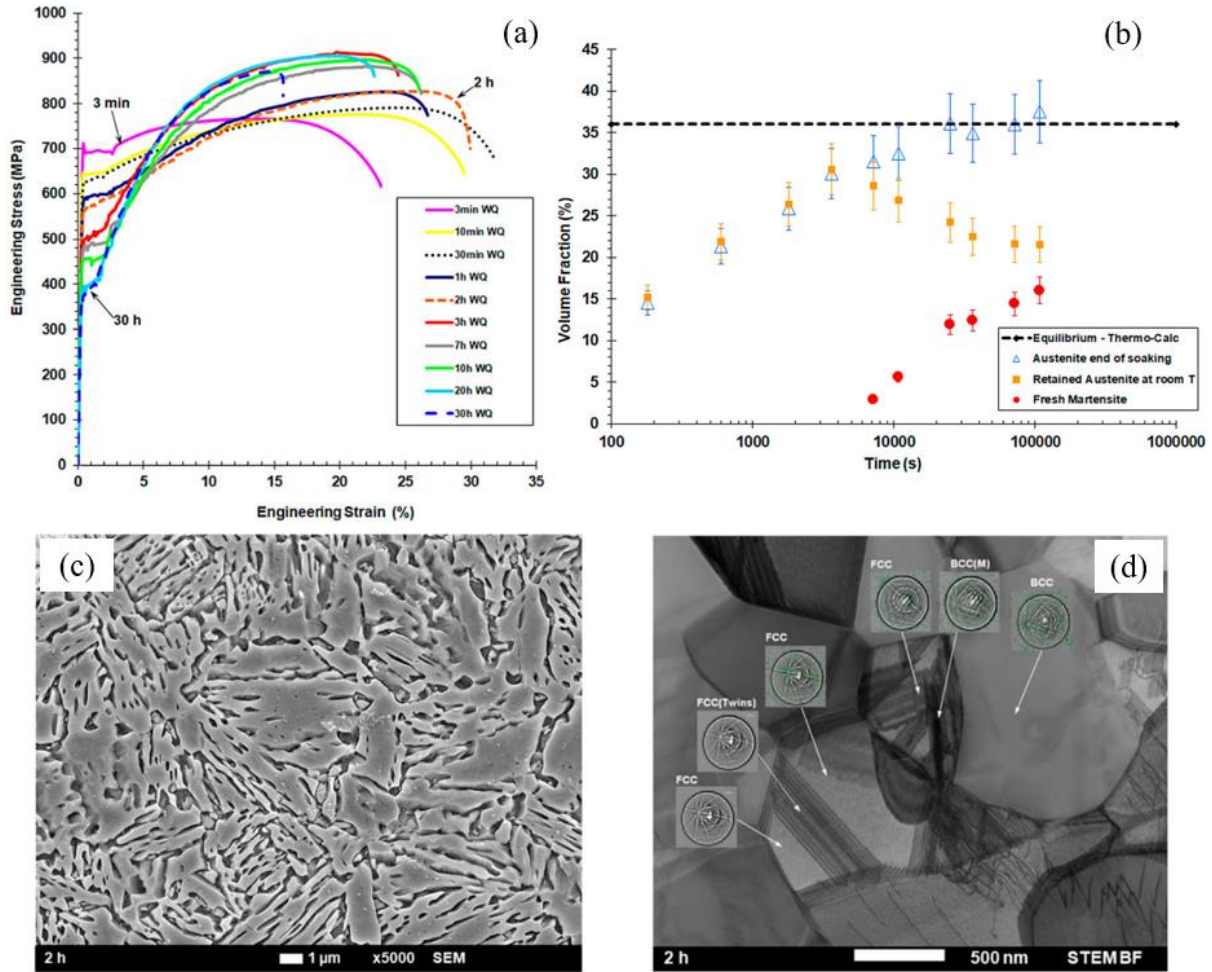
Figure 2.5: (a) Engineering stress-strain curves showing the variation in mechanical properties as a function of IA time obtained for a 0.1C-4.7Mn (wt%) steel for a starting martensitic microstructure and IA temperature of 650°C; (b) intercritical austenite, retained austenite, and fresh martensite volume fractions as a function of intercritical annealing time, with the black dashed line showing the equilibrium austenite fraction at 650°C; (c) SEM micrograph for IA time of 2 hours; (d) TEM micrograph for IA time of 2 hours showing evidence of the TRIP and TWIP effects. Figures adapted from Arlazarov et al. [79].
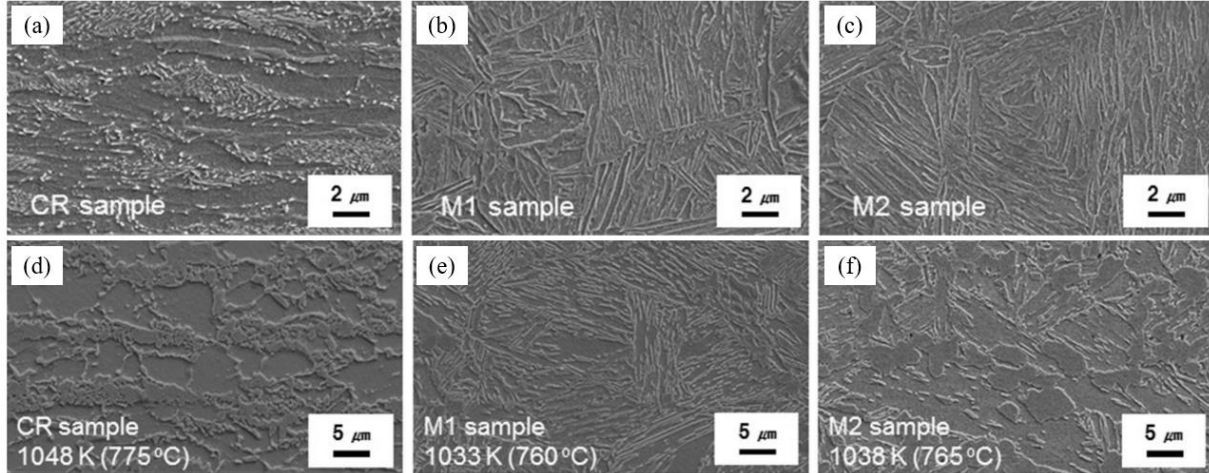
Figure 2.6: SEM micrographs of the starting microstructures before intercritical annealing: (a) cold-rolled (CR), (b) martensite + 0.03 vol% retained austenite (M1), (c) martensite - no detectable retained austenite (M2); and after intercritically annealing for 1 s: (d) CR + IA at 775°C, (e) M1 + IA at 760°C, (f) M2 + IA at 765°C. Images adapted from Kim et al. [80]

Luo and Dong [35] investigated the effects of starting microstructure and intercritical annealing temperature on the microstructural evolution and mechanical properties of 0.1C-5Mn and 0.2C-5Mn (wt%) alloys. Summative plots from this work are shown in Figure 2.7, where it is shown that the mechanical properties were a strong function of the aforementioned parameters, with the martensitic starting microstructure samples showing generally superior properties. As shown in Figure 2.7(b), they observed that austenite reversion kinetics were accelerated during intercritical annealing when using a martensitic starting microstructure as compared to a cold-rolled starting microstructure containing tempered martensite, ferrite, and cementite. The authors posited that the martensitic starting microstructure had a finer-scale lath-type structure which provided a greater number of nucleation sites for austenite as compared to the coarser recrystallized ferrite grains in the cold-rolled microstructure. However, an explicit discussion of the driving forces for austenite nucleation and growth was not included in this work. By extending the conclusions of Kim et al. [80], it can be surmised that the martensitic starting microstructure of

Luo and Dong [35] contained films of retained austenite between martensite laths that coarsened during intercritical annealing, but this was not confirmed. Luo and Dong also found that the cold-rolled starting microstructure resulted in a globular final microstructure and that the martensitic starting microstructure resulted in a lamellar final microstructure. It was proposed that the fine-grained lamellar retained austenite from the martensitic starting microstructure would be more chemically stable due to additional enrichment in C and Mn from surrounding phases and the shorter diffusion distances.
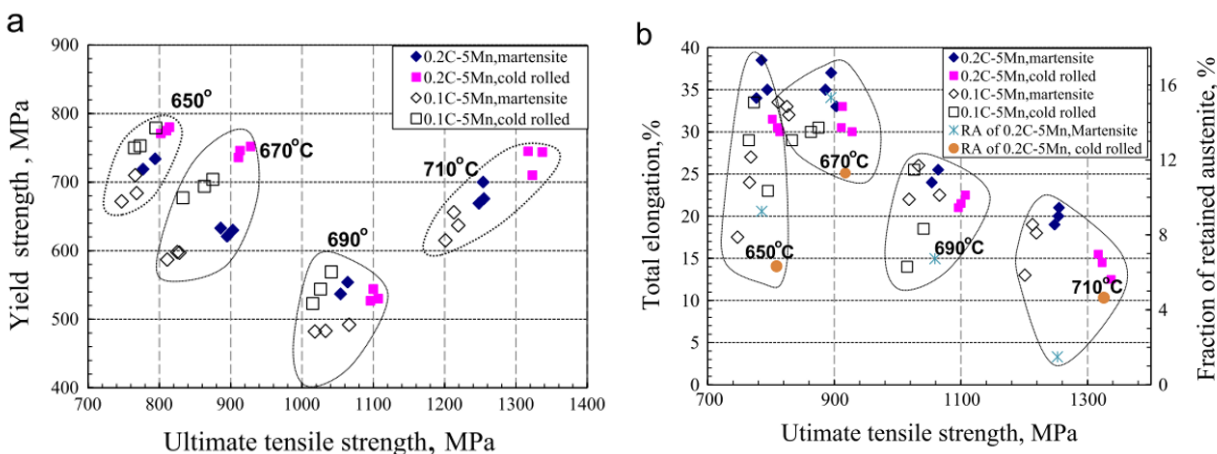
Figure 2.7: Effects of substrate chemistry, starting microstructure, and intercritical annealing temperature on (a) ultimate tensile strength and yield strength, (b) ultimate tensile strength, total elongation, and retained austenite volume fraction [35].

Bhadhon et al. [26,81] and Patel [28] have documented the austenite reversion kinetics for their 0.2C-6.1Mn-1.5Si-0.5Al-0.5Cr and 0.15C-5.5Mn-1.0Al-1.2Si (wt%) prototype medium-Mn steels, respectively, as a function of starting microstructure (cold-rolled tempered martensite or fresh martensite) and intercritical annealing temperature. Annealing times of 60 to 600s and peak annealing temperatures of 675°C or 710°C (Bhadhon et al. [26,81]) or 670°C to 740°C (Patel [28]) were investigated. The experimentally determined volume fraction of retained austenite as a function of annealing parameters for these alloys is shown in Figure 2.8. For both alloys, less time

was required to obtain the maximum volume fraction (approximately 0.3 to 0.4) of retained austenite when annealing from a martensitic starting microstructure than from the cold-rolled tempered martensite microstructure. These researchers found that the volume fraction of retained austenite after annealing tended to increase and then decrease with increasing annealing time and proposed that the longer annealing times allowed for the formation of additional intercritical austenite that was not sufficiently enriched in C and Mn to be chemically stable upon cooling. Annealing at too high of a temperature resulted in decreasing fractions of retained austenite, also likely due to the formation of large fractions of intercritical austenite that were insufficiently enriched in C and Mn to remain chemically stable upon cooling to room temperature or because of C uptake in precipitated carbides. A schematic diagram showing the predicted effects of C and Mn enrichment on austenite stabilization and final microstructural constituency as a function of intercritical annealing temperature was adapted from De Moor et al. [82] and is shown in Figure 2.9. Regardless, it is critical to note Bhadhon et al. and Patel showed that that the austenite reversion kinetics were sufficiently rapid that a peak annealing time of 60 or 120 s at an appropriate intercritical annealing temperature resulted in a final retained austenite volume fractions of 0.3 to 0.4, which is promising for CGL-compatible processing [26,28,81].

To conclude this section, the literature published on the microstructural and mechanical property development of medium-Mn 3G AHSS overwhelmingly shows that improved properties are obtained by a two-stage annealing treatment [26,28,35,78,80,81,83]. The first stage is an austenitization step wherein the cold-rolled as-received microstructure is transformed to fresh martensite, and the second stage comprises intercritical annealing (and possibly overaging) to create a final microstructure with chemically stable retained austenite in a martensitic matrix.
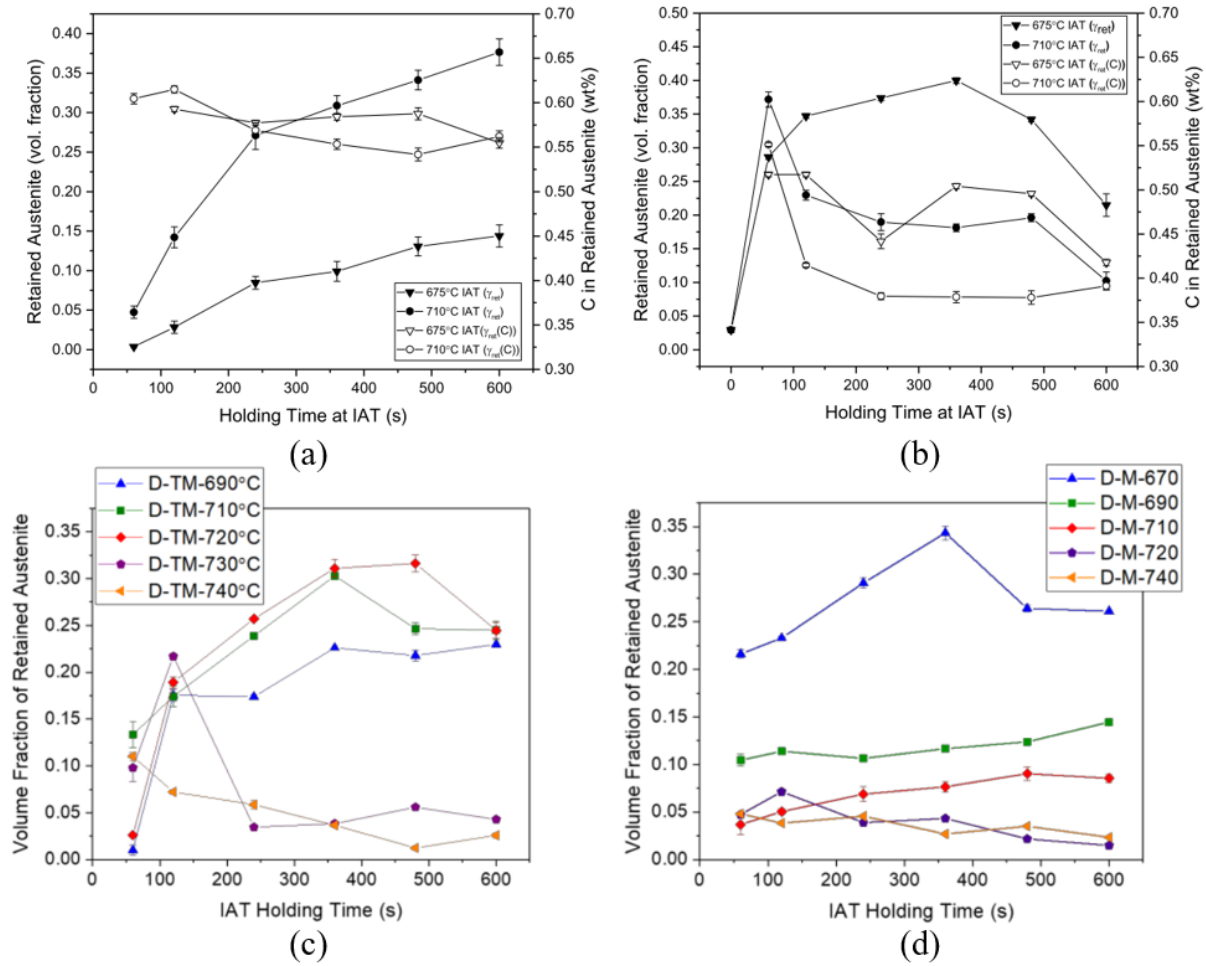
Figure 2.8: Volume fraction and calculated carbon content of retained austenite as a function of intercritical annealing time and temperature for 0.2C-6.1Mn-1.5Si-0.5Al-0.5Cr (wt%) steel: (a) cold-rolled starting structure, (b) martensitic starting structure [84]. Volume fraction of retained austenite as a function of intercritical time and temperature for 0.15C-5.5Mn-1.0Al-1.2Si (wt%) steel: (c) cold-rolled starting structure, (d) martensitic starting structure [28].
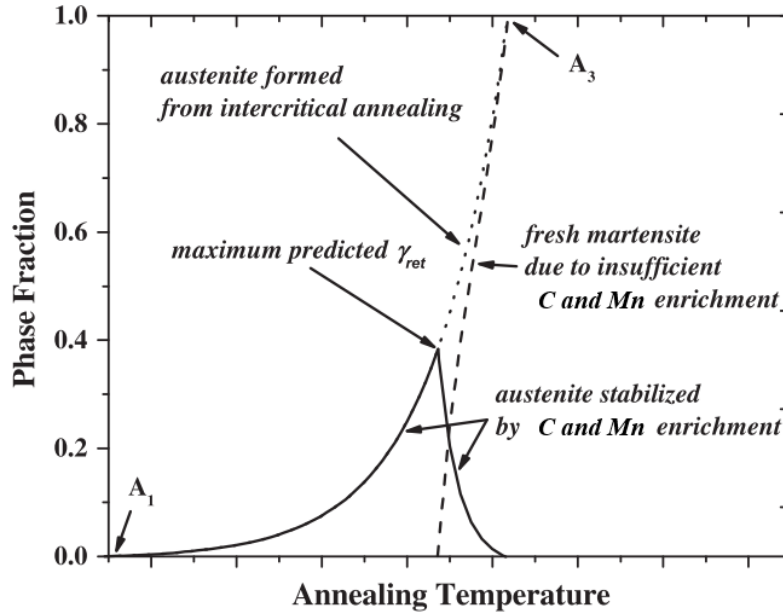
Figure 2.9: Schematic showing austenite stabilization through C and Mn enrichment as a function of annealing temperature for a hypothetical alloy, after De Moor et al. [82].

2.2.3   Strengthening Mechanisms of Medium-Mn TRIP/TWIP-Assisted Steels

The chemical composition and thermomechanical processing routes of medium-Mn TRIP/TWIP-assisted steels are designed such that the final microstructures can exploit several strengthening mechanisms to achieve the desired mechanical property targets. This section outlines several of these mechanisms, including solid solution strengthening, composite strengthening, transformation-induced plasticity, and twinning-induced plasticity.

2.2.3.1   *Solid Solution Strengthening*

The solid solution strengthening effects of various alloying elements in ferrite, as calculated by Pickering [39], are documented in Figure 2.10. It can be seen that the interstitial solutes C and N have the greatest contributions to solid solution strengthening, followed by P. However, high C, N, and P levels can be problematic as they reduce the weldability, toughness, and ductility of the substrate. Thus, elements such as Si and Mn are relied upon for their solid solution strengthening capabilities. As documented in several publications [45,50,85–88], Al can

partially replace Si to delay carbide precipitation from austenite while avoiding the formation of external Si oxides that are deleterious to reactive wetting. However, it should be noted that Al slightly reduces the yield strength of ferrite, as seen in Figure 2.10, and that significant additions of Al are also known to be problematic during continuous casting [51,89,90].
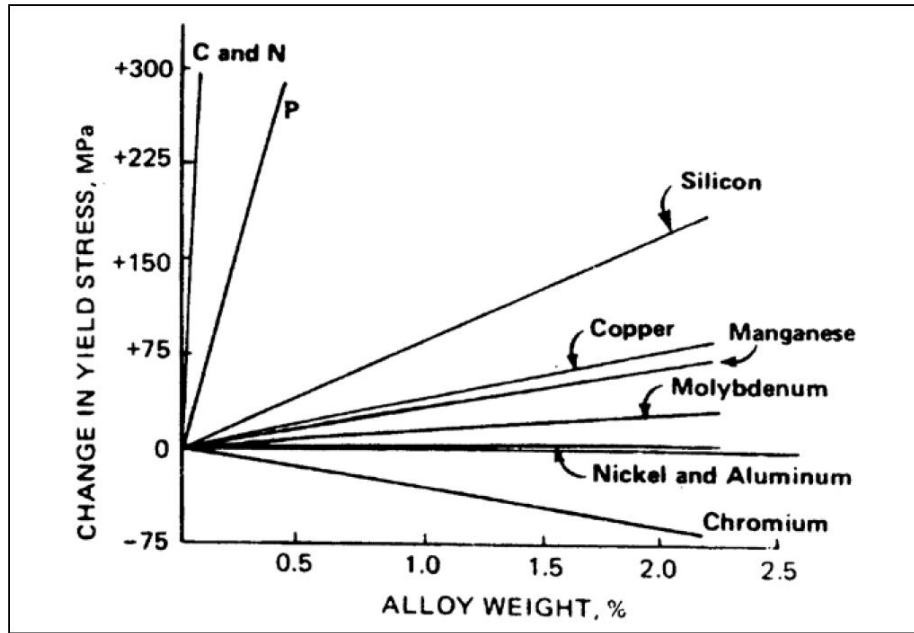
Figure 2.10: Solid solution strengthening contributions of different alloying elements as a function of their alloying content in ferrite [39].

The effects of interstitial C on the solid solution strengthening of martensite have also been extensively documented, where Krauss [91] claims that this is a dominant strengthening mechanism in martensite in addition to its high dislocation density. It should be noted that Mn also provides additional solid solution strengthening in martensite, according to work done by Nordstrom [92].

2.2.3.2 Composite Strengthening

Extensive research performed on low-alloy TRIP-assisted steels has resulted in a deeper understanding of the different yield strengths and hardness values of the constituent phases (i.e.

ferrite, bainitic ferrite, martensite, and retained austenite) that make up these microstructures. These steels resemble composite materials in that the harder phases are dispersed in the softer ferrite matrix. Furnémont [93] performed neutron diffraction experiments and reported that the yield strengths of ferrite, bainitic ferrite, retained austenite, and martensite were 500, 650, 900, and 2000 MPa, respectively. These values are generally in agreement with the results of neutron diffraction experiments reported by Jacques et al. [94], although some variability in the measured yield strengths were observed depending on the alloy composition and thermo-mechanical processing route. The same authors [94] also determined that stress and strain were partitioned between the various phases, where stronger phases (such as retained austenite and martensite) carried higher stress loads than the softer ferritic matrix, thus influencing its macroscopic stress-strain response and increasing the overall strength of the steel. The strain partitioning between ferrite and martensite was greater than the strain partitioning between ferrite and retained austenite due to the greater difference in yield strengths.

The microstructures of medium-Mn TRIP/TWIP-assisted grades can comprise ferrite, retained austenite, and martensite, albeit with different volume fractions than observed in typical low-alloy TRIP-assisted steel microstructures. The TRIP effect (which is discussed in §2.2.3.3) is synergistic with the composite strengthening mechanism, since the ongoing generation of fresh martensite throughout the deformation sustains the work hardening rate and contributes to the overall strength of the alloy. Nevertheless, the strain partitioning and damage resulting from hardness disparities between adjacent phases must be characterized. Some work has been published on the damage mechanisms of medium-Mn steels in uniaxial tension. For example, Steineder et al. [95] examined the damage behaviour of a 0.2C-6Mn (wt%) alloy that was intercritically annealed at 580°C or 620°C for 8 h and showed that failure occurred by the

coalescence of micro-voids that nucleated at interfaces between ferrite and martensite. Work by Sun et al. [68] also demonstrated that void formation at ferrite-martensite interfaces was the main failure mechanism in their 0.2C-10.4Mn-2.9Al (wt%) steel. Additional work must be done to elucidate the microstructural effects on strain partitioning and damage mechanisms during complex forming operations such as bending and hole expansion in medium-Mn steels.

2.2.3.3 *Transformation-Induced Plasticity*

Zackay et al. [96] originated the concept of transformation-induced plasticity steels in the late 1960s upon realizing the potential use of retained austenite to improve ductility in ferrous alloys. The transformation-induced plasticity effect is observed in steels which have chemically stabilized retained austenite that gradually transforms to fresh martensite upon deformation. The TRIP effect results in sustained high work hardening rates at high strains, which delays the onset of necking during deformation and results in strong combinations of both strength and ductility. The generation of fresh martensite from the retained austenite provides additional strength to the material due to composite strengthening (in the manner described in §2.2.3.2). Jacques et al. [94] used neutron diffraction to determine that the stresses were partitioned among the individual phases in their (0.3-0.4)C-1.4Mn-1.4Si-0.05Al (wt%) TRIP steels such that the retained austenite and martensite carried higher stresses and enhanced the overall strength of the material. The authors applied the rule of mixtures to calculate the hardening provided by each phase ($\sigma_i(\varepsilon)$) with respect to its volume fraction (f_i), where the global stress-strain response is described by:

$$\sigma(\varepsilon) = f_{\alpha+\alpha_b}\sigma_{\alpha+\alpha_b}(\varepsilon) + f_\gamma\sigma_\gamma(\varepsilon) + f_{\alpha'}\sigma_{\alpha'}(\varepsilon) \tag{2.1}$$

The graph in Figure 2.11(a), published by Jacques [97], shows how the measured macroscopic stress level compares to the calculated stress using only the terms for ferrite + bainitic ferrite and retained austenite, without taking martensite into account. The strengthening resulting

from the gradual formation of martensite as a result of the TRIP effect corresponds to the shaded area, showing that this is a significant contribution to the macroscopic stress-strain response of TRIP steels.
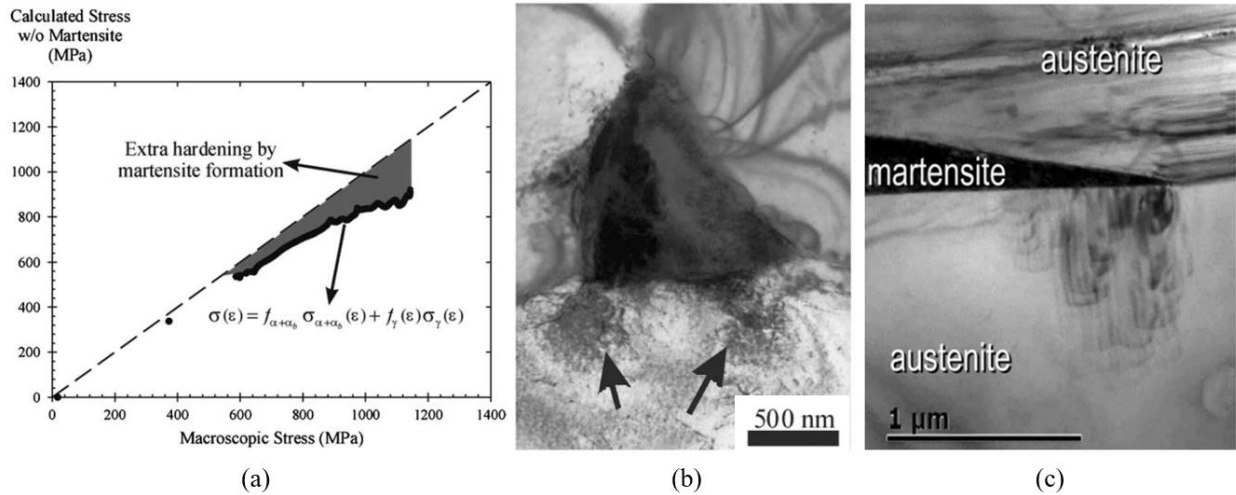
Figure 2.11: (a) Comparison between the experimentally determined macroscopic stress and the calculated stress excluding martensite, showing the hardening that was provided by the dynamic transformation of retained austenite to martensite upon deformation [97]. (b) Bright-field TEM micrograph showing geometrically necessary dislocations in the ferrite surrounding deformation-induced martensite [97]. (c) Bright-field TEM micrograph showing geometrically necessary dislocations in the austenite surrounding deformation-induced martensite [98].

In addition, the volumetric expansion of the martensite unit cell relative to the parent retained austenite unit cell results in the generation of so-called "geometrically necessary dislocations" in the surrounding phases, improving their local strength. Jacques [97] used TEM imaging to observe the geometrically necessary dislocations in ferrite that surrounded the deformation-induced martensite, and a bright field micrograph documenting this finding is shown in Figure 2.11(b). Geometrically necessary dislocations are also found in the austenite surrounding deformation-induced martensite, as shown in Figure 2.11(c).

Retained austenite stability is a critical factor in determining the rate at which the retained austenite transforms to martensite over the course of deformation. There are two considerations:

(1) mechanical stability and (2) chemical stability. It has been shown in previous investigations of low-alloy TRIP [99] and medium-Mn TRIP [28,84] steels that lamellar or lath-type retained austenite that is surrounded (and therefore mechanically constrained) by martensite and/or bainitic ferrite is more mechanically stable than polygonal retained austenite. Moreover, retained austenite that has been enriched in C, Mn, or other austenite stabilizers will be more chemically stable, i.e. resistant to the martensitic transformation, at room temperature.

The strain-induced retained austenite transformation kinetics were related to the strength-ductility balance of various low-alloyed TRIP-assisted steels in a study by Jacques et al. [100]. Samek et al. [101] also examined strain-induced martensite nucleation in low-alloyed TRIP steels and determined there were significant effects of retained austenite chemical composition and size on transformation kinetics. However, it was shown by McDermid et al. [99] that the retained austenite transformation kinetics of a conventional low-alloyed TRIP-assisted steel were best modelled as a function of normalized flow stress for temperatures above M_s^{σ} (the temperature at which the stress required to initiate the martensitic transformation is equal to the yield strength of the parent austenite grain). Compared to the strain-based transformation model of Olson and Cohen [5], the stress-based model from McDermid et al. [99] was independent of heat treatment parameters and retained austenite chemistry and stability for the two 0.2C-1.5Mn-(1-1.5)Al-(0-0.5)Si (wt%) low alloy TRIP steels studied.

2.2.3.4 Twinning-Induced Plasticity

Stacking faults are planar defects that describe a region in which the regular crystallographic stacking sequence has been altered. In the case of close-packed {111}-type planes in FCC crystals, the stacking sequence ABCABC… can be interrupted in two ways. If an additional plane is inserted into the stacking sequence (e.g. ABCAB$\underline{A}$CABC), the defect is known

as an extrinsic stacking fault. If a plane is removed from the stacking sequence (ABC<u>AC</u>ABC), the defect is an intrinsic stacking fault (and there is a twin boundary in the "ACA" sequence). This occurs when a perfect dislocation with a Burgers vector of length $a/2 < 110 >$, where a is the lattice parameter, dissociates into two Shockley partial dislocations according to the reaction in Equation 2.2 [102].

$$\frac{a}{2}[01\bar{1}] \rightarrow \frac{a}{6}[11\bar{2}] + \frac{a}{6}[\bar{1}2\bar{1}] \tag{2.2}$$

This dissociation is energetically favoured because the dislocation energy is proportional to the square of the magnitude of the Burgers vector ($|\vec{b}|^2$) [102]. The equilibrium separation (d) of two partial dislocations is defined by the balance between the repulsive force between them (due to their elastic interaction) and the attractive force between them (due to the stacking fault energy, which is a force Γ per unit length of the line). The approximate equilibrium separation d is inversely proportional to the stacking fault energy, as given by Equation 2.3 [103].

$$d = \frac{\mu |\vec{b}|^2}{4\pi\Gamma} \tag{2.3}$$

where μ is the shear modulus. Lower SFE materials have wider stacking faults and lower dislocation mobilities.

The Twinning-Induced Plasticity (TWIP) effect is a strengthening mechanism whereby austenite dynamically twins as it deforms, hence providing additional dislocation barriers and reducing the dislocation mean free path, in addition to providing sites for dislocation accumulation. This is widely known as the dynamic Hall-Petch effect [104–111]. Since the intrinsic stacking fault energy of retained austenite is believed to strongly influence the mechanism(s) by which the

material accommodates strain (i.e. dislocation glide, mechanical twinning, and/or deformation-induced ε-martensitic transformation [108,109,112–117]), the SFE is often used to predict whether the TRIP and/or TWIP mechanisms will be activated. Although the exact SFE ranges which favour the activation of the TWIP effect are disputed, it is generally believed that the target intrinsic SFE for the activation of mechanical twinning lies between 15 mJ/m^2 and 45 mJ/m^2 [118]. Lower SFE ranges (generally believed to be below 12 mJ/m^2 to 20 mJ/m^2 [118]) can result in the activation of the γ-austenite → ε-martensite transformation. It has been noted that ε-martensite, which has a hexagonal close-packed (HCP) structure (in contrast to the body-centered tetragonal, or BCT, structure of α'-martensite) has been examined via TEM and shown to be a series of stable stacking faults [119]. In addition to being a function of temperature, the SFE of austenite is largely a function of the alloy composition. In the case of retained austenite, this is in turn a strong function of the extent to which solutes are partitioned during either intercritical or overaging heat treatments.

It has also been argued that the SFE of austenite is also related to its grain size. Lee and Choi [120] suggested that the SFE in high-Mn steels increases with decreasing austenite grain size, especially below ~30 μm, due to the effects of internal stresses. Citing this work, Saeed-Akbari et al. [114] proposed a model to calculate the SFE of high-Mn steels based on a subregular solution model that incorporated the effect of grain size. However, a subsequent publication by Saeed-Akbari et al. [121] reviewed the effects of chemical composition and other parameters (including grain size) on the work-hardening behaviour of TWIP steels, leading to doubts about the proposed role of grain size on SFE. Instead, they attributed the role of grain size to changes in the activation or saturation of deformation twinning in TWIP steels.

Direct measurements of the SFE are possible via techniques such as weak-beam TEM [122] and XRD [123], but are very challenging. Thus, considerable efforts have been made to determine the intrinsic SFE of austenitic steels of various compositions and create predictive models for other steel chemistries. A number of CALPHAD-based models have been proposed [108,109,114,115,124,125], but they were constructed for different TWIP steel alloy systems. Moreover, the models are not in universal agreement about which value to use for surface energy or whether to include a strain energy term and/or grain size excess free energy term (as discussed above). As such, there has not been a model that has emerged as the preeminent choice for SFE calculations in austenitic steels. It should also be noted that these modelling endeavours have been focused on highly-alloyed austenitic steels, where the composition of the austenite is known to be the same as the bulk alloy chemistry. When applying the models to complex-phase steels to calculate the intrinsic SFE of retained austenite in either low-alloy or TRIP-assisted 3G steels, the composition of the retained austenite is unlikely to be that of the bulk alloy due to the partitioning of alloying elements during annealing treatments. Hence, some assumptions must be made and/or experiments must be performed to determine the composition to input into the SFE model.

Several authors working on medium-Mn steels have shown that the 3G AHSS mechanical property targets could be met or exceeded by activating both the TWIP and TRIP effects in succession or simultaneously and have tried to predict this behaviour with SFE calculations. For example, Lee and De Cooman [126] investigated a 0.3C-10Mn-3Al-2Si (wt%) steel and determined that an excellent strength-ductility balance (1100 MPa UTS $\times$ 65% TE) could be achieved by choosing a relatively moderate intercritical annealing temperature of 800°C (SFE = 26 mJ/m^2, per the Dumay et al. model [108]), which resulted in the activation of both the TWIP and TRIP effects. Neither plasticity-enhancing mechanism was operative after annealing at 700°C

(SFE = 36 mJ/m^2, 1250 MPa UTS × 15% TE), while premature brittle failure occurred when annealing at 900°C (SFE = 20 mJ/m^2, per the Dumay et al. model [108]) due to the low chemical stability of the retained austenite and, therefore, the rapid exhaustion of the TRIP effect and resulting excessive fractions of fresh martensite. However, the calculated SFE values did not agree with the experimentally determined deformation modes for the 800°C and 900°C samples, as the sole activation of the TWIP effect (20 < SFE ≤ 30 mJ/m^2) was predicted for the 800°C sample and the dual TRIP (in this case, γ → ε) + TWIP mode (15 < SFE ≤ 20 mJ/m^2) was predicted for the 900°C sample.

Lee et al. [34] investigated a set of medium-Mn alloys (6.0Mn-1.5Si-3.0Al (wt%)) with varying (0.15 or 0.30 wt%) C contents and chose intercritical annealing temperatures (840°C for the 0.15 wt% C grade and 780°C for the 0.3wt% C grade) where the equilibrium intercritical austenite composition would result in a room-temperature calculated SFE of approximately 20 mJ/m^2 using the Dumay et al. model [108], which is in the expected range for the activation of the TRIP + TWIP effects. The authors included three-dimensional Atom Probe Tomography (3D-APT) results showing that the retained austenite in their alloys nearly attained the predicted equilibrium composition after intercritical annealing for only 180 s, which validated their use of the equilibrium composition of the intercritical austenite for their retained austenite SFE calculations. When plotted, the two maxima in the instantaneous work hardening rate as a function of true strain corresponded to the activation of both the TWIP and TRIP effects, respectively, as shown in Figure 2.12. The activation of both mechanisms was confirmed by means of TEM examination, as seen in the micrographs in Figure 2.13. As a result, the 0.15wt% C alloy achieved a UTS × TE of 34,400 MPa% and the 0.30wt% C alloy achieved 65,360 MPa%.
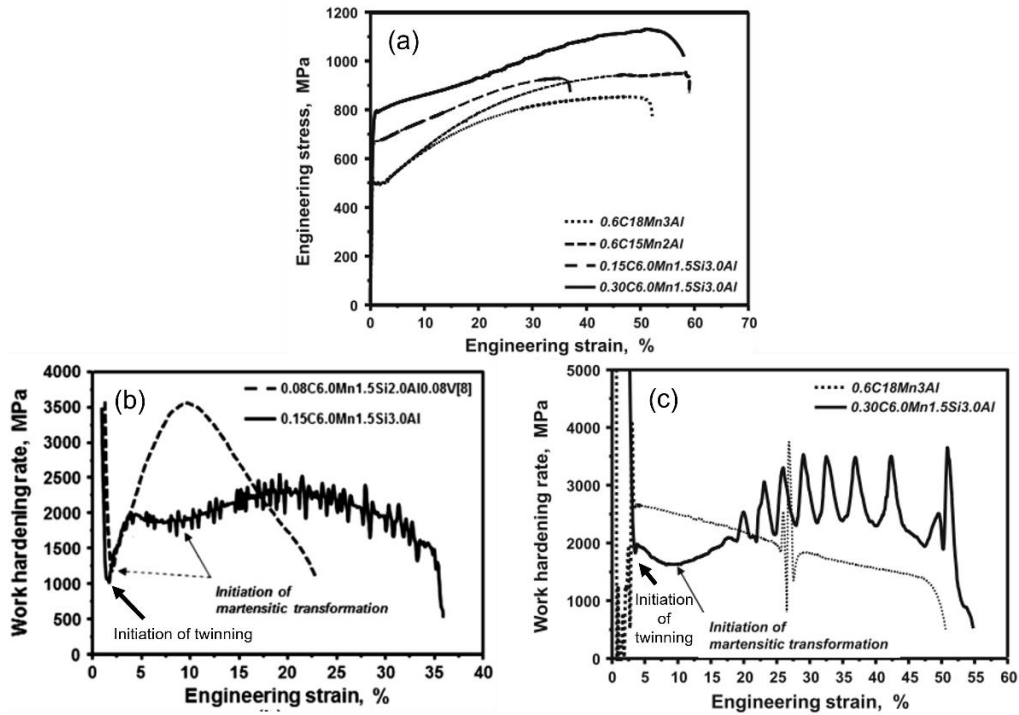
Figure 2.12: Mechanical properties of (0.15-0.30)C-6.0Mn-1.5Si-3.0Al (wt%) TRIP/TWIP alloys compared to reference 0.6C-18Mn-3Al (wt%) and 0.6C-15Mn-2Al (wt%) TWIP steels: (a) engineering stress-strain curves, (b-c) work hardening rate curves with arrows showing the initiation of the TRIP and TWIP effects. Adapted from Lee et al. [34]
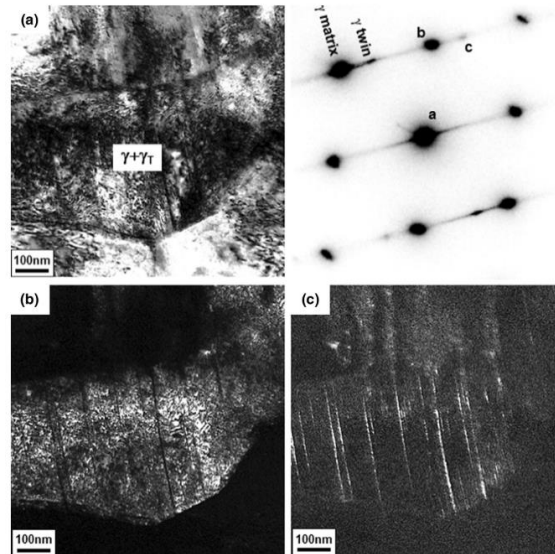
Figure 2.13: TEM micrographs of retained austenite in a strained 0.15C-6Mn-1.5Si-3Al (wt%) steel intercritically annealed at 840°C for 180 s and quenched: (a) bright-field image and selected area diffraction pattern of a twinned retained austenite grain, (b) dark-field image of the austenite matrix, (c) corresponding dark-field image of the mechanical twins [34].

Bhadhon et al. [26,81] (who studied a 0.2C-6.1Mn-1.5Si-0.5Al-0.5Cr (wt%) med-Mn alloy) and Patel [28] (who studied a 0.15C-5.6Mn-1.0Al-1.2Si (wt%) alloy) also found experimental evidence that the TWIP effect (in addition to the deformation-induced $\gamma_{ret} \rightarrow \alpha'$ TRIP effect) could be activated in their respective steels, given an appropriate choice of starting microstructure and intercritical annealing parameters. Unfortunately, no SFE calculations were reported in these publications. Regardless, these researchers showed that the 3G AHSS mechanical property target envelope could be achieved using CGL-compatible processing if both the TRIP and TWIP effects were leveraged. Bhadhon et al. [26,81] achieved 1380 MPa UTS × 19% TE by employing a martensitic starting microstructure and annealing for 120 s at 675°C. The highest properties obtained by Patel [28] (1150 MPa UTS × 29% TE) resulted from intercritical annealing at 690°C for 120 s from a martensitic starting microstructure.

2.3   Continuous Hot-Dip Galvanizing

The continuous hot-dip galvanizing process is a cost-effective means of protecting automotive steels against aqueous corrosion when in service. Zn-based metallic coatings provide barrier protection to the substrate from the external corrosive environment, but also provide galvanic protection by acting as a sacrificial anode if the physical barrier is damaged.

Marder [127] described the Sendzimir-type continuous galvanizing process, a schematic of which is shown in Figure 2.14 [128]. First, successive steel coils are welded together to form a continuous strip before being cleaned by an alkali brushing system (using hot 1.5-2.5% $NaOH_{(aq)}$) to remove surface organics and Fe fines from previous processing (usually hot or cold rolling). Electrolytic cleaning may then be used to remove more tightly adherent residual organics and Fe fines. After several rinsing stages, the strip is then dried before entering the annealing furnace, which is usually either a direct natural-gas fired furnace, a radiant tube furnace, or a combination

of both technologies. CGLs typically employ a N_2-(5-20vol%)H_2 atmosphere with a controlled

oxygen potential in order to reduce surface Fe oxides and ensure that metallic Fe is able to react

with the liquid Zn(Al, Fe) bath. After annealing, the steel is cooled to approximately the same

temperature as the bath (450°C-470°C) before immersion. Gas-jet wiping using air or N_2 is used

to control the coating thickness after the strip exits the bath. Galvanized steels can be either

naturally or force cooled upon exiting the zinc bath to solidify the coating, but the strip can be

further annealed to develop a galvannealed coating comprising a series of Fe-Zn intermetallics

before cooling the strip. After exiting the coating section of the CGL, the steel strip proceeds to

temper rolling, roller levelling, pre-phosphating, oiling, cutting, and recoiling before being

packaged and shipped.
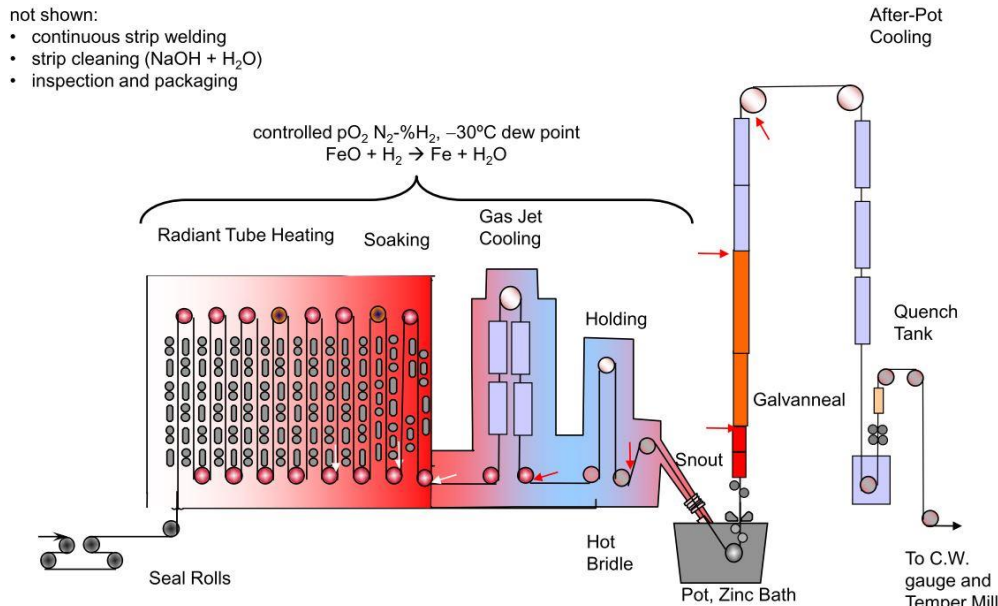
Figure 2.14: Schematic of a continuous hot-dip galvanizing line [128].

2.3.1   Selective Oxidation of Advanced High Strength Steels

The typical CGL process atmosphere is reducing to Fe oxides but oxidizing to the

commonly employed alloying elements used in AHSSs – e.g. Mn, Si, Cr and Al. The selective

oxidation of Mn, Si, Cr and Al can occur at the steel surface and prevent the metallic Fe from

reacting with the liquid bath metal to form integral and defect-free galvanized coatings [47,85,129,130]. This section includes a review of the thermodynamics of selective oxidation as well as the kinetics describing the transition from external to internal oxidation (i.e. the Wagner model and its extensions).

2.3.1.1 Gas-Metal Reactions in the CGL Furnace

The CGL process atmosphere is a N_2-(5-20 vol%)H_2 mixture with a small amount of $H_2O_{(g)}$ that is injected to control the O_2 partial pressure (pO_2). The dew point (T_{dp}) is an analog for the pO_2 in the system and is defined as the temperature at which water vapour at a fixed partial pressure pH_2O condenses from the process atmosphere, i.e. the temperature at which the reaction in Equation 2.4 is at equilibrium.

$$H_2O_{(l)} \rightleftharpoons H_2O_{(g)} \tag{2.4}$$

The partial pressure of water vapour can be related to the dew point by Equation 2.5, assuming ideal gas behaviour.

$$pH_2O_{(g)} = a_{H_2O_{(l)}} \exp\left[\frac{-\Delta G^o_{(2.5)}}{RT_{dp}}\right] \tag{2.5}$$

If liquid water is assumed to be a pure condensed species with unit activity in Equation 2.5, the pO_2 of the annealing atmosphere is fixed for a given process atmosphere temperature (T_{atm}) due to the fixed partial pressures of hydrogen gas and water vapour according to the reactions in Equations 2.6 and 2.7.

$$H_{2(g)} + \tfrac{1}{2}O_{2(g)} \rightleftharpoons H_2O_{(g)} \tag{2.6}$$

$$pO_{2(g)} = \left(\frac{pH_2O_{(g)}}{pH_{2(g)} \exp\left[\dfrac{-\Delta G^o_{(2.6)}}{RT_{atm}} \right]} \right)^2 \tag{2.7}$$

For the general oxidation of a metallic alloying element M to its given stoichiometric oxide M_xO_y:

$$xM + \tfrac{y}{2}O_{2(g)} \rightleftharpoons M_xO_y \tag{2.8}$$

Assuming unit activity for the pure condensed oxide and a known activity of M in the alloy, the critical oxygen potential above which M_xO_y is stable and below which M is stable can be calculated using Equation 2.9.

$$pO_{2(g)} = \left(\frac{a_{M_xO_y}}{a_M^x \exp\left[\dfrac{-\Delta G^o_{(2.8)}}{RT_{atm}} \right]} \right)^{\frac{2}{y}} \tag{2.9}$$

Figure 2.15 shows the critical oxygen potentials as a function of temperature for various alloying elements of relevance to medium-Mn 3G AHSS, with the thermodynamic data obtained from FREED [131] and Jung et al. [132]. North American and European CGL process atmospheres typically comprise N_2-5vol%H_2 with a -30°C dew point. As can be seen in Figure 2.15, a 5vol% H_2 CGL process atmosphere (with a T_{dp} of -30°C, -10°C, or +5°C) is reductive to Fe oxides but oxidizing to Al, Cr, Mn, and Si. The pO_2 required to oxidize these elements increases by several

orders of magnitude when calculating the metal/oxide equilibrium in the case when the activity is

non-unity (Figure 2.16), as expected in a ferrous alloy. It can be seen in Figure 2.16, however, that

conventional CGL process atmospheres are oxidizing to these elements when used in alloys.
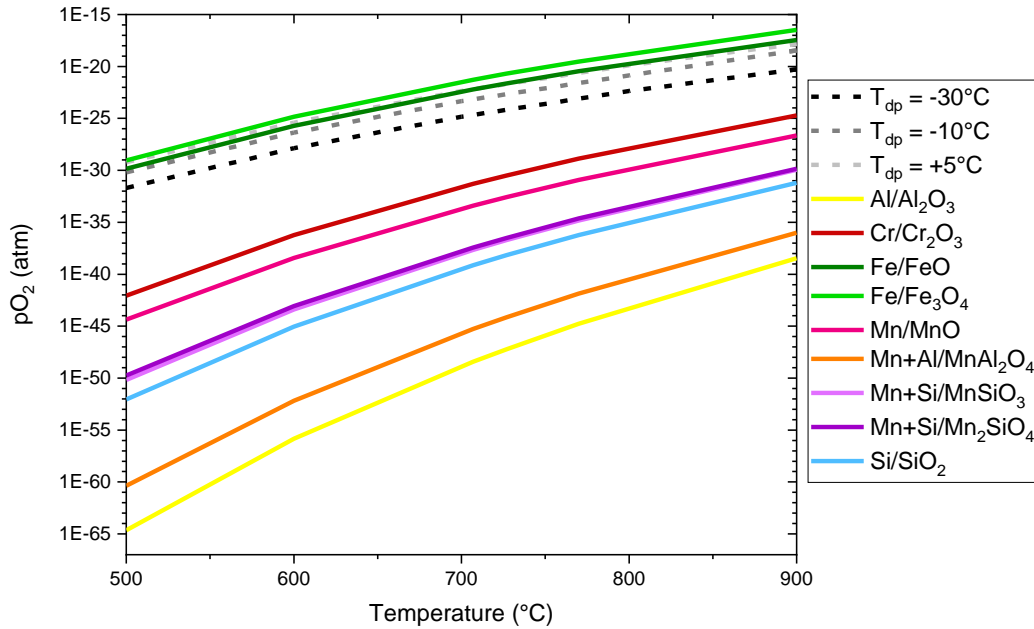
Figure 2.15: Critical oxygen partial pressures for the oxidation of various metallic elements in a
N_2-5%H_2 atmosphere as a function of annealing temperature, assuming unit activity of the
metallic species. Also indicated are the oxygen partial pressures for a -30°C, -10°C, and +5°C
dew point atmosphere. Data obtained from FREED [131] and Jung et al. [132].
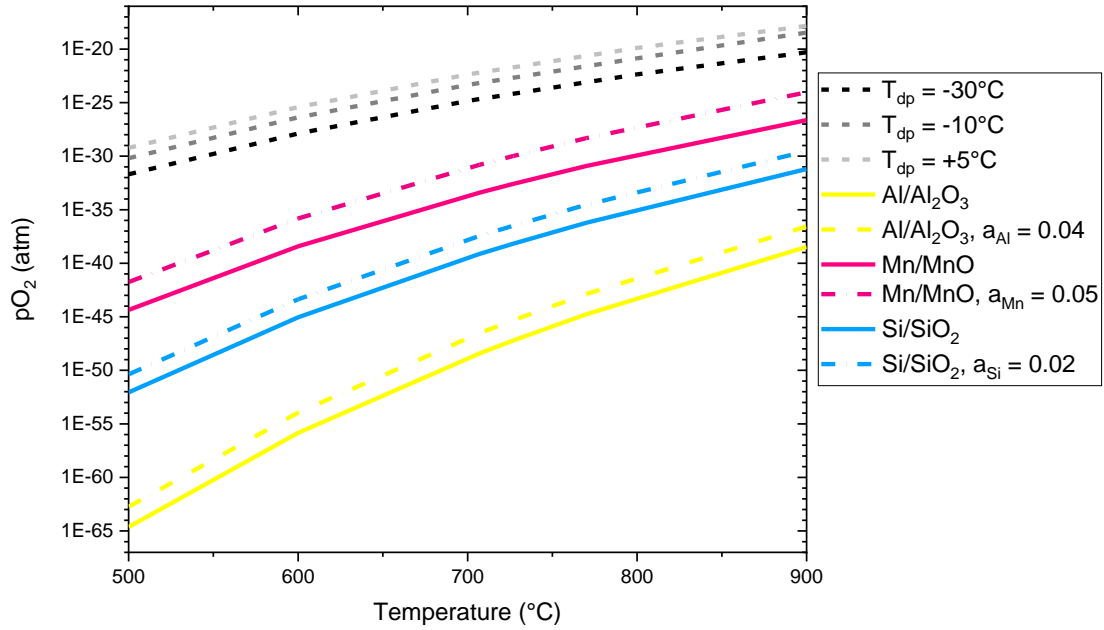
Figure 2.16: Critical oxygen partial pressures for the oxidation of Al, Mn, and Si in a N_2-5%H_2 atmosphere as a function of annealing temperature for unit and non-unit activities of these elements. Also indicated are the oxygen partial pressures for a -30°C, -10°C, and +5°C dew point atmosphere. Data obtained from FREED [131].

2.3.1.2 Internal and External Oxidation – Wagner's Model and Its Extensions

Selective oxidation can manifest itself as internal (i.e., oxide particles precipitating beneath the substrate surface) or external (i.e. oxide particles form on the substrate surface), and typically a balance is struck between the two when considering engineering alloys. Wagner [133] developed a criterion for the transition from internal to external oxidation for an ignoble solute M that oxidizes to MO_v in a noble matrix A, which will not be oxidized by the process atmosphere. The equation for this is shown in Equation 2.10:

$$\left(N_M^O\right)_{crit} = \left[\frac{\pi g^*}{2\nu} N_O^S \frac{V D_O}{V_{MO_\nu} D_M}\right]^{\frac{1}{2}} \qquad (2.10)$$

where $\left(N_M^O\right)_{crit}$ is the critical mole fraction of alloying element M for the transition from internal to external oxidation (i.e. internal oxidation occurs if $N_M < \left(N_M^O\right)_{crit}$), g^* is the critical volume fraction of oxides that results in blocked inward diffusion paths for oxygen in the case of the insoluble oxide MO_ν, ν is the stoichiometric ratio between the oxygen and metal atoms in the oxide MO_ν, V is the molar volume of the alloy, V_{MO_ν} is the molar volume of the oxide MO_ν, N_O^S is the mole fraction of adsorbed oxygen at the surface, D_O is the diffusivity of oxygen in matrix A, and D_M is the diffusivity of alloying element M in matrix A.

A derivation of the Wagner equation and explanation in English are provided in Birks et al [134]. Wagner's model is based on the criterion that the selective oxidation mode is determined by a competition between the inward diffusion of adsorbed oxygen from the vapour/substrate interface and the outward diffusion of ignoble alloying elements from the substrate. Internal oxidation is the result of greater oxygen flux inward relative to the alloying element flux outward, and the resulting oxide network obstructs further oxygen flow into the substrate. Conversely, external oxidation will occur if the outward diffusion of alloying elements to the surface is greater than the inward diffusion of oxygen atoms. As such, for a given alloy composition held at a given temperature, an increase in the process atmosphere pO2 will shift the oxidation towards the internal oxidation mode.

The Wagner model was developed for single-crystal binary alloys and has several limitations in terms of modelling the selective oxidation of complex engineering alloys. It does not

account for multiple alloying elements, grain boundary diffusion, or differences in the diffusivities of alloying elements across multiple phases (i.e., in ferrite, austenite, or martensite). The model also assumes that the oxides that form are insoluble in the matrix, which is not always true in certain instances pertaining to advanced steels – e.g. MnO has a significant solubility in both ferrite and austenite [135]. The g* term is critical in determining the transition kinetics because it represents the critical volume fraction of MO_v required to physically block inward oxygen diffusion. A value is $g* = 0.3$ has been advocated by Rapp [136], which was determined for Ag-In alloy. In the case of MnO, Lashgari et al. [137] experimentally determined that a modified value of $g* = 0.2$ would be suitable to model Mn oxidation in steel at 950°C.

Expansions of the classic Wagner equation have been proposed by several authors [135,137–140] in order to more accurately model the experimental observations of polycrystalline engineering alloys. Mataigne et al. [138] proposed a modified Wagner-type equation (Equation 2.11) wherein the accelerated diffusion of oxygen and alloying elements at grain boundaries of polycrystalline alloys could be accounted for by halving the activation energy values for bulk diffusion in Equation 2.10. Moreover, they proposed a modification to the classic Wagner model for multi-component systems in which the flux of oxidizable alloying elements towards the surface was additive: if the combined flux of ignoble elements to the surface (given by the left-hand side of Equation 2.11) exceeded the inward flux of oxygen into the substrate (given by the right-hand side of Equation 2.11), external oxidation would occur. However, it should be noted that this model does not consider the formation of complex oxides that are known to form in medium-Mn steels, such as $MnSiO_3$ and Mn_2SiO_4.

$$\sum_M N_M^O \left[v V_{MO_v} D_M \right] = \left[\frac{\pi g*}{2} N_O^S V D_O \right]^{\frac{1}{2}} \tag{2.11}$$

Huin et al. [135] expanded upon the classic Wagner model by building a finite difference model that considered the oxide solubility products and the interactions between several solute elements. They assumed the competitive consumption of the available dissolved oxygen such that MnO, SiO$_2$, and Mn$_2$SiO$_4$ formation were predicted. However, in common with the other models presented in this section, this model was restricted to an isothermal process. Some additional work has since been published by this group on the finite element modelling of selective oxidation processes. For example, Leblond et al. [141] considered that precipitated oxides would act as diffusion barriers by developing a Wagner model extension with an oxygen diffusivity that would change as a function of the volume fraction and aspect ratio of oxide precipitates. In a later publication, Leblond et al. [142] developed a finite element algorithm capable of handling many more practical cases, including the 1D anisothermal internal oxidation of five elements, 1D isothermal internal oxidation of binary alloys with non-stoichiometric oxide precipitation, or 2D isothermal internal oxidation of binary alloys involving accelerated grain boundary diffusion. It should be noted that the results of increasingly complex numerical modelling problems are not amenable to verification by analytical solutions and, therefore, must be compared to experimental data.

2.3.2   The Zn(Al, Fe) CGL Bath and Reactive Wetting

The use of a pure Zn galvanizing bath in the CGL would result in a coating with several layers of Fe-Zn intermetallic phases containing progressively lower Fe contents moving out from the substrate: gamma (Γ-Fe$_3$Zn$_{10}$), delta (δ-FeZn$_{10}$), zeta (ζ-FeZn$_{13}$, and metallic Zn. However, small amounts of Al are added to continuous galvanizing baths in order to temporarily prevent the formation of these brittle Fe-Zn intermetallic compounds at the steel/coating interface, as the thermodynamic driving force for Fe-Al intermetallic formation is significantly greater [143]. The

Fe-Al interfacial layer (η-Fe$_2$Al$_{5-x}$Zn$_x$) is known in the industry as the "inhibition" layer because it acts as a diffusion barrier between Fe and Zn and prevents the formation of their intermetallic compounds [127,144], thereby allowing the Zn to remain in its desired metallic form. The Zn-rich corner of the Zn-Al-Fe ternary system at the commonly used CGL bath temperature of 460°C, as calculated by McDermid et al. [145], is shown in Figure 2.17. At this temperature, Fe and Al have limited solubility in liquid Zn, and, therefore, several intermetallic phases can precipitate according to the global bath composition. With increasing Al bath content, the equilibrium configuration of the bath will change from L + ζ-FeZn$_{13}$ to L + δ-FeZn$_{10}$ to L + η-Fe$_2$Al$_{5-x}$Zn$_x$. A typical galvanizing bath will contain approximately 0.15-0.25 wt% dissolved Al. The term "dissolved" refers to Al that is in solution in the liquid phase and is, therefore, available for the interfacial reaction to form η-Fe$_2$Al$_{5-x}$Zn$_x$ and does not include the Al that has precipitated into intermetallic species.
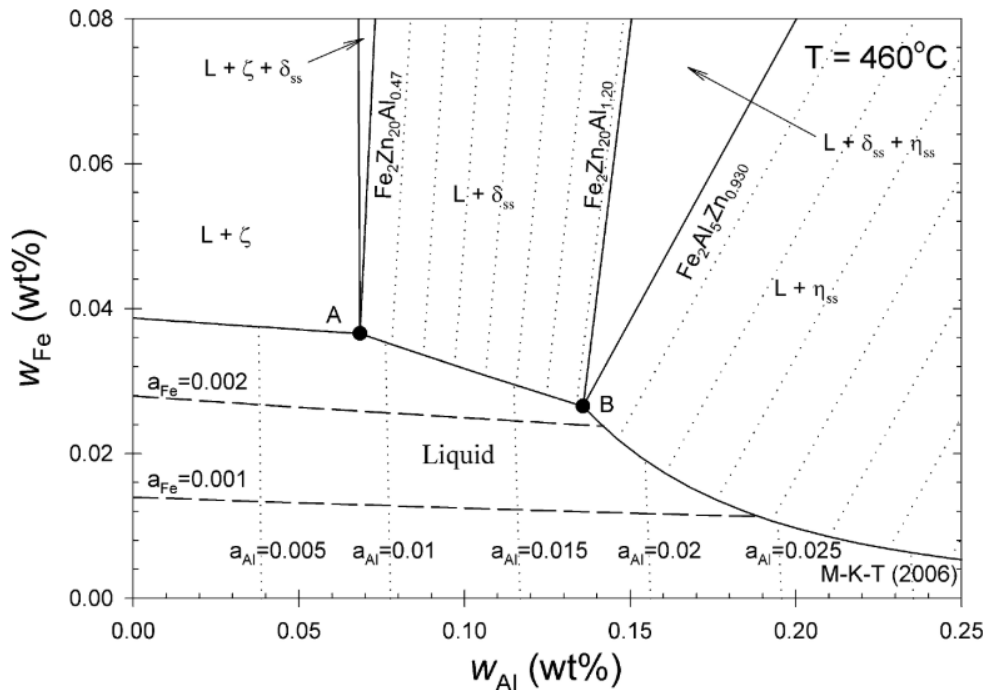
Figure 2.17: Zn-rich corner of the Zn-Al-Fe phase diagram at 460°C [145]. Isoactivity lines for Al (with respect to pure solid Al) and Fe (with respect to pure solid ferrite) are shown in the liquid phase region.

When the steel is immersed in the bath, Fe dissolution from the steel strip is driven by the metastable equilibrium between the Zn(Al, Fe) bath and substrate Fe and leads to supersaturation of the liquid Zn bath by Fe [144,146]. A graphical representation of the global and metastable equilibria was published by Nakano [147] and is shown in Figure 2.18. This local Fe supersaturation is one of the drivers for the nucleation and growth of a compact layer of fine crystals of the metastable $FeAl_3$ and/or η-$Fe_2Al_{5-x}Zn_x$ phase at the substrate/bath interface in order to restore thermodynamic equilibrium to the system. The formation of this layer prevents further Fe dissolution into the bath, but diffusion of Fe through the η-$Fe_2Al_{5-x}Zn_x$ layer continues, as does the diffusion of Zn and Al towards the substrate through the η-$Fe_2Al_{5-x}Zn_x$ layer. The transformation of $FeAl_3$ to η-$Fe_2Al_{5-x}Zn_x$ will proceed and an upper, coarse layer of η-$Fe_2Al_{5-x}Zn_x$ will grow. The resulting two-layer structure in the final interfacial layer comprises an outer layer of coarse and randomly oriented η-$Fe_2Al_{5-x}Zn_x$ crystals on top of a finer, compact layer of η-$Fe_2Al_{5-x}Zn_x$ such that the {200}-type planes are parallel to the substrate surface. For baths with lower dissolved Al, the microstructure will consist of one discontinuous sublayer, which will accelerate the breakdown of the interfacial layer and the formation of Fe-Zn intermetallic phases [127,143,148,149].
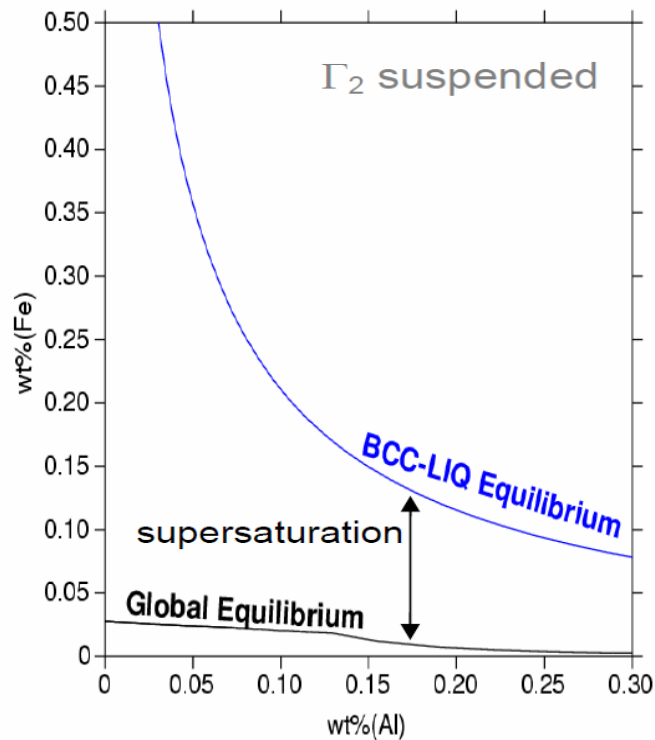
Figure 2.18: Zn-rich corner of the Zn-Al-Fe system at 450°C showing the global (black) and metastable (blue) equilibrium between the liquid and BCC phases, per Nakano [147]. The difference between the curves indicates the maximum possible degree of supersaturation of the liquid phase.

2.3.2.1 Reactive Wetting Mechanisms

Numerous contributions have been made to elucidate the reactive wetting mechanisms that facilitate the reactive wetting of 1G AHSS DP and TRIP grades in spite of the external oxidation of several alloying elements contained therein. The aluminothermic reduction of surface MnO by the galvanizing bath was proposed by Khondker et al. [150] after having observed a fully-formed η-$Fe_2Al_{5-x}Zn_x$ interfacial layer on their externally oxidized 2 wt% Mn DP steel after immersion in a 0.20 wt% Al (dissolved) galvanizing bath for typical immersion times. Kavitha and McDermid later verified this mechanism in their work on the reactive wetting of a 5.1 wt% Mn substrate [151]. Alibeigi et al. [152] showed that reactive wetting kinetics were inversely proportional to the surface MnO layer thickness (which is a function of the process atmosphere pO_2). Sagl et al. [153]

provided direct proof of the aluminothermic reduction of MnO using XPS analysis. The aluminothermic reduction of other species (such as Mn_2SiO_4) has been posited based on thermodynamic considerations [154], but has not been confirmed experimentally.

Infiltration of the liquid bath metal between oxide particles and the steel substrate has also been proposed to explain the occurrence of η-$Fe_2Al_{5-x}Zn_x$ between the substrate surface and oxide particles. Sagl et al. [153] asserted that the resultant flaking of oxides from the substrate surface had a greater contribution to galvanizability than aluminothermic reduction of surface oxides. Two infiltration routes have been proposed: 1) liquid bath metal infiltration at grain boundaries between the oxide and substrate, and 2) liquid bath metal infiltration due to thermal coefficient of expansion mismatch-assisted cracking of the oxide. The grain boundary infiltration mechanism was documented by Bellhouse and McDermid [50], who examined several substrates containing between 1-1.5 wt% Si and 1.0 wt% Al and found $Fe_2Al_{5-x}Zn_x$ under and around oxide nodules that remained on the surface after galvanizing. The oxide cracking mechanism was also described by Bellhouse and McDermid [50], who found Mn- and O-rich holes on sample surfaces after annealing a 1.5 wt% Al steel. Seyed Mousavi and McDermid [155] also found evidence of oxide cracking in their work on a 0.1C-2Mn-1.3Si (wt%) steel, as did Pourmajidian and McDermid [75] in their work on a 0.1C-6Mn-2Si (wt%) steel.

2.3.2.2 *Strategies to Improve Reactive Wetting of AHSS*

Several process modifications have been suggested to facilitate the reactive wetting of AHSS grades whose chemical compositions may make them difficult to reactively wet under conventional conditions. The schematic in Figure 2.19 provided by Cho et al. [70] shows four such examples: 1) high dew point annealing, 2) oxidation/reduction, 3) flash coating, and 4) surface active element alloying additions.
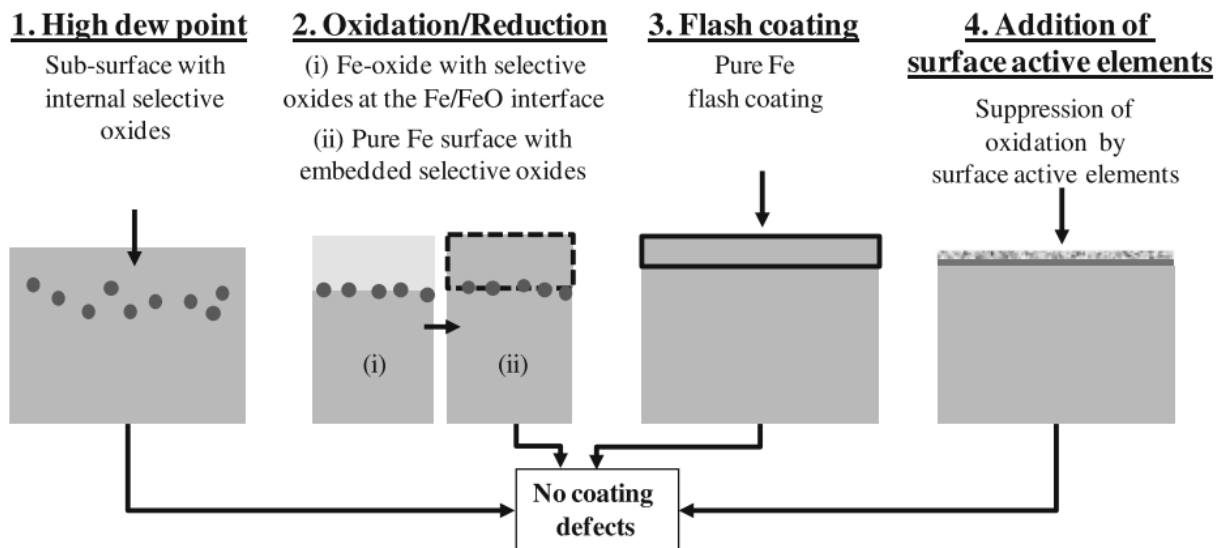
Figure 2.19: Schematic showing four proposed methods to improve the reactive wetting of AHSS by reducing coating defects caused by external oxides [70].

A higher dew point in the annealing furnace can promote the internal selective oxidation of alloying elements (per the Wagner criterion, §2.3.1.2) and has been applied to improve the reactive wetting of 1G AHSS [155–158] and medium-Mn 3G AHSS [74,75,159]. Pourmajidian and McDermid [159] selectively oxidized their model 0.1C-6Mn-2Si (wt%) steel at 800°C and showed that the external oxide chemistry and morphology was altered with increasing dew point. Examination via TEM-EELS showed an evolution of the oxide structure from a compact and layered SiO_2 + $MnSiO_3$ + MnO surface oxide structure (-50°C dew point) to a continuous layer of coarse MnO nodules (-30°C dew point) to a discontinuous layer of MnO nodules (+5°C dew point). The same authors successfully galvanized their steel after intercritical annealing at 690°C by employing dew points of -30°C or +5°C, while poor reactive wetting was observed for a dew point of -50°C [75]. A dew point of -50°C resulted in substantial surface coverage by continuous film-like MnO, while the higher dew point atmospheres resulted in minimal coverage of the surface by discontinuous MnO nodules which could be lifted off via bath metal infiltration between the oxide

51

and substrate or aluminothermically reduced by the bath metal. However, this approach to improved reactive wetting is limited if the transition from external to internal oxidation does not occur, since a higher dew point atmosphere provides more oxygen for oxide nucleation and growth. For example, Bellhouse and McDermid [50] studied the selective oxidation and reactive wetting of a 0.2C-1.5Mn-1.5Al (wt%) TRIP-assisted steel and found that a +5°C dew point led to an external MnO layer that was too thick to be aluminothermically reduced by the bath metal.

The oxidation/reduction strategy is a two-step process wherein the steel is heated in an oxygen-rich environment (air [160], N_2-O_2 atmosphere [161], or oxygen-rich gas [162]) for a short time. In this step, the pO_2 is sufficiently high to simultaneously selectively oxidize the alloying elements while also oxidizing the substrate Fe to FeO, resulting in alloying element selective oxides which are embedded within the FeO. When the Fe oxides are subsequently reduced in the conventional CGL annealing furnace (i.e., N_2-(5-10vol%) H_2 with a controlled dew point), the surface layer comprises pure Fe which can be reactively wetted by the Zn(Al, Fe) bath. However, the resulting pure Fe layer is porous due to the volume change associated with FeO reduction, as well as the defective nature of FeO [161,163,164], which can lead to a weak interfacial layer and flaking of the galvanized coating.

The flash coating method involves the electrodeposition of a thin layer of pure Ni, Fe, or Cu prior to annealing to prevent the formation of external oxides during the heat treatment [165–168]. However, this method is in development and not yet widely employed at an industrial scale [169,170].

As alluded to in §2.2.1, minor additions of so-called surface active elements such as Sn, Sb, and Bi have been shown to decrease oxidation kinetics and improve reactive wetting of 1G AHSS [70–72,158,171,172]. This novel alloy design concept was based on earlier work showing that

surface active elements slowed the rate of surface reactions such as selective oxidation of Si in electrical steels [173] and carburization of case hardening steels [171]. Grabke [174,175] determined that these elements can segregate to the surface and occupy surface adsorption sites, thereby decreasing the surface permeability of oxygen and acting as a barrier to its inward diffusion. Hondros and Seah [176,177] explained that the tendency of elements to segregate to grain boundaries is a function of surface energy and elastic energy of the matrix. As such, they asserted that solute element A in solvent B would experience a large driving force for surface segregation if the melting points of A and B were different and if there were significant atomic size differences between A and B. To this end, Cho et al. [70] determined that elements such as Bi, Sn, Sb, and S would exhibit high surface enrichment factors while elements such as Ni, Cr, Cu, and Ti would not.

Several studies on the effect of minor additions of Sn, Sb, and Bi on the selective oxidation and reactive wetting of interstitial-free and low-alloy TRIP steels have been performed. Cho et al. [70,71] examined 0.1C-1.6Mn-1.5Si-(0-1)Sn (wt%) TRIP steels and found that the surface oxides in the Sn-containing grades had a lenticular morphology while the reference alloy had continuous oxide films (as seen in Figure 2.20). Cho et al. [71] also determined that an increase in Sn content resulted in decreased oxygen solubility at the surface, thereby altering the surface oxide Mn to Si ratio. Similar findings were documented by Oh et al. [72] in their analysis of 0.1C-1.6Mn-1.5Si-(0-0.2)Bi (wt%) TRIP steels. Enrichment of Sn or Bi in the substrate beneath the external oxides resulted in an increased interfacial energy between the SiO_2 and substrate surface, leading to de-wetting of the oxides and thereby altering their morphology. The thinner and more discrete lenticular morphology of the external oxides resulted in significant improvements in reactive wetting of the Sn- or Bi-added alloys relative to the Sn- or Bi-free reference alloys.
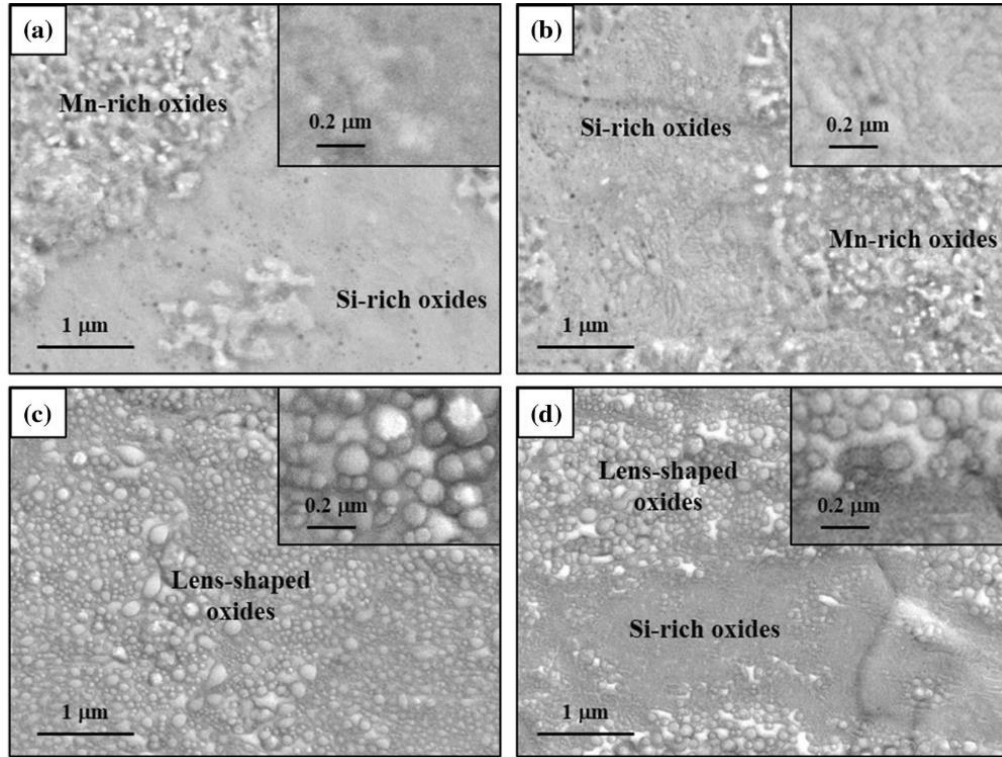
Figure 2.20: SEM images showing the altered morphology of $xMnO \cdot SiO_2$ external oxides formed during annealing for various Sn additions to a reference 0.1C-1.6Mn-1.5Si (wt%) TRIP steel: (a) 0% Sn (reference alloy), (b) 0.05 wt% Sn, (c) 0.5 wt% Sn, (d) 1 wt% Sn [71].

Pourmajidian and McDermid [74,75] applied the surface-active element alloying concept by adding 0.05 wt% Sn to their reference 0.1C-6Mn-2Si (wt%) steel. The Sn-added steel was successfully galvanized at a wider range of process atmosphere pO_2 than the reference grade (as shown in Figure 2.21) because the Sn retarded oxidation kinetics, resulting in surfaces with smaller and more discrete oxide nodules. With the aid of three-dimensional atom probe tomography (3D-APT), Pourmajidian et al. [74] showed significant Sn segregation to the oxide/metal interface, where the detected levels were approximately ten times the bulk concentration. They attributed the suppression of both internal and external oxidation kinetics to the reduced oxygen solubility at the surface due to Sn occupation of the surface adsorption sites. This hypothesis is in agreement with

several other researchers [70,173,178]. However, the effects of these elements on the strength and formability of the substrate are unknown.
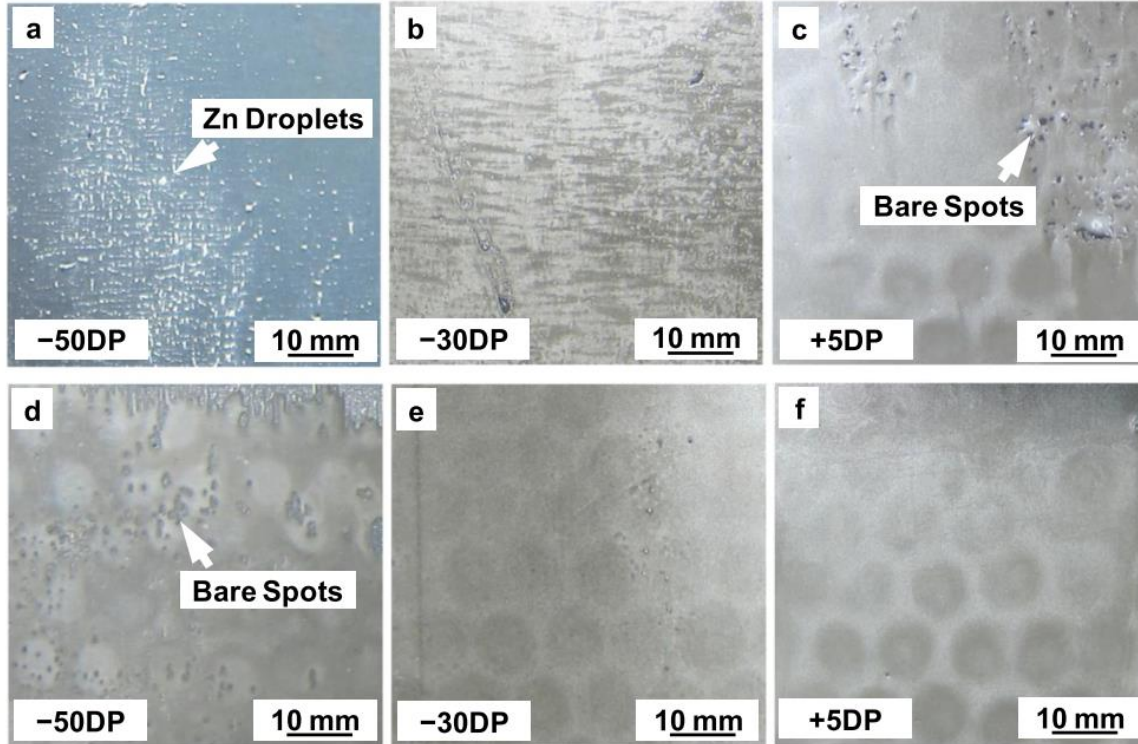
Figure 2.21: Images of the uniform coating area of the galvanized steel panels, (a-c) 0.1C-6Mn-2Si (wt%) and (d-f) 0.1C-6Mn-2Si-0.05Sn (wt%) [75].

2.4   Summary

To conclude this chapter, it is evident that significant efforts have been devoted to the development of medium-Mn 3G AHSS, but there are many outstanding questions remaining about the properties that can be achieved using CGL-compatible processing, which is essential for large-scale industrial production for automotive applications. Among the data published on the mechanical properties that can be achieved with medium-Mn steel compositions, the vast majority have employed longer annealing times at higher temperatures than are possible in conventional industrial CGLs. Moreover, the only selective oxidation and reactive wetting trials performed to date on medium-Mn substrates have been done on model alloys that had been processed through

a single annealing cycle. There is a significant knowledge gap with regard to the impact of two-stage annealing cycles (which have been optimized for microstructural and mechanical property development) on the selective oxidation and reactive wetting of these steels.

2.5   References

[1]   D.K. Matlock, J.G. Speer, Design Considerations for the Next Generation of Advanced High Strength Steel Sheets, in: H.C. Lee (Ed.), Proc. 3rd Int. Conf. Struct. Steels, Korean Institute of Metals and Materials, Seoul, Korea, 2006: pp. 774–781.

[2]   D.K. Matlock, J.G. Speer, Third Generation of AHSS: Microstructure Design Concepts, Springer, Jamshedpur, India, 2009. doi:10.1007/978-1-84882-454-6_11.

[3]   E. De Moor, P.J. Gibbs, J.G. Speer, D.K. Matlock, Strategies for Third-Generation Advanced High Strength Steel Development, AIST Trans. 7 (2010) 133–144.

[4]   D.K. Matlock, J.G. Speer, E. De Moor, P.J. Gibbs, Recent Developments in Advanced High Strength Sheet Steels for Automotive Applications: An Overview, JESTECH. 15 (2012) 1–12.

[5]   G.B. Olson, M. Cohen, Kinetics of strain-induced martensitic nucleation, Metall. Trans. A. 6 (1975) 791–795.

[6]   G.B. Olson, Transformation Plasticity and the Stability of Plastic Flow, in: G. Krauss (Ed.), Deform. Process. Struct., ASM, Metals Park, OH, 1984: pp. 391–425.

[7]   A.J. Clarke, J.G. Speer, M.K. Miller, R.E. Hackenberg, D.V. Edmonds, D.K. Matlock, F.C. Rizzo, K.D. Clarke, E. De Moor, Carbon partitioning to austenite from martensite or bainite during the quench and partition (Q&P) process: A critical assessment, Acta Mater. 56 (2008) 16–22. doi:10.1016/j.actamat.2007.08.051.

[8]   K. Mukherjee, S.S. Hazra, M. Militzer, Grain Refinement in Dual-Phase Steels, 40 (2009). doi:10.1007/s11661-009-9899-9.

[9]   M. Calcagnotto, D. Ponge, D. Raabe, Effect of grain refinement to 1 um on strength and toughness of dual-phase steels, Mater. Sci. Eng. A. 527 (2010) 7832–7840. doi:10.1016/j.msea.2010.08.062.

[10]   O. Matsumura, Y. Sakuma, H. Takechi, Enhancement of Elongation by Retained Austenite in Intercritical Annealed 0.4C-1.5Si-0.8Mn Steel, Trans. ISIJ. 27 (1987) 570–579.

[11]   O. Matsumura, Y. Sakuma, Y. Ishii, J. Zhao, Effect of Retained Austenite on Formability of High Strength Sheet Steels, ISIJ Int. 32 (1992) 1110–1116.

[12] A.Z. Hanzaki, P.D. Hodgson, S. Yue, Hot Deformation Characteristics ot Si-Mn TRIP Steels with and without Nb Microalloy Additions, ISIJ Int. 35 (1995) 324–331.

[13] F. Perrard, C. Scott, Vanadium Precipitation During Intercritical Annealing in Cold Rolled TRIP Steels, ISIJ Int. 47 (2007) 1168–1177.

[14] H.J. Jun, N. Fonstein, Microstructure and Tensile Properties of TRIP-aided CR Sheet Steels : TRIP Dual and Q & P International Conference on New Developments in Advanced High-Strength Sheet Steels, Proc. Intl. Conf. New Dev. Adv. High-Strength Sheet Steels. (2008) 155–168.

[15] K. Sugimoto, T. Iida, J. Sakaguchi, T. Kashima, Retained Austenite Characteristics and Tensile Properties in a TRIP Type Bainitic Sheet Steel, ISIJ Int. 40 (2000) 902–908.

[16] V.T.T. Miihkinen, D.V. Edmonds, Tensile deformation of two experimental high-strength bainitic low-alloy steels containing silicon, Mater. Sci. Technol. 3 (1987) 432–440.

[17] F.G. Caballero, H.K.D.H. Bhadeshia, K.J.A. Mawella, D.G. Jones, P. Brown, Design of novel high strength bainitic steels: Part 1, Mater. Sci. Technol. 17 (2001) 512–516. doi:10.1179/026708301101510348.

[18] F.G. Caballero, H.K.D.H. Bhadeshia, K.J.A. Mawella, D.G. Jones, P. Brown, Design of novel high strength bainitic steels: Part 2, Mater. Sci. Technol. 17 (2001) 517–522. doi:10.1179/026708301101510357.

[19] C. Garcia-Mateo, F.G. Caballero, H.K.D.H. Bhadeshia, Development of Hard Bainite, ISIJ Int. 43 (2003) 1238–1243.

[20] C. Garcia-Mateo, F.G. Caballero, H.K.D.H. Bhadeshia, Acceleration of Low-temperature Bainite, ISIJ Int. 43 (2003) 1821–1825.

[21] C. Garcia-Mateo, F.G. Caballero, Ultra-high–strength Bainitic Steels, ISIJ Int. 45 (2005) 1736–1740.

[22] F.G. Caballero, J. Chao, J. Cornide, C. Garcia-Mateo, M.J. Santofimia, C. Capdevila, Toughness deterioration in advanced high strength bainitic steels, Mater. Sci. Eng. A. 525 (2009) 87–95. doi:10.1016/j.msea.2009.06.034.

[23] T. Lolla, G.M. Cola, B. Narayanan, B. Alexandrov, S.S. Babu, Development of rapid heating and cooling (flash processing) process to produce advanced high strength steel microstructures, Mater. Sci. Technol. 27 (2011) 863–875. doi:10.1179/174328409X433813.

[24] G.M. Cola, Flash Bainite: Room-Temperature Stamping 1500-1800 MPa Structural and Energy-Absorbing Components to <2T Bend Radii, in: Int. Symp. New Dev. Adv. High-Strength Sheet Steels, AIST, Keystone, Colorado, 2017: pp. 261–272.

[25] B. Shassere, S.S. Babu, G.M. Cola, T. Muth, T. Watkins, Microstructure Control and Correlation to Formability of Low Alloy Steel Via Flash Processing, in: Proc. MS&T 2018, Columbus, Ohio.: pp. 321–328. doi:10.7449/2018/MST.

[26] K.M.H. Bhadhon, J.R. McDermid, X. Wang, E.A. McNally, F.E. Goodwin, Fine-Scale Microstructure Characterization And Mechanical Properties Of CGL-Compatible Heat Treated Medium-Mn TRIP Steel, in: Proc. 11th Conf. Zinc Zinc Alloy Coat. Steel Sheet, Galvatech 2017, ISIJ International, Tokyo, 2017: pp. 493–500.

[27] D.M. Pallisco, K.M.H. Bhadhon, V. Patel, M. Pourmajidian, F.E. Goodwin, J.R. McDermid, 9-11: Galvanizing of Medium-Manganese Third Generation Advanced High Strength Steels, in: Proc. 4th Int'l Conf. Med. High-Manganese Steels, 2019: pp. 375–378.

[28] V. Patel, Microstructure and Mechanical Properties of Medium Mn Steel, McMaster University, 2019.

[29] R.L. Miller, Ultrafine-Grained Microstructures and Mechanical Properties of Alloy Steels, Metall. Trans. 3 (1972) 905–912.

[30] R.A. Grange, R.L. Miller, Heat Treatment for Improving the Toughness of High Manganese Steels, United States Patent Number 4,047,979, n.d.

[31] M.J. Merwin, Low-Carbon Manganese TRIP Steels, Mater. Sci. Forum. 539–543 (2007) 4327–4332.

[32] M.J. Merwin, Microstructure and Properties of Cold Rolled and Annealed Low-Carbon Manganese TRIP Steels, Iron Steel Technol. 5 (2008) 66–84.

[33] P.J. Gibbs, E. De Moor, M.J. Merwin, B. Clausen, J.G. Speer, D.K. Matlock, Austenite stability effects on tensile behavior of manganese-enriched- austenite transformation-induced plasticity steel, Metall. Mater. Trans. A. 42 (2011) 3691–3702.

[34] S. Lee, K. Lee, B.C. De Cooman, Observation of the TWIP + TRIP Plasticity-Enhancement Mechanism in Al-Added 6 Wt Pct Medium Mn Steel, Metall. Mater. Trans. A. 46A (2015) 2356–2363. doi:10.1007/s11661-015-2854-z.

[35] H. Luo, H. Dong, New ultrahigh-strength Mn-alloyed TRIP steels with improved formability manufactured by intercritical annealing, Mater. Sci. Eng. A. 626 (2015) 207–212.

[36] K. Steineder, D. Krizan, R. Schneider, C. Béal, C. Sommitsch, On the microstructural characteristics influencing the yielding behavior of ultra-fine grained medium-Mn steels, Acta Mater. 139 (2017) 39–50.

[37] Y. Ma, Medium-manganese steels processed by austenite-reverted-transformation annealing for automotive applications, Mater. Sci. Technol. 33 (2017) 1713–1727. doi:10.1080/02670836.2017.1312208.

[38]   A. Nicholson, J.D. Murray, Surface hot shortness in low carbon steel, J. Iron Steel Inst. 203 (1965) 1007–1018.

[39]   F.B. Pickering, Physical metallurgy and the design of steels, Applied Science Publishers, 1978.

[40]   H.K.D.H. Bhadeshia, D.V. Edmonds, The bainite transformation in a silicon steel, Metall. Trans. A. 10 (1979) 895–907. doi:10.1007/BF02658309.

[41]   H.C. Chen, H. Era, M. Shimizu, Effect of Phosphorus on the Formation of Retained Austenite in Low-Carbon Steel Sheet., Metall. Trans. A. 20A (1989) 437–445.

[42]   H.K.D.H. Bhadeshia, J.W. Christian, Bainite in steels, Metall. Trans. A. 21 (1990) 767–797. doi:10.1007/BF02656561.

[43]   N. Imai, N. Komatsubara, K. Kunishige, Effect of Alloying Element and Microstructure on Mechanical Properties of Low-alloy TRIP Steels, CAMP-ISIJ. 8 (1995) 572–575.

[44]   A. Pichler, P. Stiaszny, R. Potzinger, R. Tikal, E. Werner, TRIP steels with reduced Si content, in: Proc. 40th MWSP Conf., ISS, Warrendale, PA, USA, 1998: pp. 259–274.

[45]   M. De Meyer, D. Vandershueren, B.C. De Cooman, The Influence of Substitution of Si by Al on the Properties of Cold Rolled C-Mn-Si TRIP Steels, ISIJ Int. 39 (1999) 813–822.

[46]   P.J. Jacques, E. Girault, T. Catlin, N. Geerlofs, T. Kop, S. van der Zwaag, F. Delannay, Bainite transformation of low carbon Mn–Si TRIP-assisted multiphase steels: influence of silicon content on cementite precipitation and austenite retention, Mater. Sci. Eng. A. 273–275 (1999) 475–479. doi:10.1016/S0921-5093(99)00331-7.

[47]   J. Mahieu, J. Maki, B.C. De Cooman, S. Claessens, Phase Transformation and Mechanical Properties of Si-Free CMnAl Transformation-Induced Plasticity-Aided Steel, Metall. Mater. Trans. A. 33 (2002) 2573–2580.

[48]   B. Ehrhardt, T. Gerber, H. Hofmann, T.W. Schaumann, Property related design of advanced cold rolled steels with induced plasticity, Steel Grips. 2 (2004) 247–255.

[49]   B.C. De Cooman, High Mn TWIP steel and medium Mn steel, in: R. Rana, S.B. Singh (Eds.), Automot. Steels Des. Metall. Process. Appl., Woodhead Publishing, 2017: pp. 317–385.

[50]   E.M. Bellhouse, J.R. McDermid, Selective Oxidation and Reactive Wetting during Galvanizing of a CMnAl TRIP-Assisted Steel, Metall. Mater. Trans. A. 42A (2011) 2753–2768. doi:10.1007/s11661-010-0192-8.

[51]   H.K.D.H. Bhadeshia, R.W.K. Honeycombe, Steels: Microstructure and Properties, 4th Ed., Elsevier Ltd, Oxford, United Kingdom, 2017.

[52] K. Hulka, W. Bleck, K. Papamantellos, Relationships Between Heat Treatment Conditions, Microstructure and Properties of Niobium Microalloyed TRIP Steel, in: Proc. 41st Mech. Work. Steel Process. Conf., Iron and Steel Society, Baltimore, USA, 1999: pp. 67–88.

[53] W. Bleck, S. Kranz, J. Ohlert, K. Papamantellos, Effect of the Testing Temperature on the Mechanical Behavior of Low and High Alloyed Steels Showing the TRIP Effect, in: Proc. 41st Mech. Work. Steel Process. Conf., Iron and Steel Society, Baltimore, USA, 1999: pp. 295–305.

[54] B.C. De Cooman, Structure–properties relationship in TRIP steels containing carbide-free bainite, Curr. Opin. Solid State Mater. Sci. 8 (2004) 285–303. doi:10.1016/j.cossms.2004.10.002.

[55] D. Krizan, B.C. De Cooman, J. Antonissen, Retained Austenite Stability in Cold Rolled CMnAlSiP Microalloyed TRIP Steels, in: Proc. Int. Conf. Adv. High Strength Sheet Steels Automot. Appl., AIST, Winter Park, USA, 2004: pp. 205–216.

[56] I.B. Timokhina, P.D. Hodgson, E.V. Pereloma, Effect of microstructure on the stability of retained austenite in TRIP steels, Metall. Mater. Trans. A. 35 (2004) 2331–2340. https://link.springer.com/content/pdf/10.1007%2Fs11661-006-0213-9.pdf.

[57] S. Traint, A. Pichler, M. Blaimschein, B. Röthler, C. Krempaszky, E. Werner, Alloy design, processing and properties of TRIP steels: A critical comparison (2004), in: Proc. Int. Conf. Adv. High Strength Sheet Steels Automot. Appl., AIST, Winter Park, USA, 2004: pp. 79–98.

[58] W. Bleck, A. Frehn, J. Ohlert, Niobium in dual phase and TRIP steels, in: Proc. Int. Symp. Niobium, TMS, Orlando, USA, 2001: pp. 727–752.

[59] K. Sugimoto, M. Mukherjee, TRIP aided and complex phase steels, in: R. Rana, S.B. Singh (Eds.), Automot. Steels Des. Metall. Process. Appl., Woodhead Publishing, 2017: pp. 217–257.

[60] A.Z. Hanzaki, S. Yue, P.D. Hodgson, The Influence of Bainite on Retained Austenite Characteristics in Si-Mn TRIP Steels, ISIJ Int. 35 (1995) 79–85. doi:10.2355/isijinternational.35.79.

[61] E.J. Drewes, E.F. Walker, Niobium bearing steels in the automotive industry, in: Proc. Int. Symp. Niobium, TMS, Orlando, USA, 2001: pp. 873–888.

[62] J.R. Patel, M. Cohen, Criterion for the action of applied stress in the martensitic transformation, Acta Metall. 1 (1953) 531–538.

[63] J. Wang, S. van der Zwaag, Stabilization Mechanisms of Retained Austenite in Transformation-Induced Plasticity Steel, Metall. Mater. Trans. A. 32 (2001) 1527–1539.

[64] P.J. Jacques, Q. Furnémont, F. Lani, T. Pardoen, F. Delannay, Multiscale mechanics of TRIP-assisted multiphase steels: I. Characterization and mechanical testing, Acta Mater. 55 (2007) 3681–3693. doi:10.1016/j.actamat.2007.02.029.

[65] H. Hofmann, D. Mattissen, T.W. Schaumann, Advanced Cold Rolled Steels for Automotive Applications, Steel Res. Int. 80 (2009) 22–28.

[66] D.-W. Suh, S.-J. Park, T.H. Lee, C.-S. Oh, S.-J. Kim, Influence of Al on the Microstructural Evolution and Mechanical Behavior of Low-Carbon, Manganese Transformation-Induced-Plasticity Steel, Metall. Mater. Trans. A. 41 (2010) 397–408. doi:10.1007/s11661-009-0124-7.

[67] S. Lee, Y. Estrin, B.C. De Cooman, Constitutive Modeling of the Mechanical Properties of V-added Medium Manganese TRIP Steel, Metall. Mater. Trans. A. 44A (2013) 3136–3146. doi:10.1007/s11661-013-1648-4.

[68] B. Sun, D. Palanisamy, D. Ponge, B. Gault, F. Fazeli, C. Scott, S. Yue, D. Raabe, Revealing fracture mechanisms of medium manganese steels with and without delta-ferrite, Acta Mater. 164 (2019) 683–696.

[69] D.M. Pallisco, J.R. McDermid, Mechanical property development of a 0.15C–6Mn–2Al–1Si third-generation advanced high strength steel using continuous galvanizing heat treatments, Mater. Sci. Eng. A. 778 (2020) 139111. doi:10.1016/j.msea.2020.139111.

[70] L. Cho, M.S. Kim, Y.H. Kim, B.C. De Cooman, Influence of Minor Alloying Elements on Selective Oxidation and Reactive Wetting of CMnSi TRIP Steel during Hot Dip Galvanizing, Metall. Mater. Trans. A. 45 (2014) 4484–4498. doi:10.1007/s11661-014-2394-y.

[71] L. Cho, E.J. Seo, G.S. Jung, D.W. Suh, B.C. De Cooman, Surface Selective Oxidation of Sn-Added CMnSi TRIP Steel, Metall. Mater. Trans. A. 47 (2016) 1705–1719. doi:10.1007/s11661-016-3331-z.

[72] J. Oh, L. Cho, M.S. Kim, K. Kang, B.C. De Cooman, The Effect of Bi on the Selective Oxide Formation on CMnSi TRIP Steel, Metall. Mater. Trans. A. 47 (2016) 5474–5486. doi:10.1007/s11661-016-3735-9.

[73] M. Pourmajidian, J.R. McDermid, Effect of Annealing Temperature on the Selective Oxidation and Reactive Wetting of a 0.1C-6Mn-2Si Advanced High Strength Steel During Continuous Galvanizing Heat Treatments, ISIJ Int. 58 (2018) 1635–1643. doi:10.2355/isijinternational.ISIJINT-2017-688.

[74] M. Pourmajidian, B. Langelier, J.R. McDermid, Effect of Process Atmosphere Dew Point and Tin Addition on Oxide Morphology and Growth for a Medium-Mn Third Generation Advanced Steel During Intercritical Annealing, Metall. Mater. Trans. A. 49 (2018) 5561–5573. doi:10.1007/s11661-018-4855-1.

[75]   M. Pourmajidian, J.R. McDermid, On the reactive wetting of a medium-Mn advanced high-strength steel during continuous galvanizing, Surf. Coatings Technol. 357 (2019) 418–426. doi:10.1016/j.surfcoat.2018.10.028.

[76]   G. Miyamoto, H. Usuki, Z.D. Li, T. Furuhara, Effects of Mn, Si and Cr addition on reverse transformation at 1073 K from spheroidized cementite structure in Fe-0.6 mass% C alloy, Acta Mater. 58 (2010) 4492–4502. doi:10.1016/j.actamat.2010.04.045.

[77]   W.Q. Cao, C. Wang, J. Shi, M.Q. Wang, W.J. Hui, H. Dong, Microstructure and mechanical properties of Fe–0.2C–5Mn steel processed by ART-annealing, Mater. Sci. Eng. A. 528 (2011) 6661–6666. doi:10.1016/j.msea.2011.05.039.

[78]   A. Arlazarov, A. Hazotte, O. Bouaziz, M. Goune, F. Kegel, Characterization of microstructure formation and mechanical behavior of an advanced medium Mn steel, Proc. MS&T 2012. (2012) 1124–1131.

[79]   A. Arlazarov, M. Goune, O. Bouaziz, F. Kegel, A. Hazotte, Time-evolution of microstructure and mechanical behaviour of double annealed medium Mn steel, Mater. Sci. Technol. 35 (2019) 2076–2083. doi:10.1080/02670836.2019.1585031.

[80]   J.I. Kim, J.H. Ryu, S.W. Lee, K. Lee, Y.-U. Heo, D.-W. Suh, Influence of the Initial Microstructure on the Reverse Transformation Kinetics and Microstructural Evolution in Transformation-Induced Plasticity – Assisted Steel, Metall. Mater. Trans. A. 47 (2016) 5352–5361.

[81]   K.M.H. Bhadhon, J.R. McDermid, F.E. Goodwin, Effect of Galvanizing Heat Treatment on the Microstructure and Mechanical Properties of a 6Mn-1.5Si Third Generation Advanced High Strength Steel, in: Proc. 10th Conf. Zinc Zinc Alloy Coat. Steel Sheet, Galvatech 2015, Toronto, 2015: pp. 936–943.

[82]   E. De Moor, D.K. Matlock, J.G. Speer, M.J. Merwin, Austenite stabilization through manganese enrichment, Scr. Mater. 64 (2011) 185–188. doi:10.1016/j.scriptamat.2010.09.040.

[83]   A. Arlazarov, M. Gouné, O. Bouaziz, A. Hazotte, Critical factors governing the thermal stability of austenite in an ultra-fined grained Medium-Mn steel, Philos. Mag. Lett. 97 (2017) 125–131. doi:10.1080/09500839.2017.1290293.

[84]   K.M.H. Bhadhon, Effect of Starting Microstructure and CGL Compatible Thermal Processing Cycle on the Mechanical Properties of a Medium-Mn Third Generation Advanced High Strength Steel, McMaster University, 2017.

[85]   J. Maki, J. Mahieu, B.C. De Cooman, S. Claessens, Galvanisability of silicon free CMnAl TRIP steels, Mater. Sci. Technol. 19 (2003) 125–131. doi:10.1179/026708303225009300.

[86]   E.M. Bellhouse, J.R. McDermid, Analysis of the Fe–Zn interface of galvanized high Al–low Si TRIP steels, Mater. Sci. Eng. A. 491 (2008) 39–46. doi:10.1016/j.msea.2007.12.033.

[87]   E.M. Bellhouse, J.R. McDermid, Selective Oxidation and Reactive Wetting of 1.0 Pct Si-0.5 Pct Al and 1.5 Pct Si TRIP-Assisted Steels, Metall. Mater. Trans. A. 41 (2010) 1539–1553. doi:10.1007/s11661-010-0192-8.

[88]   E.M. Bellhouse, J.R. McDermid, Selective Oxidation and Reactive Wetting During Hot-Dip Galvanizing of a 1.0 Pct Al-0.5 Pct Si TRIP-Assisted Steel, Metall. Mater. Trans. A. 43 (2012) 2426–2441. doi:10.1007/s11661-010-0192-8.

[89]   L. Li, B.C. De Cooman, R.-D. Liu, J. Vleugels, M. Zhang, W. Shi, Design of TRIP Steel With High Welding and Galvanizing Performance in Light of Thermodynamics and Kinetics, J. Iron Steel Res. Int. 14 (2007) 37–41. doi:10.1016/S1006-706X(07)60087-9.

[90]   R. Rana, Low-Density Steels, JOM. 66 (2014) 1730–1733. doi:10.1007/s11837-014-1137-2.

[91]   G. Krauss, Martensite in steel: Strength and structure, Mater. Sci. Eng. A. 273–275 (1999) 40–57. doi:10.1016/s0921-5093(99)00288-9.

[92]   L.-A. Nordstrom, On the yield strength of quenched low-carbon lath martensite, Scand. J. Met. 5 (1976) 159–165.

[93]   Q. Furnémont, The micromechanics of TRIP-assisted multiphase steels, Université catholique de Louvain, 2003.

[94]   P.J. Jacques, Q. Furnemont, S. Godet, T. Pardoen, K.T. Conlon, F. Delannay, Micromechanical characterisation of TRIP-assisted multiphase steels by in situ neutron diffraction, Philos. Mag. 86 (2006) 2371–2392. doi:10.1080/14786430500529359.

[95]   K. Steineder, D. Krizan, R. Schneider, C. Béal, C. Sommitsch, On the Damage Behavior of a 0.1C6Mn Medium-Mn Steel, Steel Res. Int. 89 (2018) 1700378. doi:10.1002/srin.201700378.

[96]   V.F. Zackay, E.R. Parker, D. Fahr, R. Busch, The enhancement of ducility in high-strength steels, ASM Trans. Q. 60 (1967) 252–259.

[97]   P.J. Jacques, Transformation-induced plasticity for high strength formable steels, Curr. Opin. Solid State Mater. Sci. 8 (2004) 259–265. doi:10.1016/j.cossms.2004.09.006.

[98]   D. Raabe, B. Sun, A. Kwiatkowski da Silva, B. Gault, H.-W. Yen, K. Sedighiani, P. Thoudden Sukumar, I.R. Souza Filho, S. Katnagallu, E. Jagle, P. Kurnsteiner, N. Kusampudi, L. Stephenson, M. Herbig, C.H. Liebscher, H. Springer, S. Zaefferer, V. Shah, S.-L. Wong, C. Baron, M. Diehl, F. Roters, D. Ponge, Current Challenges and Opportunities in Microstructure-Related Properties of Advanced High-Strength Steels, Metall. Mater. Trans. A. 51A (2020) 5517–5586. doi:10.1007/s11661-020-05947-2.

[99]   J.R. McDermid, H.S. Zurob, Y. Bian, Stability of Retained Austenite in High-Al, Low-Si TRIP-Assisted Steels Processed via Continuous Galvanizing Heat Treatments, Metall. Mater. Trans. A. 42 (2011) 3627–3637.

[100] P.J. Jacques, Q. Furnemont, A. Mertens, Delann, On the sources of work hardening in multiphase steels assisted by transformation-induced plasticity, Philos. Mag. A. 81 (2001) 1789–1812. doi:10.1080/01418610010009397.

[101] L. Samek, E. De Moor, J. Penning, B.C. De Cooman, Influence of alloying elements on the kinetics of strain-induced martensitic nucleation in low-alloy, multiphase high-strength steels, Metall. Mater. Trans. A. 37 (2006) 109–124. doi:10.1007/s11661-006-0157-0.

[102] A. Kelly, K.M. Knowles, Crystallography and Crystal Defects, 2nd Editio, John Wiley & Sons, Ltd., 2012. doi:10.1002/9783527644131.ch10.

[103] G. Schoeck, The dissociation energy of extended dislocations in fcc lattices, Philos. Mag. A Phys. Condens. Matter, Struct. Defects Mech. Prop. 79 (1999) 1207–1215. doi:10.1080/01418619908210356.

[104] L. Rémy, Twin-slip interaction in F.C.C. crystals, Acta Metall. 25 (1977) 711–714. doi:10.1016/0001-6160(77)90013-X.

[105] L. Rémy, Kinetics of F.C.C. deformation twinning and its relationship to stress-strain behaviour, Acta Metall. 26 (1978) 443–451. doi:10.1016/0001-6160(78)90170-0.

[106] O. Bouaziz, N. Guelton, Modelling of TWIP effect on work-hardening, Mater. Sci. Eng. A. 321 (2001) 246–249.

[107] O. Bouaziz, S. Allain, C. Scott, Effect of grain and twin boundaries on the hardening mechanisms of twinning-induced plasticity steels, Scr. Mater. 58 (2008) 484–487.

[108] A. Dumay, J.-P. Chateau, S. Allain, S. Migot, O. Bouaziz, Influence of addition elements on the stacking-fault energy and mechanical properties of an austenitic Fe – Mn – C steel, Mater. Sci. Eng. A. 484 (2008) 184–187.

[109] J. Nakano, P.J. Jacques, Effects of the thermodynamic parameters of the hcp phase on the stacking fault energy calculations in the Fe-Mn and Fe-Mn-C systems, CALPHAD. 34 (2010) 167–175.

[110] M. Ghasri-Khouzani, J.R. McDermid, Effect of carbon content on the mechanical properties and microstructural evolution of Fe-22Mn-C steels, Mater. Sci. Eng. A. 621 (2015) 118–127. doi:10.1016/j.msea.2014.10.042.

[111] M. Ghasri-Khouzani, J.R. McDermid, Microstructural evolution and mechanical behaviour of Fe-30Mn-C steels with various carbon contents, Mater. Sci. Technol. 33 (2017) 1159–1170. doi:10.1080/02670836.2016.1268662.

[112] R.E. Schramm, R.P. Reed, Stacking Fault Energies of Seven Commercial Austenitic Stainless Steels, Metall. Trans. A. 6 (1975).

[113] S. Allain, J. Chateau, O. Bouaziz, S. Migot, N. Guelton, Correlations between the calculated stacking fault energy and the plasticity mechanisms in Fe – Mn – C alloys, Mater. Sci. Eng. A. 397–389 (2004) 158–162.

[114] A. Saeed-Akbari, J. Imlau, U. Prahl, W. Bleck, Derivation and Variation in Composition-Dependent Stacking Fault Energy Maps Based on Subregular Solution Model in High-Manganese Steels, Metall. Mater. Trans. A. 40A (2009) 3076–3090.

[115] S. Curtze, V. Kuokkala, Dependence of tensile deformation behavior of TWIP steels on stacking fault energy , temperature and strain rate, Acta Mater. 58 (2010) 5129–5141.

[116] S. Curtze, V. Kuokkala, A. Oikari, J. Talonen, H. Ha, Thermodynamic modeling of the stacking fault energy of austenitic steels, Acta Mater. 59 (2011) 1068–1076.

[117] J. Kim, Y. Estrin, B.C. De Cooman, Constitutive Modeling of the Stacking Fault Energy-Dependent Deformation Behavior of Fe-Mn-C-(Al) TWIP Steels, Metall. Mater. Trans. A. 49 (2018) 5919–5924. doi:10.1007/s11661-018-4910-y.

[118] B.C. De Cooman, Y. Estrin, S.K. Kim, Twinning-induced plasticity (TWIP) steels, Acta Mater. 142 (2018) 283–362. doi:10.1016/j.actamat.2017.06.046.

[119] X. Liang, J.R. McDermid, O. Bouaziz, X. Wang, J.D. Embury, H.S. Zurob, Microstructural evolution and strain hardening of Fe–24Mn and Fe–30Mn alloys during tensile deformation, Acta Mater. 57 (2009) 3978–3988. doi:10.1016/j.actamat.2009.05.003.

[120] Y. Lee, C. Choi, Driving Force for $\gamma \to \varepsilon$ Martensitic Transformation and Stacking Fault Energy of γ in Fe-Mn Binary System, Metall. Mater. Trans. A. 31 (2000) 355–360.

[121] A. Saeed-Akbari, L. Mosecker, A. Schwedt, W. Bleck, Characterization and prediction of flow behavior in high-manganese twinning induced plasticity steels: Part i. mechanism maps and work-hardening behavior, Metall. Mater. Trans. A. 43 (2012) 1688–1704. doi:10.1007/s11661-011-0993-4.

[122] M.J. Whelan, Dislocation interactions in face-centred cubic metals, with particular reference to stainless steel, Proc. R. Soc. London. Ser. A. Math. Phys. Sci. 249 (1959) 114–137. doi:10.1098/rspa.1959.0011.

[123] J. Talonen, H. Hänninen, Formation of shear bands and strain-induced martensite during plastic deformation of metastable austenitic stainless steels, Acta Mater. 55 (2007) 6108–6118. doi:10.1016/j.actamat.2007.07.015.

[124] S. Allain, Caractérisation et modélisation thermomécaniques multi-échelles des mécanismes de déformation et d'écrouissage d'aciers austénitiques à haute teneur en manganèse- Application à l'effet TWIP Soutenue, Institut National Polytechnique de Lorraine, Nancy, 2004.

[125] D.T. Pierce, J.A. Jiménez, J. Bentley, D. Raabe, C. Oskay, J.E. Wittig, The influence of manganese content on the stacking fault and austenite/ε-martensite interfacial energies in Fe-Mn-(Al-Si) steels investigated by experiment and theory, Acta Mater. 68 (2014) 238–253. doi:10.1016/j.actamat.2014.01.001.

[126] S. Lee, B.C. De Cooman, Annealing Temperature Dependence of the Tensile Behavior of 10 pct Mn Multi-phase TWIP-TRIP Steel, Metall. Mater. Trans. A. 45 (2014) 6039–6052. doi:10.1007/s11661-014-2540-6.

[127] A.R. Marder, The metallurgy of zinc-coated steel, Prog. Mater. Sci. 45 (2000) 191–271.

[128] E.A. Silva, Private Communication, 2005.

[129] J. Mahieu, S. Claessens, B.C. De Cooman, Galvanizability of High-Strength Steels for Automotive Applications, Metall. Mater. Trans. A. 32 (2001) 2905–2908.

[130] P. Drillet, Z. Zermout, D. Bouleau, J. Mataigne, S. Claessens, Selective Oxidation of high Si, Mn and Al steel grade during Recrystallization Annealing, and steel/Zn reactivity, in: M.A. Baker (Ed.), Galvatech 2004 Proc., Association for Iron and Steel Technology, Chicago, IL, 2004: pp. 1123–1134.

[131] A.E. Morris, FREED Thermodynamic Database v7.8.1, (2013).

[132] I.H. Jung, Y.B. Kang, S.A. Decterov, A.D. Pelton, Thermodynamic evaluation and optimization of the MnO-Al2O 3 and MnO-Al2O3-SiO2 systems and applications to inclusion engineering, Metall. Mater. Trans. B Process Metall. Mater. Process. Sci. 35 (2004) 259–268. doi:10.1007/s11663-004-0027-3.

[133] C. Wagner, Reaktionstypen bei der Oxydation von Legierungen, Zeitschrift Für Elektrochemie. 63 (1959) 772–782.

[134] N. Birks, G.H. Meier, F.S. Pettit, Introduction to the High-Temperature Oxidation of Metals, Cambridge University Press, Cambridge, UK, 2006.

[135] D. Huin, P. Flauder, J.-B. Leblond, Numerical Simulation of Internal Oxidation of Steels during Annealing Treatments, Oxid. Met. 64 (2005) 131–167. doi:10.1007/s11085-005-5718-x.

[136] R.A. Rapp, Kinetics, Microstructures and Mechanism of Internal Oxidation - Its Effect and Prevention in High Temperature Alloy Oxidation, Corrosion. 21 (1965) 382–402. doi:10.5006/0010-9312-21.12.382.

[137] V.A. Lashgari, C. Kwakernaak, W.G. Sloof, Transition from Internal to External Oxidation of Mn Steel Alloys, Oxid. Met. 81 (2014) 435–451. doi:10.1007/s11085-013-9456-1.

[138] J.M. Mataigne, M. Lamberigts, V. Leroy, Developments in the Annealing of Sheet Steels, Minerals, Metals & Materials Society, Warrendale, PA, USA, 1992.

[139] H.J. Grabke, V. Leroy, H. Viefhaus, Segregation on the Surface of Steels in Heat Treatment and Oxidation, ISIJ Int. 35 (1995) 95–113. doi:10.2355/isijinternational.35.95.

[140] C.R. Shastry, J.A. Rotole, T.W. Kaiser, Characterization of selective oxidation of alloying elements in an advanced high strength steel from theoretical and experimental viewpoints, 7th Int. Conf. Zinc Zinc Alloy Coat. Steel Sheet. (2007) Paper B-6-2, 403-408.

[141] J.-B. Leblond, M. Pignol, D. Huin, Predicting the transition from internal to external oxidation of alloys using an extended Wagner model, Comptes Rendus Mécanique. 341 (2013) 314–322. doi:10.1016/j.crme.2013.01.003.

[142] J.-B. Leblond, J.M. Bergheau, R. Lacroix, D. Huin, Implementation and application of some nonlinear models of diffusion/reaction in solids, Finite Elem. Anal. Des. 132 (2017) 8–26. doi:10.1016/j.finel.2017.04.004.

[143] C.E. Jordan, A.R. Marder, Fe–Zn phase formation in interstitial-free steels hot-dip galvanized at 450 ° C Part II 0.20 wt% Al–Zn baths, J. Mater. Sci. 32 (1997) 5603–5610.

[144] M. Guttmann, Diffusive Phase Transformations in Hot-Dip Galvanizing, Mater. Sci. Forum. 155–156 (1994) 527–548. doi:10.4028/www.scientific.net/MSF.155-156.527.

[145] J.R. McDermid, M.H. Kaye, W.T. Thompson, Fe Solubility in the Zn-Rich Corner of the Zn-Al-Fe System for Use in Continuous Galvanizing and Galvannealing, Metall. Mater. Trans. B. 38 (2007) 215–230. doi:10.1007/s11663-007-9028-3.

[146] J. Nakano, D. V. Malakhov, S. Yamaguchi, G.R. Purdy, A full thermodynamic optimization of the Zn – Fe – Al system within the 420 – 500 ∘ C temperature range, Comput. Coupling Phase Diagrams Thermochem. 31 (2007) 125–140. doi:10.1016/j.calphad.2006.09.003.

[147] J. Nakano, Doctoral Thesis, McMaster University, 2006.

[148] L. Chen, R. Fourmentin, J.R. McDermid, Morphology and Kinetics of Interfacial Layer Formation during Continuous Hot-Dip Galvanizing and Galvannealing, Metall. Mater. Trans. A. 39A (2008) 2128–2142. doi:10.1007/s11661-008-9552-z.

[149] E. Baril, G. L'Espérance, Studies of the Morphology of the Al-Rich Interfacial Layer Formed during the Hot Dip Galvanizing of Steel Sheet, Metall. Mater. Trans. A. 30 (1999) 681–695. doi:10.1007/s11661-999-0060-6.

[150] R. Khondker, A.I.M. Mertens, J.R. McDermid, Effect of annealing atmosphere on the galvanizing behavior of a dual-phase steel, Mater. Sci. Eng. A. 463 (2007) 157–165. doi:10.1016/j.msea.2006.09.116.

[151] R. Kavitha, J.R. McDermid, On the in-situ aluminothermic reduction of manganese oxides in continuous galvanizing baths, Surf. Coat. Technol. 212 (2012) 152–158. doi:10.1016/j.surfcoat.2012.09.038.

[152] S. Alibeigi, R. Kavitha, R.J. Meguerian, J.R. McDermid, Reactive wetting of high Mn steels during continuous hot-dip galvanizing, Acta Mater. 59 (2011) 3537–3549. doi:10.1016/j.actamat.2011.02.027.

[153] R. Sagl, A. Jarosik, D. Stifter, G. Angeli, The role of surface oxides on annealed high-strength steels in hot-dip galvanizing, Corros. Sci. 70 (2013) 268–275. doi:10.1016/j.corsci.2013.01.039.

[154] Y.F. Gong, T.J. Song, H.S. Kim, J.H. Kwak, B.C. De Cooman, Development of Continuous Galvanization-compatible Martensitic Steel, in: Asia-Pacific Galvaniz. Conf. 2009 Proc., Jeju Island, South Korea, 2009: p. B-15.

[155] G. Seyed Mousavi, J.R. McDermid, Effect of dew point on the reactive wetting of a C-2Mn-1.3Si (wt%) advanced high strength steel during continuous galvanizing, Surf. Coatings Technol. 351 (2018) 11–20. doi:10.1016/j.surfcoat.2018.06.060.

[156] L. Cho, M.S. Kim, Y.H. Kim, B.C. De Cooman, Influence of gas atmosphere dew point on the galvannealing of CMnSi TRIP steel, Metall. Mater. Trans. A. 44 (2013) 5081–5095. doi:10.1007/s11661-013-1867-8.

[157] G. Seyed Mousavi, J.R. McDermid, Selective Oxidation of a C-2Mn-1.3Si (wt pct) Advanced High-Strength Steel During Continuous Galvanizing Heat Treatments, Metall. Mater. Trans. A. 49 (2018) 5546–5560. doi:10.1007/s11661-018-4854-2.

[158] G. Seyed Mousavi, B. Langelier, J.R. McDermid, Effect of Sn Addition, Process Atmosphere pO2, and Annealing Time on the Selective Oxidation of a C-2Mn-1.7Si (Wt Pct) Advanced High-Strength Steel During Continuous Galvanizing, Metall. Mater. Trans. A. 50 (2019) 2898–2911. doi:10.1007/s11661-019-05202-3.

[159] M. Pourmajidian, J.R. McDermid, Selective Oxidation of a 0.1C-6Mn-2Si Third Generation Advanced High-Strength Steel During Dew-Point Controlled Annealing, Metall. Mater. Trans. A. 49 (2018) 1795–1808. doi:10.1007/s11661-018-4513-7.

[160] I. Parezanovic, M. Spiegel, Surface Modification of Various Fe-Si and Fe-Mn Alloys by Oxidation/Reduction Treatments, Surf. Eng. 20 (2004) 285–291.

[161] Y.F. Gong, B.C. De Cooman, Influence of the oxidation-reduction process on the surface and sub-surface microstructure of intercritically annealed CMnSi TRIP steel, ISIJ Int. 51 (2011) 630–637. doi:10.2355/isijinternational.51.630.

[162] K. Kahoul, M. Turchetto, Hot-Dip Galvanizing Line at ARVEDI Producing AHSS Over 800 Mpa, in: Proc. 10th Conf. Zinc Zinc Alloy Coat. Steel Sheet, Galvatech 201510th Int. Conf. Zinc Zinc Alloy Coat. Steel Sheet, AIST, Toronto, Canada, 2015: pp. 436–443.

[163] L. Kümmel, T. Daube, F. Brühl, C. Sasse, Galvanizing of 3rd Generation AHSS-Grades with Advanced Furnace and Pre-Oxidation Technology, in: Proc. 11th Conf. Zinc Zinc Alloy Coat. Steel Sheet, Galvatech 2017, ISIJ, Tokyo, Japan, 2017: pp. 283–290.

[164] X. Jin, G. Hu, L. Wang, H. Wang, Characterization of surface layers of oxidation-reduction treated Si and Mn added advanced high strength steel, Surf. Coatings Technol. 382 (2020) 125172. doi:10.1016/j.surfcoat.2019.125172.

[165] Y.-I. Choi, W.-J. Beom, C.-J. Park, D. Paik, M.-H. Hong, Surface oxidation of the high-strength steels electrodeposited with Cu or Fe and the resultant defect formation in their coating during the following galvanizing and galvannealing processes, Metall. Mater. Trans. A. 41 (2010) 3379–3385. doi:10.1007/s11661-010-0427-8.

[166] R. Sa-nguanmoo, E. Nisaratanaporn, Y. Boonyongmaneerat, Hot-dip galvanization with pulse-electrodeposited nickel pre-coatings, Corros. Sci. 53 (2011) 122–126. doi:10.1016/j.corsci.2010.09.031.

[167] Y. Tobiyama, S. Fujita, T. Maruyama, Improvement of galvanizability of silicon-bearing steel by electrodeposited iron coating containing oxygen, ISIJ Int. 52 (2012) 115–120. doi:10.2355/isijinternational.52.115.

[168] A. Chakraborty, A. Mondal, S. Bysakh, M. Dutta, S.B. Singh, Microstructural investigation of galvanized coatings with prior flash coating of copper on DP steels, Surf. Coatings Technol. 285 (2016) 220–226. doi:10.1016/j.surfcoat.2015.11.043.

[169] Q. Zhang, S. Jiang, Development of Zinc and Zinc-Alloy Coated Steel Sheets in China, in: Proc. 12th Conf. Zinc Zinc Alloy Coat. Steel Sheet, Galvatech 2021, ASMET, Vienna, Austria, 2021: pp. 39–52.

[170] E. Zoestbergen, C. Commadeur, R.J. Snijders, E.P.M. Bakker, P.W. Hazelett, D.A. Hamilton, S.J. Widdis, T.D. Kaiser, Feeding Technology for a Continuous PVD Line, in: Proc. 12th Conf. Zinc Zinc Alloy Coat. Steel Sheet, Galvatech 2021, ASMET, Vienna, Austria, 2021: pp. 1144–1153.

[171] A. Ruck, D. Monceau, H.J. Grabke, Effects of tramp elements Cu, P, Pb, Sb and Sn on the kinetics of carburization of case hardening steels, Steel Res. Int. 67 (1996) 240–246. doi:10.1002/srin.199605484.

[172] Y. Zhang, Y. Zhang, F. Yang, Z. Zhang, Effect of Alloying Elements (Sb, B) on Recrystallization and Oxidation of Mn-Containing IF Steel, J. Iron Steel Res. Int. 20 (2013) 39–44. doi:10.1016/S1006-706X(13)60067-9.

[173] G. Lyudkovsky, The Effect of Antimony on Internal Oxidation and Magnetic Properties of Si-Al Electrical Steels, IEEE Trans. Magn. 22 (1986) 508–510.

[174] H.J. Grabke, Surface and grain boundary segregation on and in iron and steels, ISIJ Int. 29 (1989) 529–538. doi:10.2355/isijinternational.29.529.

[175] H.J. Grabke, Surface and Grain Boundary Segregation of Antimony and Tin - Effects on Steel Properties, Kovine, Zlitine, Tehnol. 30 (1996) 483–495.

[176] E.D. Hondros, M.P. Seah, Segregation to interfaces, Int. Met. Rev. 22 (1977) 262–301.

[177] M.P. Seah, Adsorption-Induced Interface Decohesion, Acta Metall. 28 (1980) 955–962.

[178] Z.T. Zhang, I.R. Sohn, F.S. Pettit, G.H. Meier, S. Sridhar, Investigation of the Effect of Alloying Elements and Water Vapor Contents on the Oxidation and Decarburization of Transformation-Induced Plasticity Steels, Metall. Mater. Trans. B. 40 (2009) 567–584. doi:10.1007/s11663-009-9255-x.

3 Mechanical Property Development of a 0.15C-6Mn-2Al-1Si Third-Generation Advanced High Strength Steel using Continuous Galvanizing Heat Treatments

Daniella M. Pallisco, Joseph R. McDermid

Department of Materials Science and Engineering, McMaster University, 1280 Main Street West, Hamilton, Ontario, Canada, L8S 4L8

3.1 Abstract

The effects of starting microstructure and intercritical annealing (IA) temperature on the mechanical properties of a prototype 0.15C-6Mn-1.5Al-1Si (wt%) third-generation medium manganese advanced high strength steel (3G AHSS) were determined. The general 3G AHSS mechanical property targets UTS $\times$ TE of 24,000-40,000 MPa% were met after a continuous galvanizing line (CGL)-compatible IA treatments at 710°C and 740°C for 120 s from an 80% martensite – 20% ferrite starting microstructure due to the as-annealed microstructure having large volume fractions of stable retained austenite. The deformation-induced retained austenite to martensite transformation – or TRansformation-induced plasticity (TRIP) – kinetics were a strong function of IA temperature and resulting retained austenite stability. In particular, the 665°C intercritical anneal produced retained austenite which only partially transformed during deformation and the 740°C intercritical anneal produced retained austenite which exhausted the TRIP effect at significantly lower strains than those observed for the 710°C treatment. It was also shown that significant deformation-induced mechanical twinning occurred in the retained austenite, aiding in sustaining the work hardening rate. Overall, it was determined that medium-Mn 3G AHSS can be produced using CGL-compatible thermal cycles, which holds promise for cost-effective production of these alloys.

3.2   Introduction

Third generation advanced high strength steels (3G AHSS) are promising candidate materials for vehicle light-weighting due to their superior combinations of high strength and ductility versus the first generation AHSS and lower alloying costs versus the so-called high Mn and similar second generation AHSS, making them reasonably cost-effective [1–4]. Among several approaches proposed, medium-Mn transformation- and twinning-induced plasticity (TRIP/TWIP)-assisted steels are being investigated due to the potential for their processing routes being compatible with the continuous galvanizing line (CGL) [5–8], which provides the robust corrosion protection required for automotive applications at reasonable cost. The mechanical properties of these grades are reliant on the chemical stabilization of large volume fractions of retained austenite, which then gradually transforms to martensite upon deformation [1–4]. In the case of medium-Mn TRIP steels, it has been shown by several authors that the starting microstructure and intercritical annealing parameters strongly affect the austenite reversion kinetics and retained austenite chemical stability and morphology and, thereby, have a significant influence on the microstructural evolution and mechanical properties of these alloys [9–16].

For example, it has been established that intercritical annealing of medium-Mn steels from an initial martensitic microstructure accelerates austenite reversion kinetics and results in the formation of lath-type retained austenite films that are more mechanically stable than the globular retained austenite obtained by intercritically annealing from a partially tempered martensitic microstructure [5–7,17–20]. In addition, alloying additions are known to affect the retained austenite stacking fault energy (SFE) [21–28], which is thought to have a strong influence on its propensity for deformation induced twin formation – i.e. the TWIP effect. The triggering of the TWIP effect provides the opportunity for the dynamic formation of additional dislocation barriers within the retained austenite during deformation and is, thereby, thought to contribute to the

maintenance of high instantaneous working hardening rates by reducing the dislocation mean free path [23,29–34]. The combination of the TRIP and (possible) TWIP effects to the maintenance of high work hardening rates delays the onset of plastic instability, thereby allowing medium-Mn steels to develop high strengths and uniform elongations.

Though many researchers have dedicated significant efforts to developing medium-Mn steels that achieve the 3G AHSS mechanical property targets, there are a very limited number of contributions that explore CGL-compatible thermal processing routes for these grades. To this end, the objective of this investigation is to determine the microstructural evolution and resulting mechanical property development of a prototype 0.15C-6Mn-2Al-1Si (wt%) transformation-induced plasticity 3G AHSS as a function of intercritical annealing (IA) temperature and starting microstructure within the context of maintaining CGL-compatible thermal processing.

3.3   Materials and Methods

The experimental steel was fabricated at United States Steel R&D (Munhall, Pennsylvania) via vacuum melting, slab casting, hot rolling, coiling, edge trimming, surface grinding and cold rolling. The thermomechanical processing route details are shown in Figure 3.1. The chemical composition of the experimental steel can be found in Table 3.1.
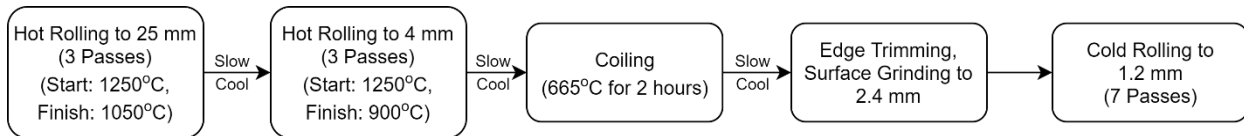
Figure 3.1: Flowchart detailing the thermomechanical processing route of the experimental steel.

Table 3.1: Chemical composition of the experimental steel (wt%).

C	Mn	Al	Si	Mo	Ti	Fe
0.15	5.56	1.89	1.10	0.08	0.01	Balance

Prior to annealing, all samples were immersed and nylon brushed in a 2% $NaOH_{(aq)}$ solution heated to 80°C to remove surface fines and organic contaminants. Annealing was performed in the

McMaster Galvanizing Simulator (MGS), details of which are provided elsewhere [35,36]. All annealing cycles utilized the MGS quartz lamp infrared furnace under a N_2-5vol% H_2 atmosphere with a controlled dew point of -30°C. The sample temperature was monitored by a type K thermocouple (0.5 mm, ±3°C) welded to the surface of the sample.

Two substrate starting microstructures were investigated and are shown in Figure 3.2. The as-received cold-rolled (CR) starting microstructure (Figure 3.2(a)) was comprised mainly of cold-rolled tempered martensite with some cold-rolled ferrite. The 80% martensite – 20% ferrite (MF) starting microstructure (Figure 3.2(b)) was obtained by heating the as-received CR steel to 890°C, holding for 600 s, and quenching at −20°C/s to room temperature, per the thermal cycle specified in Figure 3.3. XRD indicated that neither starting microstructure contained detectable amounts of retained austenite.
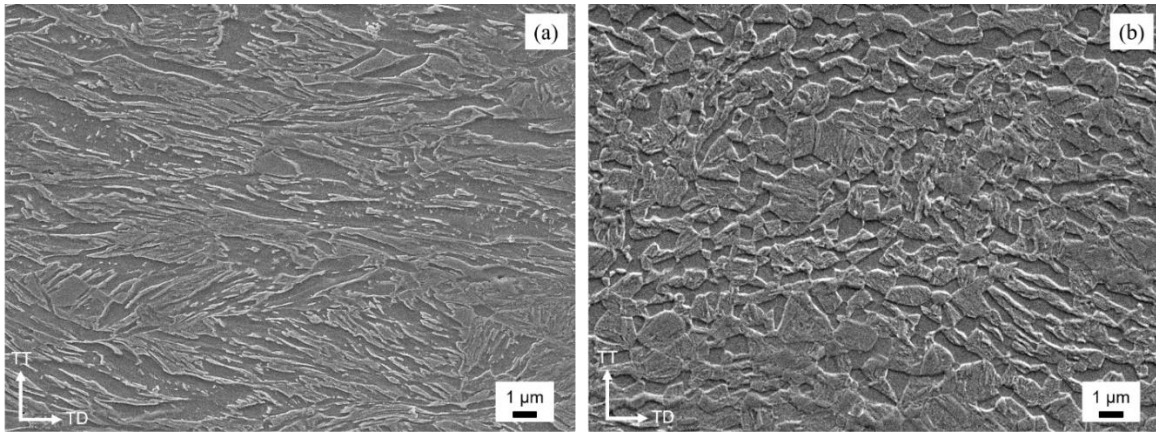
Figure 3.2: SEM-SEI images of the (a) CR (cold-rolled tempered martensite) and (b) MF (martensite-ferrite) starting microstructures.

Annealing cycles followed the schematic thermal profile shown in Figure 3.3, where the intercritical annealing (IA) parameters for processing the CR and MF starting microstructures are detailed in Table 3.2. The IA temperatures were chosen to be approximately 0%, 15%, and 30% between the Ac_2 and Ac_3 temperatures, according to the phase diagram generated using the

ThermoCalc® TCFE6 database. A peak annealing time of 120 s was chosen as it is compatible with industrial continuous galvanizing practice [5] and resulted in the stabilization of significant volume fractions of retained austenite in the as-annealed material. To simulate the pre-dipping thermal equilibration and dipping steps, an overaging treatment (OT) of 30 seconds at 460°C was used for all samples.

Table 3.2: Experimental intercritical annealing (IA) parameters and as-annealed volume fractions of retained austenite arising therefrom.

Sample ID	Starting Microstructure	Intercritical Annealing Temperature (°C)	As-Annealed Volume Fraction of Retained Austenite
CR-665°C	CR	665	0.25
MF-665°C	MF	665	0.21
MF-710°C	MF	710	0.31
MF-740°C	MF	740	0.30
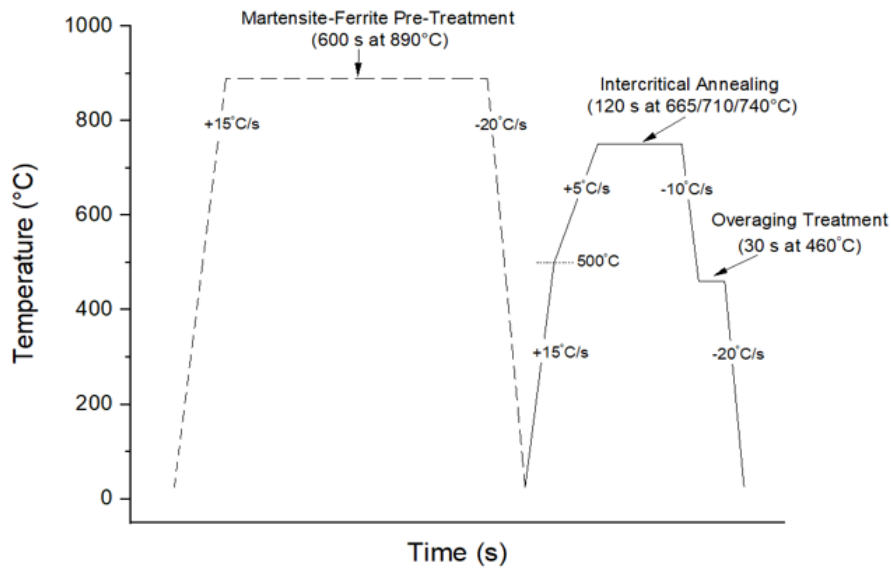
Figure 3.3: Schematic thermal profile for the experimental annealing treatments (note that the martensite-ferrite anneal was only used for the MF samples and not for the CR samples).

Samples used to evaluate bulk microstructural evolution consisted of rectangular coupons measuring 50 mm in the rolling direction (RD) and 10 mm in the transverse direction (TD). A

JEOL 7000F FEG-SEM in secondary electron imaging (SEI) mode was used for microstructural analysis of coupon cross-sections taken from the TD through thickness (TT) plane. Sample cross-sections were cold-mounted in epoxy resin and prepared using standard metallographic techniques. The polished samples were etched with 2% nitric acid in methanol for approximately five seconds in order to reveal the microstructures. The sample working surfaces were coated with a thin film of carbon to avoid charging during SEM examination. An acceleration voltage of 10 keV and working distance of 10 mm were used in all cases.

Larger panels measuring 200 mm (RD) × 120 mm (TD) were intercritically annealed, per the parameters listed in Table 3.2, to provide samples for tensile testing and additional microstructural evaluation analysis on unstrained and strained samples. Material from the 90 mm × 90 mm uniform heating zone, approximately centered on the annealed panels [17], was electric discharge machined into ASTM E8/E8M-16a [37] sub-sized tensile specimens with a gauge length of 25 mm and gauge width of 6 mm. The rolling direction was parallel to the longitudinal axis of all tensile samples. Room temperature uniaxial and load-unload-reload tensile testing was performed on a conventional 100 kN uniaxial tensile frame (MTS) with a crosshead speed of 1 mm/min. A conventional extensometer was used to measure sample elongation.

Uniaxial engineering stress – engineering strain and true stress – true strain curves were constructed from load/elongation measurements, where the engineering stress – strain curves were plotted to fracture and the true stress – strain curves plotted to the onset of necking (i.e. plastic instability), as determined using the Considère criterion (Equation 3.1):

$$\sigma = \frac{d\sigma}{d\varepsilon} \tag{3.1}$$

where σ and ε are true stress and strain, respectively. The true stress –strain curves were also linearly interpolated to the true fracture stress and strain in the neck, as determined from measurements of the fracture surface area and Equation 3.2, where A_O is the original sample cross-sectional area and A the area of the fracture surface:

$$\varepsilon_{fracture} = \ln\left(\frac{A_O}{A}\right) \tag{3.2}$$

It should be noted that the tensile curves shown below are representative examples of triplicate tests.

Interrupted tensile tests were performed in order to assess the sample retained austenite to martensite transformation kinetics as a function of tensile strain. Tensile tests were interrupted at 0.05 true strain intervals, and material from the uniform elongation region of the gauge length sectioned for subsequent analysis by XRD and TEM.

X-ray diffraction (XRD) was performed on cross-sections taken from the as-annealed, strained and fractured samples using a Bruker D8 DISCOVER with a DAVINCI.DESIGN diffractometer equipped with a Vantec 500 (MiKroGap TM technology) area detector and Co-source K_α radiation ($\lambda = 1.79026$ Å). Samples were cold-mounted in epoxy resin and ground with SiC papers (final step of 1200 grit) prior to insertion in the diffractometer. ASTM E975-13 [38] was used to calculate the volume fraction of retained austenite present using the austenite (111), (200), and (220) peaks. The resident TOPAS software (Bruker AXS) was used to perform a Rietveld refinement of the diffraction pattern (2θ range of 44° to 147°). Error bars represent the 95% confidence interval of the average retained austenite volume fraction obtained from triplicate measurements.

Fine-scale microstructural analysis was performed on a Philips CM-12 STEM/TEM operating in TEM mode. The instrument was operated at 120 keV in bright field (BF), dark field (DF) and selected area diffraction (SAD) modes. Thin foils were prepared from samples taken from the gauge lengths of tensile samples pulled to true strains of 0.05 and to fracture. Samples were mechanically polished to 80 μm thickness using progressively finer SiC papers, punched into 3 mm diameter discs, and electropolished at 20.5 V in a 10% solution of perchloric acid in methanol held at -40°C using a liquid nitrogen coolant.

Load-unload-reload tests were performed to estimate the relative magnitudes of the internal stresses, per the method described by Westphal et al. [39], based on the work of Sinclair [40] and Spencer [41]. The samples were loaded to tensile true strains increasing at 0.025 intervals up to the UTS with unloading to 15 N between loading and reloading steps. The back stress at a given value of true strain, σ_B, was calculated via Equation 3.3 [40,41], where σ_F is the forward stress prior to unloading and σ_R is the stress upon unloading (as measured by a 0.01% or 0.02% offset line, see Figure 3.4):

$$\sigma_B = \frac{\sigma_F + \sigma_R}{2} \qquad (3.3)$$

Although this technique does not directly measure the contribution of kinematic hardening to the overall flow stress, as would be the case in conventional Bauschinger tests, it does provide useful data in the trends in this contribution while avoiding buckling of the flat samples. The error bars in the load-unload-reload data presented below represent the 95% confidence interval of the mean stress value from triplicate samples.
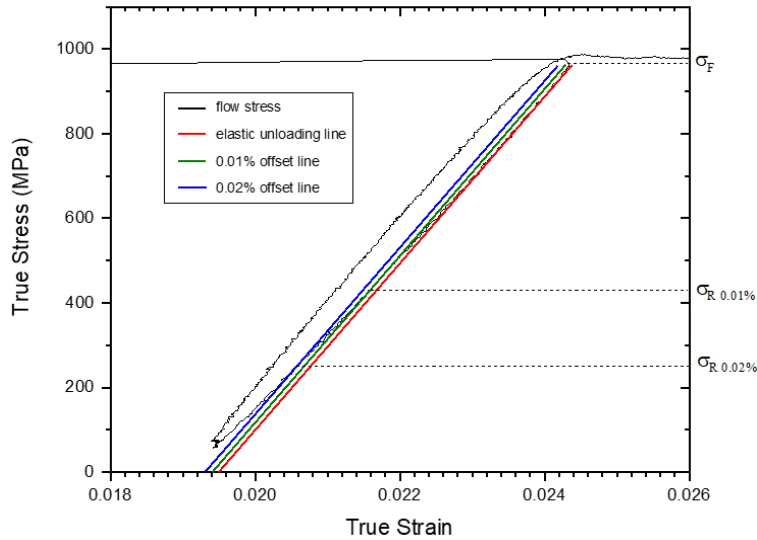
Figure 3.4: Determination of the forward, 0.01% offset reverse and 0.02% offset reverse stresses from true stress-strain data.

3.4   Results

3.4.1   Microstructures After Annealing

Secondary electron images of the as-annealed sample cross-sections are shown in Figure 3.5. Examination of Figure 3.5 will show that, in general, the microstructures consisted of islands of retained austenite/martensite and significant volume fractions of polygonal ferrite. Comparison of Figure 3.5(a) to Figure 3.5(b-d) will show that intercritically annealing from the CR starting microstructure resulted in a more globular morphology for the martensite/retained austenite phases (Figure 3.5(a)) versus the lath-like martensite/retained austenite with polygonal ferrite morphology obtained when using the MF microstructure (Figure 3.5(b-d)), irrespective of the intercritical annealing temperature. This finding is consistent with the observations of several authors [5–7,17–20], who have determined that the retained austenite/martensite morphology in intercritically annealed medium-Mn steels is strongly dependent on the starting microstructure. It should also be noted that annealing at higher IA temperatures resulted in coarsening of the polygonal ferrite (Figure 3.5(b-d)).
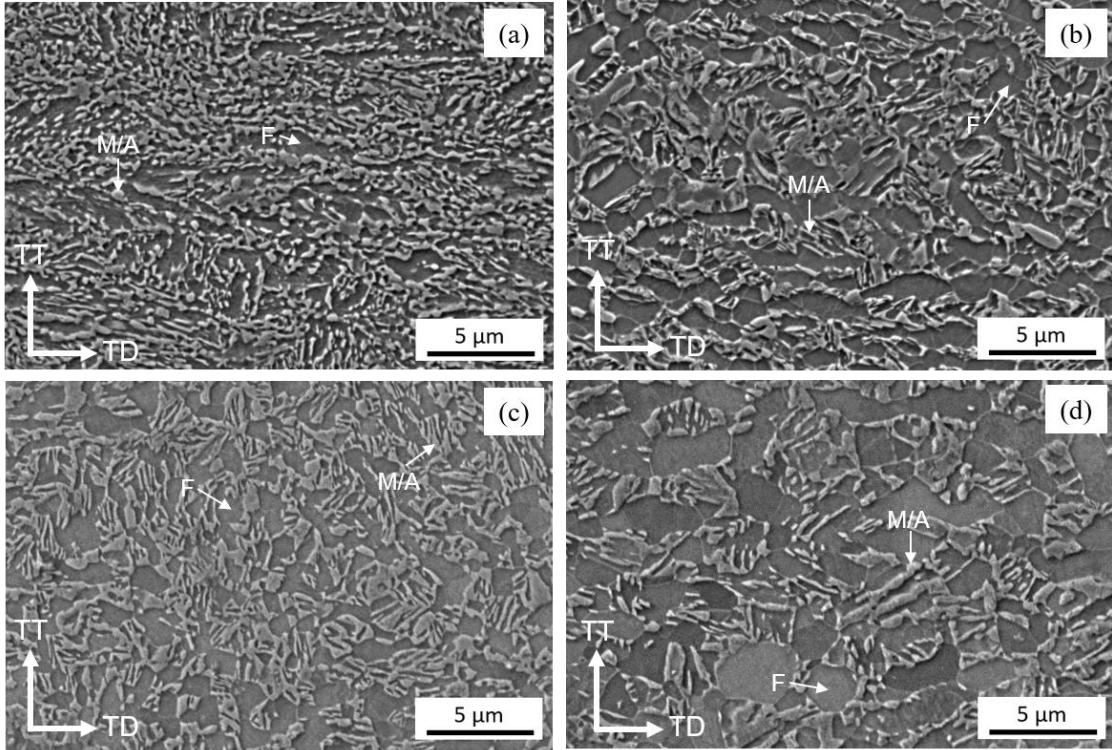
Figure 3.5: SEM-SEI images of as-annealed sample cross-sections: (a) CR-665°C; (b) MF-665°C; (c) MF-710°C; (d) MF-740°C. Polygonal ferrite is denoted by F, and the martensite/retained austenite denoted by M/A.

3.4.2 Monotonic Tensile Tests

Representative engineering stress-strain curves for each annealing condition are shown in Figure 3.6(a). A summary of the engineering stress-strain mechanical properties is provided in Table 3.3. The tensile elongation was affected by the starting microstructure, where annealing from the MF condition resulted in increased ductility for the 665°C treatments (i.e. CR-666°C vs. MF-665°C, Figure 3.6(a)). The highest yield strength was obtained from the CR-665°C treatment, where the equivalent MF-665°C treatment resulted in greater than a 100 MPa reduction in yield strength (Figure 3.6(a), Table 3.3). For the samples annealed from the MF starting microstructure, the yield strength decreased and the ultimate tensile strength increased with increasing IAT (Table 3.3). It is interesting to note that all of the MF samples showed significant yield point elongation.

The work hardening rate curves, shown in Figure 3.6(c), were obtained by taking the derivative of the true stress-true strain curves (Figure 3.6(b)) after the elasto-plastic transition. The end of yield point elongation marks the onset of plasticity-enhancing mechanisms in these samples, as indicated by the sharp increase in work hardening rate (shown by the arrows in Figure 3.6(c)) for all of the MF starting microstructure treatments. In addition to being affected by the starting microstructure, the work hardening behaviour for the MF samples was a strong function of the IA temperature, with the highest IA temperature (740°C) resulting in the highest instantaneous work hardening rates after yielding and a higher rate of decrease in work hardening rate with increasing IA and strain. For the MF-710°C treatment, the instantaneous work hardening rate after yielding was intermediate between that of the MF-740°C and MF-665°C samples, but was maintained above that of the flow stress to higher strains, thereby resulting in the highest tensile elongations observed (Figure 3.6 and Table 3.3). This latter observation is indicative of changes in the retained austenite mechanical stability with increasing IA temperature, as will be discussed below. Further examination of Table 3.3 will show that the UTS × TE product was increased by annealing from the MF condition and that the UTS × TE products which meet the 3G AHSS target of 24,000 MPa% minimum were obtained for both the MF-710°C and MF-740°C treatments. It is noteworthy that the MF-740°C treatment had a slightly lower UTS × TE product that the MF-710°C treatment, which can be linked directly to the shape of the work hardening curves presented in Figure 3.6(c).

Table 3.3: Summary of average room temperature engineering mechanical properties obtained in uniaxial tension.

Sample ID	Yield Strength (MPa)	Ultimate Tensile Strength (MPa)	Total Elongation (%)	UTS × TE (MPa %)
CR-665°C	1,166±65	1,147±100	12±3	13,764
MF-665°C	967±5	1,040±14	20±3	20,800
MF-710°C	844±31	1,209±68	23±3	27,800
MF-740°C	810±38	1,246±44	21±5	26,166
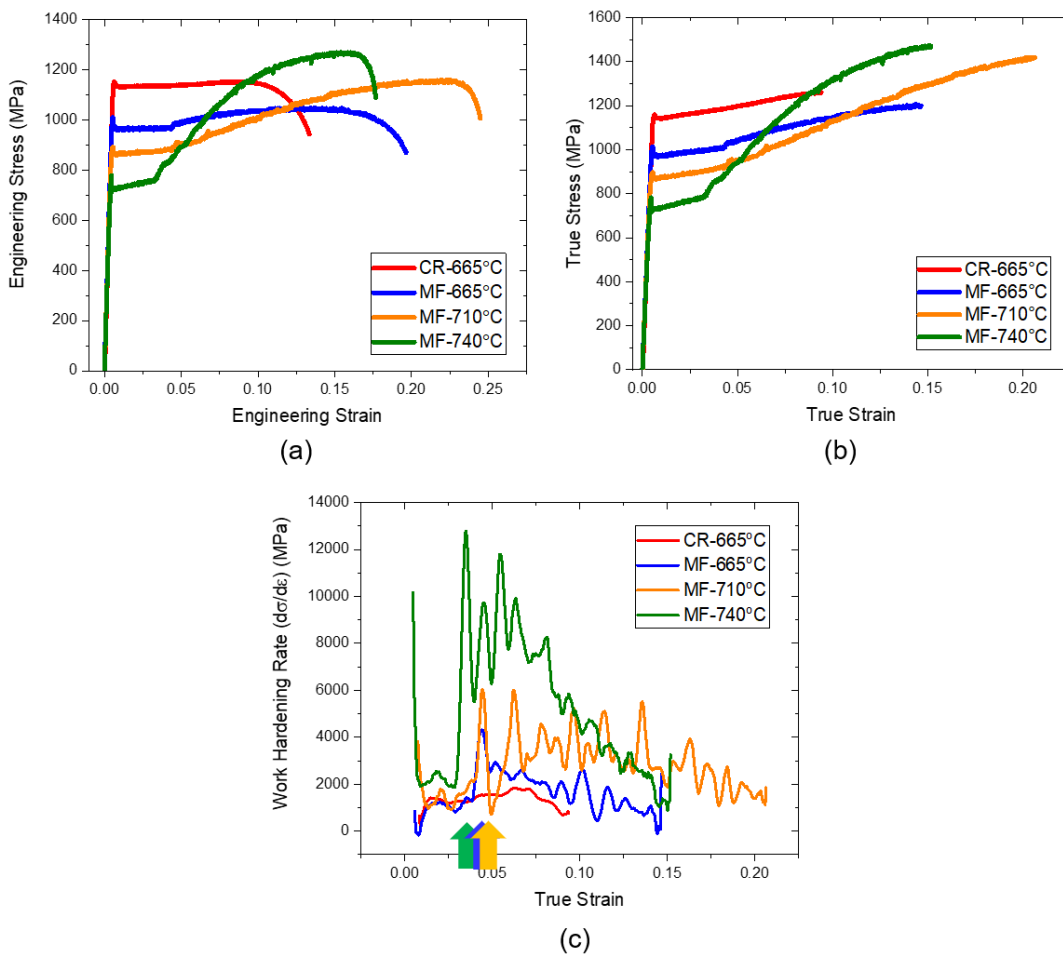
Figure 3.6: Representative (a) engineering stress-strain curves, (b) true stress-strain curves and (c) work hardening rate curves for investigated samples.

The true strain at fracture for the samples documented in Figure 3.6(b) was calculated from the surface area of the fracture surfaces and Equation 3.2. The resulting true stress-strain curves with the interpolated fracture true stress/strain are shown in Figure 3.7. The high true strains at fracture (i.e. $\varepsilon_{fracture} \geq 0.6$) for all samples show that there was significant post-uniform elongation occurring after critical damage was initiated for all of the experimental heat treatments. As it has been shown that there is a link between the true strain at fracture and material formability [42–44], this result shows promise for the ability of the alloy to be formed into parts.

Fracture surfaces were sectioned along the gauge length and these cross-sections are shown in Figure 3.8. Similar to the observations of Sun et al. [45] in the case of an 0.2C-10.4Mn-2.9Al ultra-fine grained ferrite + austenite microstructure, shear voids nucleated at ferrite-martensite/retained austenite interfaces and cracks propagated primarily by interfacial decohesion. Sun et al. asserted that different retained austenite volume fractions and stabilities altered the extent to which the TRIP effect suppressed void coalescence (as described by several authors [46–48]), but did not alter the fracture mechanism, where the present data agrees with this hypothesis.
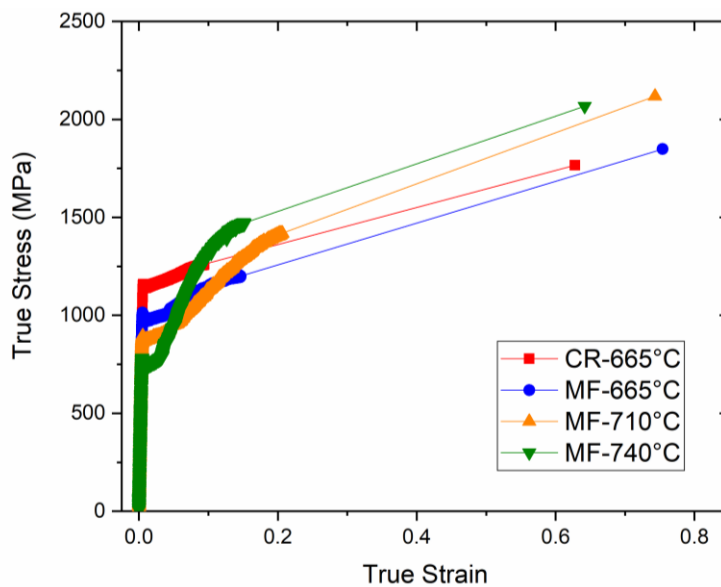
Figure 3.7: True stress-strain curves for the as-annealed samples, interpolated from the UTS to the true failure stress-strain.
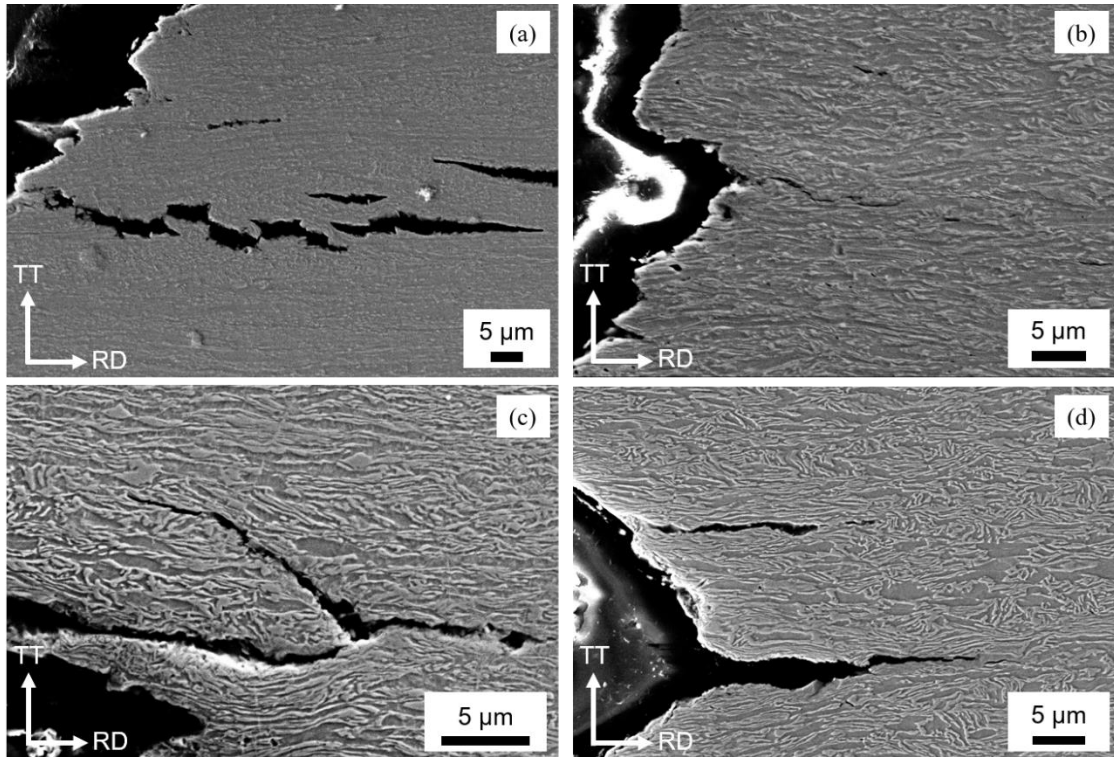
Figure 3.8: SEM-SEI images of fracture surface cross-sections: (a) CR-665°Cs; (b) MF-665°C; (c) MF-710°C; (d) MF-740°C.

3.4.3 Interrupted Tensile Tests

In order to assess the extent to which the TRIP effect influenced the mechanical properties observed, interrupted tensile tests were performed and samples from the uniform elongation portion of the gauge lengths analyzed *via* XRD to determine the volume fractions of retained austenite present as a function of true strain, as shown in Figure 3.9(a). The normalized fraction of transformed retained austenite – expressed as $(1 - V/V_O)$, where V is the instantaneous volume fraction of retained austenite and V_O is the as-annealed volume fraction of retained austenite – as a function of true strain is shown in Figure 3.9(b). Inspection of Figure 3.9(a) will show that two of the MF heat treatments (i.e. MF-710°C and MF-740°C) started with relatively high (0.30) volume fractions of retained austenite, which gradually transformed to martensite with increasing strain to a final retained austenite volume fraction of near zero at relatively high strains (Figure

3.9(b)). This is indicative of the TRIP effect – i.e. the deformation-induced retained austenite to martensite transformation – being exhausted in the case of the MF-710°C and MF-740°C heat treatments.

Comparison of the retained austenite transformation curves for the MF-710°C and MF-740°C treatments (Figure 3.9) to the work hardening curves in Figure 3.6(c) will show that there is a correlation between these curves and the resultant mechanical properties documented in Figure 3.6(a) and (b). In the case of the MF-740°C treatment, the relatively rapid initial retained austenite to martensite transformation (Figure 3.9(b)) resulted in a marked increase in the work hardening rate as a significant volume fraction of new obstacles for dislocation motion were quickly introduced into the material. As the rate of transformation decreased, the work hardening rate declined quickly until the TRIP effect was exhausted at approximately $\varepsilon = 0.15$ (Figure 3.9(b), after which tensile instability was initiated (Figure 3.6(b) and (c)). For the MF-710°C treatments, on the other hand, the retained austenite to martensite transformation rate was significantly lower, resulting in new obstacles to dislocation motion being introduced at a lower rate sufficient to increase and maintain the work hardening rate at relatively high levels to significantly larger strains – $\varepsilon = 0.22$ – after which the TRIP effect was exhausted (Figure 3.9(b)).

These results indicate that the difference in properties between the MF-710°C and MF-740°C treatments (Figure 3.6) did not likely arise solely from the volume fractions of retained austenite transformed, which were almost identical (Figure 3.9(a)), but from the effect of the heat treatments on the relative mechanical stability – as characterised by the deformation-induced martensite start parameter (i.e. M_S^σ [49,50]) – on the retained austenite transformation kinetics (Figure 3.9(b)). This parameter, which is a function of retained austenite chemical composition and mechanical constraint by surrounding phases, is related to the stress increment which is

required to induce the deformation-induced retained austenite to martensite transformation at temperatures higher than the martensite start temperature (M_s). This speaks to the relative mechanical stability of the retained austenite during room temperature deformation arising from the MF-710°C and MF-740°C treatments, where this stability is clearly more optimal in the case of the MF-710°C intercritical annealing treatment.
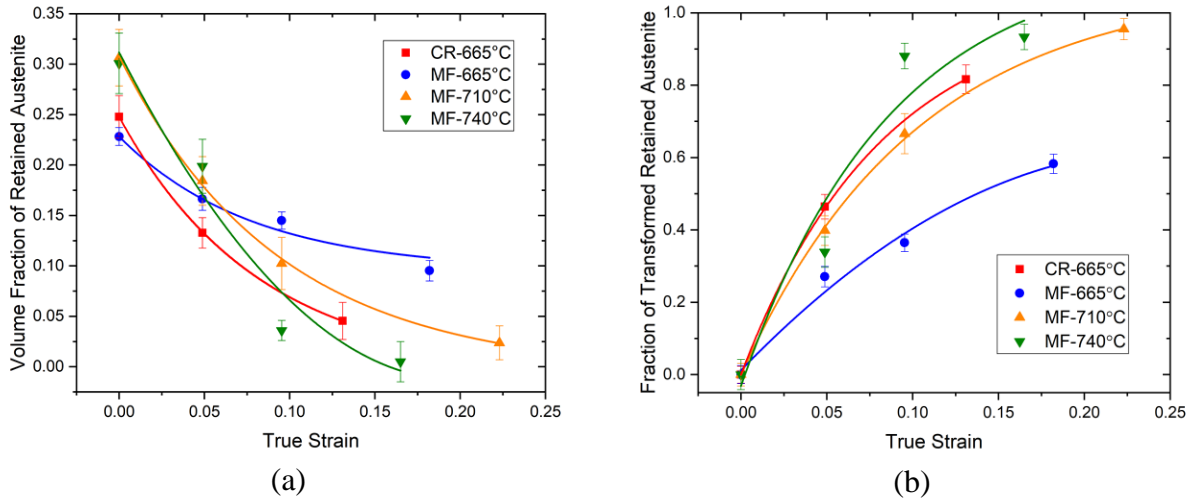
Figure 3.9: (a) Fraction of retained austenite as a function of true strain and (b) normalized volume fraction of transformed retained austenite versus true strain.

It is also clear that the mechanical stability of the retained austenite was a strong function of the starting microstructure as well as the intercritical annealing temperature. For example, the MF-665°C treatment resulted in approximately 0.55 of the initial retained austenite transforming to fresh martensite during deformation (Figure 3.9(b)). This indicates that the deformation imposed on the retained austenite from the MF-665°C sample was insufficient to complete the desired retained austenite to martensite transformation, implying that the remaining untransformed retained austenite chemistry was such that its M_S^σ was less optimal relative to room temperature – i.e. a significant portion of the retained austenite was "hyper-stable" and could not be induced to undergo the TRIP effect. Thus, a significantly smaller fraction of fresh martensite was introduced

into the microstructure (i.e. ~ 0.10, Figure 3.9(a)) for this condition. This relatively small volume fraction of fresh martensite introduced into the microstructure versus that introduced for the MF-710°C and MF-740°C treatments (i.e. ~ 0.30, Figure 3.9(a))), likely resulted in the observed lower sustained high work hardening rate.

The situation for the CR-665°C treatment was similar, despite the fact that a significantly larger volume fraction of retained austenite (~ 0.20, Figure 3.9(a)) transformed to martensite during deformation versus that of the MF-665°C treatment. In this case, examination of the transformation curves in Figure 3.9(b) will reveal that the TRIP effect was exhausted at significantly lower strains than was the case for the other heat treatments – i.e. the transformation rate of the retained austenite was quite high – implying that the incremental stress to transform large fractions of the retained austenite was relatively small and that its M_S^σ was significantly closer to room temperature. Thus, the retained austenite transformation did not contribute as strongly to maintaining the work hardening rate of this treatment, as can be seen from Figure 3.6(c). It is also likely that the more granular morphology of the retained austenite in the CR-665°C contributed to this instability as it has been reasonably well established that the more highly constrained lamellar retained austenite is more stable than the more polygonal morphology observed for this treatment (Figure 3.2) [6,10,17].

However, it is also clear from Figure 3.6 and Figure 3.9 that there may have been other mechanisms which either contributed to or failed to aid in maintaining the observed high work hardening rates in the MF-710°C and MF-740°C treatments versus the CR-665°C and MF-665°C treatments. This difference motivated a fine-scale, detailed microstructural investigation of the samples *via* TEM to elucidate the presence of any additional possible plasticity enhancing mechanisms, as will be discussed below.

3.4.4   TEM Examination

TEM techniques were used to assess the steel microstructural evolution as a function of strain and determine whether any additional work hardening mechanisms, such as mechanical twinning of the retained austenite, had occurred. TEM images from the CR-665°C samples are shown in Figure 3.10, where Figure 3.10(a)-(b) are from a sample pulled to 0.05 true strain ($\varepsilon =$ 0.05) and (c)-(d) are from the gauge length of a sample pulled to fracture (approximately 0.12 true strain, $\varepsilon \cong 0.12$). The BF images (a) and (c) show polygonal twinned retained austenite grains, as confirmed by the SAD patterns inset to (b) and (d). The SAD patterns show satellite (twin) spots, which are indicated by the red arrows in (b) and dashed lines in (d). The brightness of the twin spots was marginally brighter in the case of the $\varepsilon \cong 0.12$ sample, indicating that there was a marginal increase in twin density with increasing strain. This result suggests that the TWIP effect in the retained austenite was, at best, only a minor contributor to providing fresh obstacles to dislocation motion and, thereby, increasing the instantaneous work hardening rate of the deforming retained austenite. These observations are consistent with the relatively low work hardening rates observed for this treatment (Figure 3.6(c)).
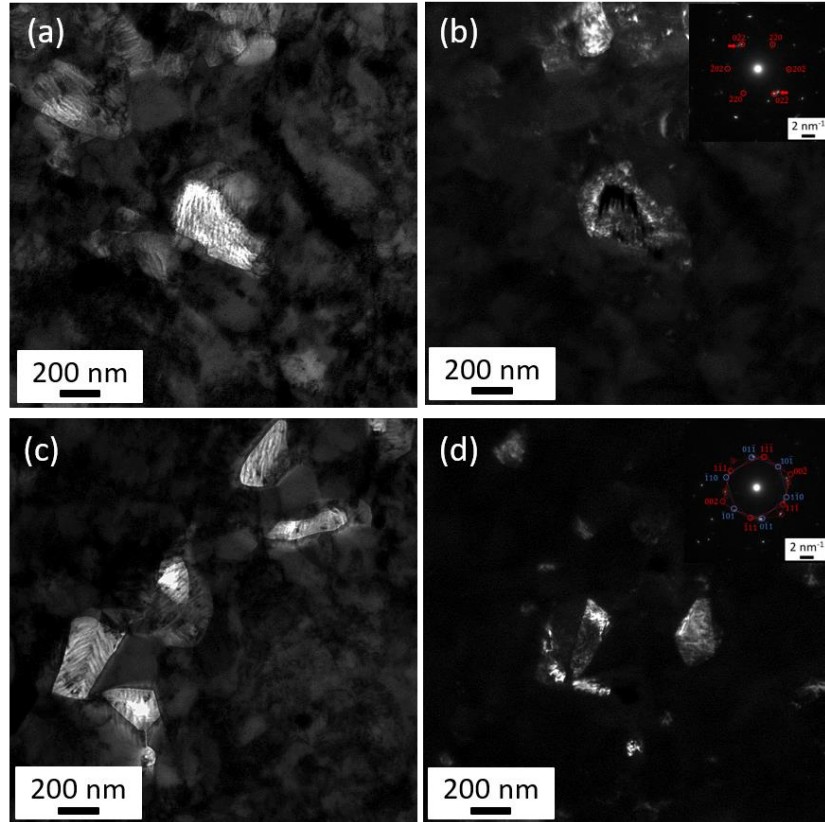
Figure 3.10: TEM images from the CR-665°C condition. For 0.05 true strain: (a) Bright Field (BF); (b) Dark field (DF) corresponding to $<02\overline{2}>_\gamma$ with inset SAD pattern corresponding to $[111]_\gamma$. For fracture: (c) BF; (d) DF corresponding to $<002>_\gamma$ with inset SAD pattern corresponding to $[110]_\gamma \parallel [111]_\alpha$.

TEM images from MF-665°C samples are shown in Figure 3.11, where (a)-(b) are from a sample pulled to $\varepsilon = 0.05$ and (c)-(d) are from the uniform elongation portion of the gauge length of a sample pulled to fracture ($\varepsilon \cong 0.20$). Unlike the CR-665°C samples shown in Figure 3.10, the retained austenite in these samples was lath-like instead of polygonal, as documented in the retained austenite dark field images in Figure 3.11(b) and (d). Some twins were observed within the retained austenite for these samples, although qualitative assessment of the DF micrographs showed that their density was very low and did not increase significantly with increasing strain. This suggests that the TWIP effect was not a major contributor to providing additional dislocation

obstacles and increased work hardening rates for this treatment and helps explain the relatively flat work hardening rate curve obtained for this condition (Figure 3.6(c)).
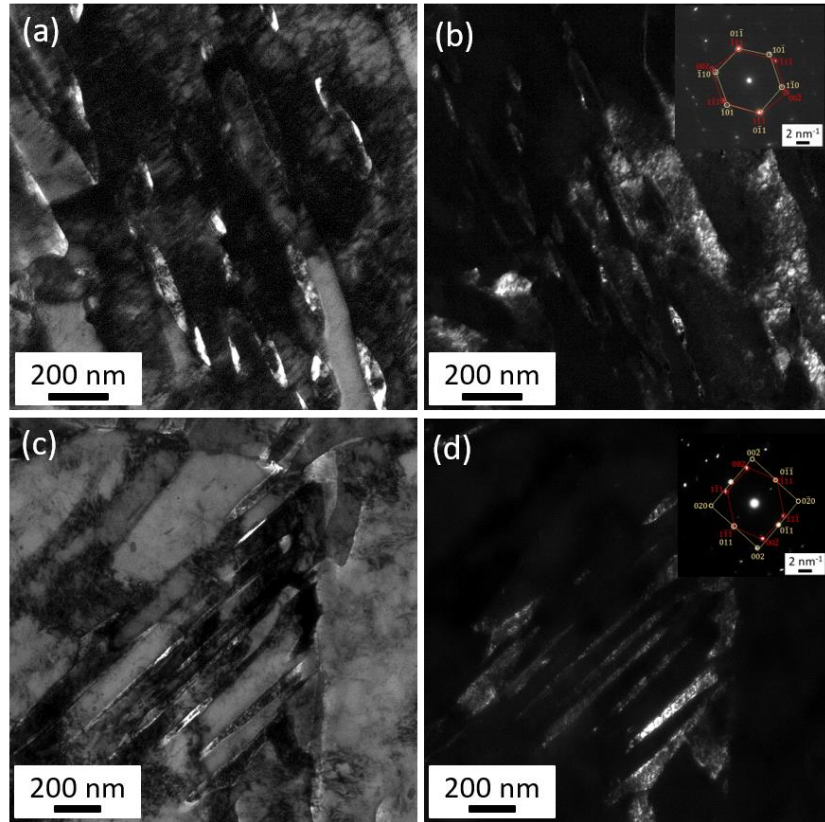
Figure 3.11: TEM images from the MF-665°C condition. For 0.05 true strain: (a) BF; (b) DF corresponding to <002>$_\gamma$ with inset SAD pattern corresponding to [111]$_{\alpha'}$|| [110]$_\gamma$. For fracture: (c) BF; (d) DF corresponding to <002>$_\gamma$ with inset SAD pattern corresponding to [100]$_{\alpha'}$|| [110]$_\gamma$.

TEM images from the MF-710°C samples are shown in Figure 3.12, where (a)-(b) are from a sample pulled to $\varepsilon = 0.05$ true strain and (c)-(d) are from the uniform elongation portion of the gauge length of a sample pulled to fracture ($\varepsilon \cong 0.25$). Similar to the observations for the MF-665°C samples (Figure 3.11), retained austenite was present in a lath-type morphology. However, a significant increase in the twin population was observed with increasing strain, as evidenced by the increasing brightness of the satellite spots on the SAD patterns and the significant increase in nano-scale twin density observed in the retained austenite of the fractured samples (i.e. Figure

3.12(b) vs. (d)). Thus, it can be surmised that the TWIP effect likely contributed in some way to the sustained higher work hardening rate observed in these alloys versus those annealed at 665°C (Figure 3.6(c)).
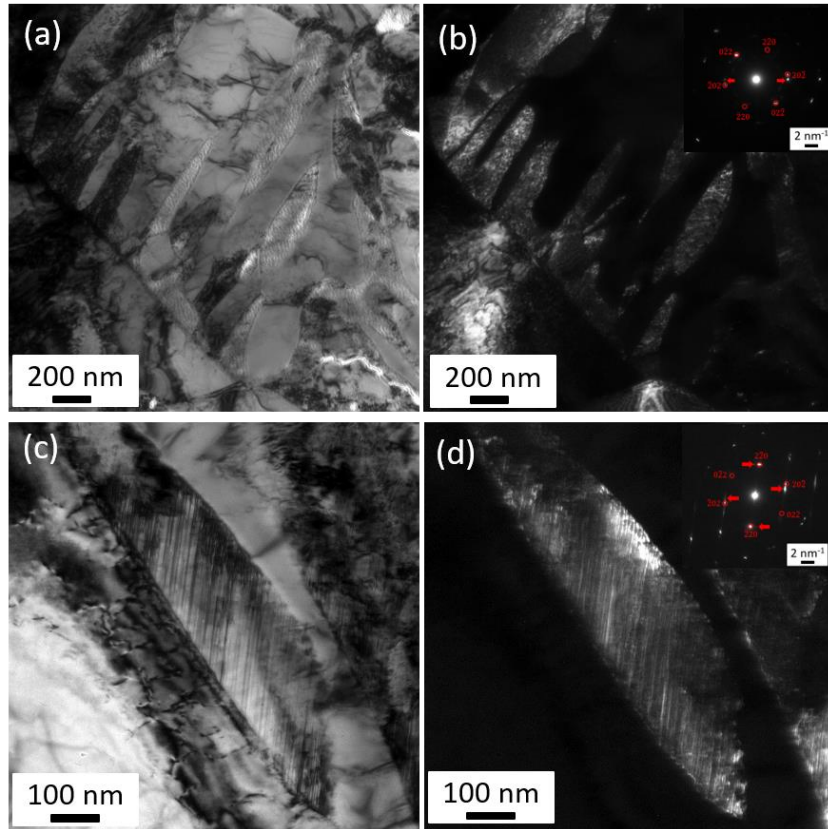
Figure 3.12: TEM images from the MF-710°C condition. For 0.05 true strain: (a) BF; (b) DF corresponding to $<02\bar{2}>_\gamma$ with inset SAD pattern corresponding to $[111]_\gamma$. For fracture: (c) BF; (d) DF corresponding to $<002>_\gamma$ with inset SAD pattern corresponding to $[110]_\gamma$.

TEM images from the MF-740°C samples are shown in Figure 3.13, where (a)-(b) are from a sample pulled to $\varepsilon = 0.05$ and (c)-(d) are from the uniform elongation portion of a sample pulled to fracture ($\varepsilon \cong 0.18$). Similar to the observations documented for the MF-710°C treatment (Figure 3.12), nano-twins were observed in the lath-shaped retained austenite grains. There was an increase in twin density with increasing strain, but not to the same extent as was observed in the MF-710°C

condition based on the brightness of the twin spots and qualitative assessment of the TEM micrographs (i.e. Figure 3.12(b) vs. (d)).
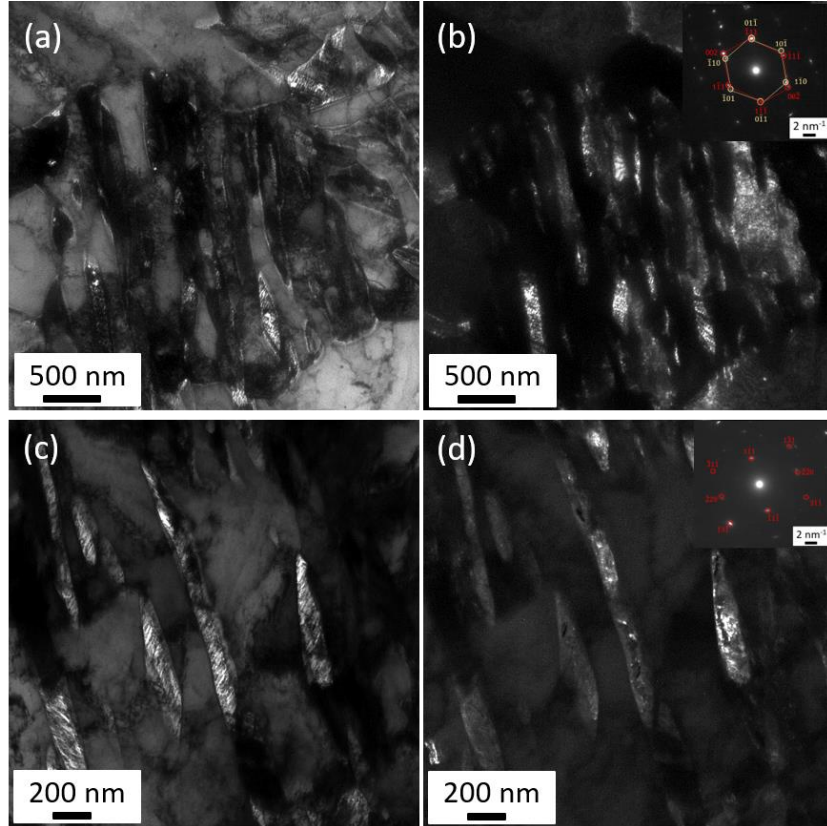
Figure 3.13: TEM images from the MF-740°C condition. For 0.05 true strain: (a) BF; (b) DF corresponding to $<00\bar{2}>_\gamma$ with inset SAD pattern corresponding to $[111]_{\alpha'} \parallel [110]_\gamma$. For fracture: (c) BF; (d) DF corresponding to $<1\bar{3}1>_\gamma$ with inset SAD pattern corresponding to $[112]_\gamma$.

3.4.5   Back Stress Evolution

In order to assess the extent to which the combined TRIP and TWIP effects contributed to kinematic hardening in the steel, load-unload-reload tests were performed and back stresses as a function of true strain determined (see Figure 3.14). The back stresses are indicative of the repulsion of dislocation strain fields that interact with obstacles to their motion and, thus, are a semi-quantitative means of assessing the kinematic hardening contribution to the overall flow stress. A continuous increase in the back stress is indicative that that existing obstacles continue

to act as effective barriers to dislocation motion and/or additional obstacles for dislocation motion are being created with increasing strain in order to maintain the instantaneous work hardening rate above that of the flow stress, thereby avoid plastic instability in the material [51–53].

In the case of the CR-665°C and MF-665°C samples, the back stress increments decreased with increasing strain and became saturated (within the limits of the error bars) at relatively low strains (Figure 3.14). This finding is consistent with the retained austenite transformation kinetics documented in Figure 3.9 and the work hardening curves in Figure 3.6(c), which show a relatively ineffective retained austenite to martensite transformation with respect to sustaining a high instantaneous work hardening rate. In the case of the MF-665°C treatment, this was because the volume fraction of retained austenite which transformed to martensite was too small to provide a sufficient population of fresh obstacles to dislocation motion, per Figure 3.9(b), resulting in the observed relatively low sustained work hardening rates and an early onset to plastic instability. In the case of the CR-665°C treatment, the TRIP effect was exhausted at a relatively low strain, which also resulted in the early onset of plastic instability.

However, in the case of MF-710°C and MF-740°C treatments, the back stresses did not saturate throughout the plastic deformation. The retained austenite transformation kinetic data (Figure 3.9) and TEM data (Figure 3.12 and Figure 3.13) data suggest that fresh, effective dislocation barriers were continuously generated both by the continuous transformation of retained austenite to martensite and the twinning of the retained austenite, resulting in the higher sustained work hardening rates observed for these treatments (Figure 3.6(c)).
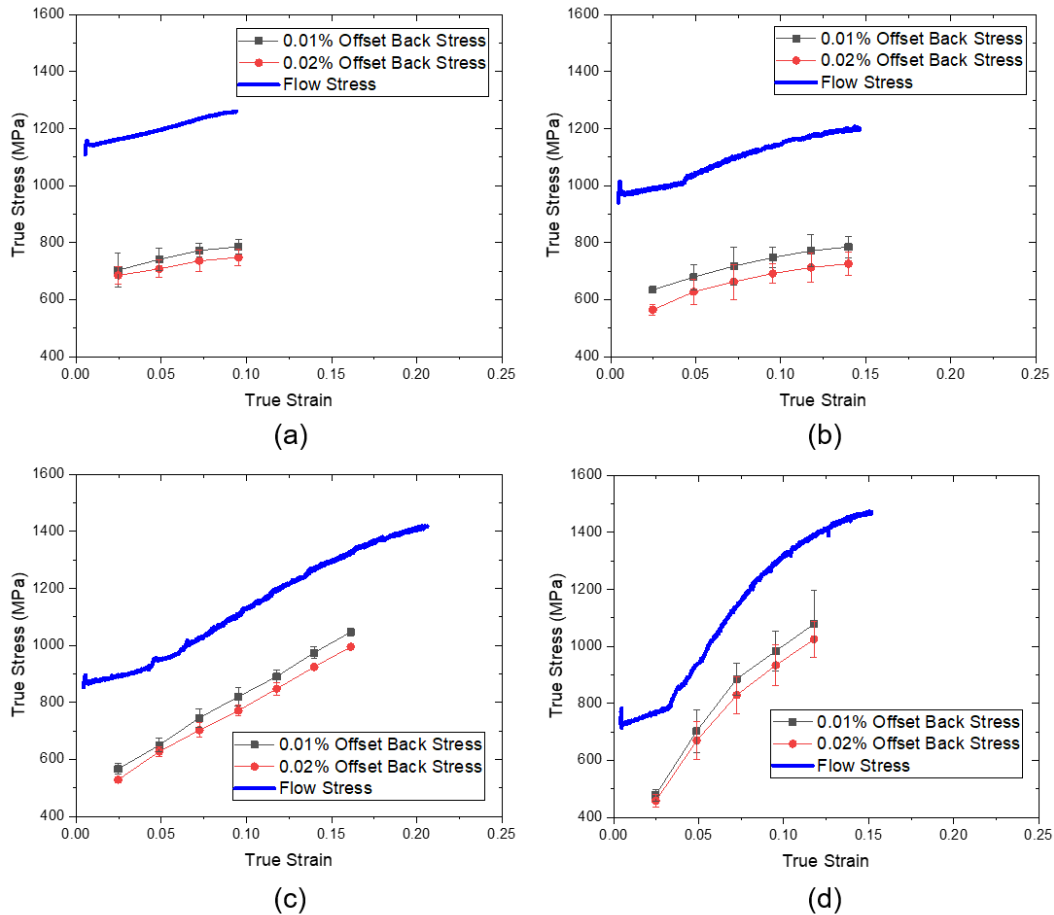
Figure 3.14: Flow and calculated back stresses using the 0.01% and 0.02% offset load lines for (a) CR-665°C; (b) MF-665°C; (c) MF-710°C; (d) MF-740°C.

3.4.6   Retained Austenite Composition Calculations

In order to qualitatively assess the stability of the retained austenite in terms of its composition (notably its C and Mn contents), two assumptions were used for calculating the austenite composition during the intercritical annealing heat treatment:

1) the retained austenite maintained the bulk alloy composition for the substitutional alloying elements (i.e. Mn, Al, Si) with the retained austenite C content being determined *via* the retained austenite XRD measurements – i.e. the paraequilibrium assumption, where no significant partitioning of the substitutional elements occurred during intercritical

annealing and with an experimentally determined retained austenite C content using Equation 3.4, below;

2) the equilibrium austenite composition for substitutional alloying elements at the IA temperature, as calculated *via* ThermoCalc, with the C content being determined *via* XRD – i.e. full partitioning of the substitutional alloying elements during intercritical annealing with an experimentally measured retained austenite C content derived from Equation 3.4.

The retained austenite C content was determined experimentally *via* the measured retained austenite lattice parameter (a_γ) obtained from XRD Rietveld refinement using Equation 3.4, which is a combination of the Dyson-Holmes and Ruhl-Cohen equations [54,55]:

$$a_\gamma = 3.572 - 0.00095(\text{wt\% Mn}) - 0.00157(\text{wt\% Si}) + 0.0056(\text{wt\% Al}) + 0.033(\text{wt\% C}) \ \overset{\circ}{\text{A}} \quad (3.4)$$

The retained austenite compositions for the various intercritical annealing treatment using cases 1 and 2 are shown in Table 3.4 along with the SFE for each computed using a modified version of the Dumay et al. model [23] that employs the expression for the Néel temperature of austenite empirically determined by Zhang et al. [56]. The as-received alloy composition (which can be considered the unadjusted baseline case) is also included in Table 3.4.

Use of the equilibrium austenite composition for substitutional alloying elements in case 2 was motivated by the work of Lee et al. [57], who showed (using dilatometry and TEM-EDS) that the retained austenite in a Fe-0.05C-6.15Mn-1.4Si-0.04Al steel approached its equilibrium composition of C and Mn (as calculated by ThermoCalc) after intercritical annealing for 180s at 640-680°C. In the case of the present experimental materials, the relatively small scale of the retained austenite – i.e. approximately 100 nm in width (Figure 3.10 – Figure 3.13) – increased the likelihood of near-equilibrium partitioning having occurred due to the relatively small diffusion distances required. It is noteworthy that examination of Table 3.4 shows that the computed retained

austenite SFE value was relatively insensitive to the solute partitioning assumptions made within a particular intercritical heat treatment. It should be cautioned, however, that the computed SFE values are shown merely to show trends in this value as a function of composition and intercritical heat treatment, as will be discussed below.

Table 3.4: Calculated/measured retained austenite compositions and SFE at 20°C for each IA treatment calculated using the model of Dumay et al. modified to include data by Zhang et al. [23,56].

Sample ID	Method	C (wt%)	Mn (wt%)	Si (wt%)	Al (wt%)	SFE (mJ/m^2)
As-received		0.15	5.56	1.10	1.89	N/A
CR-665°C	1	0.60	5.56	1.10	1.89	15.7
	2	0.55	11.15	1.34	1.09	15.4
MF-665°C	1	0.67	5.56	1.10	1.89	18.4
	2	0.62	11.15	1.34	1.09	18.0
MF-710°C	1	0.54	5.56	1.10	1.89	13.3
	2	0.52	9.28	1.28	1.24	13.1
MF-740°C	1	0.37	5.56	1.10	1.89	5.5
	2	0.37	8.40	1.25	1.34	6.0

Several noteworthy observations can be made from the data in Table 3.4. First, a direct comparison can be made between the experimentally determined retained austenite C contents of the CR-665°C and MF-665°C treatments to illustrate the significance of retained austenite morphology on C partitioning. Per Table 3.4, the MF-665°C treatment had a higher retained austenite C content than the CR-665°C sample for both partitioning formalisms, likely due to the shorter diffusion distances between the retained austenite lamellae and the adjacent C-rich martensite. Second, according to the case 2 calculations for the MF samples, the calculated Mn and experimentally determined retained austenite C contents decreased with increasing IA temperature. This was likely due to the C and Mn having to partition to higher volume fractions of intercritical austenite with increasing IA temperature, thereby lowering the average C and Mn concentrations of the retained austenite.

Both of these trends have a strong implication for the retained austenite chemical stability and resultant M_S^σ as it is well known that both C and Mn are potent austenite stabilizers, implying that the stress increment required to initiate the retained austenite to martensite transformation decreased with increasing intercritical annealing temperature. This trend is in agreement with the observations of the retained austenite deformation-induced transformation kinetics highlighted in Figure 3.9, which showed that the retained austenite mechanical stability – and, therefore, M_S^σ – decreased with increasing intercritical annealing temperature. In the case of the CR-665°C and MF-665°C treatments, the end result of the higher retained austenite C and (likely) Mn contents resulted in a retained austenite phase which only partially transformed during deformation (Figure 3.9). In the case of the MF-665°C treatment retained austenite, the lamellar morphology further decreased the deformation-induced transformation driving force. As mentioned previously, these factors resulted in these treatments having a relatively low sustained work hardening rates, resulting in inferior properties versus the 3G targets (Figure 3.6 and Table 3.3).

For the MF-740°C treatment, a lower C and Mn retained austenite composition (Table 3.4) resulted in too rapid a transformation rate in the early stages of deformation, indicating a M_S^σ value too close to room temperature. The result was a work hardening rate which was not maintained at a high enough value to provide the best observed properties, although it should be noted that the MF-740°C properties did meet the 3G UTS × TE target. In the case of the MF-710°C, however, the composition of the retained austenite was such that a gradual, deformation-induced martensite transformation – as characterised by its M_S^σ value – provided the best combination of strength and uniform elongation observed in the present work.

It should also be mentioned that the chemical composition of the retained austenite (Table 3.4) likely played a significant role in the activation of deformation-induced mechanical twinning,

which very likely contributed to maintaining the high work hardening rates (Figure 3.6(c)) and lack of back stress saturation observed for the MF-710°C and MF-740°C treatments (Figure 3.14). It is generally accepted that there is a strong link between austenite composition, its resultant stacking fault energy (SFE) and both the activation [33] and kinetics of mechanically-induced twinning [33,58] as well as the propensity for deformation induced mechanical twinning [31,32]. In particular, Ghasri-Khouzani and McDermid showed that the activation of twinning in high-Mn TWIP steels was directly proportional to the SFE [33]. Examining the SFE trends in Table 3.4, it can be seen that both the CR-665°C and MF-665°C treatments had SFE values larger than those of the MF-710°C or MF-740°C treatments, indicating that deformation induced twinning was likely more difficult to activate in the case of the former two treatments. This result is in qualitative agreement with the microstructural results in Figure 3.10 – Figure 3.13, with the back stress saturation observations of Figure 3.14 and the resultant mechanical property trends in Figure 3.6. Thus, although it is difficult to partition the relative contributions of the deformation-induced TRIP and TWIP effects to the mechanical properties of the alloys, the compositional and morphological trends on M_S^σ and on the activation of mechanical twinning are consistent with the observed properties for the experimental steels.

3.5 Discussion

In the present work, the TEM observations showed that both the Kurdjumov-Sachs (K-S) [59] and Nishiyama-Wassermann (N-W) [60,61] orientation relationships were observed between the retained austenite and martensite phases (examples in Figure 3.11 and Figure 3.13) suggesting that the austenite grew from parent martensite during intercritical annealing or from inter-lath retained austenite films. It is also clear from the SEM (Figure 3.5) and TEM images (Figure 3.10 – Figure 3.13) that annealing from the as received, cold rolled tempered martensite microstructure

resulted in a globular or polygonal morphology for the retained austenite and martensite phases, while annealing from a martensite-ferrite starting microstructure resulted in a lath-like morphology for the retained austenite and martensite. This is consistent with the findings of several authors working on similar grades of medium-Mn steels [6,17,19,20,62,63]. Previous investigations of low-alloy TRIP and medium-Mn TRIP steels have shown that lamellar retained austenite is more mechanically stable (due to the mechanical constraint imposed by surrounding martensitic and/or bainitic ferrite phases) than its polygonal counterpart [10,17,18].

In general, it was shown for all of the experimental heat treatments that significant post-uniform elongation – in excess of true strains of 0.6 – were observed for all of the alloy starting microstructures and heat treatments (Figure 3.7), indicating that all of the heat treatments likely resulted in good alloy formability due to the known correlation between elongation at fracture and such forming operations as hole expansion ratio and bending [42–44]. In addition, it was also shown that the fundamental damage mechanism for all of the experimental heat treatments was decohesion along grain boundaries, particularly between harder and softer phases.

As discussed above, the mechanical properties and low sustained work hardening rates observed for the CR-665°C and MF-665°C treatments (Figure 3.6) likely arose from a combination of factors: the higher C and (likely) Mn contents of the retained austenite (Table 3.4) resulting in too large a stress increment – as characterised by the M_S^σ parameter – being required for a complete deformation-induced transformation of the retained austenite (Figure 3.9), too high a SFE to activate significant mechanical twinning (Table 3.4) and, in the case of the CR-665°C treatment, too rapid a deformation-induced transformation of the less geometrically stable polygonal retained austenite [6,10,17]. All of these factors led to insufficient populations of fresh obstacles to dislocation motion being introduced in these alloys, resulting in the low sustained

work hardening rates observed for these alloys (Figure 3.6(c)) and the saturation of existing dislocation obstacles at relatively low strains, as exemplified by the back stress saturation in Figure 3.14, all of which led to the relatively early onset of plastic instability. This combination of factors further resulted in these alloy heat treatments being unable to achieve the desired 3G UTS × TE minimum target of 24,000 MPa%. In this case, the retained austenite was too stable for an effective combination of the TRIP and TWIP effect plasticity enhancing mechanism to be activated – i.e., the retained austenite was hyper-stable.

The trends were quite the opposite in the case of MF-740°C treatment. In this case, the lower C and (likely) Mn contents of the retained austenite (Table 3.4) resulted in a small stress increment $\left(M_S^{\sigma}\right)$ being required to complete the deformation-induced retained austenite to martensite transformation (Figure 3.9). This early exhaustion of the TRIP effect led to the large incremental increase in the instantaneous work hardening effect at lower strains observed in Figure 3.6(c) due to a large volume fraction of new dislocation obstacles being introduced, but was not able to be sustained to strains in excess of 0.20 (Figure 3.6). The SFE trends in Table 3.4 also indicate that mechanical twinning in the retained austenite (Figure 3.13) may have been activated at lower strains and perhaps could also have been exhausted at lower strains [33], although this is purely speculative. Overall, the lack of back-stress saturation (Figure 3.14) indicates that fresh obstacles were being introduced into the microstructure at a reasonable, although sub-optimal rate, versus the MF-710°C treatment. It should be pointed out, however, that this alloy treatment met the target UTS × TE target properties for 3G AHSSs (Table 3.3), as defined by Matlock et al. [1,2], and it can be concluded that the CGL processing window for obtaining 3G properties extends to the MF-740°C treatment.

Finally, the combination of an intermediate retained austenite C and Mn contents (Table 3.4) for the MF-710°C treatment clearly resulted in the most promising combination of deformation-induced retained austenite to martensite transformation kinetics (Figure 3.9) and a SFE consistent with additional plasticity enhancement via the TWIP effect in the retained austenite (Table 3.4, Figure 3.12) such that fresh dislocation obstacles were introduced in a manner that the work hardening rate was sustained to strains greater than 0.20 (Figure 3.6) without becoming saturated (Figure 3.14). Overall, can be concluded that the present 0.15C-5.56Mn-1.1Si-1.89Al alloy meets and exceeds the 3G AHSS UTS × TE using the CGL-compatible MF-710°C or MF-740°C heat treatments. As it has been previously shown that a 0.10C-6Mn-2Si model alloy can be successfully Zn-coated by tailoring the annealing atmosphere dew point [64], the above results show promise for the industrial production of Zn-coated 3G AHSSs.

3.6   Conclusions

1) The 0.15C-6Mn-1.5Al-1Si (wt%) medium-Mn experimental steel investigated in this work achieved the general mechanical property targets for 3G AHSS (UTS × TE of 24,000-40,000 MPa%) using a CGL-compatible intercritical annealing treatment at 710°C or 710°C for 120 s from a martensite-ferrite starting microstructure, suggesting that there is likely an industrially-relevant process window to achieve the desired 3G AHSS properties.

2) The highest UTS × TE combination of mechanical properties was observed for the heat treatment that had the more optimal retained austenite stability (i.e. MF-710°C), as determined by the retained austenite to martensite transformation kinetics. In this case, the complete transformation of ~0.30 vol fraction of retained austenite to martensite occurred gradually over the deformation, sustaining a high work hardening rate that delayed the onset of necking. In the case of the MF-665°C condition, the retained austenite did not

completely transform due to its hyper-stability and, therefore, this condition had a relatively low work hardening rate. In the case of the MF-740°C condition, the retained austenite was less stable than that in the MF-710°C condition and, therefore, it transformed completely at lower strains than in the MF-710°C case, resulting in a high initial but unsustainable work hardening rate after yielding.

3) Two different retained austenite C contents and SFE values were calculated for each condition, based on different partitioning formalisms for substitutional alloying elements. The computed SFE values for the CR-665°C and MF-665°C conditions were higher than those for the MF-710°C and MF-740°C conditions, suggesting that the activation energy for twinning was higher for the former two cases. TEM evidence of significant mechanical twinning was observed for the MF-710°C and MF-740°C, and it is likely that the TWIP effect contributed to the high work hardening rates observed for those samples.

3.7 Acknowledgements

3.8 References

[1] D.K. Matlock, J.G. Speer, Design Considerations for the Next Generation of Advanced High Strength Steel Sheets, in: H.C. Lee (Ed.), Proc. 3rd Int. Conf. Struct. Steels, Korean Institute of Metals and Materials, Seoul, Korea, 2006: pp. 774–781.

[2]   D.K. Matlock, J.G. Speer, Third Generation of AHSS: Microstructure Design Concepts, Springer, Jamshedpur, India, 2009. doi:10.1007/978-1-84882-454-6_11.

[3]   D.K. Matlock, J.G. Speer, E. De Moor, P.J. Gibbs, Recent Developments in Advanced High Strength Sheet Steels for Automotive Applications: An Overview, JESTECH. 15 (2012) 1–12.

[4]   E. De Moor, P.J. Gibbs, J.G. Speer, D.K. Matlock, Strategies for Third-Generation Advanced High Strength Steel Development, AIST Trans. 7 (2010) 133–144.

[5]   K.M.H. Bhadhon, J.R. McDermid, F.E. Goodwin, Effect of Galvanizing Heat Treatment on the Microstructure and Mechanical Properties of a 6Mn-1.5Si Third Generation Advanced High Strength Steel, in: Proc. 10th Conf. Zinc Zinc Alloy Coat. Steel Sheet, Galvatech 2015, Toronto, 2015: pp. 936–943.

[6]   K.M.H. Bhadhon, J.R. McDermid, X. Wang, E.A. McNally, F.E. Goodwin, Fine-Scale Microstructure Characterization And Mechanical Properties Of CGL-Compatible Heat Treated Medium-Mn TRIP Steel, in: Proc. 11th Conf. Zinc Zinc Alloy Coat. Steel Sheet, Galvatech 2017, Tokyo, 2017: pp. 493–500.

[7]   D.M. Pallisco, J.R. McDermid, E.A. McNally, F.E. Goodwin, Effect of Starting Microstructure and Intercritical Annealing Parameters on the Mechanical Property Development of a Medium-Mn Third-Generation Advanced High Strength Steel, in: Proc. 11th Conf. Zinc Zinc Alloy Coat. Steel Sheet, Galvatech 2017, Tokyo, 2017: pp. 782–789.

[8]   D.M. Pallisco, K.M.H. Bhadhon, V. Patel, M. Pourmajidian, F.E. Goodwin, J.R. McDermid, 9-11: Galvanizing of Medium-Manganese Third Generation Advanced High Strength Steels, in: Proc. 4th Int'l Conf. Med. High-Manganese Steels, 2019: pp. 375–378.

[9]   K. Sugimoto, M. Misu, M. Kobayashi, H. Shirasawa, Effects of Second Phase Morphology on Retained Austenite Morphology and Tensile Properties in a TRIP-aided Dual-phase Steel Sheet, ISIJ Int. 33 (1993) 775–782.

[10]   J.R. McDermid, H.S. Zurob, Y. Bian, Stability of Retained Austenite in High-Al, Low-Si TRIP-Assisted Steels Processed via Continuous Galvanizing Heat Treatments, Metall. Mater. Trans. A. 42 (2011) 3627–3637.

[11]   J. Chiang, B. Lawrence, J.D. Boyd, A.K. Pilkey, Effect of microstructure on retained austenite stability and work hardening of TRIP steels, Mater. Sci. Eng. A. 528 (2011) 4516–4521.

[12]   J. Chiang, J.D. Boyd, A.K. Pilkey, Effect of microstructure on retained austenite stability and tensile behaviour in an aluminum-alloyed TRIP steel, Mater. Sci. Eng. A. 638 (2015) 132–142.

[13] P.J. Gibbs, E. De Moor, M.J. Merwin, B. Clausen, J.G. Speer, D.K. Matlock, Austenite stability effects on tensile behavior of manganese-enriched- austenite transformation-induced plasticity steel, Metall. Mater. Trans. A. 42 (2011) 3691–3702.

[14] S. Zhang, K.O. Findley, Quantitative assessment of the effects of microstructure on the stability of retained austenite in TRIP steels, Acta Mater. 61 (2013) 1895–1903.

[15] J. Han, Y.-K. Lee, The effects of the heating rate on the reverse transformation mechanism and the phase stability of reverted austenite in medium Mn steels, Acta Mater. 67 (2014) 354–361.

[16] Z.H. Cai, H. Ding, R.D.K. Misra, Z.Y. Ying, Austenite stability and deformation behavior in a cold-rolled transformation-induced plasticity steel with medium manganese content, Acta Mater. 84 (2015) 229–236.

[17] V. Patel, Microstructure and Mechanical Properties of Medium Mn Steel, McMaster University, 2019.

[18] K.M.H. Bhadhon, Effect of Starting Microstructure and CGL Compatible Thermal Processing Cycle on the Mechanical Properties of a Medium-Mn Third Generation Advanced High Strength Steel, McMaster University, 2017.

[19] H. Luo, H. Dong, New ultrahigh-strength Mn-alloyed TRIP steels with improved formability manufactured by intercritical annealing, Mater. Sci. Eng. A. 626 (2015) 207–212.

[20] K. Steineder, D. Krizan, R. Schneider, C. Béal, C. Sommitsch, On the microstructural characteristics influencing the yielding behavior of ultra-fine grained medium-Mn steels, Acta Mater. 139 (2017) 39–50.

[21] R.E. Schramm, R.P. Reed, Stacking Fault Energies of Seven Commercial Austenitic Stainless Steels, Metall. Trans. A. 6 (1975).

[22] S. Allain, J. Chateau, O. Bouaziz, S. Migot, N. Guelton, Correlations between the calculated stacking fault energy and the plasticity mechanisms in Fe – Mn – C alloys, Mater. Sci. Eng. A. 397–389 (2004) 158–162.

[23] A. Dumay, J.-P. Chateau, S. Allain, S. Migot, O. Bouaziz, Influence of addition elements on the stacking-fault energy and mechanical properties of an austenitic Fe – Mn – C steel, Mater. Sci. Eng. A. 484 (2008) 184–187.

[24] S. Curtze, V. Kuokkala, Dependence of tensile deformation behavior of TWIP steels on stacking fault energy , temperature and strain rate, Acta Mater. 58 (2010) 5129–5141.

[25] S. Curtze, V. Kuokkala, A. Oikari, J. Talonen, H. Ha, Thermodynamic modeling of the stacking fault energy of austenitic steels, Acta Mater. 59 (2011) 1068–1076.

[26]   A. Saeed-Akbari, J. Imlau, U. Prahl, W. Bleck, Derivation and Variation in Composition-Dependent Stacking Fault Energy Maps Based on Subregular Solution Model in High-Manganese Steels, Metall. Mater. Trans. A. 40A (2009) 3076–3090.

[27]   J. Kim, Y. Estrin, B.C. De Cooman, Constitutive Modeling of the Stacking Fault Energy-Dependent Deformation Behavior of Fe-Mn-C-(Al) TWIP Steels, Metall. Mater. Trans. A. 49 (2018) 5919–5924. doi:10.1007/s11661-018-4910-y.

[28]   J. Nakano, P.J. Jacques, Effects of the thermodynamic parameters of the hcp phase on the stacking fault energy calculations in the Fe-Mn and Fe-Mn-C systems, CALPHAD. 34 (2010) 167–175.

[29]   L. Rémy, Twin-slip interaction in F.C.C. crystals, Acta Metall. 25 (1977) 711–714. doi:10.1016/0001-6160(77)90013-X.

[30]   L. Rémy, Kinetics of F.C.C. deformation twinning and its relationship to stress-strain behaviour, Acta Metall. 26 (1978) 443–451. doi:10.1016/0001-6160(78)90170-0.

[31]   O. Bouaziz, N. Guelton, Modelling of TWIP effect on work-hardening, Mater. Sci. Eng. A. 321 (2001) 246–249.

[32]   O. Bouaziz, S. Allain, C. Scott, Effect of grain and twin boundaries on the hardening mechanisms of twinning-induced plasticity steels, Scr. Mater. 58 (2008) 484–487.

[33]   M. Ghasri-Khouzani, J.R. McDermid, Effect of carbon content on the mechanical properties and microstructural evolution of Fe-22Mn-C steels, Mater. Sci. Eng. A. 621 (2015) 118–127. doi:10.1016/j.msea.2014.10.042.

[34]   M. Ghasri-Khouzani, J.R. McDermid, Microstructural evolution and mechanical behaviour of Fe-30Mn-C steels with various carbon contents, Mater. Sci. Technol. 33 (2017) 1159–1170. doi:10.1080/02670836.2016.1268662.

[35]   E.M. Bellhouse, J.R. McDermid, Analysis of the Fe–Zn interface of galvanized high Al–low Si TRIP steels, Mater. Sci. Eng. A. 491 (2008) 39–46. doi:10.1016/j.msea.2007.12.033.

[36]   E.M. Bellhouse, A.I.M. Mertens, J.R. McDermid, Development of the surface structure of TRIP steels prior to hot-dip galvanizing, Mater. Sci. Eng. A. 463 (2007) 147–156.

[37]   ASTM E8/E8M-16a: Standard Test Methods for Tension Testing of Metallic Materials, West Conshohocken, PA, USA, 2016.

[38]   ASTM E975-13: Standard Practice for X-Ray Determination of Retained Austenite in Steel with Near Random Crystallographic Orientation, West Conshohocken, PA, USA, 2013.

[39] M. Westphal, J.R. McDermid, J.D. Boyd, J.D. Embury, Novel Thermal Processing of Dual Phase Steels: II – Work Hardening and Fracture Mechanisms, Can. Metall. Q. 49 (2010) 91–97.

[40] C.W. Sinclair, Co-Deformation of a Two-Phase FCC/BCC Material, McMaster University, 2001.

[41] K. Spencer, The work hardening of austenitic stainless steel, applied to the fabrication of high-strength conductors, McMaster University, 2004.

[42] J. Datsko, C.T. Yang, Correlation of bendability of materials with their tensile properties, J. Manuf. Sci. Eng. Trans. ASME. 82 (1960) 309–312. doi:10.1115/1.3664236.

[43] J. Sarkar, T.R.G. Kutty, D.S. Wilkinson, J.D. Embury, D.J. Lloyd, Tensile properties and bendability of T4 treated AA6111 aluminum alloys, Mater. Sci. Eng. A. 369 (2004) 258–266. doi:10.1016/j.msea.2003.11.022.

[44] P. Larour, J. Freudenthaler, T. Weissböck, Reduction of cross section area at fracture in tensile test: Measurement and applications for flat sheet steels, J. Phys. Conf. Ser. 896 (2017). doi:10.1088/1742-6596/896/1/012073.

[45] B. Sun, D. Palanisamy, D. Ponge, B. Gault, F. Fazeli, C. Scott, S. Yue, D. Raabe, Revealing fracture mechanisms of medium manganese steels with and without delta-ferrite, Acta Mater. 164 (2019) 683–696.

[46] R.H. Leal, Transformation Toughening of Metastable Austenitic Steels, MIT, 1984.

[47] C.-C. Young, Transformation Toughening in Phosphocarbide-Strengthened Austenitic Steels, MIT, 1988.

[48] P.J. Jacques, Q. Furnémont, T. Pardoen, F. Delannay, On the role of martensitic transformation on damage and cracking resistance in TRIP-assisted multiphase steels, Acta Mater. 49 (2001) 139–152.

[49] J.R. Patel, M. Cohen, Criterion for the action of applied stress in the martensitic transformation, Acta Metall. 1 (1953) 531–538.

[50] H.K.D.H. Bhadeshia, R.W.K. Honeycombe, Steels: Microstructure and Properties, 4th Ed., Elsevier Ltd, Oxford, United Kingdom, 2017.

[51] J. Gerbase, J.D. Embury, R.M. Hobbs, The mechanical behavior of some dual phase steels - with emphasis on the initial work hardening rate, in: R.A. Kot, J.W. Morris (Eds.), Struct. Prop. Dual-Phase Steels, TMS-AIME, New Orleans, 1979: pp. 118–144.

[52] Y. Bian, Microstructure and Mechanical Properties of Al and Al/Si Alloyed TRIP-assisted Steels Produced through Galvanizing Heat Treatments, McMaster University, 2009.

[53]   U.F. Kocks, H. Mecking, Physics and phenomenology of strain hardening: the FCC case, Prog. Mater. Sci. 48 (2003) 171–273.

[54]   D.J. Dyson, B. Holmes, Effect of Alloying Additions of the Lattice Parameter of Austenite, J. Iron Steel Inst. 208 (1970) 469–474.

[55]   R. Ruhl, M. Cohen, Splat Quenching of Iron-Carbon Alloys, Trans. TMS-AIME. 245 (1969) 241–251.

[56]   Y.S. Zhang, X. Lu, X. Tian, Z. Qin, Compositional dependence of the Neel transition, structural stability, magnetic properties and electrical resistivity in Fe–Mn–Al–Cr–Si alloys, Mater. Sci. Eng. A. A334 (2002) 19–27.

[57]   S.-J. Lee, S. Lee, B.C. De Cooman, Mn partitioning during the intercritical annealing of ultrafine-grained 6% Mn transformation-induced plasticity steel, Scr. Mater. 64 (2011) 649–652.

[58]   K. Renard, P.J. Jacques, On the relationship between work hardening and twinning rate in TWIP steels, Mater. Sci. Eng. A. 542 (2012) 8–14. doi:10.1016/j.msea.2012.01.123.

[59]   G. Kurdjumov, G. Sachs, Uber der Mechanismus der Stahlhartung (On the mechanism of hardening of steel), Z. Phys. 64 (1930) 325–343.

[60]   G. Wassermann, Influence of the α-γ transformation of an irreversible Ni steel onto crystal orientation and tensile strength, Arch. Eisenhuttenwes. 126 (1933) 647–654.

[61]   Z. Nishiyama, X -ray investigation of the mechanism of the transformation from face-centered cubic lattice to body- centered cubic, Sci. Rep. Tohoku Univ. 23 (1934) 637–664.

[62]   J.I. Kim, J.H. Ryu, S.W. Lee, K. Lee, Y.-U. Heo, D.-W. Suh, Influence of the Initial Microstructure on the Reverse Transformation Kinetics and Microstructural Evolution in Transformation-Induced Plasticity – Assisted Steel, Metall. Mater. Trans. A. 47 (2016) 5352–5361.

[63]   A. Arlazarov, A. Hazotte, O. Bouaziz, M. Goune, F. Kegel, Characterization of microstructure formation and mechanical behavior of an advanced medium Mn steel, Proc. MS&T 2012. (2012) 1124–1131.

[64]   M. Pourmajidian, J.R. McDermid, On the reactive wetting of a medium-Mn advanced high-strength steel during continuous galvanizing, Surf. Coatings Technol. 357 (2019) 418–426. doi:10.1016/j.surfcoat.2018.10.028.

4   On the Selective Oxidation of a 0.15C-6Mn-2Al-1Si Third-Generation Advanced High Strength Steel During Two-Stage Annealing Treatments

Daniella M. Pallisco, Joseph R. McDermid

Draft Manuscript

4.1   Abstract

The selective oxidation of a 0.15C-5.6Mn-1.9Al-1.1Si (wt%) prototype third-generation advanced high strength steel during dew point-controlled two-stage annealing with intermediate flash pickling was documented. After annealing at 890°C for 600 s, the surfaces had compact nodules of MnO on top of co-precipitated nodules of $MnSiO_3/Mn_2SiO_4$ and $MnAl_2O_4$. The intermediate flash pickling treatment dissolved the external MnO and Mn-Si oxides, leaving behind $MnAl_2O_4$ nodules. Subsequent intercritical annealing at 710°C for 120 s resulted in no changes to the $MnAl_2O_4$ nodules due to the depletion of solute from the near-surface matrix during the first annealing step.

4.2   Introduction

The development of advanced high-strength steels (AHSS) has been motivated by the increasing demands on the automotive industry to improve fuel efficiency while also improving passenger safety. In particular, the third generation (3G) AHSS are under investigation due to their superior mechanical properties relative to the currently employed first generation AHSS while being leaner in composition than the second generation AHSS [1–4]. Among the proposed strategies for 3G AHSS development, medium-Mn 3G AHSS grades are promising candidates for automotive body-in-white applications due to the compatibility of their processing routes with existing continuous galvanizing line (CGL) capabilities [5–10]. This is highly desirable since the CGL is a cost-effective means of providing the substrate with essential corrosion protection.

The selective oxidation of the primary alloying elements (specifically Mn, Si, and Al) in the CGL annealing furnace is a well-documented phenomenon [11–17]. It is known that the furnace process atmosphere oxygen partial pressures (pO_2) are reducing to Fe but oxidizing to other alloying elements that are added to obtain the desired microstructure and mechanical properties. The thermodynamically stable oxides that form during annealing can preclude successful reactive wetting by the molten galvanizing bath metal by preventing the dissolved Al in the bath from reacting with the substrate Fe to form the $Fe_2Al_{5-x}Zn_x$ interfacial layer required for an adherent, defect-free, and formable coating [12–14,18–23].

Several authors have still reported successful reactive wetting of Mn-, Si-, and Al-containing substrates, provided the external oxides were of an appropriate chemistry, thickness, and morphology [12,13,30,14,15,24–29]. As proposed by Suzuki et al. [31], maintaining a Si/Mn ratio ≤ 0.5 can promote the formation of nodular MnO and avoid film-type SiO_2 (which is particularly problematic for reactive wetting [18–20,32,33]). It has been shown that MnO can be aluminothermically reduced during immersion in the bath metal [19,25,28,34], although the thickness should be limited to 80 nm for typical immersion times [28]. It is also known that wide spacing of oxide nodules can facilitate reactive wetting [12,24,27,34], as can infiltration of bath metal through cracks at the oxide/substrate interface [12,15,27,34]. In addition, the oxidation kinetics can be retarded by adding surface active elements like Sn [35–39], Sb [35], or Bi [40]. Moreover, relatively high process atmosphere pO_2 can be used to suppress external oxidation and promote internal oxidation of alloying elements, thereby increasing the area fraction of substrate available for reactive wetting [14,15,39,41–43]. These efforts have generally been focused on 1G AHSS grades, although recently these approaches were successfully employed by Pourmajidian

and McDermid in their selective oxidation and reactive wetting studies on 0.1C-6Mn-2Si-(0-0.5)Sn (wt%) model alloys [16,34,37,39].

However, the work published thus far on medium-Mn 3G AHSS has focused on the selective oxidation occurring during a single annealing cycle. It has been shown in previous work by the present authors [10] and several other researchers [5–9,44–46] that a two-stage heat treatment process results in improved mechanical properties relative to a one-stage intercritical annealing cycle for these alloys. The first stage is a high-temperature austenitization process designed to create a freshly martensitic microstructure, and the second stage comprises an intercritical annealing step for austenite reversion and overaging for CGL processing compatibility. Depending on substrate chemistry and exact choice of annealing parameters, the resulting microstructure contains significant (0.2-0.4) volume fractions of ultra-fine grained lamellar retained austenite in a martensitic matrix, along with some ferrite. As such, robust mechanical properties within the 24,000 MPa% $\leq$ UTS $\times$ TE $\leq$ 40,000 MPa% target window for 3G AHSS (as defined by Matlock and Speer [1,2]) can be achieved. However, additional work must be done to document the selective oxidation of the alloying elements in the substrates during this process. The chemical and morphological characterization of these surface structures is a critical component in overcoming the current knowledge gap of appropriate annealing parameter selection to successfully galvanize medium-Mn 3G AHSS substrates.

To this end, the objective of this work is to determine the effects of process atmosphere pO_2 on the selective oxide chemistry, morphology, and distribution for a prototype 0.15C-5.6Mn-1.9Al-1.1Si (wt %) alloy as it is thermally processed through a two-stage CGL-compatible annealing cycle with intermediate flash pickling.

4.3   Experimental Procedure

The experimental substrate used in this investigation was fabricated at United States Steel Research (Munhall) via vacuum melting, slab casting, hot rolling, simulated coiling, edge trimming, surface grinding, and cold rolling, with additional details outlined in a previous publication [10]. The chemical composition of the substrate, as determined via combustion analysis and inductively-coupled optical emission spectroscopy, is shown in Table 4.1. The substrate was received in the cold-rolled condition with a microstructure comprising tempered martensite and ferrite. The strip thickness was 1.2 mm. It was shown in previous work published by the present authors that the general 3G AHSS mechanical property targets were achieved by this experimental steel grade after it had been thermally processed through the two-stage annealing treatment shown in the schematic thermal profile in Figure 4.1 [10] (YS = 844 MPa, UTS = 1209 MPa, TE = 23%, UTS $\times$ TE = 27,800 MPa%). The process atmosphere oxygen partial pressure (pO_2) values employed during each annealing stage are documented in Table 4.2.

Table 4.1: Chemical composition of the experimental substrate (in wt%)

C	Mn	Al	Si	Mo	Ti	Fe
0.15	5.56	1.89	1.10	0.08	0.01	Balance
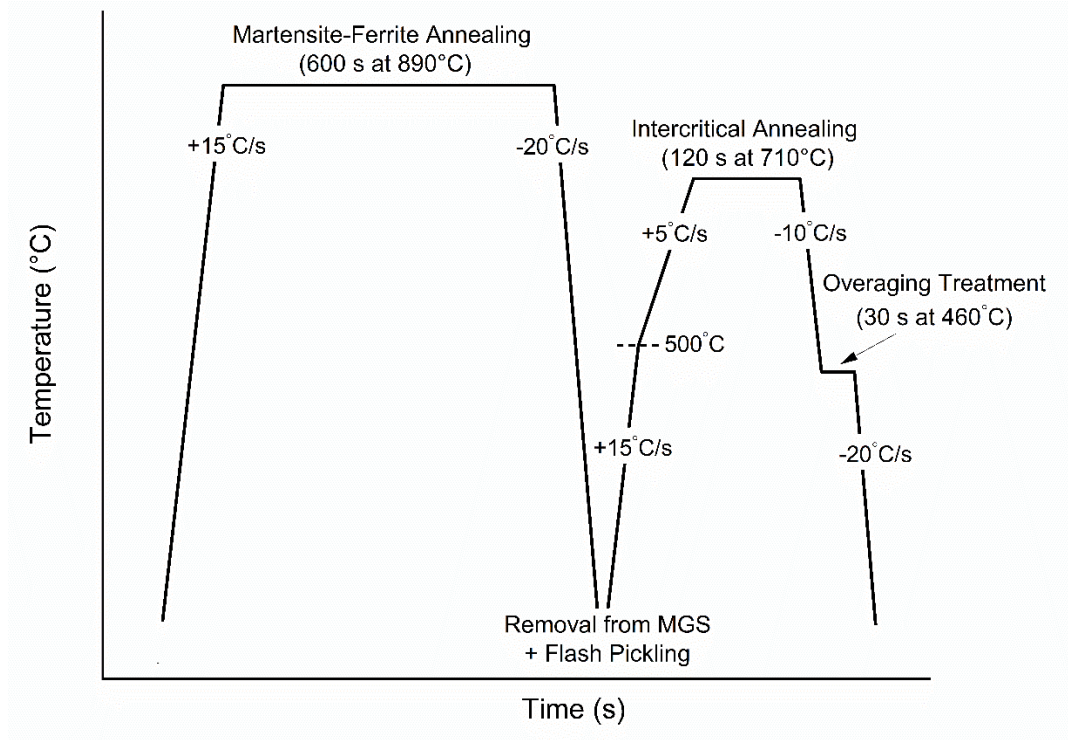
Figure 4.1: Schematic thermal profile for the experimental steel.

Table 4.2: Compositions of the 95 vol% N_2-5 vol% H_2 process atmosphere for the MF and IA annealing temperatures. Process atmosphere pO_2 values were calculated using the FREED thermodynamic database [47].

Annealing Stage (Temperature)	Atmosphere ID	Dew Point (°C)	pH_2O/pH_2	pO_2 (atm)
MF (890°C)	−30°C dp	−30	9.98×10^{-3}	3.27×10^{-21}
	−10°C dp	−10	5.62×10^{-2}	1.04×10^{-19}
	+5°C dp	+5	1.71×10^{-1}	9.62×10^{-19}
IA (710°C)	−30°C dp	−30	9.98×10^{-3}	2.71×10^{-25}
	−10°C dp	−10	5.62×10^{-2}	8.58×10^{-24}
	+5°C dp	+5	1.71×10^{-1}	7.96×10^{-23}

Coupons measuring 20 mm (TD) × 50 mm (RD) were prepared and degreased in a 80°C 2 vol% NaOH solution, rinsed in deionized water, rinsed in ethanol, and dried with warm air. The coupons were polished on one side using 4,000 grit SiC paper to minimize the effects of surface texture from cold rolling on subsequent analyses. All samples were cleaned with acetone wipes immediately prior to annealing. Annealing cycles were performed in the McMaster Galvanizing

Simulator (MGS, Iwatani-Surtec), according to the details documented in previously published literature [26,48]. A 0.5 mm type K thermocouple was welded directly to the samples in order to control the thermal cycle.

Three sets of samples were prepared in order to isolate the effects of the process atmosphere pO_2 and annealing stage on selective oxidation: 1) austenitization anneal resulting in a martensite-ferrite microstructure (MF) only; 2) austenitization anneal + flash pickling treatment (P); 3) austenitization anneal + flash pickling + intercritical anneal (IA). Flash pickling was performed by lightly agitating samples for 60 s in a 30°C solution comprising 64.5 mL deionized water + 59.6 mL concentrated hydrochloric acid + 0.25 g hexamethylenetetramine (which acts as an inhibiting agent to prevent pitting of the substrate), agitating in room temperature deionized water for 20 s, rinsing with ethanol, and drying in warm air.

The spatial distribution and morphology of the external oxides were documented using a Zeiss NVision 40 dual-beam SEM/FIB operated in SEM mode. The FIB capabilities of this instrument were also used to prepare two 15 μm-wide trenches per sample perpendicular to the steel surface such that its SEM capabilities could be used to image the external and internal oxides visible in the sample cross-section. The external oxides in the area of interest were protected during Ga^+-ion milling by first depositing a layer of W onto the surface. The external oxide thickness and internal oxide depth were measured using ImageJ 1.52a software on tilt-corrected SEM images. Per the methodology described by Pourmajidian and McDermid [37], at least 150 measurements were taken from each trench utilizing a grid to ensure random sampling. The external oxide thickness and internal oxide depth data are presented in box-and-whisker plots with the box showing the sample mean, median, interquartile range and the whiskers encompassing the 10-90th percentiles.

Elemental depth profiles were acquired *via* X-ray photoelectron spectroscopy (XPS) using a PHI Quantera XSM XPS equipped with an Al Kα X-ray source (1487.7 eV) and a hemispherical detector. The take-off angle was 45° and the spot size was 100 μm. Ar sputtering was performed on a 2×2 mm^2 area and the spectra were acquired with a pass energy of 140 eV and a step size of 0.25 eV. Data processing was performed using MultiPak 6.0 software. The spectra were calibrated using the metallic iron binding energy of 706.62 eV and are considered accurate to within ±0.1 eV. Depth measurements are considered to be accurate within 10% of the recorded sputtering depth.

Cross-sections from selected samples were prepared for transmission electron microscopy (TEM) via FIB milling. High-resolution scanning transmission electron microscopy (HR-STEM) micrographs were acquired using a Thermo Scientific Talos 200X TEM operated at 200 keV or a FEI Titan 80–300 HB TEM operated at 300 keV in STEM mode. Electron energy loss spectroscopy (EELS) was performed to determine the elemental distribution and chemical structure of the external and internal oxides. The spectra were obtained using a CMOS (Talos 200X) or Gatan Quantum GIF (Titan 80–300 HB) detector and the elemental maps were constructed using Digital Micrograph v3.43 software.

4.4   Results

SEM images showing the surfaces resulting from MF annealing prior to and after pickling are shown in Figure 4.2. Figure 4.2 (a-c) show that after MF annealing, extensive external oxidation was observed irrespective of the dew point employed. The nodular external oxides were dispersed among extruded Fe nodules. Figure 4.2 (d-f) show that the pickling treatment was effective at denuding the surface of most of the oxide population, with dispersed nodules measuring tens of nm remaining undissolved. The pickled surfaces were textured due to extruded Fe nodules and the dissolution of oxides into the sub-surface.
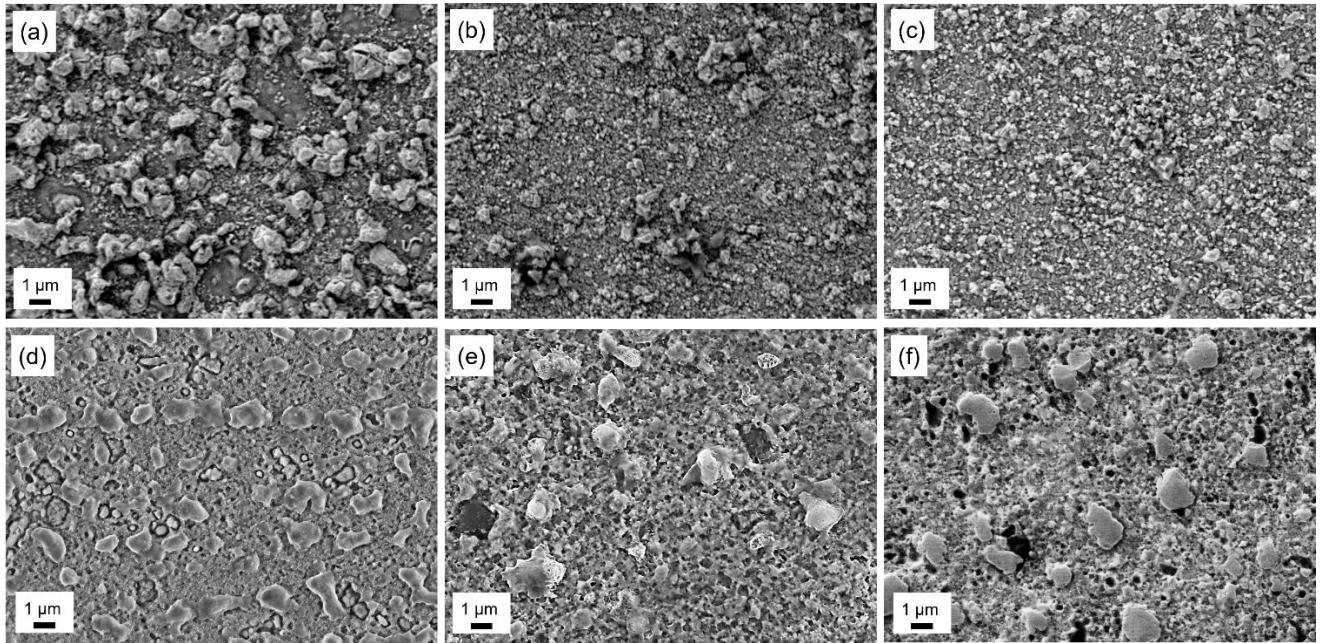
Figure 4.2: SEM images showing external oxidation and Fe nodule extrusion on samples after MF annealing: (a) MF –30°C dp, (b) MF –10°C dp, (c) MF +5°C dp; and after pickling: (d) P –30°C dp, (e) P –10°C dp, (f) P +5°C dp.

FIB-prepared trench cuts were prepared from the samples in Figure 4.2 and are shown in Figure 4.3, where the as-annealed surfaces are shown in (a-c) and the pickled surfaces are shown in (d-f). These images show the effectiveness of the flash pickling treatment in removing most of the external oxides, leaving behind only dispersed nano-scaled oxide nodules. It can also be seen that some of the near-surface internal oxide structures were selectively dissolved by the flash pickling solution.
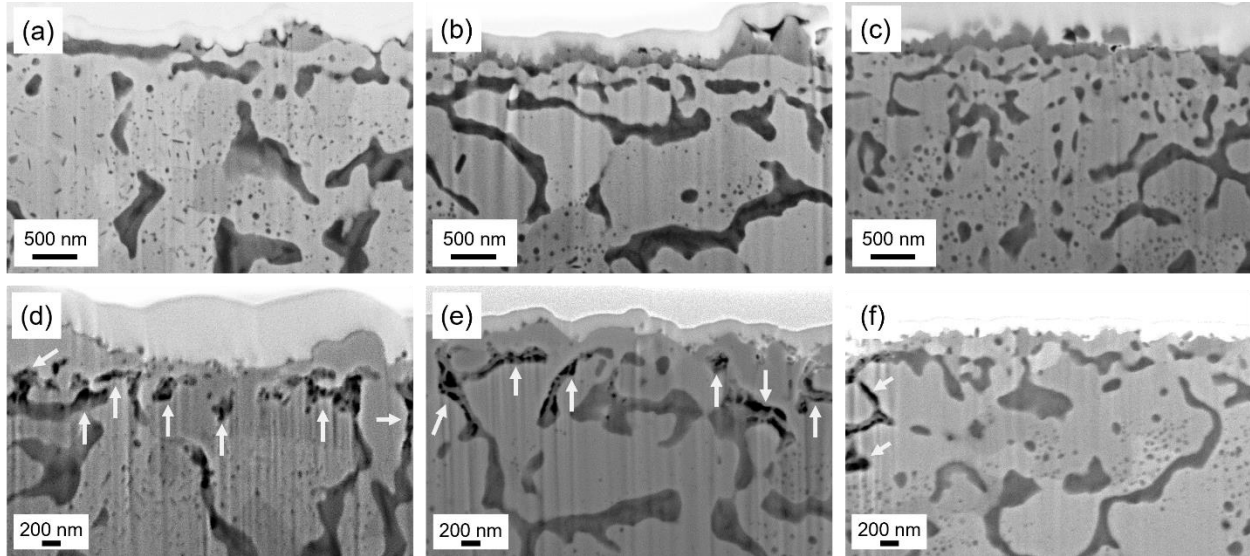
Figure 4.3: SEM images of FIB-prepared trench cuts showing internal and external oxidation on samples after MF annealing: (a) MF –30°C dp, (b) MF –10°C dp, (c) MF +5°C dp; and after pickling: (d) P –30°C dp, (e) P –10°C dp, (f) P +5°C dp. Arrows indicate selectively dissolved near-surface internal oxide structures as a result of flash pickling.

SEM images showing the surfaces after intercritical annealing are shown in Figure 4.4. Dispersed and discrete nodule-type nano-scale oxides were present after annealing at all dew point combinations explored. Moreover, the extruded Fe nodules were preserved, as were the pores from selective oxide dissolution during the pickling process. The FIB trench cut images in Figure 4.5 present a wider view of the trenches for further examination of the scale of the internal oxide structures by the reader.
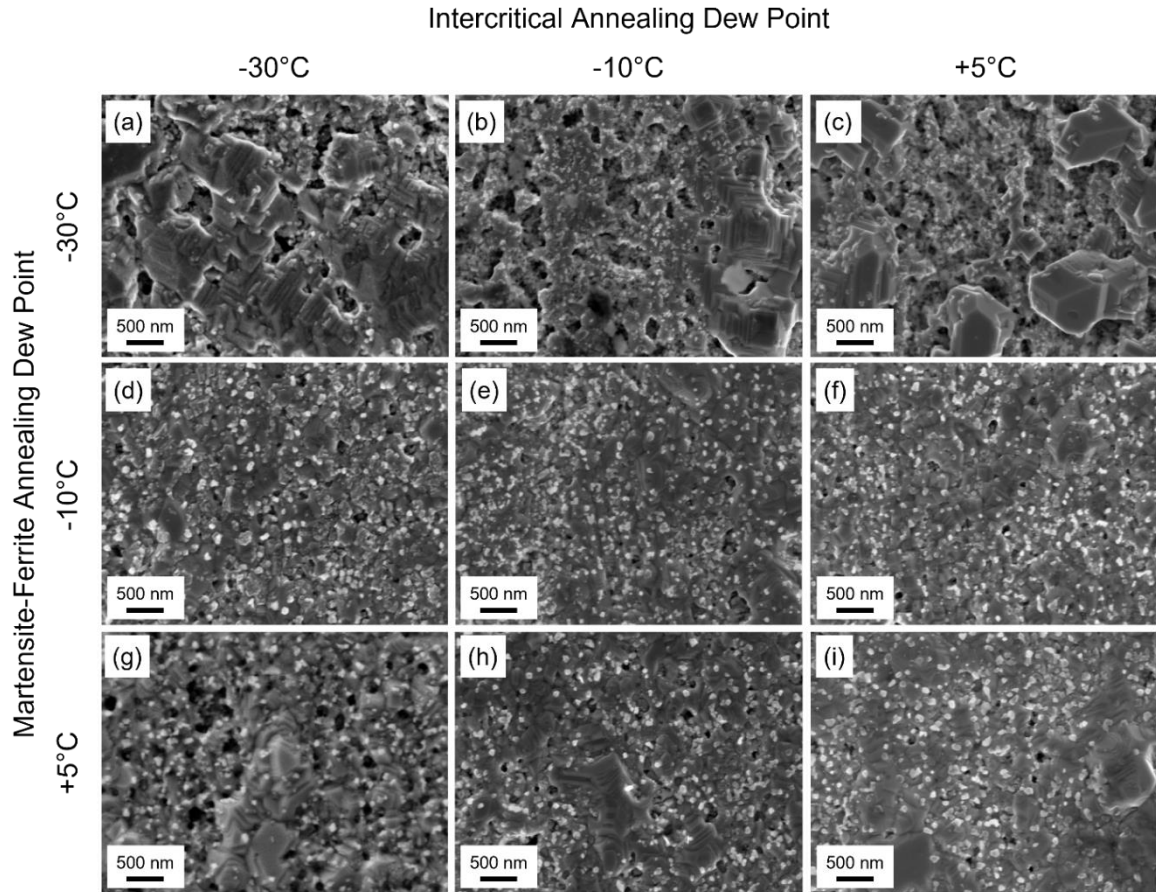
Figure 4.4: SEM images showing the selectively oxidized surfaces after intercritical annealing: (a) IA –30°C/–30°C dp; (b) IA –30°C/–10°C dp; (c) IA –30°C/–10°C dp; (d) IA –10°C/–30°C dp; (e) IA –10°C/–10°C dp; (f) IA –10°C/+5°C dp; (g) IA +5°C/–30°C dp; (h) IA +5°C/–10°C dp; (i) IA +5°C/+5°C dp.
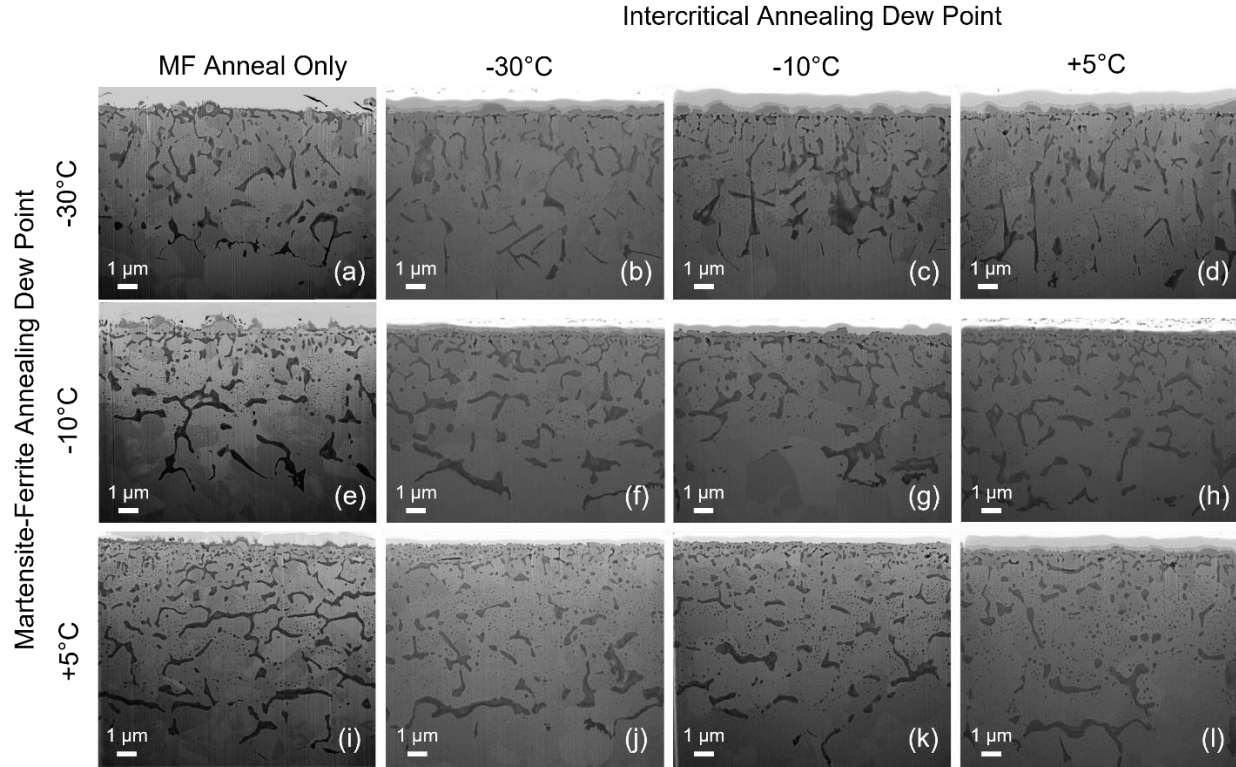
Figure 4.5: SEM images of the FIB-prepared trench cuts showing a wider view of the internal and external selective oxides after intercritical annealing: (a) MF –30°C dp; (b) IA –30°C/–30°C dp; (c) IA –30°C/–10°C dp; (d) IA –30°C/–10°C dp; (e) MF –10°C dp; (f) IA –10°C/–30°C dp; (g) IA –10°C/–10°C dp; (h) IA –10°C/+5°C dp; (i) MF +5°C dp; (j) IA +5°C/–30°C dp; (k) IA +5°C/–10°C dp; (l) IA +5°C/+5°C dp.

Box-and-whisker plots showing the measured data for external oxide thickness and internal oxide depth as a function of annealing stage are shown in Figure 4.6 (external) and Figure 4.7 (internal). Examination of Figure 4.6 shows that the mean external oxide thickness after the MF treatment was between 160-210 nm, irrespective of the dew point employed. After flash pickling, the mean external oxide thickness decreased to approximately 50 nm, and this was invariant with intercritical annealing conditions. In addition, examination of Figure 4.7 shows that the depth of internal oxidation did not increase significantly from the MF to the IA condition. This suggests that the available near-surface solute was selectively oxidized during the MF annealing step and that there was insufficient solute diffusion for further oxide evolution during the IA annealing step.
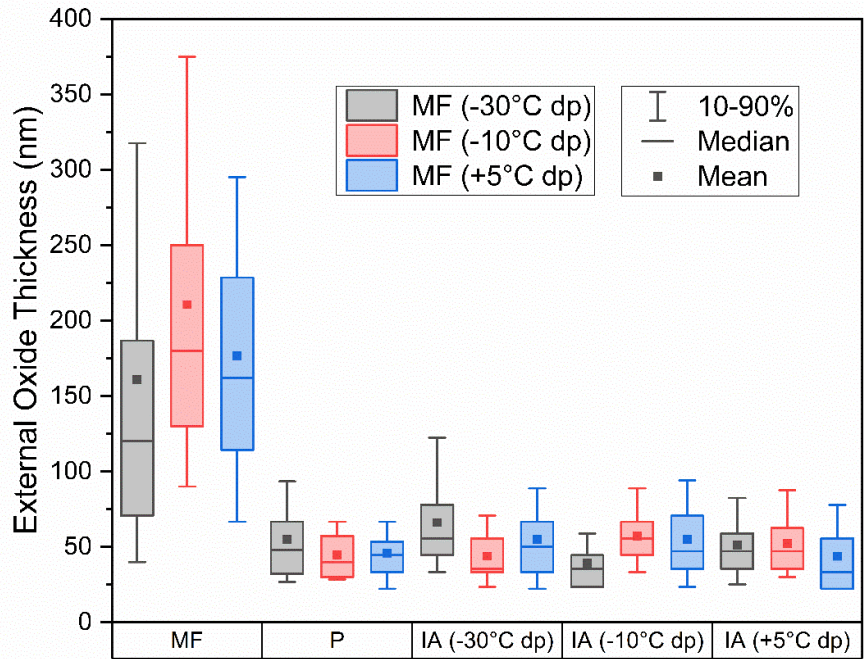
Figure 4.6: Box-and-whisker plot showing the distribution of external oxide thickness measurements as a function of process atmosphere during each annealing step. The box encloses 25-75% of the data and the whiskers enclose 10-90% of the data.
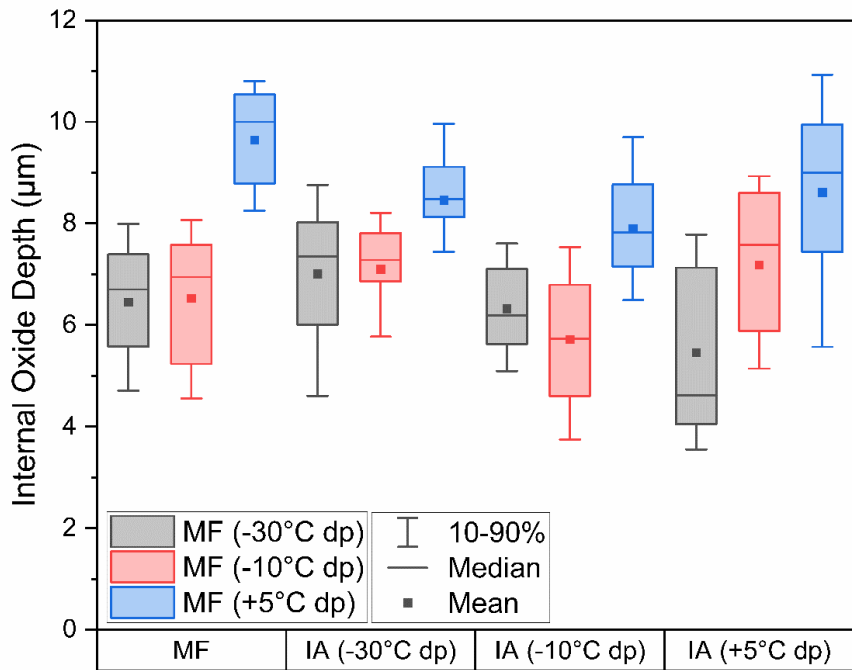
Figure 4.7: Box-and-whisker plot showing the distribution of internal oxide depth measurements as a function of process atmosphere during each annealing step. The box encloses 25-75% of the data and the whiskers enclose 10-90% of the data.

High resolution XPS scans of the MF –30°C dp, MF –10°C dp, MF +5°C dp, and P –10°C dp sample were obtained in order to identify the chemical species present at the surfaces of these samples. The measured Al 2p, Mn $2p_{3/2}$, and Si 2p binding energies are shown in Table 4.3. The respective binding energies of Al, Mn, and Si did not vary significantly between samples, indicating that these species were present in similar chemical states irrespective of the dew point employed during the MF annealing step. The binding energies correlate to published literature values for MnO, Mn_2SiO_4, $MnAl_2O_4$, and Al_2O_3 [49–54].

XPS was also used to acquire elemental depth profiles of the MF –30°C dp, MF –10°C dp, and MF +5°C dp samples to ascertain the segregation of Mn, Si, and Al towards the surface and approximate the thickness of the external oxide layer. These are shown in Figure 4.8 in addition to XPS elemental depth profiles of the P –10°C sample which were obtained to quantify the effectiveness of the pickling treatment. The depth profiles for the MF –30°C dp, MF –10°C dp, and MF +5°C dp samples (Figure 4.8(a-c)) are similar and show significant enrichment of O and Mn at the surface. Moreover, the gradual increase in the Fe suggests the existence of a non-planar oxide-substrate interface. The elemental depth profiles for the P –10°C dp (Figure 4.8(d)) show that the external selective oxide layer was effectively removed by the pickling treatment. Moreover, the Mn and Si levels were depleted relative to the unpickled MF samples, corroborating the SEM images (Figure 4.2 and Figure 4.3) showing the dissolution of some near-surface oxide species in the pickled samples.
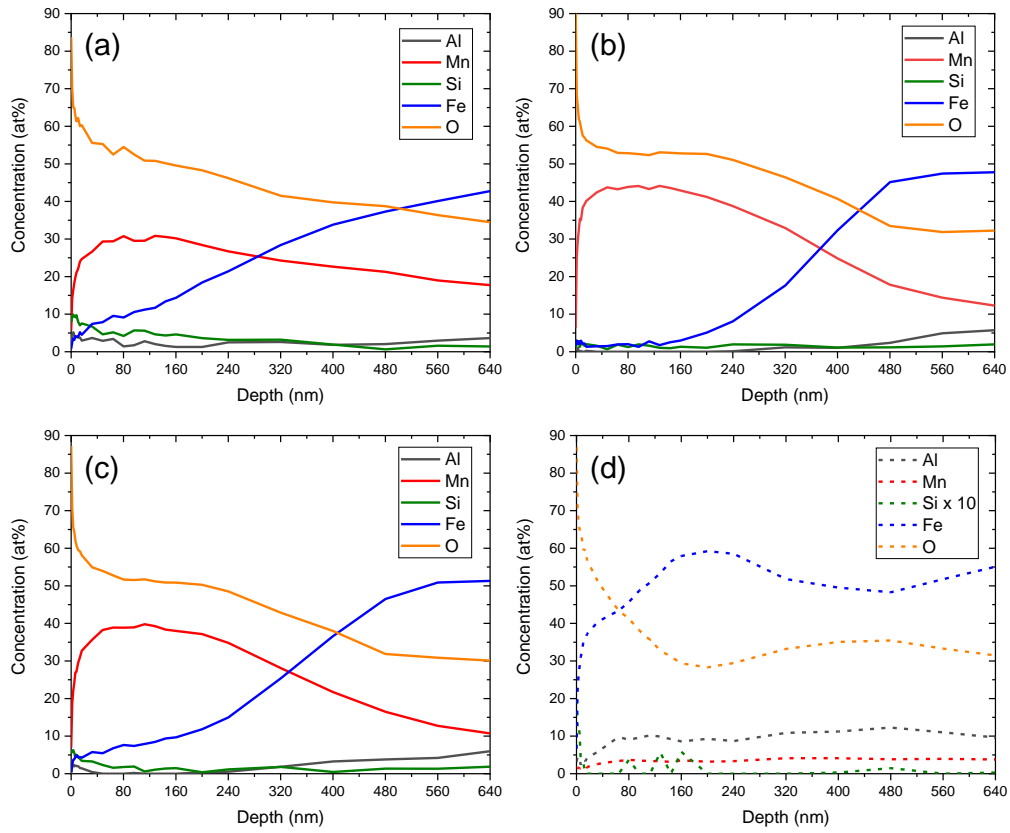
Figure 4.8: XPS elemental depth profiles for Al, Mn, Si, Fe, and O concentrations for (a) MF –30°C dp, (b) MF –10°C dp, (c) MF + 5°C dp, and (d) P–10°C dp.

Table 4.3: Identification of surface oxide species present after MF treatments via measured XPS binding energies

Sample	Measured XPS Binding Energies (eV)			Oxide Species Present
	Al 2p	Mn 2p$_{3/2}$	Si 2p	
MF –30°C dp	73.8	640.4	101.8	Al$_2$O$_3$ [50,51,53] MnAl$_2$O$_4$ [51,54] Mn$_2$SiO$_4$ [54] MnO [49,53]
MF –10°C dp	74.0	640.8	101.7	Al$_2$O$_3$ [50,51,53] MnAl$_2$O$_4$ [51,54] Mn$_2$SiO$_4$ [54] MnO [49,53]
P –10°C dp	74.4	641.5	101.6	Al$_2$O$_3$ [50,51,53] MnAl$_2$O$_4$ [51,54] Mn$_2$SiO$_4$ [54]
MF +5°C dp	73.6	640.7	101.4	Al$_2$O$_3$ [50,51,53] Mn$_2$SiO$_4$ [54] MnO [49,53]

XPS depth profiles of Mn, Si, and Al were taken for selected intercritically annealed samples in the experimental matrix and are shown in Figure 4.9, in addition to the P –10°C dp sample presented in Figure 4.8(d) to facilitate comparison by the reader. Like the P –10°C dp sample, the three IA samples exhibited rapid increases in their respective Fe curves at shallow (<20 nm) depths, suggesting that there was not significant additional external oxidation during intercritical annealing. This corroborates the SEM images in Figure 4.4 that show nodular and dispersed nano-scaled selective oxides on the IA samples. In the three IA cases, the Si levels were depleted relative to the bulk concentration of 2 at%, likely due to the formation of Si-containing oxides during the MF annealing step and subsequent dissolution of these species by the flash pickling process.
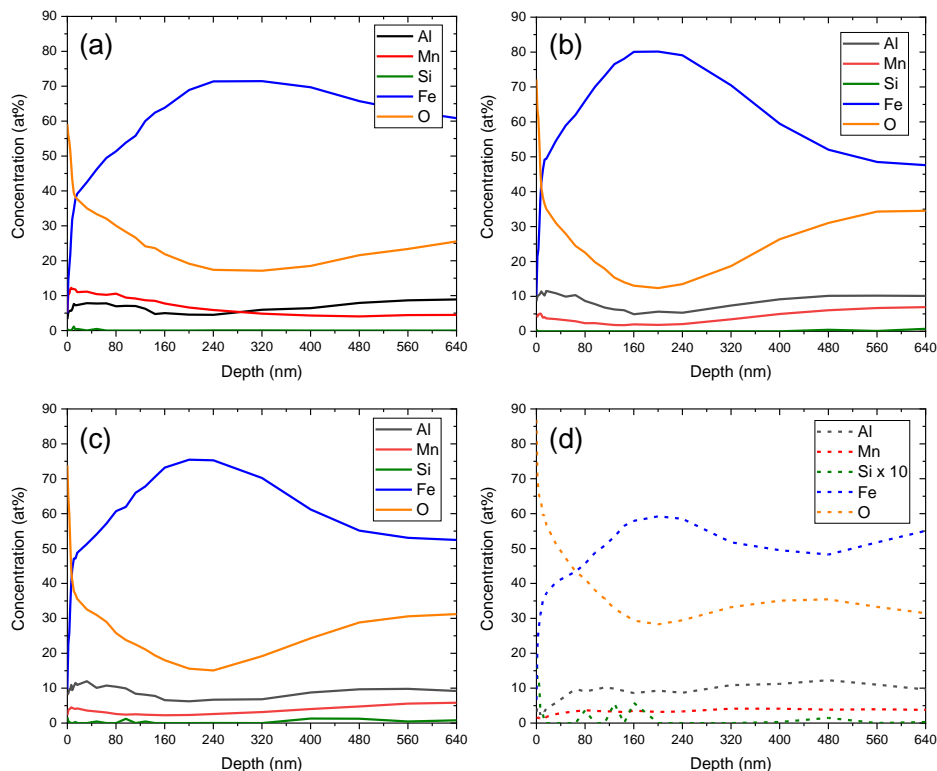
Figure 4.9: XPS elemental depth profiles for Al, Mn, Si, Fe, and O concentrations for (a) – 30°C/–30°C dp, (b) –10°C/–10°C dp, (c) +5°C/+5°C dp, and (d) P–10°C dp.

High-resolution XPS analysis was also performed on these samples to elucidate the effects of process atmosphere (in both annealing stages) on the surface oxide chemistry. Table 4.4 shows the Al 2p, Mn 2p$_{3/2}$, and Si 2p XPS binding energies obtained at the surfaces of the analyzed samples, in addition to the proposed oxide species present. The experimentally determined binding energies for Al 2p align closely with the reported values for Al$_2$O$_3$ [50,51,53] and MnAl$_2$O$_4$ [51,54]. The measured binding energies for Si 2p match closely with that of Mn$_2$SiO$_4$ [54]. This suggests that SiO$_2$ (reported binding energy of 103.3 [53] or 103.9 eV [50,52]) formation was avoided, which is promising for future galvanizing studies since the film-like morphology of SiO$_2$ is known to be deleterious to reactive wetting [18–20,32,33]. It should also be noted, however, that the low atomic fraction of Si obtained for each sample suggests that the areal coverage of Mn$_2$SiO$_4$ is likely to be insignificant relative to elemental Fe and other external oxide species. Furthermore,

the experimentally determined binding energies for Mn 2p$_{3/2}$ do not align as closely with a single reference value. This, in combination with the relative broadness of the peaks, suggests that Mn was present in multiple oxide states. It can be deduced from the aforementioned Al 2p and Si 2p peak information that Mn was present in the form of MnAl$_2$O$_4$ [51,54] and Mn$_2$SiO$_4$ [54], in addition to MnO [51,53].

Table 4.4: Identification of surface oxide species present after intercritical annealing treatments via measured XPS binding energies

IA Sample	Measured XPS Binding Energies (eV)			Oxide Species Present
	Al 2p	Mn 2p$_{3/2}$	Si 2p	
–30°C/–30°C dp	74.2	641.0	101.6	Al$_2$O$_3$ [50,51,53] MnAl$_2$O$_4$ [51,54] Mn$_2$SiO$_4$ [54] MnO [49,53]
–10°C/–10°C dp	74.3	641.4	101.4	Al$_2$O$_3$ [50,51,53] MnAl$_2$O$_4$ [51,54] Mn$_2$SiO$_4$ [54] MnO [49,53]
+5°C/+5°C dp	74.1	641.0	101.5	Al$_2$O$_3$ [50,51,53] MnAl$_2$O$_4$ [51,54] Mn$_2$SiO$_4$ [54] MnO [49,53]

The morphology and chemical structure of the selective oxides formed during each annealing stage were determined using STEM-EELS elemental mapping and spectral analysis. Based on the aforementioned XPS analysis, the MF –10°C dp sample was selected for STEM-EELS analysis of the selective oxides formed during the MF annealing step. A lift-out of the P – 10°C dp sample was also prepared to examine the effects of flash pickling on the surface and near-surface structures. Subsequently, STEM-EELS mapping of the IA –10°C/–30°C dp, IA –10°C/– 10°C dp, and IA –10°C/+5°C dp samples was performed to determine the effects of subsequent intercritical annealing on the selective oxides formed during the first annealing step.

4.4.1   Evolution of External Oxide Structures

EELS elemental maps of the MF –10°C dp surface are shown in Figure 4.10 with EELS spectra from selected locations included in Figure 4.11. A compact and layered selective oxide structure was observed. The most external oxide species (Region 4 in Figure 4.10) observed was a compact layer of Mn oxide nodules approximately 100-200 nm thick, which are identified as MnO based on the EELS spectra [55] in Figure 4.11. In some areas, these MnO nodules grew directly on top of the substrate in direct contact with the Fe, however, in other areas, these MnO nodules grew on top of a discontinuous mixed Mn-Si (Regions 1 and 3 in Figure 4.10) and Mn-Al (Region 2 in Figure 4.10) oxide layer. The mixed Mn-Al and Mn-Si oxides also co-precipitated internally at grain boundaries. Based on the EELS spectra in Figure 4.11, these species were identified as $MnAl_2O_4$, $MnSiO_3$, and Mn_2SiO_4 [54]. It is also noteworthy that spectra taken from the top 200 nm of the matrix showed no appreciable signal from Mn, Si, or Al, as shown in the spectra from Region 5 in Figure 4.11.
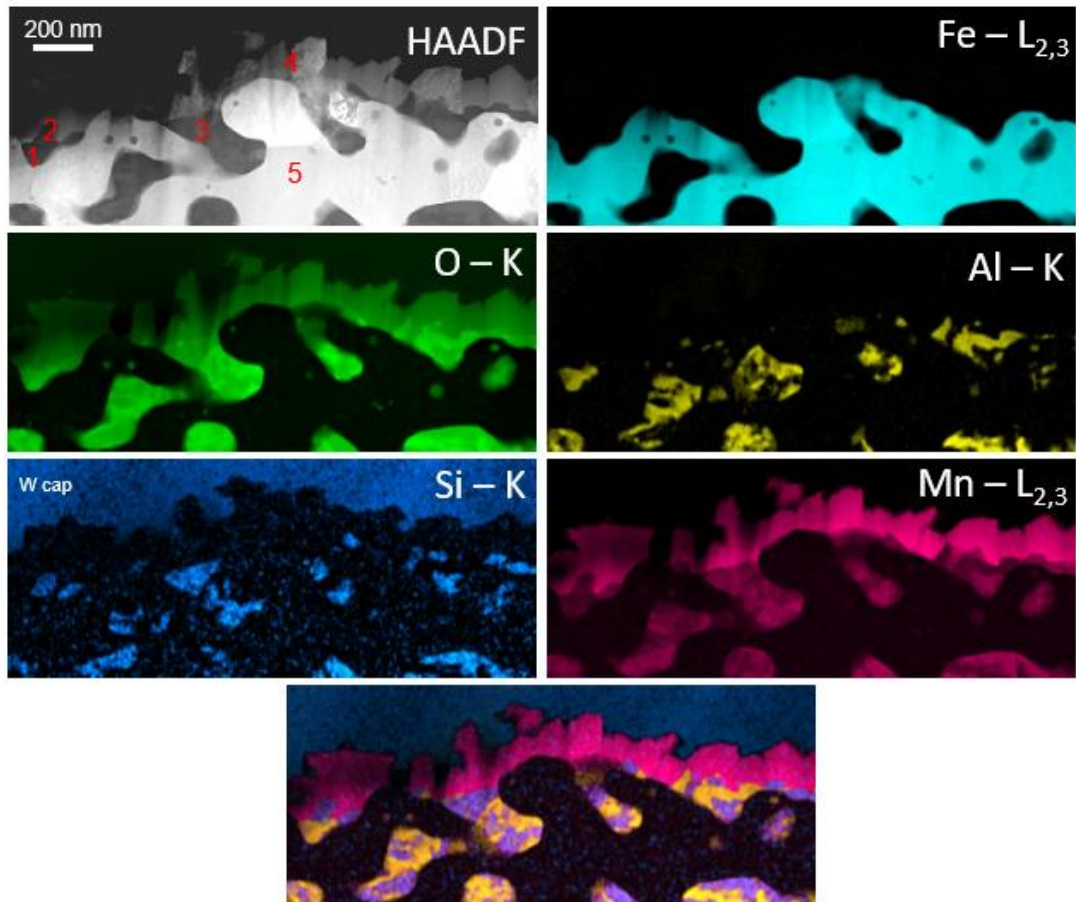
Figure 4.10: HAADF image and EELS elemental maps of Fe, O, Al, Si, and Mn showing the selectively oxidized MF –10°C dp surface. A composite map of Al, Si, and Mn is also included.

Figure 4.11: EELS spectra showing the O-K, Mn-L$_{2,3}$, Al-K, and Si-K edges from the numbered regions in Figure 4.10 (MF –10°C dp).

EELS elemental maps of the P –10°C dp surface are shown in Figure 4.12, with corresponding EELS spectra from selected locations included in Figure 4.13. It is evident that the pickling treatment effectively removed the surface MnO, MnSiO$_3$, and Mn$_2$SiO$_4$ species but left behind the MnAl$_2$O$_4$ [56,57] nodules (Regions 2 and 3 in Figure 4.12 and Figure 4.13). The holes in the near-surface internal oxide structure due to the selective dissolution of internal Mn-Si oxides were preserved. This is consistent with literature showing that MnO [58], MnSiO$_3$ [59], and Mn$_2$SiO$_4$ [60] are largely soluble in hydrochloric acid solutions over a wide pH range with

reasonably rapid kinetics, whereas the present authors could find no such studies published for

$MnAl_2O_4$.
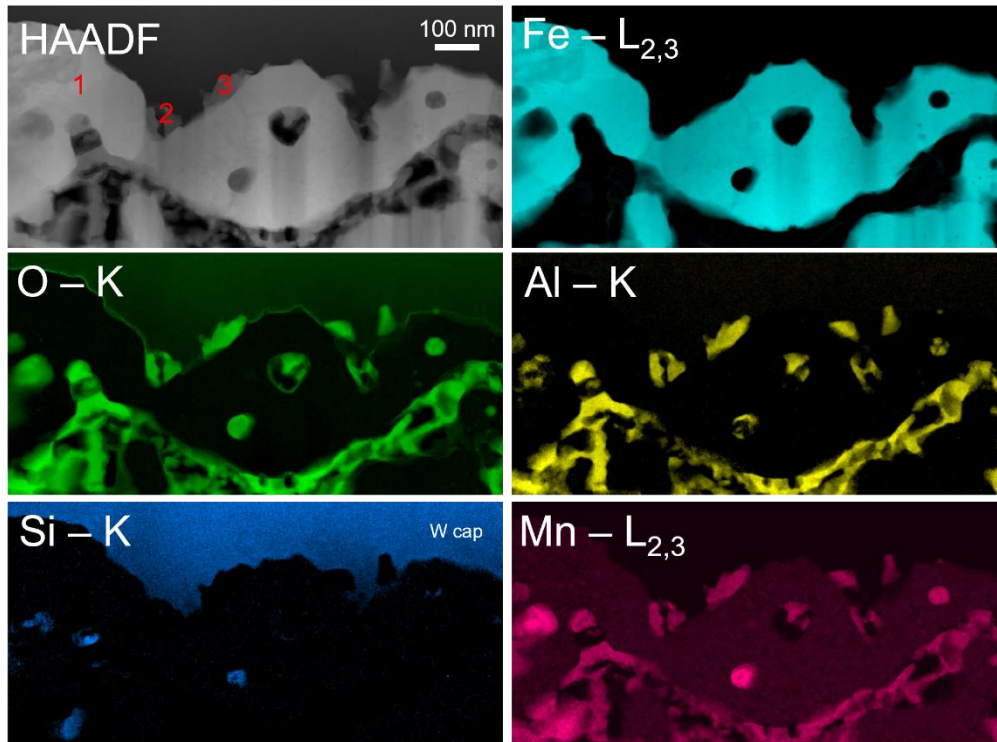
Figure 4.12: HAADF image and EELS elemental maps of Fe, O, Al, Si, and Mn showing the selective oxides remaining after flash pickling (P –10°C dp sample).

Figure 4.13: EELS spectra showing the O-K, Mn-L$_{2,3}$, Al-K, and Si-K edges from the numbered regions in Figure 4.12 (P –10°C dp).

The effects of intercritical annealing on the further development of the external selective oxides are shown in the STEM-EELS elemental maps of the IA –10°C/–30°C dp sample surface shown in Figure 4.14. This image is also representative of the IA –10°C/–10°C dp and IA –10°C/+5°C dp samples (not pictured). Speciation was performed via EELS spectral analysis and it was determined that the dispersed external nodular Mn-Al oxides observed on these samples were MnAl$_2$O$_4$, like on the surface of the P –10°C dp sample (Figure 4.12). This suggests that the MnAl$_2$O$_4$ nodules remaining after flash pickling did not evolve during intercritical annealing and would be the pre-immersion surface structures that would enter the galvanizing bath. Examination of Figure 4.14 also shows that the pores created during flash pickling were preserved during intercritical annealing.
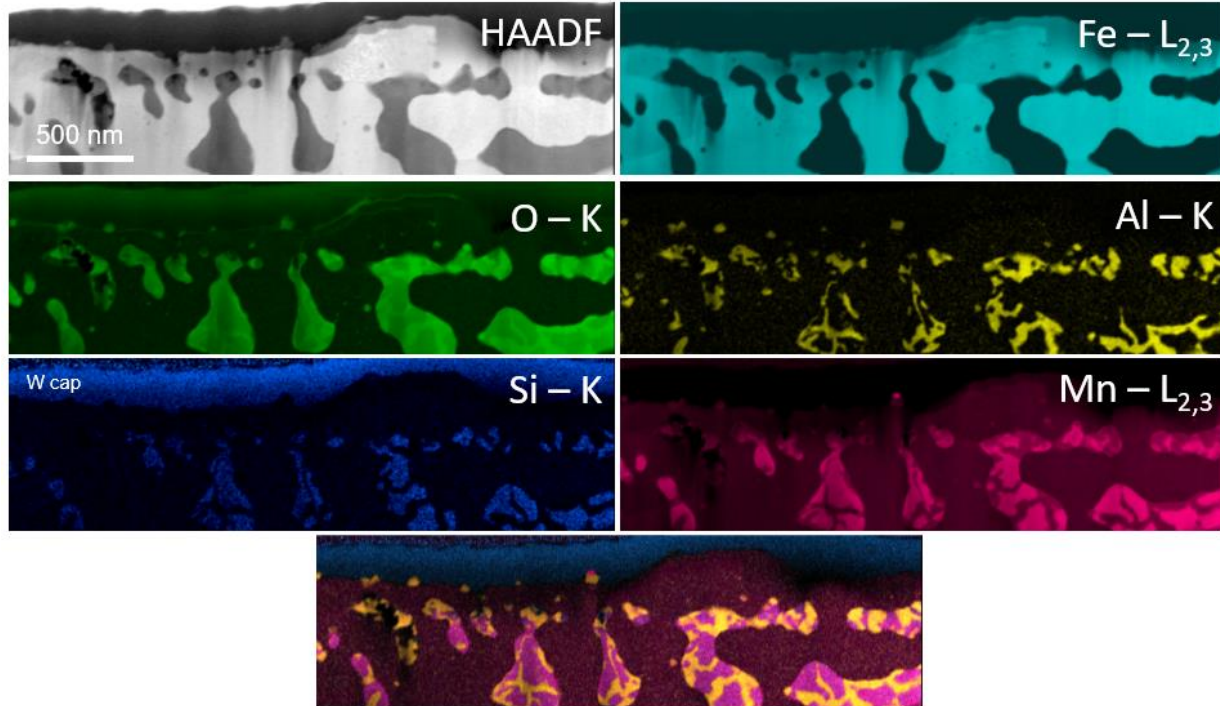
Figure 4.14: Representative HAADF image and EELS elemental maps of Fe, O, Al, Si, and Mn showing the selective oxides remaining after intercritical annealing (IA –10°C/–30°C dp sample pictured). A composite map of Al, Mn, and Si is also included.

4.4.2   Evolution of Internal Oxide Structures

Figure 4.15 comprises the STEM-EELS maps of grain boundary oxides observed approximately 3 μm beneath the surface of the MF –10°C dp sample. These grain boundary oxides formed in a core-shell morphology, with Al and Mn enrichment in the oxide core and Mn and Si enrichment in the shell. EELS spectral analysis (Figure 4.16) confirmed that the core oxides comprised Al_2O_3 [56,57] and $MnAl_2O_4$ [54] while the shells comprised mainly Mn_2SiO_4 [54]. These findings are similar to those documented by other authors who investigated low-alloy TRIP [17,41,61–65] and medium-Mn [16,34] steels containing varying amounts of Mn, Si, and Al, but these authors mostly described selective oxides comprising a SiO_2 core surrounded by $MnSiO_3/Mn_2SiO_4$ shell. However, the present findings are comparable to those of Li et al. [66], who found that some internal selective oxides in their 0.15C-1.55Mn-0.29Si-1.51Al-0.51Cu (wt%)

TRIP steel comprised an Al oxide core and Mn-Si oxide shell. Examination of the spectrum taken from Region 4 in Figure 4.16 shows that the matrix surrounding this oxide was depleted in Mn, Al, and Si.
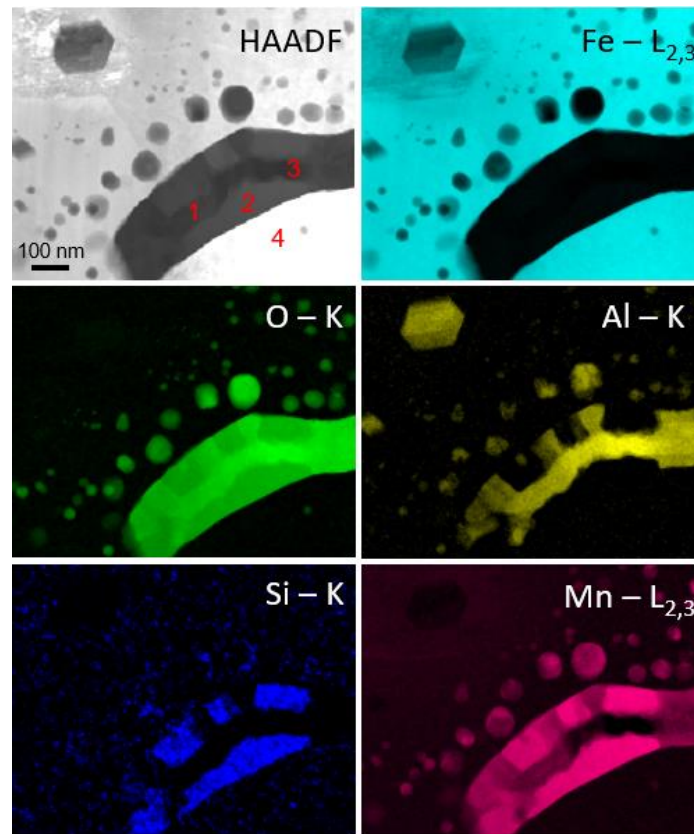
Figure 4.15: HAADF image and EELS elemental maps of Fe, O, Al, Si, and Mn showing a representative grain boundary oxide structure from the MF –10°C dp sample.
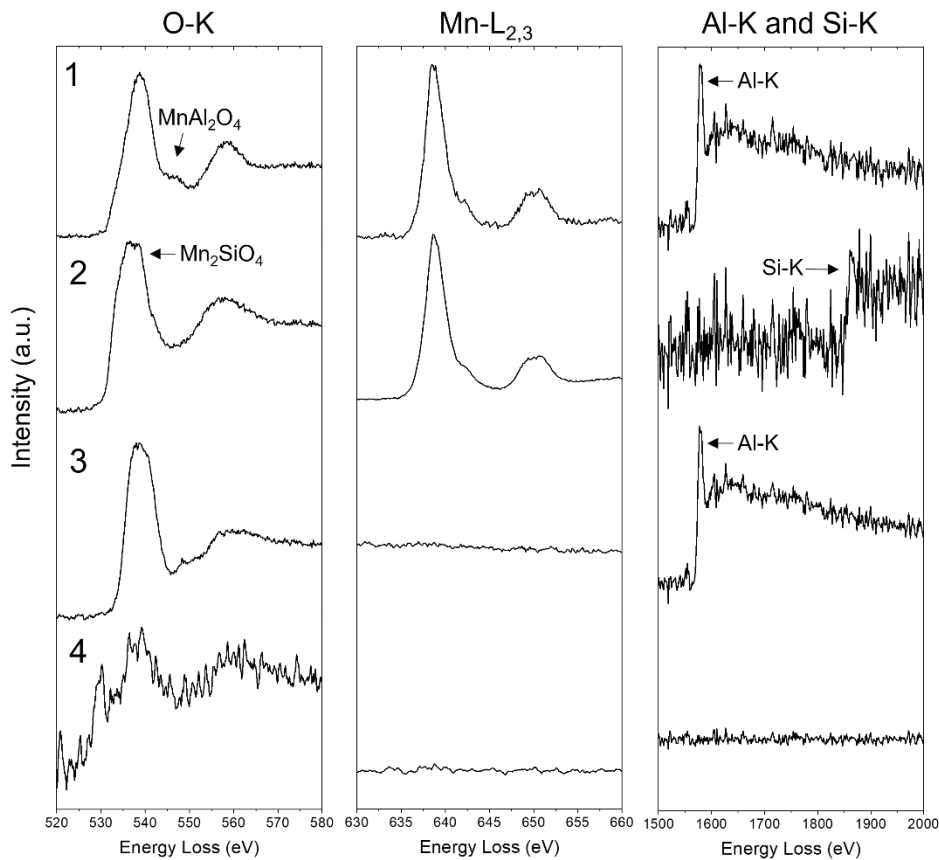
Figure 4.16: EELS spectra showing the O-K, Mn-L$_{2,3}$, Al-K, and Si-K edges from the numbered regions in Figure 4.15 (MF –10°C dp).

The deepest internal oxides observed in the MF –10°C dp sample are typified by the STEM-EELS elemental maps shown in Figure 4.17. This oxide grouping was found approximately 8 μm deep into the sample and comprised a Si-rich oxide capping an Al-rich oxide, with a very thin layer of Mn oxide precipitating on the Si oxide cap. Analysis of the EELS spectra (Figure 4.18) confirmed that the major oxide species were SiO$_2$ [67,68] and Al$_2$O$_3$ [56,57], and that the local matrix was depleted in Al and Si but contained some Mn. This suggests that the local dissolved O content was too low to selectively oxidize Mn, although relative diffusion rates of alloying elements and the relatively high solubility of MnO in ferrite may have also contributed to the lack of Mn oxides. The calculated solubility products at 890°C for the oxides of interest are shown in Table 4.5 [69–71].

Table 4.5: Calculated solubility products for oxide species of interest in ferrite at 890°C.

Oxide Species	Al_2O_3	$MnAl_2O_4$	MnO	Mn_2SiO_4	SiO_2
Solubility Product	8.08×10^{-15} $(ppm)^5$	5.82×10^{-15} $(ppm)^7$	43.46 $(ppm)^2$	1.84×10^{-2} $(ppm)^7$	1.19×10^{-3} $(ppm)^3$
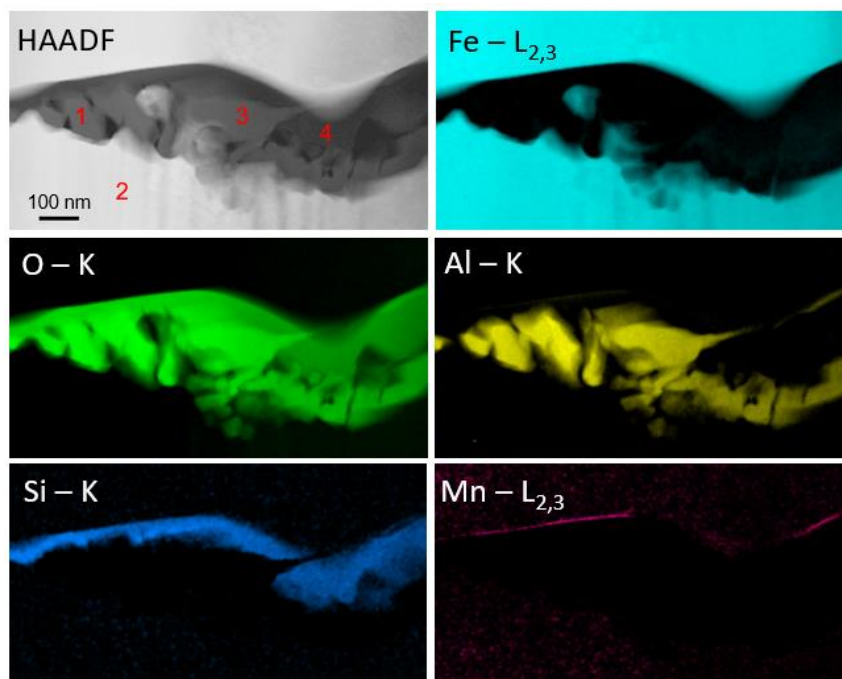
Figure 4.17: HAADF image and EELS elemental maps of Fe, O, Al, Si, and Mn showing a grain boundary oxide in the deepest part of the oxide network in the MF –10°C dp sample.
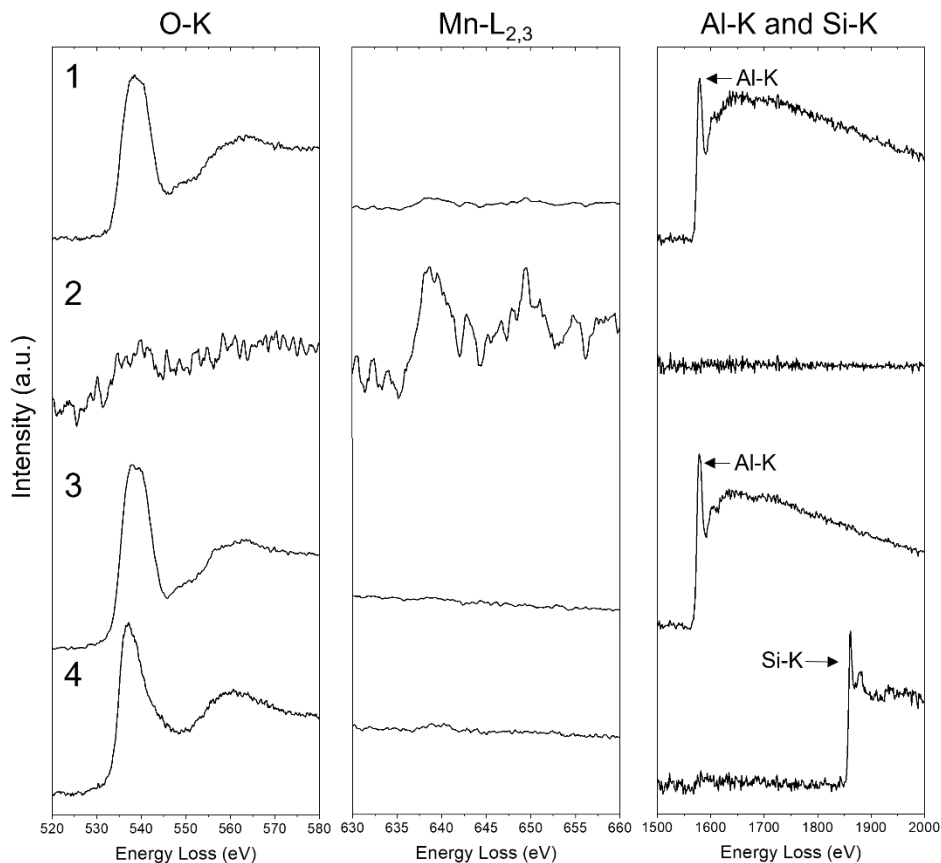
Figure 4.18: EELS spectra showing the O-K, Mn-L$_{2,3}$, Al-K, and Si-K edges from the numbered regions in Figure 4.17 taken from the MF –10°C dp sample.

The internal oxide structures observed in the IA –10°C/–30°C dp, IA –10°C/–10°C dp, and IA –10°C/+5°C dp samples were similar to those observed in the MF –10°C dp sample (Figure 4.15 and Figure 4.17). A representative grain boundary taken from the IA –10°C/–10°C dp sample is shown in the EELS elemental maps in Figure 4.19 (with corresponding EELS spectra in Figure 4.20). Analysis of the EELS spectra showed that the shells were primarily composed of Mn$_2$SiO$_4$ and nodules of MnO precipitated on the shell (like in region 4 in Figure 4.19).
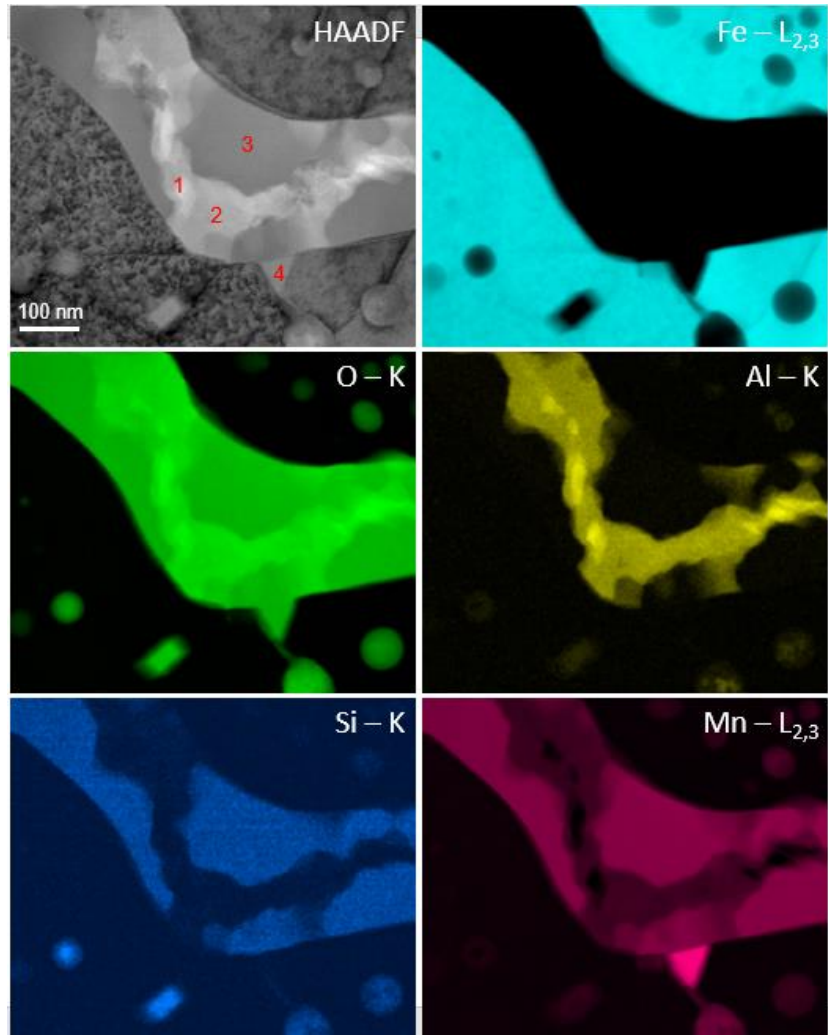
Figure 4.19: HAADF image and EELS elemental maps of Fe, O, Al, Si, and Mn showing a representative selective grain boundary oxide structure in the IA –10°C/–10°C dp sample.
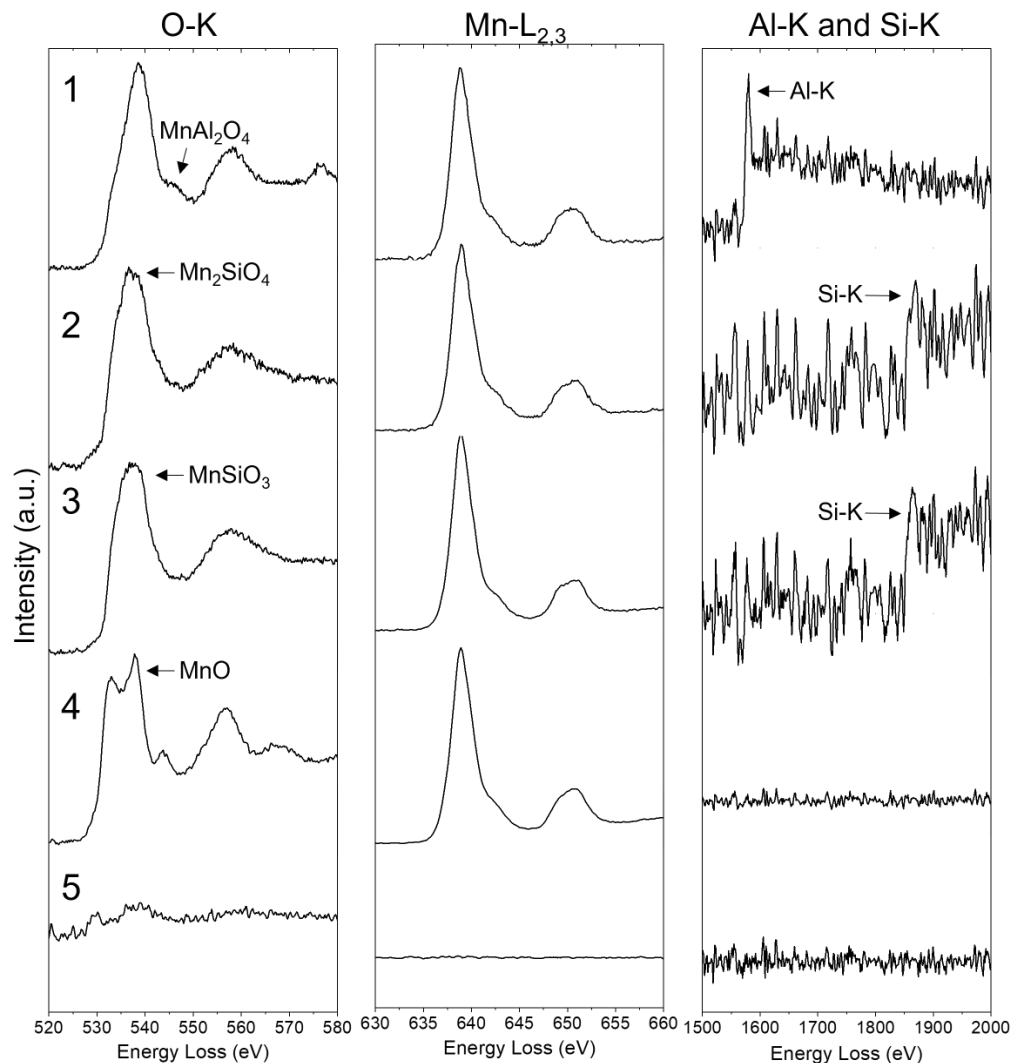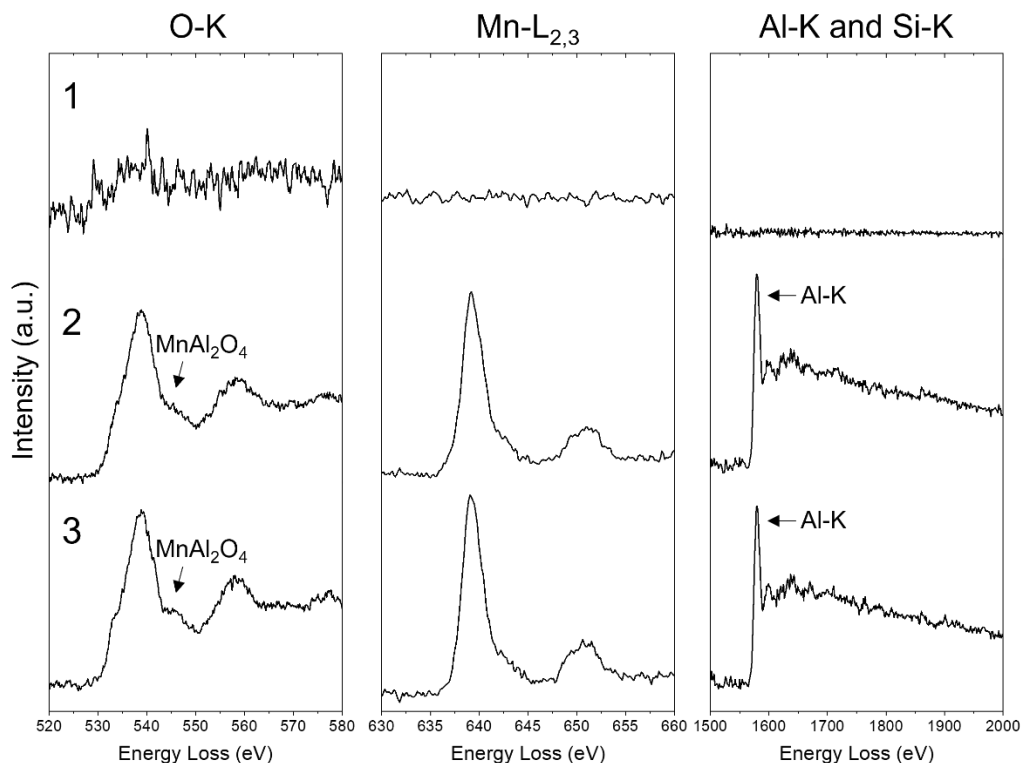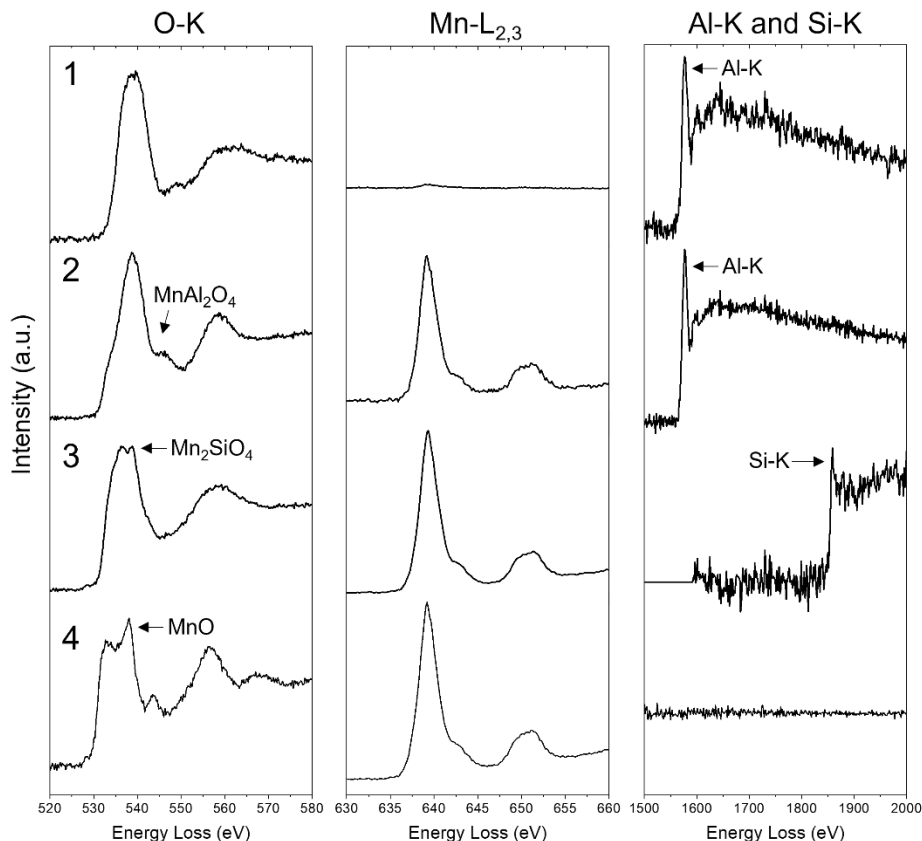
Figure 4.20: EELS spectra showing the O-K, Mn-L$_{2,3}$, Al-K, and Si-K edges from the numbered regions in Figure 4.19 (IA –10°C/–10°C dp sample).

4.5 Discussion

The spatial distribution and morphology of the external oxides is of particular interest due to the known consequences of external oxides on reactive wetting of steel substrates by Zn(Al,Fe) galvanizing baths. Given that the flash pickling treatment did not remove the MnAl$_2$O$_4$, the co-precipitation of MnAl$_2$O$_4$ and MnSiO$_3$/Mn$_2$SiO$_4$ (such that neither species formed a continuous layer, see Figure 4.10) beneath the MnO nodules is a favourable outcome that preserved significant area fractions of metallic Fe on the substrate surface.

A comparison of the pickled (Figure 4.3 and Figure 4.12) and intercritically annealed samples (Figure 4.4 and Figure 4.14) reveals that the morphology and chemical composition of the external oxide nodules did not evolve during intercritical annealing. This is corroborated by the box plot in Figure 4.6 showing similar external oxide thickness distributions for the pickled

and intercritically annealed samples, as well as the XPS profiles in Figure 4.9 showing similar elemental depth profiles for the P –10°C dp and the intercritically annealed samples. This is attributed to the local depletion of alloying elements in the near-surface bulk material, as shown by the lack of Al, Mn, and Si signals in EELS spectra for Region 5 in the MF –10°C dp sample (Figure 4.10 and Figure 4.11) and Region 1 in the P –10°C dp sample (Figure 4.12 and Figure 4.13). The intercritical annealing cycle was apparently insufficiently long and at an insufficiently high temperature to allow for additional diffusion of alloying elements from deeper in the substrate to the surface, and so the surface structures were maintained.

These results can be modeled approximately using the solution to Fick's second law of diffusion for the case of diffusion between two semi-infinite solids with different initial solute concentrations. The present case assumes that the near-surface layer with an initial solute concentration of 0 wt% is coupled with the bulk substrate at the initial bulk concentration for each element (i.e., 5.6 wt% Mn, 1.9 wt% Al, and 1.1 wt% Si). The solution is shown in Equation 4.1:

$$C(y,t) = C_1 + \frac{C_2 - C_1}{2}\left[1 + erf\left(\frac{y}{2\sqrt{Dt}}\right)\right] \qquad (4.1)$$

where $C(y,t)$ is the concentration of solute at position y (where $y=0$ represents the interface between the two solids) at time t (in s); C_1 is the bulk concentration of solute in wt%; C_2 is the concentration of solute in wt% in the near-surface pre-oxidized layer; and D is the diffusivity of solute in the matrix at 710°C (calculated from the data presented in Table 4.6). The initial conditions for the system are shown in Equations 4.2 and 4.3, where the extreme case of 0 wt% solute in the near-surface layer represents the most severe approach to modelling solute diffusion.

$$C(y,t) = C_1 = \text{ bulk concentration in wt% for } y < 0 \qquad (4.2)$$

$$C(y,t) = C_2 = 0 \text{ wt% for } y \geq 0 \qquad (4.3)$$

Table 4.6: Diffusion data and values for the Al, Mn, and Si in ferrite and austenite used to calculate their approximate diffusion distances after 120 s at 710°C.

Phase	Element/ Compound	$D_i^{\cdot}$ (cm²/s)	Q_i (10^3 J/mol)	Reference
Ferrite	Mn	0.756	224.35	[72]
	Al	5.15	245.8	[73]
	Si	0.927	219.786	[74]
Austenite	Mn	0.178	264.2	[72]
	Al	5.9	241.58	[75]
	Si	0.21	242	[76]

The resulting concentration gradients for Mn, Al, and Si diffusion are presented in Figure 4.21 and show that the diffusion distances after 120 s at 710°C are insufficient to enrich the surface layer with solute, even when modelling the most extreme solute gradient. In the most pessimistic scenario (i.e., in ferrite), only 500 nm is re-enriched during intercritical annealing, but the internal oxide network (and therefore the solute-depleted matrix) is several microns deep (as shown in Figure 4.7) and the EELS maps and spectra in Region 4 of Figure 4.15 and Figure 4.16 show solute depletion to approximately 3 μm in depth. Therefore, no significant amount of Al, Si, or Mn would be expected to diffuse to the surface during intercritical annealing to oxidize and modify the surface structures from the antecedent MnAl$_2$O$_4$ nodules found after flash pickling. This corroborates the findings in Figure 4.4, Figure 4.6, Figure 4.9, and Figure 4.14 showing that the external oxide structures did not evolve during the IA treatment.
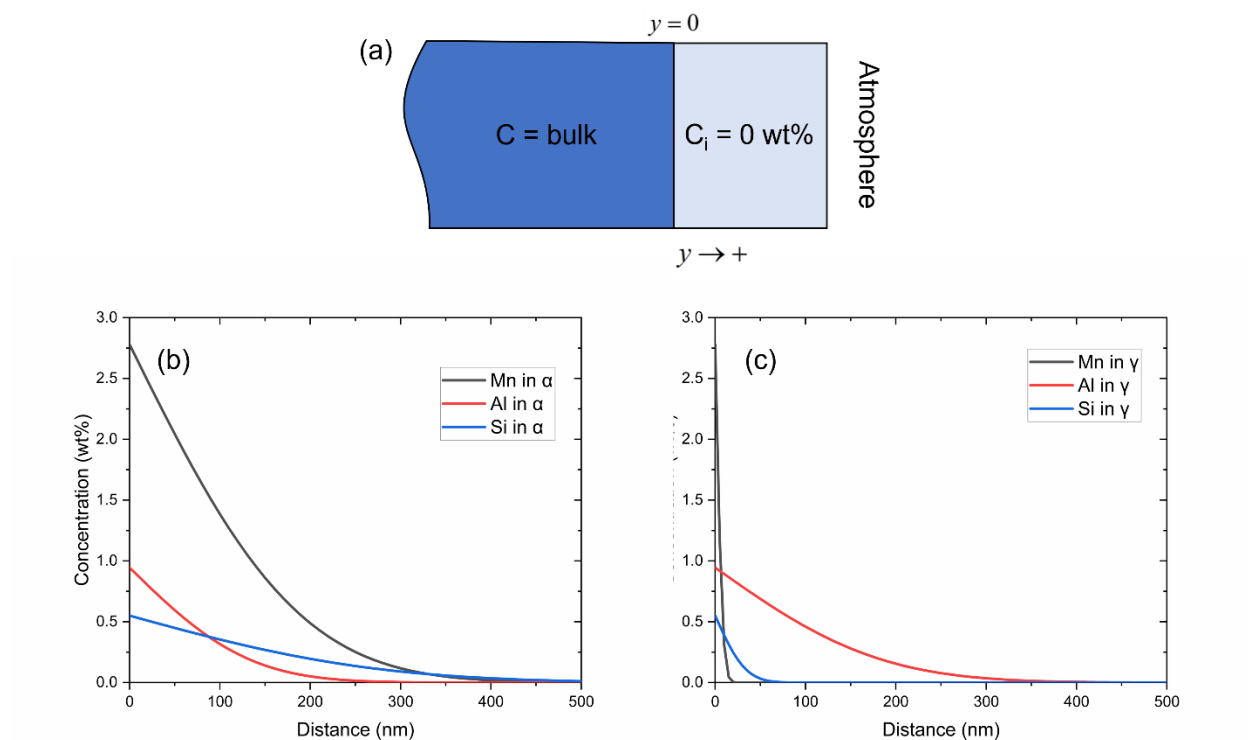
Figure 4.21: (a) Schematic of the diffusion couple proposed to model the diffusion of the solute from the substrate bulk to the pre-oxidized near-surface layer; calculated concentrations of Mn, Al, and Si as a function of distance from the interface after 120 s at 710°C for solutes diffusing in (b) ferrite and (c) austenite.

The internal oxide network that formed during the MF annealing step also did not evolve significantly during the intercritical annealing process. The MF and corresponding IA samples had similar internal oxide depths (as shown in Figure 4.7) and structures (comparing Figure 4.15 (MF –10°C dp) and Figure 4.19 (IA –10°C/–10°C dp)). The core-shell oxide structures formed during MF annealing comprised an Al_2O_3 or $MnAl_2O_4$ core surrounded with a Mn_2SiO_4 shell. Intercritical annealing may have allowed for occasional MnO nodule precipitation on the shell (Figure 4.19) and MnO reaction with core Al_2O_3 to form additional $MnAl_2O_4$. The deepest part of the oxide network in both MF and IA samples comprised Al_2O_3 and SiO_2 (such as the oxide shown in Figure 4.17), suggesting that these insoluble and thermodynamically stable oxide species formed initially

and provided a scaffold for MnO nucleation and complex oxidation. A summative schematic of

the oxide and surface structure evolution is shown in Figure 4.22.
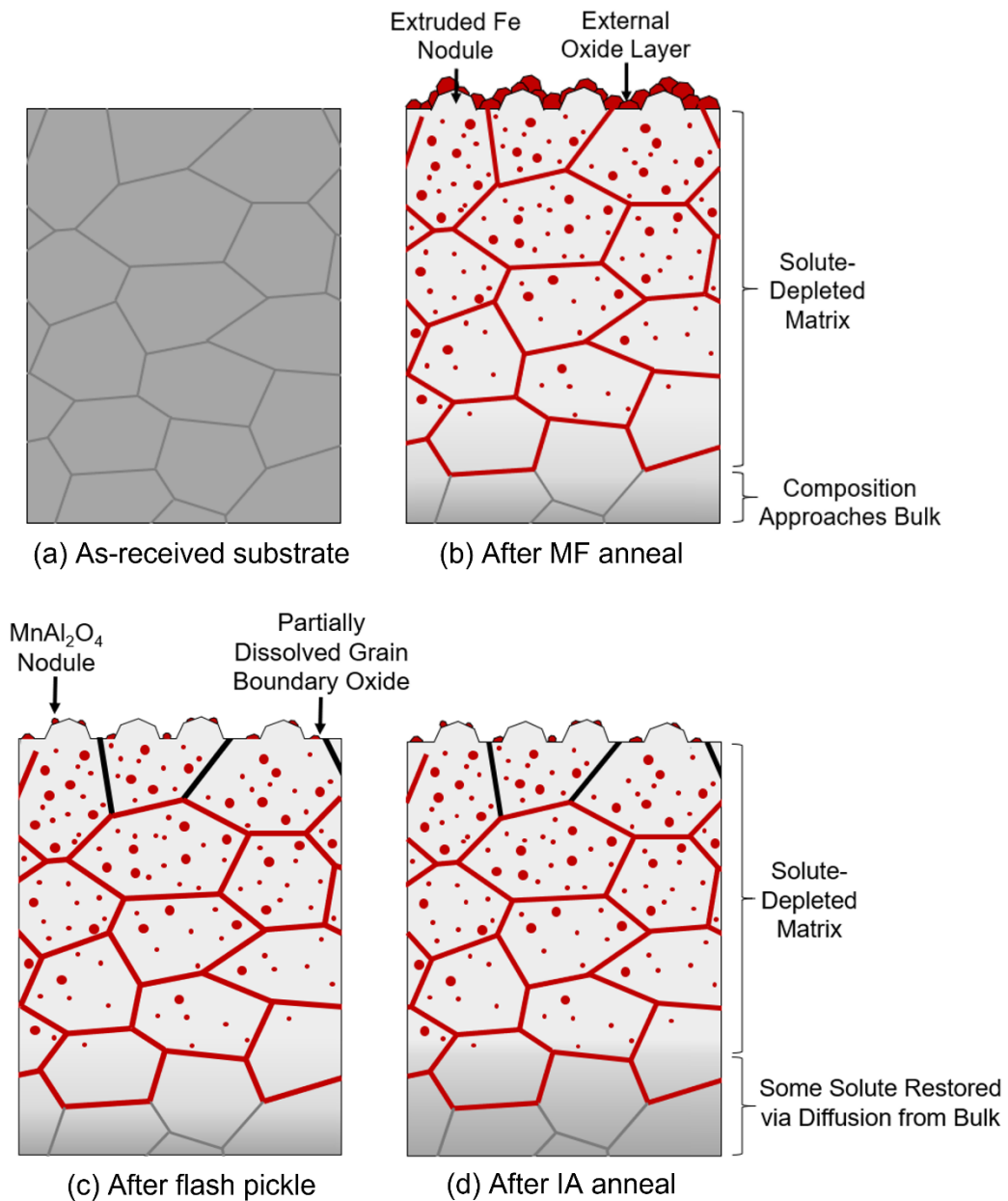
Figure 4.22: Summative schematic of the evolution of the surface and subsurface structures after each processing step.

4.6   Conclusions

The selective oxidation of the 0.15C-5.6Mn-1.9Al-1.1Si (wt%) prototype steel during two-stage annealing with intermediate flash pickling was documented using SEM+FIB, XPS, and TEM-EELS techniques.

The first annealing step of 890°C for 600s (designed to produce a martensitic-ferritic microstructure) resulted in the formation of a thick, compact external oxide layer, irrespective of dew point. Fe nodule extrusion occurred due to the development of an extensive internal oxide network. XPS analyses confirmed that MnO, Mn_2SiO_4, and $MnAl_2O_4$ /Al_2O_3 were the major oxide species present at the surface. TEM-EELS elemental maps and spectral analyses confirmed that compact nodules of MnO formed on top of co-precipitated nodules of $MnSiO_3$/Mn_2SiO_4 and $MnAl_2O_4$. Analysis of FIB-prepared trench cuts showed that the depth of internal oxidation increased with increasing dew point.

The intermediate flash pickling treatment effectively dissolved the external MnO, $MnSiO_3$, and Mn_2SiO_4. In addition, the flash pickling solution selectively dissolved some near-surface internal oxide structures. TEM-EELS analysis confirmed that $MnAl_2O_4$ was the only major external oxide species present after flash pickling due to its lack of solubility in hydrochloric acid solutions.

No significant changes to external oxide thickness, surface density, or chemical speciation were observed after intercritical annealing. During the MF treatment, the near-surface matrix was depleted in solute due to the oxidation of Mn, Si, and Al. The depletion zone was approximately 3 µm deep for Mn and approximately 8 µm deep for Si and Al. As such, the subsequent IA time and temperature were insufficient for to allow for adequate diffusion of these species from the bulk matrix to the surface to result in further external oxidation.

The selectively oxidized surfaces documented in this investigation show promise for future galvanizing trials due to the wide spacing of nano-scaled oxide nodules, presence of extruded Fe nodules, and the selective dissolution of internal oxides that could allow for liquid bath metal infiltration into the substrate.

4.7   Acknowledgements

4.8   References

[1]   D.K. Matlock, J.G. Speer, Design Considerations for the Next Generation of Advanced High Strength Steel Sheets, in: H.C. Lee (Ed.), Proc. 3rd Int. Conf. Struct. Steels, Korean Institute of Metals and Materials, Seoul, Korea, 2006: pp. 774–781.

[2]   D.K. Matlock, J.G. Speer, Third Generation of AHSS: Microstructure Design Concepts, Springer, Jamshedpur, India, 2009. doi:10.1007/978-1-84882-454-6_11.

[3]   E. De Moor, P.J. Gibbs, J.G. Speer, D.K. Matlock, Strategies for Third-Generation Advanced High Strength Steel Development, AIST Trans. 7 (2010) 133–144.

[4]   D.K. Matlock, J.G. Speer, E. De Moor, P.J. Gibbs, Recent Developments in Advanced High Strength Sheet Steels for Automotive Applications: An Overview, JESTECH. 15 (2012) 1–12.

[5]   K.M.H. Bhadhon, J.R. McDermid, F.E. Goodwin, Effect of Galvanizing Heat Treatment on the Microstructure and Mechanical Properties of a 6Mn-1.5Si Third Generation Advanced High Strength Steel, in: Proc. 10th Conf. Zinc Zinc Alloy Coat. Steel Sheet, Galvatech 2015, Toronto, 2015: pp. 936–943.

[6]   K.M.H. Bhadhon, J.R. McDermid, X. Wang, E.A. McNally, F.E. Goodwin, Fine-Scale Microstructure Characterization And Mechanical Properties Of CGL-Compatible Heat Treated Medium-Mn TRIP Steel, in: Proc. 11th Conf. Zinc Zinc Alloy Coat. Steel Sheet, Galvatech 2017, ISIJ International, Tokyo, 2017: pp. 493–500.

[7]   D.M. Pallisco, J.R. McDermid, E.A. McNally, F.E. Goodwin, Effect of Starting Microstructure and Intercritical Annealing Parameters on the Mechanical Property Development of a Medium-Mn Third-Generation Advanced High Strength Steel, in: Proc. 11th Conf. Zinc Zinc Alloy Coat. Steel Sheet, Galvatech 2017, Tokyo, 2017: pp. 782–789.

[8]   D.M. Pallisco, K.M.H. Bhadhon, V. Patel, M. Pourmajidian, F.E. Goodwin, J.R. McDermid, 9-11: Galvanizing of Medium-Manganese Third Generation Advanced High Strength Steels, in: Proc. 4th Int'l Conf. Med. High-Manganese Steels, 2019: pp. 375–378.

[9]   V. Patel, Microstructure and Mechanical Properties of Medium Mn Steel, McMaster University, 2019.

[10]   D.M. Pallisco, J.R. McDermid, Mechanical property development of a 0.15C–6Mn–2Al–1Si third-generation advanced high strength steel using continuous galvanizing heat treatments, Mater. Sci. Eng. A. 778 (2020) 139111. doi:10.1016/j.msea.2020.139111.

[11]   J. Mahieu, S. Claessens, B.C. De Cooman, F.E. Goodwin, Surface and Sub-surface Characterization of Si-, Al- and P-alloyed TRIP-aided Steel, in: M.A. Baker (Ed.), Galvatech 2004 Proc., Association for Iron and Steel Technology, Chicago, IL, 2004: pp. 529–538.

[12]   E.M. Bellhouse, J.R. McDermid, Selective Oxidation and Reactive Wetting during Galvanizing of a CMnAl TRIP-Assisted Steel, Metall. Mater. Trans. A. 42A (2011) 2753–2768. doi:10.1007/s11661-010-0192-8.

[13]   E.M. Bellhouse, J.R. McDermid, Selective Oxidation and Reactive Wetting During Hot-Dip Galvanizing of a 1.0 Pct Al-0.5 Pct Si TRIP-Assisted Steel, Metall. Mater. Trans. A. 43 (2012) 2426–2441. doi:10.1007/s11661-010-0192-8.

[14]   R. Sagl, A. Jarosik, D. Stifter, G. Angeli, The role of surface oxides on annealed high-strength steels in hot-dip galvanizing, Corros. Sci. 70 (2013) 268–275. doi:10.1016/j.corsci.2013.01.039.

[15]   R. Sagl, A. Jarosik, G. Angeli, T. Haunschmied, G. Hesser, D. Stifter, Tailoring of oxide morphology and crystallinity on advanced high-strength steel surfaces prior hot-dip galvanizing, Acta Mater. 72 (2014) 192–199. doi:10.1016/j.actamat.2014.03.037.

[16] M. Pourmajidian, J.R. McDermid, Selective Oxidation of a 0.1C-6Mn-2Si Third Generation Advanced High-Strength Steel During Dew-Point Controlled Annealing, Metall. Mater. Trans. A. 49 (2018) 1795–1808. doi:10.1007/s11661-018-4513-7.

[17] G. Seyed Mousavi, J.R. McDermid, Selective Oxidation of a C-2Mn-1.3Si (wt pct) Advanced High-Strength Steel During Continuous Galvanizing Heat Treatments, Metall. Mater. Trans. A. 49 (2018) 5546–5560. doi:10.1007/s11661-018-4854-2.

[18] J. Mahieu, S. Claessens, B.C. De Cooman, Galvanizability of High-Strength Steels for Automotive Applications, Metall. Mater. Trans. A. 32 (2001) 2905–2908.

[19] P. Drillet, Z. Zermout, D. Bouleau, J. Mataigne, S. Claessens, Selective Oxidation of high Si, Mn and Al steel grade during Recrystallization Annealing, and steel/Zn reactivity, in: M.A. Baker (Ed.), Galvatech 2004 Proc., Association for Iron and Steel Technology, Chicago, IL, 2004: pp. 1123–1134.

[20] E.M. Bellhouse, J.R. McDermid, Selective Oxidation and Reactive Wetting of 1.0 Pct Si-0.5 Pct Al and 1.5 Pct Si TRIP-Assisted Steels, Metall. Mater. Trans. A. 41 (2010) 1539–1553. doi:10.1007/s11661-010-0192-8.

[21] S. Alibeigi, R. Kavitha, R.J. Meguerian, J.R. McDermid, Reactive wetting of high Mn steels during continuous hot-dip galvanizing, Acta Mater. 59 (2011) 3537–3549. doi:10.1016/j.actamat.2011.02.027.

[22] S. Prabhudev, S. Swaminathan, M. Rohwerder, Effect of oxides on the reaction kinetics during hot-dip galvanizing of high strength steels, Corros. Sci. 53 (2011) 2413–2418. doi:10.1016/j.corsci.2011.03.027.

[23] M. Norden, M. Blumenau, T. Wuttke, K.J. Peters, The change of steel surface chemistry regarding oxygen partial pressure and dew point, Appl. Surf. Sci. 271 (2013) 19–31. doi:10.1016/j.apsusc.2012.12.103.

[24] Y. Tobiyama, C. Kato, Effect of the Substrate Compositions on the Growth of Fe-Al Interfacial Layer Formed during Hot Dip Galvanizing, Tetsu-to-Hagané. 89 (2003) 38–45.

[25] R. Khondker, A.I.M. Mertens, J.R. McDermid, Effect of annealing atmosphere on the galvanizing behavior of a dual-phase steel, Mater. Sci. Eng. A. 463 (2007) 157–165. doi:10.1016/j.msea.2006.09.116.

[26] E.M. Bellhouse, J.R. McDermid, Analysis of the Fe–Zn interface of galvanized high Al–low Si TRIP steels, Mater. Sci. Eng. A. 491 (2008) 39–46. doi:10.1016/j.msea.2007.12.033.

[27] E.M. Bellhouse, J.R. McDermid, Effect of Continuous Galvanizing Heat Treatments on the Microstructure and Mechanical Properties of High Al-Low Si Transformation Induced Plasticity Steels, Metall. Mater. Trans. A. 41 (2010) 1460–1473. doi:10.1007/s11661-010-0185-7.

[28]   R. Kavitha, J.R. McDermid, On the in-situ aluminothermic reduction of manganese oxides in continuous galvanizing baths, Surf. Coat. Technol. 212 (2012) 152–158. doi:10.1016/j.surfcoat.2012.09.038.

[29]   L. Cho, J.S. Lee, M.S. Kim, Y.H. Kim, B.C. De Cooman, Influence of Gas Atmosphere Dew Point on the Selective Oxidation and the Reactive Wetting During Hot Dip Galvanizing of CMnSi TRIP Steel, Metall. Mater. Trans. A. 44A (2013) 362–371. doi:10.1007/s11661-012-1392-1.

[30]   L. Cho, M.S. Kim, Y.H. Kim, B.C. De Cooman, Influence of gas atmosphere dew point on the galvannealing of CMnSi TRIP steel, Metall. Mater. Trans. A. 44 (2013) 5081–5095. doi:10.1007/s11661-013-1867-8.

[31]   Y. Suzuki, T. Yamashita, Y. Sugimoto, S. Fujita, S. Yamaguchi, Thermodynamic Analysis of Selective Oxidation Behavior of Si and Mn-added Steel during Recrystallization Annealing, ISIJ Int. 49 (2009) 564–573.

[32]   O. Matsumura, Y. Sakuma, H. Takechi, Enhancement of Elongation by Retained Austenite in Intercritical Annealed 0.4C-1.5Si-0.8Mn Steel, Trans. ISIJ. 27 (1987) 570–579.

[33]   J. Maki, J. Mahieu, B.C. De Cooman, S. Claessens, Galvanisability of silicon free CMnAl TRIP steels, Mater. Sci. Technol. 19 (2003) 125–131. doi:10.1179/026708303225009300.

[34]   M. Pourmajidian, J.R. McDermid, Effect of Annealing Temperature on the Selective Oxidation and Reactive Wetting of a 0.1C-6Mn-2Si Advanced High Strength Steel During Continuous Galvanizing Heat Treatments, ISIJ Int. 58 (2018) 1635–1643. doi:10.2355/isijinternational.ISIJINT-2017-688.

[35]   L. Cho, M.S. Kim, Y.H. Kim, B.C. De Cooman, Influence of Minor Alloying Elements on Selective Oxidation and Reactive Wetting of CMnSi TRIP Steel during Hot Dip Galvanizing, Metall. Mater. Trans. A. 45 (2014) 4484–4498. doi:10.1007/s11661-014-2394-y.

[36]   L. Cho, E.J. Seo, G.S. Jung, D.W. Suh, B.C. De Cooman, Surface Selective Oxidation of Sn-Added CMnSi TRIP Steel, Metall. Mater. Trans. A. 47 (2016) 1705–1719. doi:10.1007/s11661-016-3331-z.

[37]   M. Pourmajidian, B. Langelier, J.R. McDermid, Effect of Process Atmosphere Dew Point and Tin Addition on Oxide Morphology and Growth for a Medium-Mn Third Generation Advanced Steel During Intercritical Annealing, Metall. Mater. Trans. A. 49 (2018) 5561–5573. doi:10.1007/s11661-018-4855-1.

[38]   G. Seyed Mousavi, B. Langelier, J.R. McDermid, Effect of Sn Addition, Process Atmosphere pO2, and Annealing Time on the Selective Oxidation of a C-2Mn-1.7Si (Wt Pct) Advanced High-Strength Steel During Continuous Galvanizing, Metall. Mater. Trans. A. 50 (2019) 2898–2911. doi:10.1007/s11661-019-05202-3.

[39] M. Pourmajidian, J.R. McDermid, On the reactive wetting of a medium-Mn advanced high-strength steel during continuous galvanizing, Surf. Coatings Technol. 357 (2019) 418–426. doi:10.1016/j.surfcoat.2018.10.028.

[40] J. Oh, L. Cho, M.S. Kim, K. Kang, B.C. De Cooman, The Effect of Bi on the Selective Oxide Formation on CMnSi TRIP Steel, Metall. Mater. Trans. A. 47 (2016) 5474–5486. doi:10.1007/s11661-016-3735-9.

[41] Y.F. Gong, H.S. Kim, B.C. De Cooman, Internal Oxidation during Intercritical Annealing of CMnSi TRIP Steel, ISIJ Int. 49 (2009) 557–563. doi:10.2355/isijinternational.49.557.

[42] L. Cho, G.S. Jung, B.C. De Cooman, On the transition of internal to external selective oxidation on CMnSi TRIP steel, Metall. Mater. Trans. A. 45 (2014) 5158–5172. doi:10.1007/s11661-014-2442-7.

[43] G. Seyed Mousavi, J.R. McDermid, Effect of dew point on the reactive wetting of a C-2Mn-1.3Si (wt%) advanced high strength steel during continuous galvanizing, Surf. Coatings Technol. 351 (2018) 11–20. doi:10.1016/j.surfcoat.2018.06.060.

[44] H. Luo, H. Dong, New ultrahigh-strength Mn-alloyed TRIP steels with improved formability manufactured by intercritical annealing, Mater. Sci. Eng. A. 626 (2015) 207–212.

[45] K.M.H. Bhadhon, Effect of Starting Microstructure and CGL Compatible Thermal Processing Cycle on the Mechanical Properties of a Medium-Mn Third Generation Advanced High Strength Steel, McMaster University, 2017.

[46] K. Steineder, D. Krizan, R. Schneider, C. Béal, C. Sommitsch, On the microstructural characteristics influencing the yielding behavior of ultra-fine grained medium-Mn steels, Acta Mater. 139 (2017) 39–50.

[47] A.E. Morris, FREED Thermodynamic Database v7.8.1, (2013).

[48] E.M. Bellhouse, A.I.M. Mertens, J.R. McDermid, Development of the surface structure of TRIP steels prior to hot-dip galvanizing, Mater. Sci. Eng. A. 463 (2007) 147–156.

[49] M. Oku, K. Hirokawa, X-ray photoelectron spectroscopy of Co3O4, Fe3O4, Mn3O4 and related compounds, J. Electron Spectros. Relat. Phenomena. 8 (1976) 475–481.

[50] S.L.T. Andersson, M.S. Scurrell, Infrared and ESCA Studies of a Heterogenized Rhodium Carbonylation Catalyst, J. Catal. 59 (1979) 340–356.

[51] B.R. Strohmeier, D.M. Hercules, Surface Spectroscopic Characterization of Mn/Al2O3 Catalysts, J. Phys. Chem. 88 (1984) 4922–4929.

[52]   J. Finster, Co-ordination-Characterization by Core Level Spectroscopy (XPWXAES), 12 (1988) 309–314.

[53]   J.F. Moulder, W.F. Stickle, P.E. Sobol, K.D. Bomben, Handbook of X-ray Photoelectron Spectroscopy, Physical Electronics, Inc., Eden Prairie, MN, 1995.

[54]   A.P. Grosvenor, E.M. Bellhouse, A. Korinek, M. Bugnet, J.R. McDermid, XPS and EELS characterization of Mn2SiO4, MnSiO3 and MnAl2O4, J. Appl. Surf. Sci. 379 (2016) 242–248. doi:10.1016/j.apsusc.2016.03.235.

[55]   J.H. Rask, B.A. Miner, P.R. Buseck, Determination of Manganese oxidation states in solides by electron energy-loss spectroscopy, Ultramicroscopy. 21 (1987) 321–326.

[56]   M. Sternitzke, G. Müller, EELS Study of Oxygen Diffusion in Aluminum Nitride, J. Am. Ceram. Soc. 77 (1994) 737–742. doi:10.1111/j.1151-2916.1994.tb05358.x.

[57]   K. Naoe, M. Nishiki, K. Sato, Microstructure and Electron Energy-Loss Spectroscopy Analysis of Interface Between Cu Substrate and Al2O3Film Formed by Aerosol Deposition Method, J. Therm. Spray Technol. 23 (2014) 1333–1338. doi:10.1007/s11666-014-0172-4.

[58]   C.F. Jones, R.S.C. Smart, P.S. Turner, Dissolution kinetics of manganese oxides. Effects of preparation conditions, pH and oxidation/reduction from solution, J. Chem. Soc. Faraday Trans. 86 (1990) 947–953. doi:10.1039/FT9908600947.

[59]   J.F. Banfield, G.G. Ferruzzi, W.H. Casey, H.R. Westrich, HRTEM study comparing naturally and experimentally weathered pyroxenoids, Geochemica Cosm. Acta. 59 (1995) 19–31.

[60]   W.H. Casey, M.F. Hochella, H.R. Westrich, The surface chemistry of manganiferous silicate minerals as inferred from experiments on tephroite (Mn2SiO4), Geochim. Cosmochim. Acta. 57 (1993) 785–793. doi:10.1016/0016-7037(93)90168-V.

[61]   C.R. Shastry, J.A. Rotole, T.W. Kaiser, Characterization of selective oxidation of alloying elements in an advanced high strength steel from theoretical and experimental viewpoints, 7th Int. Conf. Zinc Zinc Alloy Coat. Steel Sheet. (2007) Paper B-6-2, 403-408.

[62]   X.S. Li, S.-I. Baek, C.-S. Oh, S.-J. Kim, Y.-W. Kim, Oxide formation of transformation-induced plasticity-aided steel during dew-point control, Scr. Mater. 57 (2007) 113–116. doi:10.1016/j.scriptamat.2007.03.040.

[63]   Y.F. Gong, H.S. Kim, B.C. De Cooman, Formation of Surface and Subsurface Oxides during Ferritic, Intercritical and Austenitic Annealing of CMnSi TRIP Steel, ISIJ Int. 48 (2008) 1745–1751. doi:10.2355/isijinternational.48.1745.

[64]   Y.F. Gong, Y.R. Lee, H.S. Kim, B.C. De Cooman, CMnAl TRIP Steel Surface Modification during CGL Processing, in: Asia-Pacific Galvaniz. Conf. 2009 Proc., Jeju Island, South Korea, 2009: p. A-41.

[65]   G. Seyed Mousavi, J.R. McDermid, Effect of annealing parameters on selective oxidation and reactive wetting of CMnSi advanced high strength steel, in: Proc. 11th Conf. Zinc Zinc Alloy Coat. Steel Sheet, Galvatech 2017, 2017: pp. 485–492.

[66]   X.S. Li, S.-I. Baek, C.-S. Oh, S.-J. Kim, Y.-W. Kim, Dew-point controlled oxidation of Fe–C–Mn–Al–Si–Cu transformation-induced plasticity-aided steels, Scr. Mater. 59 (2008) 290–293. doi:10.1016/j.scriptamat.2008.03.025.

[67]   C.C. Ahn, O.L. Krivanek, Gatan Inc., Arizona State University, EELS atlas: A reference collection of electron energy loss spectra covering all stable elements, Gatan, Inc., Warrendale, PA, USA, 1983.

[68]   G. Kissinger, M.A. Schubert, D. Kot, T. Grabolla, Investigation of the Composition of the Si/SiO2 Interface in Oxide Precipitates and Oxide Layers on Silicon by STEM/EELS, ECS J. Solid State Sci. Technol. 6 (2017) N54–N63. doi:10.1149/2.0061707jss.

[69]   G. Eriksson, P. Wu, M. Blander, A.D. Pelton, Critical Evaluation and Optimization of the Thermodynamic Properties and Phase Diagrams of the MnO-SiO2 and CaO-SiO2 Systems, Can. Metall. Q. 13 (1994) 13–21. doi:https://doi.org/10.1179/cmq.1994.33.1.13.

[70]   Thermodata, Thermodata. Electronic data bank for thermodynamic quantities, available online at the address http://thermodata.online.fr (2005)., (2005). http://thermodata.online.fr.

[71]   D. Huin, P. Flauder, J.-B. Leblond, Numerical Simulation of Internal Oxidation of Steels during Annealing Treatments, Oxid. Met. 64 (2005) 131–167. doi:10.1007/s11085-005-5718-x.

[72]   H. Oikawa, Technology Reports, 1983.

[73]   J. Takada, S. Yamamoto, S. Kikuchi, M. Adachi, Internal oxidation of Fe-Al alloys in the a-phase region, Oxid. Met. 25 (1986) 93–105.

[74]   R.J. Borg, D.Y.F. Lai, Diffusion in a-Fe-Si Alloys, J. Appl. Phys. 41 (1970) 5193–5200.

[75]   Diffusion Information Center, Diffusion Data: A Continuous Compilation of New Reference Data on Diffusion Processes in Inorganic Solids and Their Melts, 1969.

[76]   J. Takada, K. Kashiwagi, M. Adachi, Internal oxidation of Fe-Si alloys in γ-phase region, J. Mater. Sci. 19 (1984) 3451–3458. doi:10.1007/BF00549838.

.

5 Reactive wetting of a 0.15C-6Mn-2Al-1Si third-generation advanced high strength steel during continuous galvanizing heat treatments

Daniella M. Pallisco, Joseph R. McDermid

Department of Materials Science and Engineering, McMaster University, 1280 Main Street West, Hamilton, Ontario, Canada, L8S 4L8

5.1 Abstract

This work presents the effects of process atmosphere pO_2 on the reactive wetting during galvanizing of a prototype 0.15C-5.6Mn-1.9Al-1.1Si (wt%) third-generation advanced high strength steel. The two-stage thermal processing route comprised an austenitization anneal followed by flash pickling and an intercritical anneal, where all annealing treatments were conducted in a N_2-5%H_2 process atmosphere with a controlled dew point. The substrate panels were austenitized at a dew point of –10°C, intercritically annealed at a dew point of –30°C, –10°C, or +5°C, and then galvanized using a conventional 0.2 wt% Al (dissolved) bath. The pre-immersion surfaces comprised a near-pure Fe layer with dispersed nano-scaled oxide nodules. The primary reactive wetting mechanism was the direct wetting of the surface Fe, while oxide wetting, oxide cracking and lift-off, and oxide bridging by the liquid metal bath were secondary reactive wetting mechanisms. Zn ingress into the substrate via pores in the oxide network from selective dissolution during flash pickling was also noted. A fully-developed $Fe_2Al_{5-x}Zn_x$ interfacial layer was observed for all conditions. The resultant coatings were of excellent quality and showed outstanding adherence after three-point bend testing.

5.2 Introduction

There have been significant research efforts dedicated to the development of third-generation advanced high-strength steels (3G AHSS) for automotive applications due to their

superior mechanical properties relative to the currently employed first-generation AHSS and low alloying costs relative to the second-generation AHSS. The 3G AHSS are promising candidates for structural components and could facilitate passenger safety improvements while reducing the mass of the vehicle and improving fuel economy or extending the range of the next generation of electric vehicles [1–7].

Among the alloying and processing strategies being investigated for 3G AHSS, there has been work devoted to medium-Mn steel grades such that their processing routes are compatible with existing industrial continuous galvanizing line (CGL) capabilities [8–14]. CGL processing is the most cost-effective way to provide the required robust corrosion protection for automotive steels, and it is of paramount importance that the selective oxidation and reactive wetting phenomena of medium-Mn steels are well-studied and documented in order to support industrial adoption of these steels.

It is well established that alloying elements such as Mn, Si, Al, and Cr in steels selectively oxidize during annealing in typical CGL furnace process atmospheres [15–29]. The resulting oxides at the substrate surface can prevent adequate dissolution of substrate Fe into the molten Zn(Al,Fe) bath, which could, in turn, preclude the formation of the $Fe_2Al_{5-x}Zn_x$ interfacial layer at the substrate/coating interface that is associated with high-quality, adherent, and formable galvanized coatings [15,16]. However, previous work on 1G AHSS dual-phase (DP) and transformation-induced plasticity (TRIP) steels has shown that the external oxidation of the aforementioned alloying elements does not necessarily prevent successful reactive wetting. Particular attention has been given to cases where MnO nodules were the primary external oxide species. Khondker et al. [30] proposed the mechanism of aluminothermic reduction of surface MnO to explain the fully-developed $Fe_2Al_{5-x}Zn_x$ interfacial layer that formed on their 2 wt% Mn

DP steel after typical immersion times in a 0.20 wt% Al (dissolved) galvanizing bath. This mechanism was later verified by Kavitha and McDermid [31] in their work on a 5.1 wt% Mn substrate. Alibeigi et al. [32] galvanized steels of up to 5 wt% Mn and showed that the reactive wetting kinetics were inversely proportional to the thickness of the surface MnO layer, which was itself a function of process atmosphere oxygen partial pressure (pO_2). Other significant reactive wetting mechanisms that have contributed to the successful galvanizing of 1G AHSS include spalling and cracking of external oxides due to differences in thermal expansion coefficients [18,33] and oxide flaking and lift-off due to bath metal infiltration between the oxide and substrate [18,27]

There has been limited research on the reactive wetting of medium-Mn substrates thus far. Pourmajidian and McDermid [34] successfully galvanized a model 0.1C-6Mn-2Si (wt%) steel and showed that aluminothermic reduction of MnO and surface oxide lift-off from liquid bath metal infiltration facilitate the successful galvanizing of their model medium-Mn substrates, provided that the external oxides were sufficiently thin and dispersed. The desired oxide morphology was achieved by using higher process atmosphere pO_2 to promote internal oxidation. The same authors also employed a surface active alloying element concept from electrical steels [35–38], which was later successfully employed on low alloy Si/Mn TRIP-assisted steels [39–42], to reduce selective oxidation kinetics and facilitate reactive wetting. To this end, Pourmajidian et al. [21,34] showed that a 0.05 wt% addition of Sn to their reference 6wt% Mn substrate retarded oxidation kinetics, and the resulting surfaces that were more easily reactively wetted due to the smaller and more discrete oxide nodule morphology. However, more complex alloys and processing cycles are typically required to achieve 3G AHSS mechanical property envelopes, and the effects of minor

Sn additions on end-user properties (such as bendability, stretch flangeability and hole expansion) are unknown.

However, there is scarce literature concerning the reactive wetting of medium-Mn 3G AHSSs that have been processed through a two-stage annealing cycle, often employed to improve mechanical properties relative to a one-stage intercritical annealing treatment [9–14,43–45]. Moreover, selective oxidation studies conducted on the 0.15C-5.6Mn-1.9Al-1.1Si (wt%) prototype alloy to be used in this study have shown that the most abundant pre-immersion external oxide species is $MnAl_2O_4$ [46] rather than MnO such that the resulting effects on reactive wetting are unclear. To this end, this goal of this work was to determine the effects of process atmosphere pO_2 in a two-step annealing cycle on the reactive wetting of a prototype 0.15C-5.6Mn-1.9Al-1.1Si (wt%) medium-Mn 3G AHSS. It is noteworthy that the present authors have shown that the experimental substrate to be used in this study achieved target 3G AHSS properties (YS = 844 MPa, UTS = 1209 MPa, TE = 23%, UTS × TE = 27,800 MPa% [14]) using the two stage, CGL-compatible thermal treatment to be employed in this work.

5.3   Experimental Procedure

The experimental substrate was fabricated at United States Steel Research (Munhall) via vacuum melting, slab casting, hot rolling, coiling and coil box cooling, edge trimming, surface grinding, and cold rolling to a final sheet thickness of 1.2 mm. The chemical composition of the substrate, as measured by combustion analysis (C and S, LECO C/S 744) and inductively-coupled optical emission spectroscopy (all other elements, Varian Vista Pro ICP-OES), is shown in Table 5.1.

Table 5.1: Chemical composition of the experimental substrate (in wt%)

C	Mn	Al	Si	Mo	Ti	Fe
0.15	5.56	1.89	1.10	0.08	0.01	Balance

Coupons measuring 20×50 mm^2 were prepared from the as-received cold-rolled steel sheets in order to perform selective oxidation studies without galvanizing. Coupons were ground with 4,000 grit SiC papers to remove rolling marks prior to annealing in order to facilitate subsequent analyses. Full-sized 120×200 mm^2 panels were also prepared from the as-received cold-rolled steel sheets for galvanizing trials. The coupons and panels were degreased in 2 wt% NaOH solution heated to 80°C, rinsed in deionized water, rinsed in ethanol and dried with warm air. The panels were wiped with acetone immediately prior to annealing. All experiments were performed in the McMaster Galvanizing Simulator (MGS, Iwatani-Surtec), details of which are documented elsewhere [24,47]. The two-stage thermal processing treatment shown in Figure 5.1 was that used to obtain the 3G AHSS mechanical properties documented in [14]. A flash pickling treatment was performed after the first annealing stage in order to remove the existent surface oxides prior to the intercritical annealing and galvanizing steps. This involved lightly agitating the samples for 60 s in a 30°C solution of 645 mL deionized water + 596 mL concentrated hydrochloric acid + 2.5 g hexamethylenetetramine (which acts as an inhibiting agent to prevent pitting of the substrate), lightly agitating in room temperature deionized water for 20 s before a final rinse with ethanol and drying with a warm air stream.

The MGS process atmosphere comprised a mixture of 95 vol% N$_2$ + 5 vol% H$_2$ with trace amounts of water vapour to achieve the desired process atmosphere oxygen partial pressure (pO$_2$). Details of the experimental process atmosphere dew points and pO$_2$ values (as calculated from the FREED thermodynamic database [48]) are found in Table 5.2. After removal from the MGS, the selective oxidation coupons were stored in anhydrous isopropanol and kept in a desiccator. Galvanizing trials on the larger 120×200 mm^2 panels were performed in duplicate according to the same thermal cycle shown in Figure 5.1. During galvanizing experiments, the panels were

immersed in a 460°C Fe-saturated 0.2 wt% Al (dissolved) [49] bath for 4 s. The dipping direction was aligned with the rolling direction of the substrate. After removal from the simulator, the galvanized panels were individually wrapped in paper towels to prevent scratches and stored in a desiccator. After the full panels were imaged, a 90×90 mm^2 uniform coating area centered near the bottom of the panel [50] was excised from each one for subsequent analysis across multiple length scales. In this work, samples will be identified by the process atmosphere dew point (dp) used during intercritical annealing (i.e. –30/–10/+5°C dp).
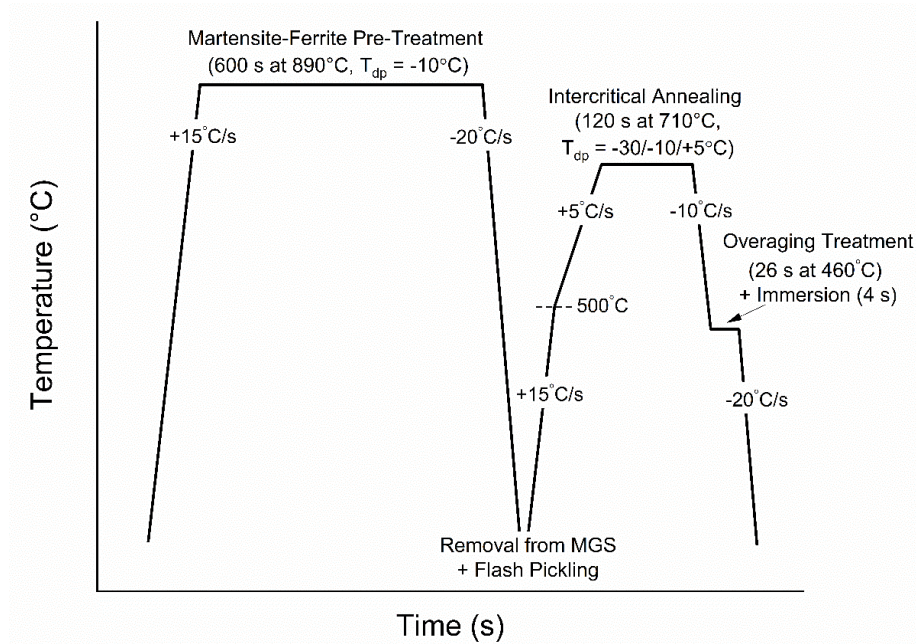
Figure 5.1: Schematic thermal processing route for the experimental steel.

Table 5.2: Experimental process atmospheres.

Annealing Stage +Temperature	Process Atmosphere Dew Point	pH$_2$O/pH$_2$	pO$_2$ (atm)
Martensite-Ferrite (MF) (890°C)	–10°C	5.62×10^{-2}	1.04×10^{-19}
Intercritical (IA) (710°C)	–30°C	9.98×10^{-3}	2.71×10^{-25}
	–10°C	5.62×10^{-2}	8.58×10^{-24}
	+5°C	1.71×10^{-1}	7.96×10^{-23}

The selective oxidation coupon pre-immersion surface structures were imaged using focussed ion beam (FIB) equipped scanning electron microscope (SEM, Zeiss Vision40 SEM+FIB) at an accelerating voltage of 5 keV using the in-lens secondary electron detector.

In the case of the galvanized panels, the presence of the desired $Fe_2Al_{5-x}Zn_x$ interfacial layer – indicative of reactive wetting between the substrate and the Zn(Al) galvanizing bath – was determined by stripping the zinc overlay using fuming HNO_3 and examination using a scanning electron microscope (SEM). It should be noted that this treatment will also dissolve any Fe-Zn interfacial intermetallics which may be present. Thus, a second set of samples was prepared by stripping the zinc overlay with a 10 vol% H_2SO_4 aqueous solution to expose any interfacial $Fe_2Al_{5-x}Zn_x$ and/or Fe-Zn intermetallic compounds. In all cases, a JEOL 7000F field-emission gun SEM operated in secondary electron imaging (SEI) mode at an accelerating voltage of 15 keV was employed for these examinations. The samples were coated in a thin film of carbon prior to SEM examination in order to minimize charging.

The interfacial layer products that remained after chemically stripping the zinc overlay using both of the above techniques were also characterized using X-ray diffraction (XRD). XRD data were collected using a D8 DISCOVER (Bruker AXS) diffractometer equipped with a Co source ($\lambda = 1.79026$ Å) and a Vantec 500 (MiKroGap TM technology) or Eiger2 R 500K (Bruker AXS) area detector operated in 2D mode. The resident DIFFRAC.EVA software (Bruker AXS) was used to analyze the diffraction pattern (2θ range of 10° to 64°), where peaks from the International Centre for Diffraction Data Powder Diffraction File PDF-4 database [51] were used to identify the phases present.

Coating adherence was assessed via an adaptation of the ASTM A653/A653M standard [52] that was modified for medium-Mn steels, as documented by Pourmajidian and McDermid

[34]. The test dies (punch radius of 4.76 mm) were installed on a 10 kN universal tensile machine (Instron 5566). Four 10 mm-wide test samples were excised from the uniformly coated area of one galvanized panel from each condition. Three of these samples were bent beyond the point of necking, whilst the coating adherence test on the remaining sample was stopped just before the onset of necking. After bending, all four samples were examined under a Keyence VH-ZST dual objective zoom lens light optical microscope to determine whether the coatings flaked, cracked, or delaminated. As part of the coating adhesion test, Scotch Tape (3M) was adhered to the outer radius of each bent sample, after which the tape was removed and examined under the light optical microscope at 50x magnification to check for coating flakes. The sample that did not exceed the necking limit was sectioned along the longitudinal midline. The cross-section was mounted in epoxy resin, polished using standard metallographic techniques, coated in a thin film of carbon and examined using a JEOL 7000F FEG-SEM. This was done in order to determine the extent to which the coating was damaged during the bending process.

Three ASTM E-8 [53] subsized tensile samples were prepared from the uniform coating region at the center of one galvanized panel from each condition, where the longitudinal axis of the tensile sample was aligned with the steel rolling direction. The samples were tested in uniaxial tension on a conventional 100 kN tensile frame (MTS) with a crosshead speed of 1 mm/minute. The coatings were examined for damage using a JEOL 6610LV SEM at an acceleration voltage of 10 keV.

TEM liftouts of the substrate-coating interface were prepared via FIB milling using the Zeiss NVision 40 SEM-FIB. A W cap was deposited on the sample surface prior to milling in order to mitigate milling damage. High-resolution scanning transmission electron microscopy (HR-STEM) was performed using a FEI Titan 80-300HB TEM operated at 300 keV or a Thermo

Scientific Talos 200X TEM operated at 200 keV. Electron energy loss spectroscopy (EELS) elemental maps were acquired during HR-STEM examination using a Gatan Quantum GIF (on the FEI Titan) or a CETA CMOS (on the Thermo Scientific Talos) detector. The resultant elemental maps were processed using Digital Micrograph v3.43 software.

5.4   Results

Figure 5.2 comprises SEM micrographs of the as-annealed surfaces of the coupons showing the pre-immersion surfaces that would enter the galvanizing bath. In all cases, discrete oxide particles (previously shown to be $MnAl_2O_4$ [46] were dispersed among nodules of extruded Fe from the substrate resulting from the volumetric expansion associated with internal oxidation [33,54–56]. The Fe nodule size increased with increasing process atmosphere pO_2, likely due to the larger volume of Fe displaced as a result of more extensive internal oxidation [46].
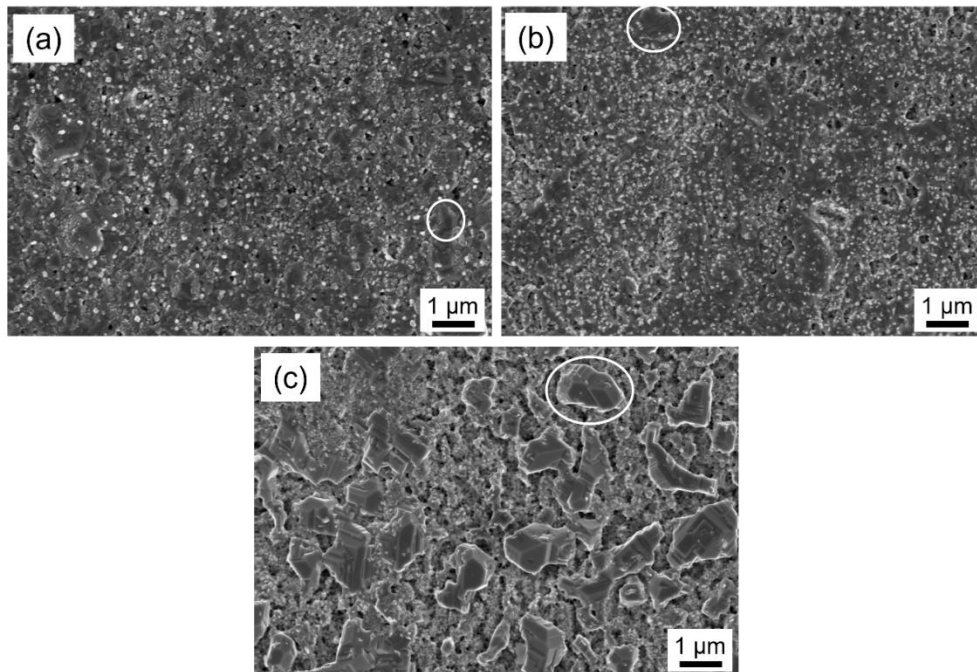
Figure 5.2: SEM images of the annealed surfaces showing discrete oxide particles dispersed among extruded Fe nodules (circled): (a) –30°C dp, (b) –10°C dp, and (c) +5°C dp.

The uniform coating area of panel galvanized under each of the process atmospheres (Table 5.2) is shown in Figure 5.3. Excellent coating quality was obtained for all process atmospheres, where no significant bare spots or other coating defects were observed.
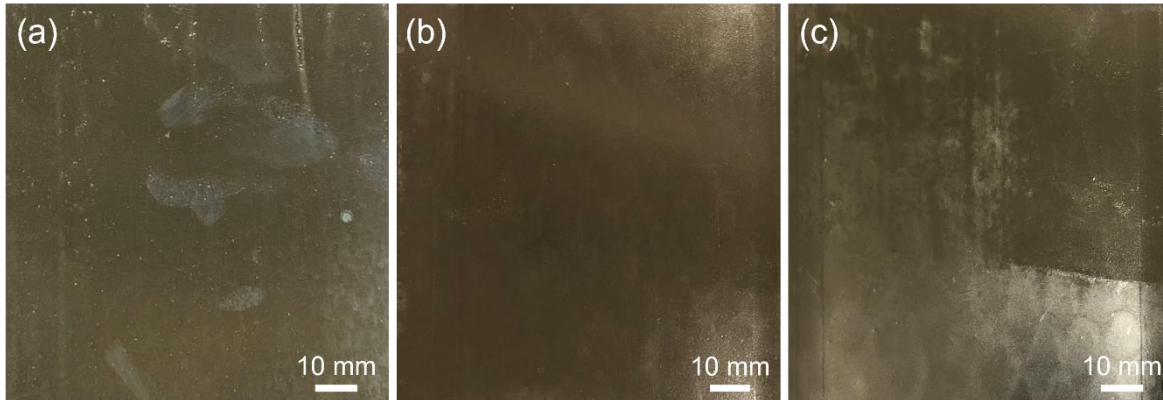
Figure 5.3: Uniform coating area of the galvanized panels showing high-quality coatings with no bare spots or other visible defects: (a) –30°C dp, (b) –10°C dp, and (c) +5°C dp.

Assessment of coating adherence was performed via the modified three-point bend test discussed above. It can be seen from the representative images in Figure 5.4 that the coatings were adherent and there was no evidence of cracking or flaking of the zinc layer, despite the substrate necking. No flakes were observed when Scotch Tape (3M) was applied to the outer bend surface and then removed. From these positive coating adherence results, it is strongly implied that full reactive wetting was achieved. It should also be noted that the enclosed bend angles of the coated samples were not statistically different than those of the uncoated samples (approximately 36°), as documented in Figure 5.5.
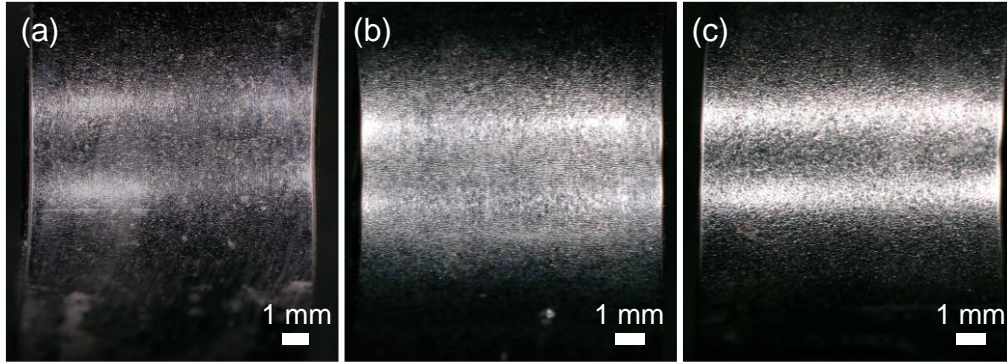
Figure 5.4: Coating adherence test samples showing no coating cracking or flaking despite necking of the substrate: (a) –30°C dp, (b) –10°C dp, and (c) +5°C dp.
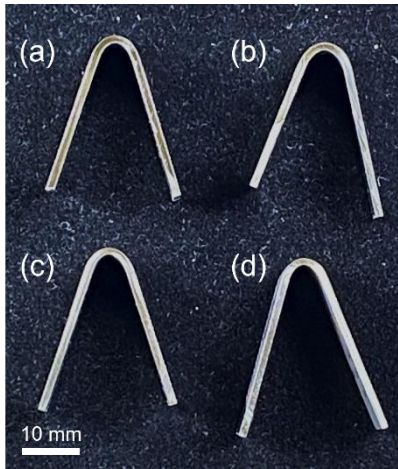
Figure 5.5: Representative coating adherence test samples showing similar enclosed bend angles for (a) annealed but uncoated steel, (b) –30°C dp, (c) –10°C dp, and (d) +5°C dp.

Cross-sections of the coating adherence test samples, where deformation was stopped just prior to the onset of substrate necking, were examined via SEM. In general, the coatings on the outside bend surface remained integral, despite cracking in the internal oxide network, as seen in Figure 5.6(a). There was evidence that these cracks were initiated at the substrate/coating interface and within the grain boundary oxide network itself, as shown in Figure 5.6(b). In some cases, the cracks initiating in the grain boundary oxide network propagated into the coating. Typically, the crack propagation did not extend completely through the coating, as shown in Figure 5.6(c). In rare instances, however, there were cracks observed in the coating that were coincident with cracks

from the grain boundary oxide network, as shown in Figure 5.6(d). The crack depth, frequency, and propagation into the coating were invariant of the intercritical annealing pO_2. As previously mentioned, there were no flakes of coating that adhered to the Scotch Tape, so the cracks observed in these images are not of significant concern.
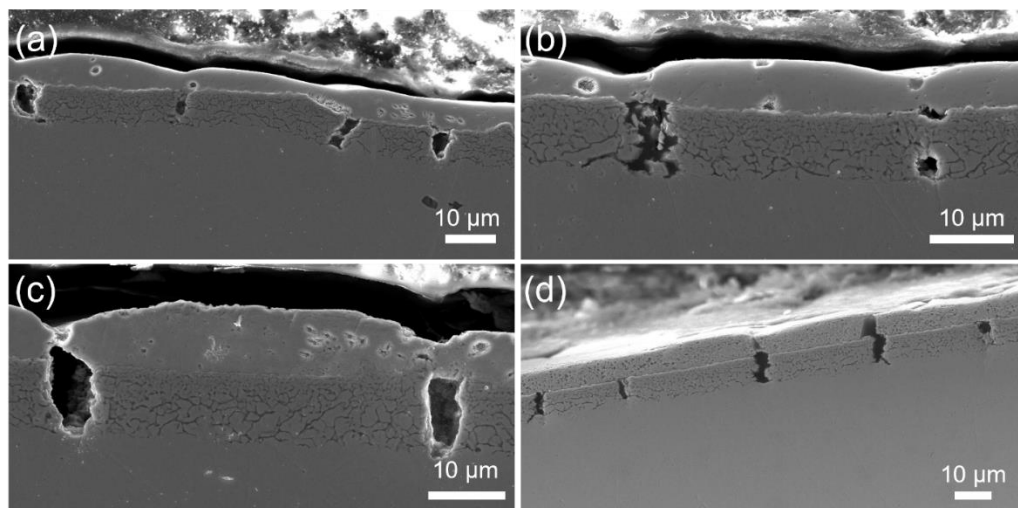
Figure 5.6: Representative secondary electron images of coating adherence test sample cross-sections: (a-c) –10°C dp, (d) –30°C dp.

The fractured tensile samples were examined via SEM, with images of the coated surface shown in Figure 5.7. These images were taken from a –10°C dp sample but are representative of all experimental conditions. Figure 5.7(a) is a macroscopic overview of the tensile sample neck and shows that the decohesion of the Zn-overlay grain boundaries was, predictably, most significant close to the fracture surface. The higher magnification image in Figure 5.7(b) confirms that there was some coating grain boundary decohesion, but there was no other damage (e.g. intragranular fracture or flaking of the coating) present, even in the most highly deformed regions. Figure 5.7(c) is a higher magnification image of the coating in the uniformly deformed region of the tensile sample, where it can be seen that the coating remained intact and there was no evidence of grain boundary decohesion or other damage.
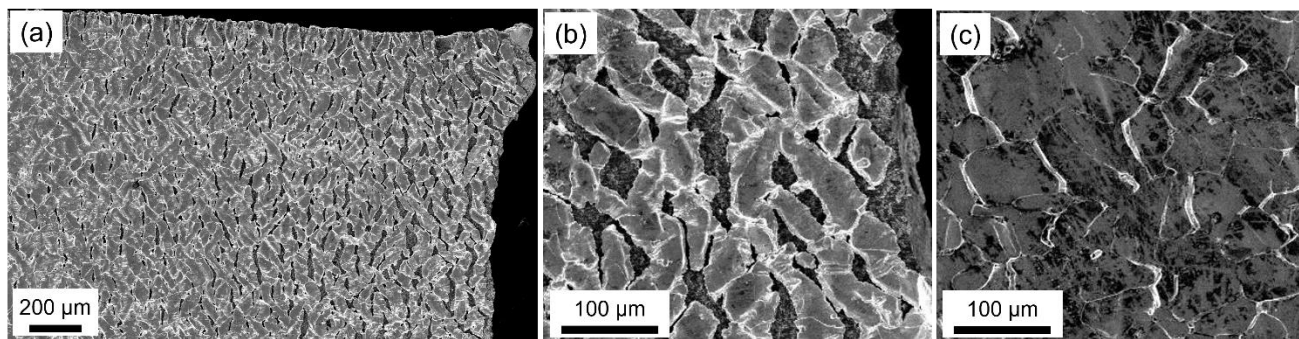
Figure 5.7: Representative images of the coated tensile samples, where (a) is an overview of the neck, (b) is a higher-magnification image of the coating in the sample neck, and (c) is a higher-magnification image of the coating in the uniformly deformed region.

The X-ray diffractograms collected from the –30°C dp samples stripped with fuming nitric acid and 10 vol% sulphuric acid are shown in Figure 5.8(a) and (b), respectively, and are representative of the XRD diffractograms collected for the other process atmosphere conditions. Peaks corresponding to $Fe_2Al_{5-x}Zn_x$ (powder diffraction file (PDF) PDF 00-047-1435) and ζ-$FeZn_{13}$ (PDF 00-034-1314) were identified, as well as peaks from several oxide species including Mn_2SiO_4 (PDF 00-035-0748), $MnAl_2O_4$ (PDF 01-076-6585), and MnO (PDF-077-2360) [51]. From this result, it can be concluded that the desired $Fe_2Al_{5-x}Zn_x$ intermetallic crystals were formed at the substrate/coating interface during galvanizing.
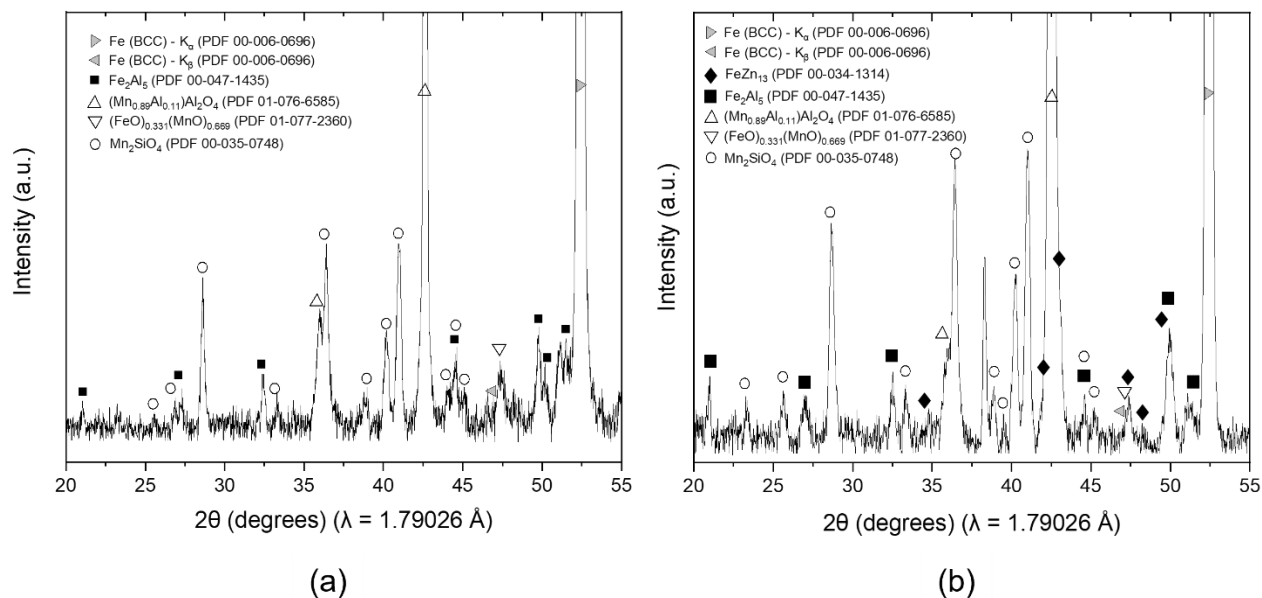
Figure 5.8: Diffraction patterns collected from the –30°C dp samples stripped with (a) fuming nitric acid, showing evidence of $Fe_2Al_{5-x}Zn_x$ formation; (b) 10 vol% H_2SO_4 in water, showing evidence of $Fe_2Al_{5-x}Zn_x$ and ζ-$FeZn_{13}$ formation. The patterns were indexed using the PDF-4 database [51].

The $Fe_2Al_{5-x}Zn_x$ interfacial layer revealed by chemical stripping of the coating using fuming nitric acid was imaged via SEM, as seen in Figure 5.9(a-c). A well-developed and continuous layer of $Fe_2Al_{5-x}Zn_x$ intermetallic crystals was observed, although there were some holes observed in the interfacial layer for the –30°C dp condition (Figure 5.9(a)). These images are consistent with the XRD data presented in Figure 5.8(a) and (b). In addition, chemical stripping of the coating via 10 vol% H_2SO_4 in water revealed an extensive population of Fe-Zn intermetallic crystals, primarily ζ-$FeZn_{13}$, as shown in Figure 5.9(d-f), which is consistent with the XRD data presented in Figure 5.8(b).
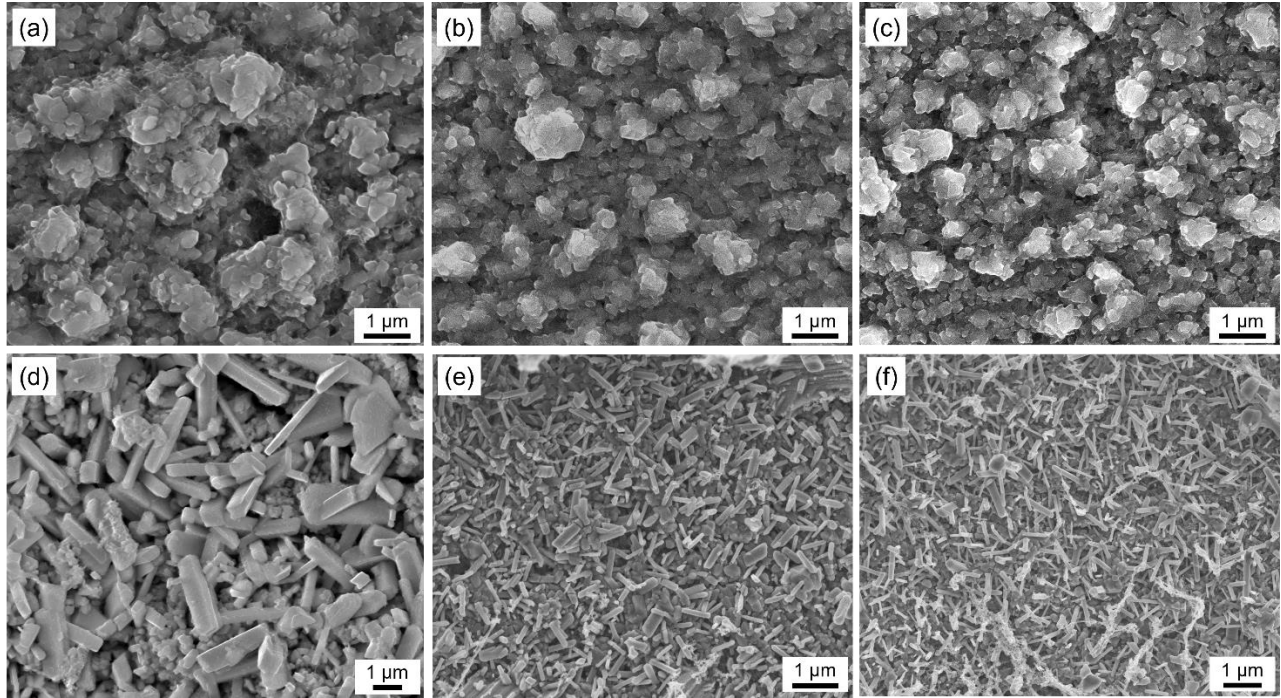
Figure 5.9: $Fe_2Al_{5-x}Zn_x$ interfacial layer for (a) –30°C dp, (b) –10°C dp, and (c) +5°C dp. Interfacial Fe-Zn intermetallic crystals for (d) –30°C dp, (e) –10°C dp, and (f) +5°C dp.

Samples for STEM-EELS analysis of the substrate/coating interface and internal oxide structures were prepared via FIB milling. The high angle annular dark field scanning transmission electron microscope (HAADF-STEM) micrograph along with the EELS elemental maps corresponding to Zn, Al, Fe, Mn, Si, and O for the –30°C dp sample are shown in Figure 5.10. It should be noted that the holes in the sample were an artifact of the FIB milling process. An almost continuous interfacial layer of $Fe_2Al_{5-x}Zn_x$ was observed, with one gap located in the lower interfacial layer (location B) where a Mn-Si rich oxide film was present. Evidence of several reactive wetting mechanisms can be seen in the composite elemental map, namely direct reactive wetting of the substrate, wetting of oxides (direct contact between the $Fe_2Al_{5-x}Zn_x$ and oxide nodules, location C in Figure 5.10), oxide lift-off (location A in Figure 5.10), and bath metal ingress (location D in Figure 5.10). EELS spectra from the locations A-D in the composite elemental map in Figure 5.10 are shown in Figure 5.11, where the oxide film was identified as

163

MnSiO$_4$ and the lifted-off oxide, wetted oxide, and internal oxide infiltrated by liquid bath metal were determined to be MnAl$_2$O$_4$ [57].
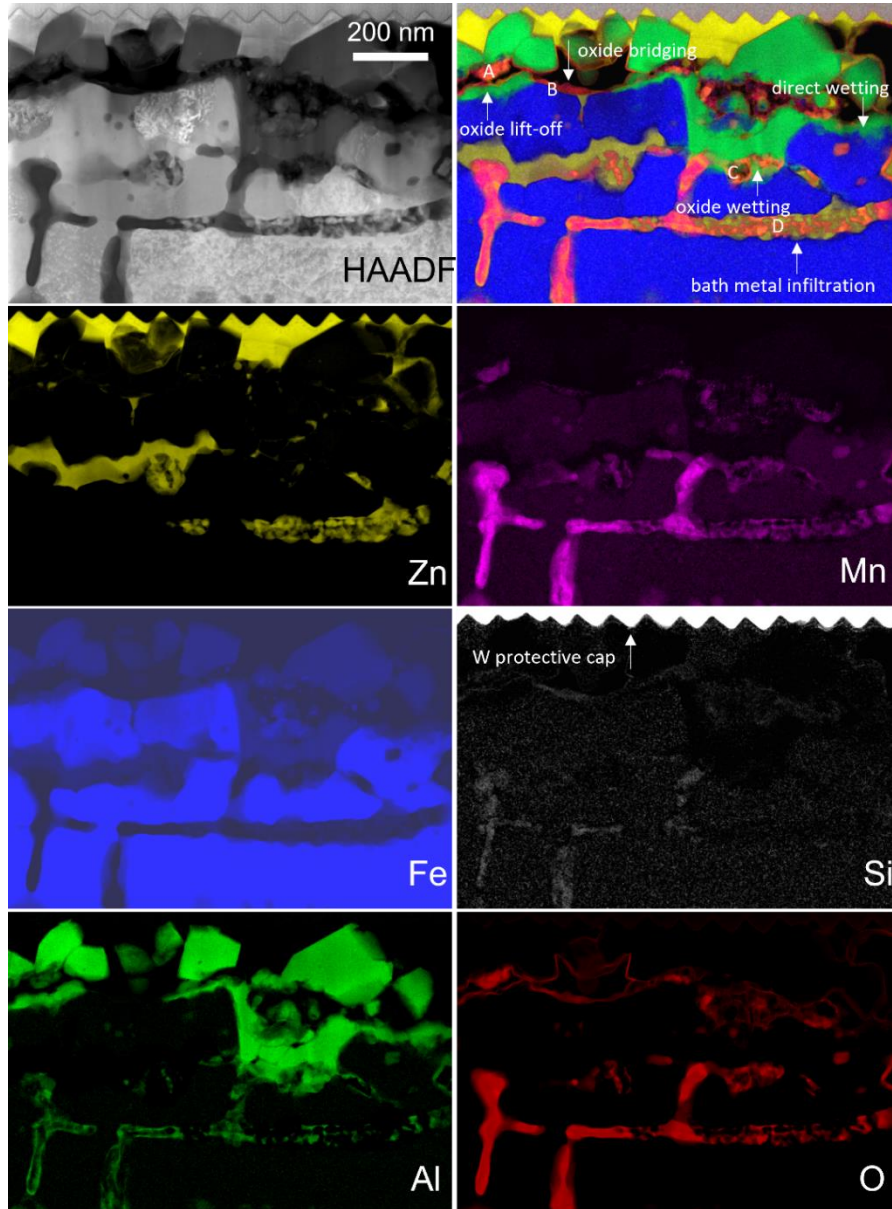
Figure 5.10: HAADF-STEM image along with the EELS elemental maps of the substrate/coating interface of the –30°C dp sample. The composite map shows evidence of reactive wetting mechanisms: direct substrate wetting, oxide bridging, oxide wetting, oxide lift-off; and bath metal ingress. EELS spectra from the regions labelled A-D are shown in Figure 5.11.
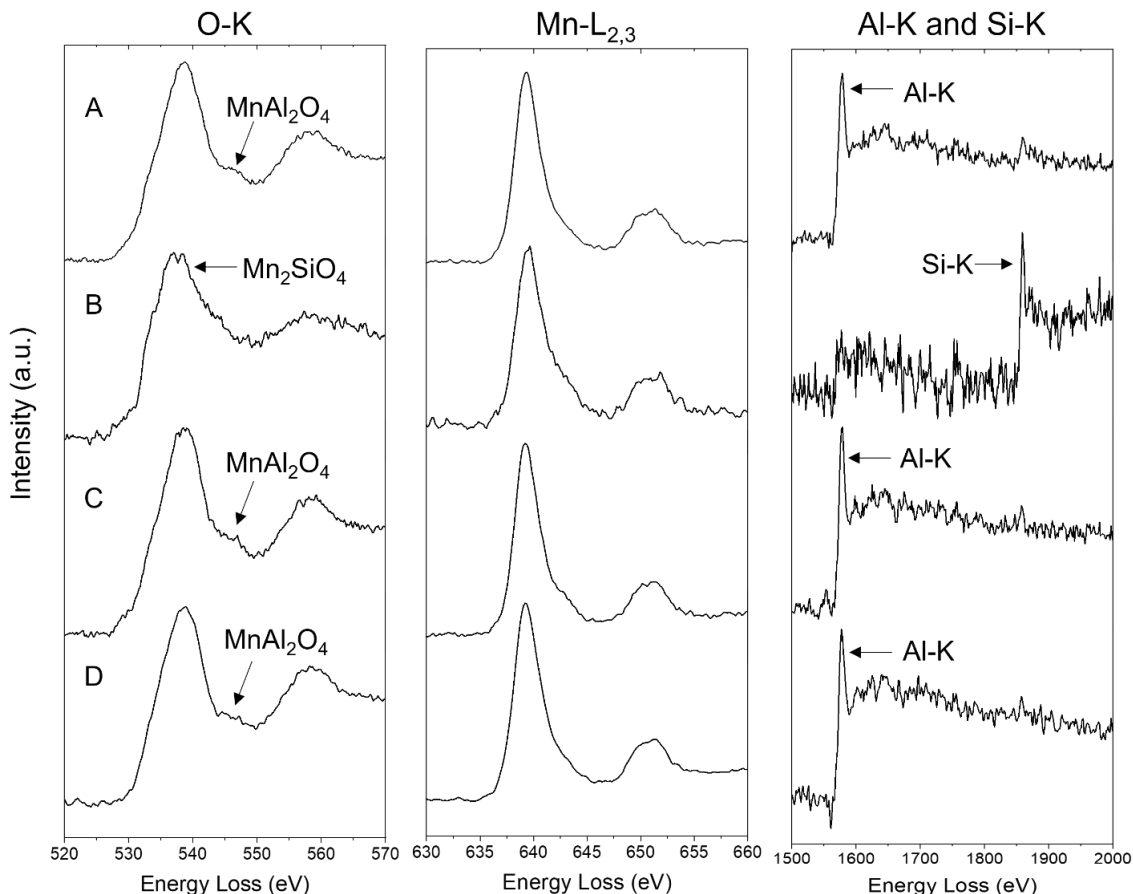
Figure 5.11: EELS spectra taken from regions A-D in the EELS elemental maps of the –30°C dp sample (Figure 5.10). Chemical speciation was determined by comparison with the reference spectra of Grosvenor et al. [57].

The HAADF-STEM micrograph along with the EELS elemental maps corresponding to Zn, Al, Fe, Mn, Si, and O for the –10°C dp sample are shown in Figure 5.12. Except for two holes created during FIB milling, a compact layer of Fe-Al crystals was formed at the interface between the substrate and the Zn coating, indicating full reactive wetting was achieved. As was observed for the case of the –30°C dp samples (Figure 5.10), direct substrate wetting, oxide wetting, oxide lift-off, and significant Zn ingress into the substrate were observed. The dominant external oxide species present was $MnAl_2O_4$ and no Mn-Si film-type oxides were observed. Similar observations

can be made from the HAADF-STEM image and EELS elemental maps corresponding to Zn, Al,

Fe, Mn, Si, and O for the +5°C dp sample, not shown in this work.
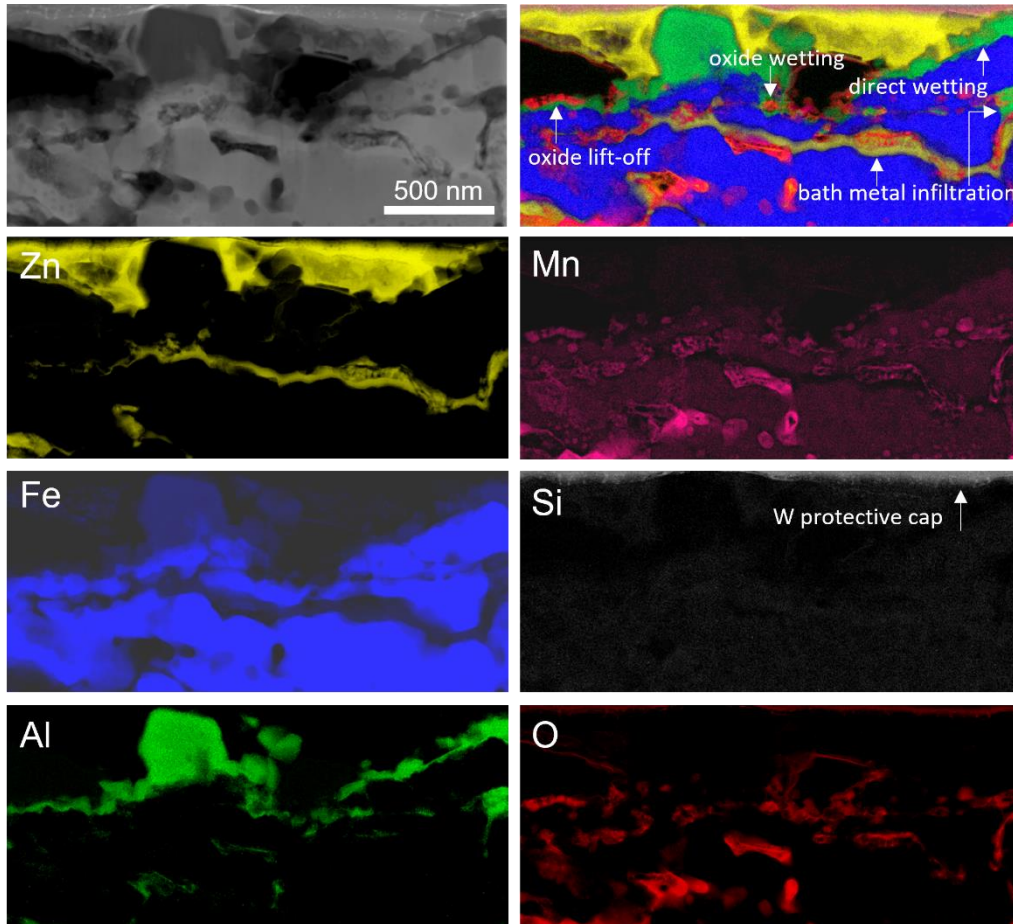
Figure 5.12: HAADF-STEM image along with the EELS elemental maps of the substrate/coating interface of the –10°C dp sample. The arrows in the composite map show evidence of reactive wetting mechanisms: direct substrate wetting, oxide wetting, oxide cracking/spalling, and bath metal ingress.

5.5   Discussion

Informed by the work of Wagner [58] and others [59–63], many authors working on 1G

AHSS [18,19,25,28,29,33,64,65] and, lately, medium-Mn model alloys [34,66] have improved the

reactive wetting of their substrates by suppressing external oxidation of ignoble alloying elements

by increasing the process atmosphere pO_2 (i.e. annealing at dew points above the commonly-

employed –30°C). The present work illustrates that the use of a two-stage thermal processing cycle can widen the range of pO_2 used during intercritical annealing to successfully galvanize a medium-Mn 3G AHSS.

The SEM images of the pre-immersion surfaces (Figure 5.2) show discrete and dispersed nano-scaled oxides that were identified as $MnAl_2O_4$ [46]. The surfaces were also covered with extruded Fe nodules, which provided additional oxide-free Fe surfaces to react with the galvanizing bath metal to form $Fe_2Al_{5-x}Zn_x$ crystals (as seen in Figure 5.9(a-c)). Although there was cracking in the internal oxidation network during bending, as seen in Figure 5.6, the cracks did not propagate into the substrates and were rarely observed to propagate into the coatings. The integrity of the coatings in tension and bending, along with the well-developed interfacial layer of $Fe_2Al_{5-x}Zn_x$ crystals observed via SEM (Figure 5.9), suggested that the $MnAl_2O_4$ nodules did not preclude successful reactive wetting of this substrate by the liquid bath metal.

Significant evidence of direct reactive wetting of the substrate by the liquid metal bath (i.e. regions of direct contact between the Fe-Al crystals and the substrate, such as those in Figure 5.10 (–30°C dp) and Figure 5.12 (–10°C dp)), was observed along much of the substrate-coating interface. This is the dominant reactive wetting mechanism and was facilitated by the large area fraction of relatively solute-free Fe available for dissolution by the galvanizing bath. However, this mechanism clearly operated in tandem with several others to enable full reactive wetting of the substrate.

A network of ζ-FeZn$_{13}$ crystals was observed at the coating/substrate interface of all samples (see Figure 5.9(d-f)), even though the formation of this phase is not expected when employing a 0.2 wt% dissolved Al galvanizing bath [67]. In fact, a bath containing more than 0.15 wt% dissolved Al should result in full inhibition by a continuous layer of $Fe_2Al_{5-x}Zn_x$ [67]. It is

known that Al uptake at the substrate/coating interface is a two-stage process, where heterogeneously nucleated $Fe_2Al_{5-x}Zn_x$ grows by a Fe diffusion-controlled/precipitation process, necessitating constant Al replenishment from the bath to the bath/$Fe_2Al_{5-x}Zn_x$ interface [68]. Thus, the presence of ζ-$FeZn_{13}$ can be indicative of $Fe_2Al_{5-x}Zn_x$ breakdown due to Zn diffusion through the $Fe_2Al_{5-x}Zn_x$ layer, Fe saturation by Zn and its subsequent nucleation [69–71]. Alternatively, ζ-$FeZn_{13}$ formation can be associated with the depletion of bath Al in the mass transport boundary layer, which other researchers [27,32,72] have cited as indirect evidence of aluminothermic reduction of surface MnO. However, in the present case, no significant MnO was observed on the pre-immersion surfaces and no Al_2O_3 was observed in the coating. It is, therefore, posited that the ζ-$FeZn_{13}$ was present due to the dissolution of the extruded Fe nodules (which have a large surface-to-volume ratio) by the galvanizing bath, leading to local Fe supersaturation of the bath [73] and the restoration of equilibrium via the precipitation of ζ-$FeZn_{13}$ crystals on the substrate surface.

Several secondary reactive wetting mechanisms contributed to the observed full reactive wetting of the substrate, despite the presence of surface oxide nodules. Surface oxide bridging by the liquid bath due to surface tension effects has been described by Bellhouse and McDermid [24,64] and was seen in Figure 5.10 (–30°C dp), where the $Fe_2Al_{5-x}Zn_x$ crystals bridged (but were not in direct contact with) the Mn_2SiO_4 film. Given that $MnAl_2O_4$ nodules (and not Mn_2SiO_4 films) were the most common oxide species present after intercritical annealing, as well as the substrate/coating interfaces examined in this work, it is not expected that this is a dominant reactive wetting mechanism for this substrate.

A significant contributor to the observed degree of reactive wetting is likely to be from oxide wetting by the bath metal, as seen in Figure 5.10 (–30°C dp) and Figure 5.12 (–10°C dp) where the $Fe_2Al_{5-x}Zn_x$ crystals were in direct contact with the $MnAl_2O_4$ nodules. The oxide wetting

mechanism had previously been described by Bellhouse and McDermid [64] for unspeciated Mn-Al-Si oxides and small Mn-rich oxide nodules and was attributed to the chemistry and size of the oxides. Similar to the work of Bellhouse and McDermid, the wetting of the oxides in this work is attributed to the nano-scale of the oxides and their chemical composition (i.e. they were rich in Mn and Al but contained no detectable Si).

The oxide cracking and spalling mechanism, whereby bath metal infiltrates the substrate-oxide interface and allows the formation of $Fe_2Al_{5-x}Zn_x$ underneath the oxide, is also proposed to be an important, albeit secondary, reactive wetting mechanism for the substrate in this investigation. Evidence of this mechanism was seen for all processing conditions explored (Figure 5.10 (–30°C dp) and Figure 5.12 (–10°C dp)), and these images corroborate the findings of several authors [18,25,29,33,66] working on 1G AHSS [18,25,29,33] and prototype medium-Mn 3G AHSS [34,66] grades. Bellhouse and McDermid [33] postulated that oxide spalling and cracking could occur upon cooling from the peak annealing temperature to the bath equilibration temperature due to the differences in the coefficients of thermal expansion of the substrate and surface oxide species. Internal oxide cracking might have also created routes into which the liquid metal could ingress, as seen in Figure 5.10 (–30°C dp) and Figure 5.12 (–10°C dp).

However, an additional mechanism for Zn ingress into the substrate is proposed to be via the selective dissolution of MnO, $MnSiO_3$, and Mn_2SiO_4 during the flash pickling process. Previous work by the present authors [46] showed that the flash pickling used to restore the substrate surfaces also dissolved some of the internal oxide structures that were connected to the surface. These partially-dissolved structures were preserved during the intercritical annealing step and could allow for bath metal infiltration and mechanical interlock of the coating with the substrate. This is particularly well illustrated in Figure 5.10 (–30°C dp) and Figure 5.12 (–10°C

dp), which show a network of $MnAl_2O_4$ with Zn ingress where Mn-Si oxides might have been dissolved during flash pickling.

From the above evidence, it can be concluded that the austenitization step (Figure 5.1) results in solute depletion of the near-surface matrix, leaving behind a low alloy content, almost fully-dense, metallic Fe layer with a surface that is populated with small, dispersed $Mn_2Al_2O_4$ oxides and extruded Fe nodules. No significant additional oxidation occurs during intercritical annealing because the time and temperature (120 s at 710°C) are insufficient for significant outward diffusion of solute from deeper within the bulk, especially because the existing internal oxides act as diffusion barriers. Given that the external oxides are small, dispersed, and nodular, there is a large area fraction of relatively solute-free surface Fe available to be reactively wet by the galvanizing bath by the well-established Fe dissolution and $Fe_2Al_{5-x}Zn_x$ precipitation and growth reactive wetting process. A summative schematic of the evolution of the substrate surface during the two-stage thermal cycle and subsequent immersion in the galvanizing bath is shown in Figure 5.13.

.
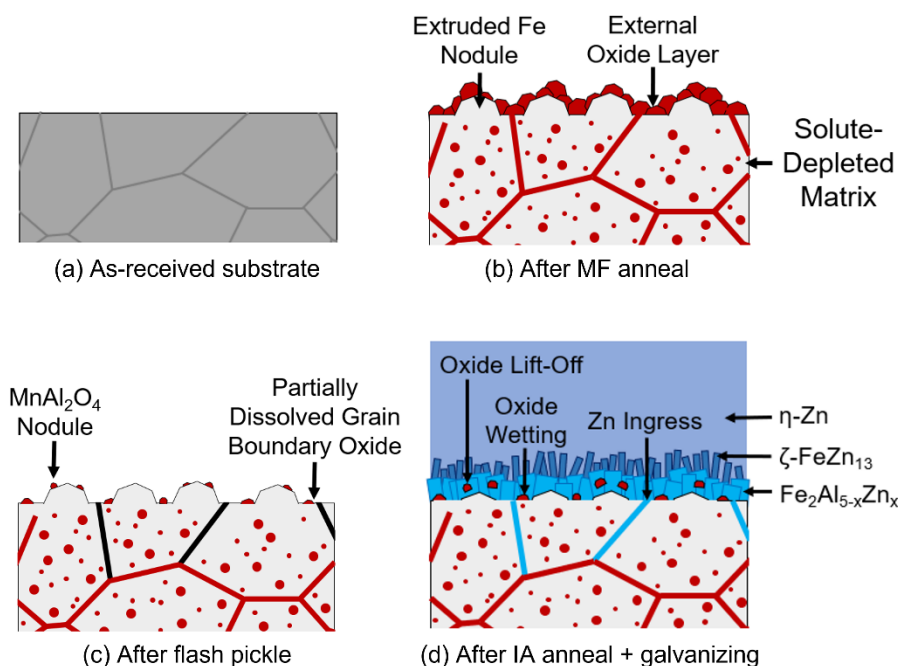
Figure 5.13: Summative schematic showing the evolution of surface and near-surface structures at each stage in the thermal cycle.

5.6 Conclusions

The reactive wetting of a prototype 0.15C-5.6Mn-1.9Al-1.1Si (wt%) third-generation advanced high-strength steel was achieved by a conventional Zn(Al,Fe) continuous galvanizing bath containing 0.2 wt% dissolved Al. The austenitization treatment (890°C for 600 s, dew point of –10°C) served to pre-oxidize the near-surface solutes, and most of these oxides were removed during the subsequent flash pickling treatment. Following this, intercritical annealing (710°C for 120 s) was performed in a wide span of process atmosphere pO_2 (dew points of –30, –10, or +5°C), resulting in successful reactive wetting and adherent galvanized coatings.

The pre-immersion oxides following the intercritical anneal were discrete and dispersed nano-scaled $MnAl_2O_4$, which meant that much of the substrate Fe was accessible for reactive wetting by the galvanizing bath metal. Moreover, the internal oxidation of ignoble alloying elements resulted in the extrusion of Fe nodules at the surface and increased the available surface

area for Fe dissolution and the formation of the desired $Fe_2Al_{5-x}Zn_x$ interfacial layer. In addition, there was evidence of several secondary reactive wetting mechanisms that had previously been identified for low-alloyed 1G AHSS and model 0.1C-6Mn-2Si-(0-0.05)Sn (wt%) substrates, namely oxide cracking and lift-off, and oxide bridging by the liquid metal bath. Furthermore, liquid bath metal penetration into the substrate occurred through a combination of internal oxide cracking and the newly proposed reactive wetting mechanism of infiltration via porous internal oxide structures that manifested due to the dissolution of MnO, $MnSiO_3$, and Mn_2SiO_4 during flash pickling. These mechanisms resulted in high-quality coatings with an integral $Fe_2Al_{5-x}Zn_x$ interfacial layer, irrespective of dew point employed during intercritical annealing. The coatings resisted significant cracking and flaking during uniaxial tension and three-point bending.

In conclusion, this work showcases a prospective processing route to facilitate the galvanizing of medium-Mn 3G AHSS by selectively oxidizing the near-surface solute during the austenitization step and dissolving the external oxides by flash pickling. During intercritical annealing, no significant additional external oxidation would occur and the substrate could then be reactively wet by a conventional galvanizing bath after intercritical annealing at a wide range of process atmosphere pO_2.

5.7 Acknowledgements

The authors would also like to acknowledge the technical assistance provided by Mr. John Thomson and Mr. Raymond Fullerton (McMaster Steel Research Centre); Dr. Natalie Hamada and Mr. Travis Casagrande (Canadian Centre for Electron Microscopy); Dr. James Britten, Ms. Maureen Fitzpatrick, and Ms. Victoria Jarvis (Brockhouse Institute for Materials Research); Dr. Xiaogang Li and Mr. Doug Culley (McMaster Department of Materials Science and Engineering); and Dr. Elizabeth McNally and Dr. Moisei Bruhis (Centre for Automotive Materials and Corrosion).

5.8   References

[1]   D.K. Matlock, J.G. Speer, Design Considerations for the Next Generation of Advanced High Strength Steel Sheets, in: H.C. Lee (Ed.), Proc. 3rd Int. Conf. Struct. Steels, Korean Institute of Metals and Materials, Seoul, Korea, 2006: pp. 774–781.

[2]   D.K. Matlock, J.G. Speer, Third Generation of AHSS: Microstructure Design Concepts, Springer, Jamshedpur, India, 2009. doi:10.1007/978-1-84882-454-6_11.

[3]   H.J. Kim, C. McMillan, G.A. Keoleian, S.J. Skerlos, Greenhouse Gas Emissions Payback for Lightweighted Vehicles Using Aluminum and High-Strength Steel, J. Ind. Ecol. 14 (2010) 929–946. doi:10.1111/j.1530-9290.2010.00283.x.

[4]   E. De Moor, P.J. Gibbs, J.G. Speer, D.K. Matlock, Strategies for Third-Generation Advanced High Strength Steel Development, AIST Trans. 7 (2010) 133–144.

[5]   D.K. Matlock, J.G. Speer, E. De Moor, P.J. Gibbs, Recent Developments in Advanced High Strength Sheet Steels for Automotive Applications: An Overview, JESTECH. 15 (2012) 1–12.

[6]   L. Zanchi, M. Delogu, M. Ierides, H. Vasiliadis, Life Cycle Assessment and Life Cycle Costing as Supporting Tools for EVs Lightweight Design, in: R. Setchi, R. Howlett, Y. Liu, P. Theobald (Eds.), Sustain. Des. Manuf. 2016, 2016: pp. 335–348. doi:https://doi.org/10.1007/978-3-319-32098-4_29.

[7]   P. Egede, Electric Vehicles, Lightweight Design, and Environmental Impacts, in: Environ. Assess. Light. Electr. Veh. Sustain. Prod. Life Cycle Eng. Manag., Springer, Cham, 2017: pp. 9–40. doi:https://doi.org/10.1007/978-3-319-40277-2_2.

[8]   K.M.H. Bhadhon, J.R. McDermid, F.E. Goodwin, Effect of Galvanizing Heat Treatment on the Microstructure and Mechanical Properties of a 6Mn-1.5Si Third Generation Advanced High Strength Steel, in: Proc. 10th Conf. Zinc Zinc Alloy Coat. Steel Sheet, Galvatech 2015, Toronto, 2015: pp. 936–943.

[9]   K.M.H. Bhadhon, J.R. McDermid, X. Wang, E.A. McNally, F.E. Goodwin, Fine-Scale Microstructure Characterization And Mechanical Properties Of CGL-Compatible Heat Treated Medium-Mn TRIP Steel, in: Proc. 11th Conf. Zinc Zinc Alloy Coat. Steel Sheet, Galvatech 2017, Tokyo, 2017: pp. 493–500.

[10]   K.M.H. Bhadhon, Effect of Starting Microstructure and CGL Compatible Thermal Processing Cycle on the Mechanical Properties of a Medium-Mn Third Generation Advanced High Strength Steel, McMaster University, 2017.

[11]   D.M. Pallisco, J.R. McDermid, E.A. McNally, F.E. Goodwin, Effect of Starting Microstructure and Intercritical Annealing Parameters on the Mechanical Property Development of a Medium-Mn Third-Generation Advanced High Strength Steel, in: Proc. 11th Conf. Zinc Zinc Alloy Coat. Steel Sheet, Galvatech 2017, Tokyo, 2017: pp. 782–789.

[12]   D.M. Pallisco, K.M.H. Bhadhon, V. Patel, M. Pourmajidian, F.E. Goodwin, J.R. McDermid, 9-11: Galvanizing of Medium-Manganese Third Generation Advanced High Strength Steels, in: Proc. 4th Int'l Conf. Med. High-Manganese Steels, 2019: pp. 375–378.

[13]   V. Patel, Microstructure and Mechanical Properties of Medium Mn Steel, McMaster University, 2019.

[14]   D.M. Pallisco, J.R. McDermid, Mechanical property development of a 0.15C–6Mn–2Al–1Si third-generation advanced high strength steel using continuous galvanizing heat treatments, Mater. Sci. Eng. A. 778 (2020) 139111. doi:10.1016/j.msea.2020.139111.

[15]   J. Mahieu, S. Claessens, B.C. De Cooman, Galvanizability of High-Strength Steels for Automotive Applications, Metall. Mater. Trans. A. 32 (2001) 2905–2908.

[16]   J. Maki, J. Mahieu, B.C. De Cooman, S. Claessens, Galvanisability of silicon free CMnAl TRIP steels, Mater. Sci. Technol. 19 (2003) 125–131. doi:10.1179/026708303225009300.

[17]   L. Liu, G. Jiang, H. Wang, H. Teng, Effect of dew point during heating on selective oxidation of TRIP steels, Metall. Res. Technol. 114 (2017) 609. doi:10.1051/metal/2017070.

[18]   G. Seyed Mousavi, J.R. McDermid, Effect of dew point on the reactive wetting of a C-2Mn-1.3Si (wt%) advanced high strength steel during continuous galvanizing, Surf. Coatings Technol. 351 (2018) 11–20. doi:10.1016/j.surfcoat.2018.06.060.

[19]   G. Seyed Mousavi, B. Langelier, J.R. McDermid, Effect of Sn Addition, Process Atmosphere pO2, and Annealing Time on the Selective Oxidation of a C-2Mn-1.7Si (Wt Pct) Advanced High-Strength Steel During Continuous Galvanizing, Metall. Mater. Trans. A. 50 (2019) 2898–2911. doi:10.1007/s11661-019-05202-3.

[20]   M. Pourmajidian, J.R. McDermid, Selective Oxidation of a 0.1C-6Mn-2Si Third Generation Advanced High-Strength Steel During Dew-Point Controlled Annealing, Metall. Mater. Trans. A. 49 (2018) 1795–1808. doi:10.1007/s11661-018-4513-7.

[21]   M. Pourmajidian, B. Langelier, J.R. McDermid, Effect of Process Atmosphere Dew Point and Tin Addition on Oxide Morphology and Growth for a Medium-Mn Third Generation Advanced Steel During Intercritical Annealing, Metall. Mater. Trans. A. 49 (2018) 5561–5573. doi:10.1007/s11661-018-4855-1.

[22]   J. Mahieu, S. Claessens, B.C. De Cooman, F.E. Goodwin, Surface and Sub-surface Characterization of Si-, Al- and P-alloyed TRIP-aided Steel, in: M.A. Baker (Ed.), Galvatech 2004 Proc., Association for Iron and Steel Technology, Chicago, IL, 2004: pp. 529–538.

[23]   P. Drillet, Z. Zermout, D. Bouleau, J. Mataigne, S. Claessens, Selective Oxidation of high Si, Mn and Al steel grade during Recrystallization Annealing, and steel/Zn reactivity, in: M.A. Baker (Ed.), Galvatech 2004 Proc., Association for Iron and Steel Technology, Chicago, IL, 2004: pp. 1123–1134.

[24]   E.M. Bellhouse, J.R. McDermid, Analysis of the Fe–Zn interface of galvanized high Al–low Si TRIP steels, Mater. Sci. Eng. A. 491 (2008) 39–46. doi:10.1016/j.msea.2007.12.033.

[25]   E.M. Bellhouse, J.R. McDermid, Selective Oxidation and Reactive Wetting of 1.0 Pct Si-0.5 Pct Al and 1.5 Pct Si TRIP-Assisted Steels, Metall. Mater. Trans. A. 41 (2010) 1539–1553. doi:10.1007/s11661-010-0192-8.

[26]   Y.F. Gong, H.S. Kim, B.C. De Cooman, Internal Oxidation during Intercritical Annealing of CMnSi TRIP Steel, ISIJ Int. 49 (2009) 557–563. doi:10.2355/isijinternational.49.557.

[27]   R. Sagl, A. Jarosik, D. Stifter, G. Angeli, The role of surface oxides on annealed high-strength steels in hot-dip galvanizing, Corros. Sci. 70 (2013) 268–275. doi:10.1016/j.corsci.2013.01.039.

[28]   L. Cho, G.S. Jung, B.C. De Cooman, On the transition of internal to external selective oxidation on CMnSi TRIP steel, Metall. Mater. Trans. A. 45 (2014) 5158–5172. doi:10.1007/s11661-014-2442-7.

[29]   R. Sagl, A. Jarosik, G. Angeli, T. Haunschmied, G. Hesser, D. Stifter, Tailoring of oxide morphology and crystallinity on advanced high-strength steel surfaces prior hot-dip galvanizing, Acta Mater. 72 (2014) 192–199. doi:10.1016/j.actamat.2014.03.037.

[30]   R. Khondker, A.I.M. Mertens, J.R. McDermid, Effect of annealing atmosphere on the galvanizing behavior of a dual-phase steel, Mater. Sci. Eng. A. 463 (2007) 157–165. doi:10.1016/j.msea.2006.09.116.

[31] R. Kavitha, J.R. McDermid, On the in-situ aluminothermic reduction of manganese oxides in continuous galvanizing baths, Surf. Coat. Technol. 212 (2012) 152–158. doi:10.1016/j.surfcoat.2012.09.038.

[32] S. Alibeigi, R. Kavitha, R.J. Meguerian, J.R. McDermid, Reactive wetting of high Mn steels during continuous hot-dip galvanizing, Acta Mater. 59 (2011) 3537–3549. doi:10.1016/j.actamat.2011.02.027.

[33] E.M. Bellhouse, J.R. McDermid, Selective Oxidation and Reactive Wetting during Galvanizing of a CMnAl TRIP-Assisted Steel, Metall. Mater. Trans. A. 42A (2011) 2753–2768. doi:10.1007/s11661-010-0192-8.

[34] M. Pourmajidian, J.R. McDermid, On the reactive wetting of a medium-Mn advanced high-strength steel during continuous galvanizing, Surf. Coatings Technol. 357 (2019) 418–426. doi:10.1016/j.surfcoat.2018.10.028.

[35] E.D. Hondros, M.P. Seah, Segregation to interfaces, Int. Met. Rev. 22 (1977) 262–301.

[36] G. Lyudkovsky, The Effect of Antimony on Internal Oxidation and Magnetic Properties of Si-Al Electrical Steels, IEEE Trans. Magn. 22 (1986) 508–510.

[37] H.J. Grabke, Surface and grain boundary segregation on and in iron and steels, ISIJ Int. 29 (1989) 529–538. doi:10.2355/isijinternational.29.529.

[38] H.J. Grabke, Surface and Grain Boundary Segregation of Antimony and Tin - Effects on Steel Properties, Kovine, Zlitine, Tehnol. 30 (1996) 483–495.

[39] A. Ruck, D. Monceau, H.J. Grabke, Effects of tramp elements Cu, P, Pb, Sb and Sn on the kinetics of carburization of case hardening steels, Steel Res. Int. 67 (1996) 240–246. doi:10.1002/srin.199605484.

[40] L. Cho, M.S. Kim, Y.H. Kim, B.C. De Cooman, Influence of Minor Alloying Elements on Selective Oxidation and Reactive Wetting of CMnSi TRIP Steel during Hot Dip Galvanizing, Metall. Mater. Trans. A. 45 (2014) 4484–4498. doi:10.1007/s11661-014-2394-y.

[41] L. Cho, E.J. Seo, G.S. Jung, D.W. Suh, B.C. De Cooman, Surface Selective Oxidation of Sn-Added CMnSi TRIP Steel, Metall. Mater. Trans. A. 47 (2016) 1705–1719. doi:10.1007/s11661-016-3331-z.

[42] J. Oh, L. Cho, M.S. Kim, K. Kang, B.C. De Cooman, The Effect of Bi on the Selective Oxide Formation on CMnSi TRIP Steel, Metall. Mater. Trans. A. 47 (2016) 5474–5486. doi:10.1007/s11661-016-3735-9.

[43] H. Luo, Mechanical properties of Medium-Mn steel after a short intercritical annealing and its dependence on starting microstructures, in: 2nd HMnS Conf. Proc., 2014: pp. K2-85.

[44] H. Luo, H. Dong, New ultrahigh-strength Mn-alloyed TRIP steels with improved formability manufactured by intercritical annealing, Mater. Sci. Eng. A. 626 (2015) 207–212.

[45] M.M. McCosby, E.A. Silva, D.P. Hoydick, U.S. Steel 3rd Generation Steel: Customer-Friendly Chemistry, Properties, and Manufacturability Enabled by Unique Processing, in: Proc. 12th Conf. Zinc Zinc Alloy Coat. Steel Sheet, Galvatech 2021, ASMET, Vienna, Austria, 2021: pp. 134–144.

[46] D.M. Pallisco, J.R. McDermid, F.E. Goodwin, Effect of CGL-compatible heat treatments on the selective oxidation of a 0.15C-6Mn-2Al-1Si third-generation advanced high strength steel, in: Proc. 12th Conf. Zinc Zinc Alloy Coat. Steel Sheet, Galvatech 2021, ASMET, Vienna, Austria, 2021: pp. 154–163.

[47] E.M. Bellhouse, A.I.M. Mertens, J.R. McDermid, Development of the surface structure of TRIP steels prior to hot-dip galvanizing, Mater. Sci. Eng. A. 463 (2007) 147–156.

[48] A.E. Morris, FREED Thermodynamic Database v7.8.1, (2013).

[49] J.R. McDermid, M.H. Kaye, W.T. Thompson, Fe Solubility in the Zn-Rich Corner of the Zn-Al-Fe System for Use in Continuous Galvanizing and Galvannealing, Metall. Mater. Trans. B. 38 (2007) 215–230. doi:10.1007/s11663-007-9028-3.

[50] E.M. Bellhouse, Galvanizing of Al-Si TRIP-Assisted Steels, McMaster University, 2010.

[51] S. Gates-Rector, T. Blanton, The Powder Diffraction File: a quality materials characterization database, Powder Diffr. 34 (2019) 352–360. doi:10.1017/S0885715619000812.

[52] ASTM A653/A653M-19a: Standard Specification for Steel Sheet, Zinc-Coated (Galvanized) or Zinc-Iron Alloy-Coated (Galvannealed) by the Hot-Dip Process, West Conshohocken, PA, USA, 2019. doi:10.1520/A0653.

[53] ASTM E8/E8M-16a: Standard Test Methods for Tension Testing of Metallic Materials, West Conshohocken, PA, USA, 2016.

[54] J.R. Mackert, R.D. Ringle, C.W. Fairhurst, High-temperature Behavior of a Pd-Ag Alloy for Porcelain, J. Dent. Res. 62 (1983) 1229–1235. doi:10.1177/00220345830620121201.

[55] S. Guruswamy, S.M. Park, J.P. Hirth, R.A. Rapp, Internal oxidation of Ag-in alloys: Stress relief and the influence of imposed strain, Oxid. Met. 26 (1986) 77–100. doi:10.1007/BF00664274.

[56] Z.T. Zhang, I.R. Sohn, F.S. Pettit, G.H. Meier, S. Sridhar, Investigation of the Effect of Alloying Elements and Water Vapor Contents on the Oxidation and Decarburization of Transformation-Induced Plasticity Steels, Metall. Mater. Trans. B. 40 (2009) 567–584. doi:10.1007/s11663-009-9255-x.

[57] A.P. Grosvenor, E.M. Bellhouse, A. Korinek, M. Bugnet, J.R. McDermid, XPS and EELS characterization of Mn2SiO4, MnSiO3 and MnAl2O4, J. Appl. Surf. Sci. 379 (2016) 242–248. doi:10.1016/j.apsusc.2016.03.235.

[58] C. Wagner, Reaktionstypen bei der Oxydation von Legierungen, Zeitschrift Für Elektrochemie. 63 (1959) 772–782.

[59] D. Huin, P. Flauder, J.-B. Leblond, Numerical Simulation of Internal Oxidation of Steels during Annealing Treatments, Oxid. Met. 64 (2005) 131–167. doi:10.1007/s11085-005-5718-x.

[60] V.A. Lashgari, C. Kwakernaak, W.G. Sloof, Transition from Internal to External Oxidation of Mn Steel Alloys, Oxid. Met. 81 (2014) 435–451. doi:10.1007/s11085-013-9456-1.

[61] J.M. Mataigne, M. Lamberigts, V. Leroy, Developments in the Annealing of Sheet Steels, Minerals, Metals & Materials Society, Warrendale, PA, USA, 1992.

[62] H.J. Grabke, V. Leroy, H. Viefhaus, Segregation on the Surface of Steels in Heat Treatment and Oxidation, ISIJ Int. 35 (1995) 95–113. doi:10.2355/isijinternational.35.95.

[63] C.R. Shastry, J.A. Rotole, T.W. Kaiser, Characterization of selective oxidation of alloying elements in an advanced high strength steel from theoretical and experimental viewpoints, 7th Int. Conf. Zinc Zinc Alloy Coat. Steel Sheet. (2007) Paper B-6-2, 403-408.

[64] E.M. Bellhouse, J.R. McDermid, Selective Oxidation and Reactive Wetting During Hot-Dip Galvanizing of a 1.0 Pct Al-0.5 Pct Si TRIP-Assisted Steel, Metall. Mater. Trans. A. 43 (2012) 2426–2441. doi:10.1007/s11661-010-0192-8.

[65] L. Cho, J.S. Lee, M.S. Kim, Y.H. Kim, B.C. De Cooman, Influence of Gas Atmosphere Dew Point on the Selective Oxidation and the Reactive Wetting During Hot Dip Galvanizing of CMnSi TRIP Steel, Metall. Mater. Trans. A. 44A (2013) 362–371. doi:10.1007/s11661-012-1392-1.

[66] M. Pourmajidian, J.R. McDermid, Effect of Annealing Temperature on the Selective Oxidation and Reactive Wetting of a 0.1C-6Mn-2Si Advanced High Strength Steel During Continuous Galvanizing Heat Treatments, ISIJ Int. 58 (2018) 1635–1643. doi:10.2355/isijinternational.ISIJINT-2017-688.

[67] N.Y. Tang, Thermodynamics and Kinetics of Alloy Formation in Galvanized Coatings, in: F.E. Goodwin (Ed.), Proc. Int'l Symp. Zinc-Based Steel Coat. Syst. Prod. Performance, TMS 1998, TMS, San Antonio, TX, 1998: pp. 3–12.

[68]   N.Y. Tang, Modeling Al Enrichment in Galvanized Coatings, Metall. Mater. Trans. A. 26 (1995) 1699–1704.

[69]   M. Guttmann, Diffusive Phase Transformations in Hot-Dip Galvanizing, Mater. Sci. Forum. 155–156 (1994) 527–548. doi:10.4028/www.scientific.net/MSF.155-156.527.

[70]   C.E. Jordan, A.R. Marder, Fe–Zn phase formation in interstitial-free steels hot-dip galvanized at 450°C Part II 0.20 wt% Al–Zn baths, J. Mater. Sci. 32 (1997) 5603–5610.

[71]   A.R. Marder, The metallurgy of zinc-coated steel, Prog. Mater. Sci. 45 (2000) 191–271.

[72]   R. Kavitha, J.R. McDermid, Aluminothermic Reduction of Manganese Oxides in the Continuous Galvanizing Bath, in: Proc. 8th Int. Conf. Zinc Alloy Coat. Steel Sheet - Galvatech 2011, Associazione Italiana di Metallurgia, Milan, Italy, 2011: p. P-68.

[73]   J. Nakano, D. V. Malakhov, S. Yamaguchi, G.R. Purdy, A full thermodynamic optimization of the Zn – Fe – Al system within the 420 – 500°C temperature range, Comput. Coupling Phase Diagrams Thermochem. 31 (2007) 125–140. doi:10.1016/j.calphad.2006.09.003.

6   Global Discussion

This chapter will present a summative discussion of the main results from Chapters 3 to 5. The microstructural and mechanical property development of the alloy will be discussed first and lead into an analysis of the effects of process atmosphere pO_2 on the selective oxidation and reactive wetting of the substrate.

6.1   Microstructural and Mechanical Property Development

The microstructural and mechanical property evolution of the experimental alloy in the present work was determined as a function of starting microstructure and CGL-compatible intercritical annealing parameters. It was determined that the mechanical properties achieved were related to the morphology and chemistry of the retained austenite in the final microstructure, which affected its mechanical and chemical stability (and therefore its TRIP kinetics), as well as its stacking fault energy (and therefore its TWIP kinetics).

A comparison of the CR-665°C and MF-665°C SEM (Figure 3.5(a-b)) and TEM (Figure 3.10 and Figure 3.11) micrographs demonstrates the clear role of starting microstructure on the morphology of the microstructures obtained after intercritical annealing. The retained austenite in the MF-665°C sample was lamellar (Figure 3.5(b) and Figure 3.11), as opposed to the polygonal retained austenite in the CR-665°C sample (Figure 3.5(a) and Figure 3.10). Previous work on low-alloy TRIP and medium-Mn steels has shown that the lamellar retained austenite is more mechanically stable than polygonal retained austenite due to the mechanical constraint imposed by surrounding high-strength phases (namely martensite and/or bainitic ferrite) [1–4]. In addition to its higher mechanical stability, it has been proposed that lamellar retained austenite is more chemically stable because the C and Mn from the surrounding martensite only need diffuse across the relatively small half-lath retained austenite width (~50 nm) instead of a larger polygonal

retained austenite grain (at least ~100 nm), leading to a more significant accumulation of C within the lath-like retained austenite and, thus, higher chemical stability [5,6].

In the present work, these hypotheses are supported by comparing the volume fraction of retained austenite as a function of true strain for the CR-665°C and MF-665°C samples in Figure 3.9(b). Examination of this plot shows that these samples had approximately the same initial volume fraction of retained austenite (0.23-0.25) after intercritical annealing; however, the CR-665°C sample had accelerated TRIP kinetics compared to the MF-665°C sample. It is also important to note that the MF-665°C sample did not exhaust the TRIP effect, i.e., the retained austenite therein was hyperstable and did not completely transform to martensite during deformation. An additional point of comparison of the chemical stability of the retained austenite in these samples can be made by examining their respective chemical compositions in Table 3.4. The experimentally determined C content was higher for the retained austenite in the MF-665°C samples than for the CR-665°C samples, which supports the argument that the lamellar retained austenite in the MF-665°C sample was more chemically stable due to the shorter diffusion distances for C enrichment from the surrounding martensite. Consequently, the calculated SFE of the CR-665°C samples was lower than that of the MF-665°C samples (approximately 15 vs. 18 mJ/m^2) (Table 3.4), which are within the typically accepted range for the activation of the TWIP effect [7]. Indeed, some evidence of deformation twinning was observed via TEM (Figure 3.10 and Figure 3.11), however, this mechanism was likely not sufficient to provide the required work hardening rates to achieve the 3G AHSS mechanical property target envelope of 24,000 MPa% $\leq$ UTS $\times$ TE $\leq$ 40,000 MPa% [8–10], as shown in Table 3.3.

As shown in Table 3.3 and Figure 3.6, improved mechanical properties were obtained for the MF-710°C and MF-740°C samples relative to the CR-665°C and MF-665°C samples, with the

best combination of strength and ductility offered by the MF-710°C treatment. It should be noted that both the MF-710°C and MF-740°C samples achieved the general mechanical property targets for 3G AHSS [8,9], as shown in Table 3.3. Similar to the MF-665°C samples, the MF-710°C and MF-740°C samples had lamellar retained austenite (see SEM images in Figure 3.5(c-d) and TEM micrographs in Figure 3.12 and Figure 3.13). The retained austenite in these samples likely had similar mechanical stability to the retained austenite in the MF-665°C sample, but had different chemical compositions (Table 3.4) and, thus, lower chemical stabilities. Thus, the overall TRIP kinetics were more rapid for the MF-710°C and MF-740°C samples than for the CR-665°C and MF-665°C samples, leading to improved work hardening rates for the former two compared to the latter two (Figure 4.6(c)). The TRIP effect was exhausted more rapidly in the case of the MF-740°C sample relative to the MF-710°C sample (Figure 3.9), implying that the chemical stability of the retained austenite decreased with increasing annealing temperature. This is in agreement with Steineder et al. [11,12], who showed showing that higher intercritical annealing temperatures resulted in the formation of more intercritical austenite with a lower C and Mn content.

The inflections in the work hardening rate plot (Figure 3.6(c)) suggested that a plasticity-enhancing mechanism was activated, and this was experimentally confirmed via XRD (Figure 3.9) and TEM (Figure 3.12 and Figure 3.13). A quantitative assessment of the TWIP kinetics was not performed, but the differences in the mechanical properties observed between the MF-710°C and MF-740°C samples can be largely explained by the differences in TRIP kinetics in these samples, as evidenced by the TRIP kinetics data shown in Figure 3.9. To summarize, the retained austenite in the MF-740°C samples transformed more rapidly than in the MF-710°C samples (Figure 3.9), which resulted in higher initial work hardening rates (Figure 3.6(c)) for the MF-740°C samples. However, the retained austenite in the MF-740°C samples completely transformed to martensite

(i.e., the TRIP effect was exhausted) at a lower true strains (Figure 3.9) compared to the MF-710°C samples, which resulted in the onset of plastic instability at lower strains and, thus, the observed lower total elongation (Figure 3.6(a), Table 3.3).

It should be noted that all of the experimental heat treatments resulted in significant post-uniform elongations (in excess of true strains of 0.6), as documented in Figure 3.7. This is promising for alloy formability as it is known that there is a correlation between cross-sectional area reduction at fracture in uniaxial tension and performance in local forming operations, such as hole expansion ratio and bending [13–16].

The work presented in Chapter 3 allowed for the identification of a thermal processing route that could achieve 3G AHSS mechanical property targets using CGL-compatible intercritical annealing parameters. Moreover, it was shown that the mechanical properties were sensitive to intercritical annealing parameters due to their effect on the chemical stability of the retained austenite, which affected TRIP kinetics. Accordingly, an intercritical annealing temperature could be strategically selected to tailor the strength-ductility balance of the steel. It was also demonstrated that the desired lamellar morphology of retained austenite could be achieved from a mostly martensitic starting microstructure. The MF-710°C processing cycle was identified as a candidate heat treatment for the subsequent selective oxidation and reactive wetting trials that were presented in Chapters 4 and 5, respectively, as discussed in the following section.

6.2   Selective Oxidation and Reactive Wetting

The selective oxidation study in Chapter 4 sought to determine the effect of process atmosphere pO_2 during both the MF and IA stages of the MF-710°C processing cycle selected from the results discussed in Chapter 3. The FIB-prepared trench cuts in Figure 4.3 show a compact, multi-layered, and complex external oxide structure formed regardless of the pO_2

employed during the MF treatment. All samples exhibited some degree of external oxidation, even at the highest dew point investigated (+5°C, Figure 4.2, Figure 4.3, Figure 4.6, and Figure 4.8). In addition to possible oxidation during heating to the peak temperature, this has been attributed to the accelerated diffusion of solute through the heavily dislocated cold-rolled martensitic microstructure. Previous work by Rapp [17] on Ag-In alloys indirectly verified that cold work increases solute diffusivity and, thus, increased the pO_2 required for the transition from external to internal oxidation.

The MF -10°C dp external oxide structure (Figure 4.10) documented in this work is somewhat unique compared to previously documented external oxide structures observed on 1G AHSS [18–21] and a model 0.2C-6Mn-2Si-(0-0.05Sn) (wt%) steel [22,23]. In the present case, the external co-precipitation of $MnSiO_3$, Mn_2SiO_4, and $MnAl_2O_4$ nodules (rather than layers) beneath a compact MnO layer (Figure 4.10) after the MF -10°C dp anneal is inextricably tied to the excellent reactive wetting that was observed for the samples presented in Chapter 5 (Figure 5.3 and Figure 5.4), i.e., MF (-10°C dp)+IA (-30°C dp, -10°C dp, or +5°C dp). The external oxide layer arising from the MF –10°C dp annealing treatment was too thick (approximately 150-200 nm) (Figure 4.3, Figure 4.6, and Figure 4.10) to attempt intercritical annealing and galvanizing without an intermediate flash pickling treatment, as previous studies have shown that a typical 4 s immersion time can only reduce approximately 80 nm of MnO [24]. Moreover, the aluminothermic reduction of other oxide species, such as $MnSiO_3$, Mn_2SiO_4, and $MnAl_2O_4$, has not been experimentally proven. A conventional HCl-based flash pickling solution effectively removed the MnO and Mn-Si oxides [25–27] (Figure 4.12). As shown in Figure 4.12, Figure 5.10, and Figure 5.12, the $MnAl_2O_4$ nodules present after intercritical annealing were sufficiently spaced that these nodules did not preclude reactive wetting of the substrate by the galvanizing bath.

In addition, the MF annealing step resulted in the formation of an extensive internal oxide network ranging from approximately 6 to 10 μm in depth depending on the dew point (Figure 4.5 and Figure 4.7). The formation of this internal oxide network had two primary consequences for the external pre-immersion structures on the substrate surface: (1) the extrusion of Fe nodules (Figure 4.2), and (2) the effective depletion of solute from the near-surface region (Region 5 in Figure 4.10 and Figure 4.11; Region 1 in Figure 4.12 and Figure 4.13; Region 4 in Figure 4.15 and Figure 4.16). The extrusion of Fe nodules is due to the volumetric expansion associated with internal oxidation, has been documented by several authors [28–32] and is known to facilitate direct reactive wetting by increasing the amount of metallic Fe available to react with the galvanizing bath metal [31,32]. The internal oxidation of Mn, Si, and Al resulted in a multi-micron deep solute-depleted layer of metallic Fe at the substrate surface. Meanwhile, the extensive internal oxide network retarded the diffusion of solute from deeper within the substrate (at the bulk composition) to the solute-depleted surface. The calculations presented in Chapter 4 (Figure 4.21) show that 120 s at 710°C would be insufficient to restore the solute-depleted surface layer, and thus, no significant additional selective oxidation occurred during intercritical annealing (Figure 4.6 and Figure 4.14). Accordingly, the most significant contributor to the reactive wetting observed for this substrate is the solute-depleted and highly textured surface metallic Fe layer caused by the pre-oxidation of near-surface solute and extrusion of Fe nodules.

Several secondary reactive wetting mechanisms were leveraged in order to fully reactively wet the substrate despite the antecedent $MnAl_2O_4$ nodules (Figure 4.4, Figure 4.14, Figure 5.2). Some comparisons can be made with previous work on model 0.2C-6Mn-2Si-(0-0.05Sn) (wt%) steels by Pourmajidian and McDermid [33], who showed that improvements in coating quality were achieved after annealing at 690°C for 120 s by using higher dew points (-30°C and +5°C vs.

-50°C) and by making minor Sn additions to retard external oxidation kinetics. Their Sn-added grade that was intercritically annealed at –30°C and +5°C dew points was completely reactively wetted by means of previously documented mechanisms such as aluminothermic reduction of MnO, oxide bridging, molten bath metal ingress between the oxide and substrate, and oxide lift-off. In the present case, excellent reactive wetting was achieved for all conditions explored (Figure 5.3, Figure 5.4, and Figure 5.9(a-c)). In this work, no evidence of aluminothermic reduction was observed and there was only a single observation of Mn_2SiO_4 oxide film bridging by $Fe_2Al_{5-x}Zn_x$ crystals (Figure 5.10, location B). Instead, the secondary reactive wetting mechanisms were the wetting and lift-off of $MnAl_2O_4$ nodules, as documented via TEM-EELS analysis (Figure 5.10 and Figure 5.12). In addition, a novel mechanism of bath metal infiltration via partially dissolved internal oxide structures has been proposed in this thesis to explain the veins of Zn and Fe-Al compounds embedded in the top 200 nm of substrate (Figure 5.10 and Figure 5.12). The publications by Pourmajidian and McDermid [23,33,34] undeniably show that this is not necessary for good reactive wetting of medium-Mn substrates, since their steels were not flash pickled and were successfully galvanized without this mechanism. However, the present work shows that medium-Mn substrates that are processed in a two-stage annealing treatment with intermediate flash pickling may have some near-surface channels from selectively dissolved oxides which can be effectively impregnated by liquid bath metal. The infiltrated bath metal solidified without significant shrinkage porosity (Figure 5.10 and Figure 5.12), provided mechanical interlocking of the coating with the substrate, and did not adversely affect the bending performance or coating adherence of the material (Figure 5.4 and Figure 5.5).

Accordingly, this substrate (and similar) would likely be strong candidates for processing through conventional CGL infrastructure and would not necessarily require strategies such as high

dew point annealing or surface-active element alloying additions. The two-stage thermal cycle simultaneously promotes more robust mechanical properties than a single-step intercritical annealing cycle while facilitating reactive wetting of the substrate. A summative schematic showing the evolution of the substrate bulk and surface at each step in the processing route is presented in Figure 6.1.
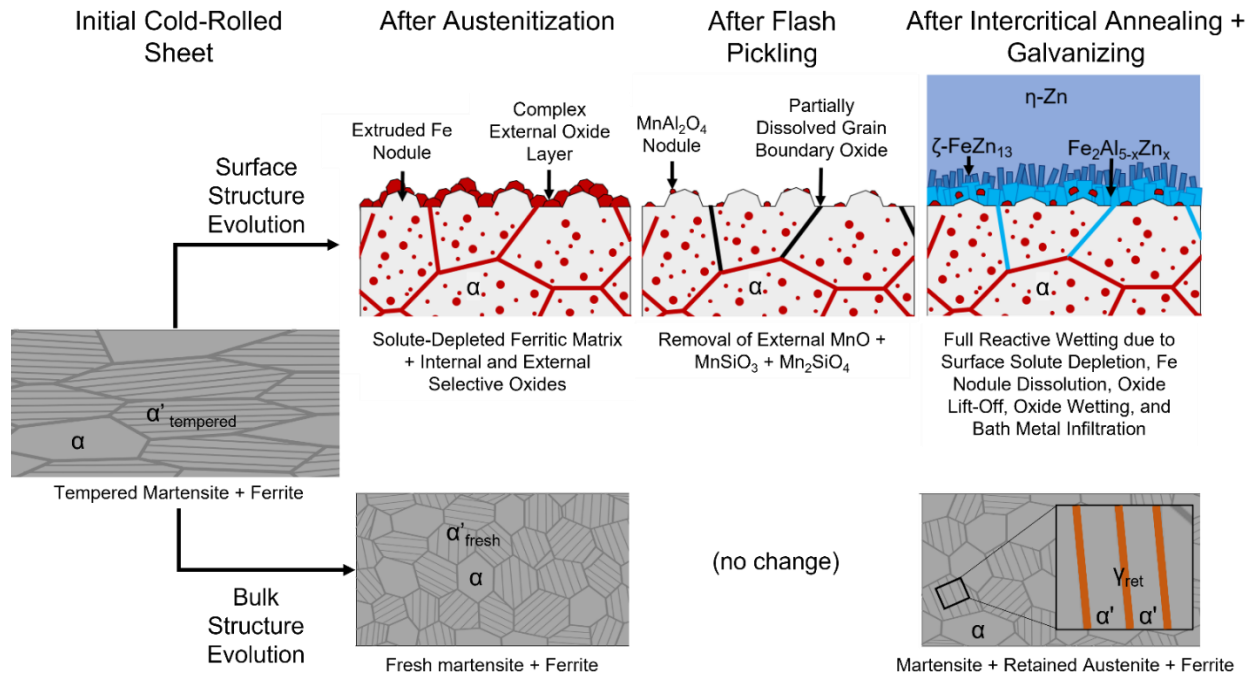
Figure 6.1: Summative schematic showing the evolution of the surface and bulk structures at each stage in the processing cycle, leading to the desired final bulk microstructure and successful galvanizing of the substrate.

6.3   References

[1]   J.R. McDermid, H.S. Zurob, Y. Bian, Stability of Retained Austenite in High-Al, Low-Si TRIP-Assisted Steels Processed via Continuous Galvanizing Heat Treatments, Metall. Mater. Trans. A. 42 (2011) 3627–3637.

[2]   K.M.H. Bhadhon, Effect of Starting Microstructure and CGL Compatible Thermal Processing Cycle on the Mechanical Properties of a Medium-Mn Third Generation Advanced High Strength Steel, McMaster University, 2017.

[3]   K.M.H. Bhadhon, J.R. McDermid, X. Wang, E.A. McNally, F.E. Goodwin, Fine-Scale Microstructure Characterization And Mechanical Properties Of CGL-Compatible Heat Treated Medium-Mn TRIP Steel, in: Proc. 11th Conf. Zinc Zinc Alloy Coat. Steel Sheet, Galvatech 2017, Tokyo, 2017: pp. 493–500.

[4]   V. Patel, Microstructure and Mechanical Properties of Medium Mn Steel, McMaster University, 2019.

[5]   S. Lee, B.C. De Cooman, On the selection of the optimal intercritical annealing temperature for medium Mn TRIP steel, Metall. Mater. Trans. A. 44 (2013) 5018–5024. doi:10.1007/s11661-013-1860-2.

[6]   H. Luo, H. Dong, New ultrahigh-strength Mn-alloyed TRIP steels with improved formability manufactured by intercritical annealing, Mater. Sci. Eng. A. 626 (2015) 207–212.

[7]   B.C. De Cooman, Y. Estrin, S.K. Kim, Twinning-induced plasticity (TWIP) steels, Acta Mater. 142 (2018) 283–362. doi:10.1016/j.actamat.2017.06.046.

[8]   D.K. Matlock, J.G. Speer, Design Considerations for the Next Generation of Advanced High Strength Steel Sheets, in: H.C. Lee (Ed.), Proc. 3rd Int. Conf. Struct. Steels, Korean Institute of Metals and Materials, Seoul, Korea, 2006: pp. 774–781.

[9]   D.K. Matlock, J.G. Speer, Third Generation of AHSS: Microstructure Design Concepts, Springer, Jamshedpur, India, 2009. doi:10.1007/978-1-84882-454-6_11.

[10]   D.K. Matlock, J.G. Speer, E. De Moor, P.J. Gibbs, Recent Developments in Advanced High Strength Sheet Steels for Automotive Applications: An Overview, JESTECH. 15 (2012) 1–12.

[11]   K. Steineder, D. Krizan, R. Schneider, C. Béal, C. Sommitsch, The effects of intercritical annealing temperature and initial microstructure on the stability of retained austenite in a 0.1C-6Mn steel, Mater. Sci. Forum. 879 (2017) 1847–1852. doi:10.4028/www.scientific.net/MSF.879.1847.

[12]   K. Steineder, D. Krizan, R. Schneider, C. Béal, C. Sommitsch, On the Damage Behavior of a 0.1C6Mn Medium-Mn Steel, Steel Res. Int. 89 (2018) 1700378. doi:10.1002/srin.201700378.

[13]   J. Datsko, C.T. Yang, Correlation of bendability of materials with their tensile properties, J. Manuf. Sci. Eng. Trans. ASME. 82 (1960) 309–312. doi:10.1115/1.3664236.

[14]   J. Sarkar, T.R.G. Kutty, D.S. Wilkinson, J.D. Embury, D.J. Lloyd, Tensile properties and bendability of T4 treated AA6111 aluminum alloys, Mater. Sci. Eng. A. 369 (2004) 258–266. doi:10.1016/j.msea.2003.11.022.

[15]   B. Hance, Advanced high strength steel: Deciphering local and global formability, in: Proc. Int. Automot. Body Congr. (IABC 2016 Dearborn), Dearborn, MI, 2016.

[16]   P. Larour, J. Freudenthaler, T. Weissböck, Reduction of cross section area at fracture in tensile test: Measurement and applications for flat sheet steels, J. Phys. Conf. Ser. 896 (2017). doi:10.1088/1742-6596/896/1/012073.

[17]   R.A. Rapp, Kinetics, Microstructures and Mechanism of Internal Oxidation - Its Effect and Prevention in High Temperature Alloy Oxidation, Corrosion. 21 (1965) 382–402. doi:10.5006/0010-9312-21.12.382.

[18]   Y.F. Gong, H.S. Kim, B.C. De Cooman, Formation of Surface and Subsurface Oxides during Ferritic, Intercritical and Austenitic Annealing of CMnSi TRIP Steel, ISIJ Int. 48 (2008) 1745–1751. doi:10.2355/isijinternational.48.1745.

[19]   G. Seyed Mousavi, J.R. McDermid, Selective Oxidation of a C-2Mn-1.3Si (wt pct) Advanced High-Strength Steel During Continuous Galvanizing Heat Treatments, Metall. Mater. Trans. A. 49 (2018) 5546–5560. doi:10.1007/s11661-018-4854-2.

[20]   G. Seyed Mousavi, J.R. McDermid, Effect of dew point on the reactive wetting of a C-2Mn-1.3Si (wt%) advanced high strength steel during continuous galvanizing, Surf. Coatings Technol. 351 (2018) 11–20. doi:10.1016/j.surfcoat.2018.06.060.

[21]   G. Seyed Mousavi, B. Langelier, J.R. McDermid, Effect of Sn Addition, Process Atmosphere pO2, and Annealing Time on the Selective Oxidation of a C-2Mn-1.7Si (Wt Pct) Advanced High-Strength Steel During Continuous Galvanizing, Metall. Mater. Trans. A. 50 (2019) 2898–2911. doi:10.1007/s11661-019-05202-3.

[22]   M. Pourmajidian, B. Langelier, J.R. McDermid, Effect of Process Atmosphere Dew Point and Tin Addition on Oxide Morphology and Growth for a Medium-Mn Third Generation Advanced Steel During Intercritical Annealing, Metall. Mater. Trans. A. 49 (2018) 5561–5573. doi:10.1007/s11661-018-4855-1.

[23]   M. Pourmajidian, J.R. McDermid, Selective Oxidation of a 0.1C-6Mn-2Si Third Generation Advanced High-Strength Steel During Dew-Point Controlled Annealing, Metall. Mater. Trans. A. 49 (2018) 1795–1808. doi:10.1007/s11661-018-4513-7.

[24]   R. Kavitha, J.R. McDermid, On the in-situ aluminothermic reduction of manganese oxides in continuous galvanizing baths, Surf. Coat. Technol. 212 (2012) 152–158. doi:10.1016/j.surfcoat.2012.09.038.

[25]   C.F. Jones, R.S.C. Smart, P.S. Turner, Dissolution kinetics of manganese oxides. Effects of preparation conditions, pH and oxidation/reduction from solution, J. Chem. Soc. Faraday Trans. 86 (1990) 947–953. doi:10.1039/FT9908600947.

[26]   J.F. Banfield, G.G. Ferruzzi, W.H. Casey, H.R. Westrich, HRTEM study comparing naturally and experimentally weathered pyroxenoids, Geochemica Cosm. Acta. 59 (1995) 19–31.

[27]   W.H. Casey, M.F. Hochella, H.R. Westrich, The surface chemistry of manganiferous silicate minerals as inferred from experiments on tephroite (Mn2SiO4), Geochim. Cosmochim. Acta. 57 (1993) 785–793. doi:10.1016/0016-7037(93)90168-V.

[28]   J.R. Mackert, R.D. Ringle, C.W. Fairhurst, High-temperature Behavior of a Pd-Ag Alloy for Porcelain, J. Dent. Res. 62 (1983) 1229–1235. doi:10.1177/00220345830620121201.

[29]   S. Guruswamy, S.M. Park, J.P. Hirth, R.A. Rapp, Internal oxidation of Ag-in alloys: Stress relief and the influence of imposed strain, Oxid. Met. 26 (1986) 77–100. doi:10.1007/BF00664274.

[30]   Z.T. Zhang, I.R. Sohn, F.S. Pettit, G.H. Meier, S. Sridhar, Investigation of the Effect of Alloying Elements and Water Vapor Contents on the Oxidation and Decarburization of Transformation-Induced Plasticity Steels, Metall. Mater. Trans. B. 40 (2009) 567–584. doi:10.1007/s11663-009-9255-x.

[31]   E.M. Bellhouse, Galvanizing of Al-Si TRIP-Assisted Steels, McMaster University, 2010.

[32]   E.M. Bellhouse, J.R. McDermid, Selective Oxidation and Reactive Wetting during Galvanizing of a CMnAl TRIP-Assisted Steel, Metall. Mater. Trans. A. 42A (2011) 2753–2768. doi:10.1007/s11661-010-0192-8.

[33]   M. Pourmajidian, J.R. McDermid, On the reactive wetting of a medium-Mn advanced high-strength steel during continuous galvanizing, Surf. Coatings Technol. 357 (2019) 418–426. doi:10.1016/j.surfcoat.2018.10.028.

[34]   M. Pourmajidian, J.R. McDermid, Effect of Annealing Temperature on the Selective Oxidation and Reactive Wetting of a 0.1C-6Mn-2Si Advanced High Strength Steel During Continuous Galvanizing Heat Treatments, ISIJ Int. 58 (2018) 1635–1643. doi:10.2355/isijinternational.ISIJINT-2017-688.

7   Conclusions

It has been determined that CGL-compatible annealing parameters can be selected for medium-Mn 3G AHSS grades that result in the desired mechanical property targets and the formation of high-quality galvanized coatings. The key findings from the present work are summarized below.

The prototype 0.15C-6Mn-1.9Al-1.1 Si (wt%) steel achieved the general mechanical property targets for 3G AHSS using a two-stage CGL-compatible intercritical annealing treatment. The MF annealing step (890°C for 600 s) resulted in a 80% martensitic-20% ferritic microstructure with no detectable retained austenite. Subsequent intercritical annealing for 120 s from this martensitic-ferritic microstructure resulted in significant volume fractions of lamellar retained austenite whose chemical composition was a strong function of intercritical annealing temperature. As a result, several different mechanical property profiles were obtained due to differences in TRIP kinetics. The MF-710°C samples had the highest UTS × TE combination, which was attributed to these samples having a retained austenite chemical composition which enabled gradual exhaustion of the TRIP effect due to an appropriate M_s^{σ} , as well as extensive mechanical twinning due to an appropriate stacking fault energy. Although the properties of the experimental substrate in this work were highly sensitive to IA temperature, it was determined that the desired 3G AHSS mechanical properties could be achieved using CGL-compatible thermal processing routes.

The effects of process atmosphere pO_2 on internal and external oxidation during each annealing step were determined. The MF treatment at dew points of -30°C, -10°C, and +5°C resulted in the formation of a 150-200 nm thick, compact external oxide layer comprising MnO, $MnAl_2O_4$ and $MnSiO_3/Mn_2SiO_4$. Only discrete nodules of $MnAl_2O_4$ remained after flash pickling. No significant changes to the external oxide thickness or chemical speciation with process atmosphere dew point were found after intercritical annealing at 710°C for 120 s, since the solute

in the near-surface matrix had already selectively oxidized during the prior MF annealing step. The pre-immersion surface microstructure, therefore, comprised dispersed $MnAl_2O_4$ nodules (approximately 50 nm thick) and extruded Fe nodules from the oxide molar volume increase associated with internal oxidation. The internal grain boundary oxides had a core-shell oxide morphology, with Mn_2SiO_4 shells surrounding Al_2O_3 and $MnAl_2O_4$ cores. Subsequent intercritical annealing at 710°C for 120s at a dew point of -30°C, -10°C, or +5°C did not significantly alter the internal oxidation depth or oxide morphology.

Successful reactive wetting was achieved for the experimental substrate by a conventional Zn(Al,Fe) continuous galvanizing bath containing 0.2 wt% dissolved Al using a 4 s immersion time. High-quality, formable galvanized coatings were formed when using an MF dew point of -10°C and all experimental IA dew points. The dominant reactive wetting mechanism was direct dissolution and wetting of the solute depleted Fe surface by the liquid bath metal on account of the large area fraction of metallic Fe available arising from the flash pickling treatment and the extruded Fe nodules from internal oxidation. Several secondary reactive wetting mechanisms such as oxide cracking and lift-off, oxide wetting, and oxide bridging were documented. Moreover, bath metal penetration into the substrate by infiltration into partially dissolved internal oxide structures was identified as a novel reactive wetting mechanism. The coatings resisted cracking or flaking during three-point bending.

8   Opportunities for Future Research

8.1   Future Research Directions

There are numerous research directions worthy of future investigation that would accelerate the industrial development and implementation of galvanized medium-Mn 3G AHSS for automotive applications. Some of the next steps that could be explored as a continuation of the work presented in this thesis are:

1) *Modifying the chemical compositions of the prototype substrate to include micro-alloying elements (such as V, Nb, Ti).* It is expected that the precipitation strengthening effects of V/Nb/Ti-carbides/nitrides/carbonitrides would improve the mechanical properties of the substrate. However, it would be helpful to determine the extent to which the retained austenite laths that surround these particles would be depleted in C (and therefore the extent to which the retained austenite would be chemically destabilized relative to a V/Nb/Ti-free reference alloy). This would likely affect the thermal processing requirements, TRIP/TWIP kinetics, formability, etc.

2) *Modifying the chemical compositions of the prototype substrate to include surface-active elements (such as Sn, Sb, Bi).* Surface active elements have been shown to retard selective oxidation kinetics and thus improve reactive wetting [1–7]. This thesis has shown that the two-stage processing of medium-Mn substrates can result in a relatively pure Fe surface that is available to react with the galvanizing bath due to the oxidation of solute near the surface during austenitization. However, the surface-active element alloying strategy may be beneficial for medium-Mn substrates undergoing a one-stage intercritical annealing process without the surface solute-depleting effects of the austenitization step. In these cases, it would be essential to know whether these additions would deleteriously impact

complex forming processes (such as hole-expansion and bending) due to grain boundary embrittlement [8].

3) *Additional formability testing, including high strain rate mechanical property assessment.* The mechanical properties and fracture mechanisms of medium-Mn 3G AHSS in bending, plane strain, biaxial tension, hole expansion, and other common forming operations should be documented in order for these alloys to be applied by the industry. It would also be helpful to know the strain rate sensitivity of medium-Mn 3G AHSS in order to determine optimal forming process windows and model the deformation of vehicle components during crash events.

4) *Weldability studies.* Resistance spot welding (RSW) is a common joining technique for automotive sheet, so the dynamic resistance profile, heat generation, and weld development during the RSW process must be well-understood for 3G AHSS. Galvanized coatings are known to affect the RSW process and alter the dynamic resistance curve [9,10]. Moreover, work on a 0.1C-2Mn-0.7Si steel has shown that the internal Mn and Si oxides that form during annealing can increase the overall resistance of the faying surfaces, decrease the heat generation during welding, and shift the weld lobe curve to higher values of applied current or welding cycle time [11]. Appropriate modifications to the weld schedule should be made to accommodate these changes.

5) *Modelling of the selective oxidation process.* Though many efforts to model the selective oxidation of medium-Mn 3G AHSS alloys under CGL conditions are underway by various research groups, these efforts have primarily focused on thermodynamic considerations. Ideally the results would converge to a model (like that of Wagner [12], with accurate

values of g*, diffusion coefficients, etc.) that would account for the kinetics of the formation of complex oxides observed in this and many other works.

6) *Reactive wetting of medium-Mn 3G AHSS by other bath compositions (such as galvanneal or various Zn-Al-Mg alloys).* The effects of bath chemistry and process atmosphere pO_2 on the reactive wetting; coating phase morphology and distribution; interfacial layer formation and breakdown; and corrosion performance would be interesting to document.

7) *Fatigue performance of coated medium-Mn 3G AHSS.* This would be a two-pronged investigation to determine the resistance of the substrate to failure by fatigue, in addition to the determination of the effects of repeated loading on the intactness and corrosion resistance of the galvanized coating.

8.2   References

[1]   M. Pourmajidian, J.R. McDermid, On the reactive wetting of a medium-Mn advanced high-strength steel during continuous galvanizing, Surf. Coatings Technol. 357 (2019) 418–426. doi:10.1016/j.surfcoat.2018.10.028.

[2]   A. Ruck, D. Monceau, H.J. Grabke, Effects of tramp elements Cu, P, Pb, Sb and Sn on the kinetics of carburization of case hardening steels, Steel Res. Int. 67 (1996) 240–246. doi:10.1002/srin.199605484.

[3]   L. Cho, M.S. Kim, Y.H. Kim, B.C. De Cooman, Influence of Minor Alloying Elements on Selective Oxidation and Reactive Wetting of CMnSi TRIP Steel during Hot Dip Galvanizing, Metall. Mater. Trans. A. 45 (2014) 4484–4498. doi:10.1007/s11661-014-2394-y.

[4]   L. Cho, E.J. Seo, G.S. Jung, D.W. Suh, B.C. De Cooman, Surface Selective Oxidation of Sn-Added CMnSi TRIP Steel, Metall. Mater. Trans. A. 47 (2016) 1705–1719. doi:10.1007/s11661-016-3331-z.

[5]   J. Oh, L. Cho, M.S. Kim, K. Kang, B.C. De Cooman, The Effect of Bi on the Selective Oxide Formation on CMnSi TRIP Steel, Metall. Mater. Trans. A. 47 (2016) 5474–5486. doi:10.1007/s11661-016-3735-9.

[6]   M. Pourmajidian, B. Langelier, J.R. McDermid, Effect of Process Atmosphere Dew Point and Tin Addition on Oxide Morphology and Growth for a Medium-Mn Third Generation Advanced Steel During Intercritical Annealing, Metall. Mater. Trans. A. 49 (2018) 5561–5573. doi:10.1007/s11661-018-4855-1.

[7]   G. Seyed Mousavi, B. Langelier, J.R. McDermid, Effect of Sn Addition, Process Atmosphere pO2, and Annealing Time on the Selective Oxidation of a C-2Mn-1.7Si (Wt Pct) Advanced High-Strength Steel During Continuous Galvanizing, Metall. Mater. Trans. A. 50 (2019) 2898–2911. doi:10.1007/s11661-019-05202-3.

[8]   H.J. Grabke, Surface and Grain Boundary Segregation of Antimony and Tin - Effects on Steel Properties, Kovine, Zlitine, Tehnol. 30 (1996) 483–495.

[9]   S.A. Gedeon, Resistance Spot Welding of Galvanized Sheet Steel, Massachusetts Institute of Technology, 1984.

[10] N.T. Williams, J.D. Parker, Review of resistance spot welding of steel sheets: Part 1 - Modelling and control of weld nugget formation, Int. Mater. Rev. 49 (2004) 45–75. doi:10.1179/095066004225010523.

[11] X. Han, C. DiGiovanni, J.R. McDermid, E. Biro, N.Y. Zhou, Effect of internal oxidation on the weldability of CMnSi steels, Weld. World. 63 (2019) 1633–1639. doi:10.1007/s40194-019-00798-x.

[12] C. Wagner, Reaktionstypen bei der Oxydation von Legierungen, Zeitschrift Für Elektrochemie. 63 (1959) 772–782.